

# Higher Order Couplings in the Clustering of Biased Tracers of Large-Scale Structure



**Syed Muntazir Mehdi Abidi**

Supervisor: Dr. Tobias Baldauf

Department of Applied Mathematics and Theoretical Physics  
University of Cambridge

This dissertation is submitted for the degree of  
*Doctor of Philosophy*

I dedicate this thesis to my late parents for their unconditional love, support, and for everything.

## Declaration

I hereby declare that except where specific reference is made to the work of others, the contents of this dissertation are original and have not been submitted in whole or in part for consideration for any other degree or qualification in this, or any other university. This dissertation is my own work and contains nothing which is the outcome of work done in collaboration with others, except as specified in the text and Acknowledgements. Chapter 4 contains my original work published in [2], and is done in collaboration with Tobias Baldauf. Chapter 5 is based on my work done in collaboration with Omar Darwaish, Simon Foreman, Tobias Baldauf, Blake Sherwin and Daan Meerburg [59]. In [59], density field reconstruction using numerical simulations is my original work, also all other results and figures in the paper have been cross-checked by my own independent code. All figures in this thesis are obtained from my code, except as specified in the text. Chapter 6 is my original unpublished work and will be submitted for publication soon.

Syed Muntazir Mehdi Abidi  
August 2020

## Abstract

**Thesis Title:** Higher Order Couplings in the Clustering of Biased Tracers of Large-Scale Structure

**Author's Name:** Syed Muntazir Mehdi Abidi

The Large-Scale Structure (LSS) of the Universe, i.e. the distribution of matter and luminous tracers (such as galaxies), contains a wealth of information about the origin, composition, and evolution of the Universe. In order to extract this information, the non-linearities present in late-time observables provided by LSS surveys must be understood well. In general, there are three main sources of non-linearities: (1) non-linear matter clustering due to gravity; (2) non-linear biasing, i.e. the relation between the distribution of tracers and dark matter; and (3) primordial non-Gaussianity, which induces non-linearities in the initial conditions. The Effective Field Theory of Large-Scale Structure (EFTofLSS) provides a powerful framework to model the non-linear clustering due to gravity. In this thesis, we focus on understanding the non-linearities due to galaxy biasing using the EFTofLSS and numerical  $N$ -body simulations. This thesis is comprised of the following three projects:

1. In the first part, we present a novel method to constrain quadratic and cubic galaxy bias parameters in dark matter simulations. The natural statistics to constrain quadratic and cubic bias parameters are tree-level bispectrum and trispectrum, respectively. Since these statistics are computationally quite expensive, we use efficient squared and cubic field estimators that contain integrated bispectrum and trispectrum information. We use the constraints to model the one-loop halo-matter power spectrum and show that the results agree with simulations up to  $k_{\max} = 0.1h \text{ Mpc}^{-1}$  once an additional derivative bias is implemented (Published in: Abidi & Baldauf, JCAP07(2018)029 [2]).
2. In the second part, we develop a formalism to reconstruct the linear density field based on quadratic couplings in galaxy clustering. We employ a quadratic estimator inspired

by Cosmic Microwave Background (CMB) lensing reconstruction. We incorporate non-linearities due to gravity, galaxy biasing and primordial non-Gaussianity, and verify our predictions with  $N$ -body simulations. We perform a Fisher matrix analysis on how the reconstructed field in combination with the biased tracer field can improve constraints on local type primordial non-Gaussianity. We find significant improvement on constraints due to cosmic variance cancellation resulting from the additional correlated modes of the reconstructed field, similar to multitracer analyses (in preparation for submission to Physical Review D; e-print: [59]).

3. In the third part, we develop a method to constrain non-linear galaxy bias parameters using the two- and three-point functions of projected galaxy clustering in correlation with CMB lensing convergence. The project thus aims to bring the methodology developed in project 1 above closer to data. We develop the quadratic field method for projected fields to avoid complications from non-linear redshift space distortions. We perform a Fisher forecast to show that this method can indeed be used to put constraints on bias parameters and the amplitude of matter fluctuations. Finally, using  $N$ -body simulations we ascertain that the projected statistics do indeed reduce the impact of finger-of-god corrections (in preparation for submission to JCAP).

## Acknowledgements

First and foremost, I would like to thank my supervisor, Dr Tobias Baldauf, for everything during these four years of my PhD. His support and guidance - academically, professionally and personally - have been genuinely valuable. This PhD work would have not been possible without his help, and I am incredibly indebted to him for all of this. The most valuable lesson I have learned from him is how to do research. His way of understanding a problem, breaking it down to fundamentals and being very careful about details are truly inspiring. I also learned that the best way to do research is to start working on a research problem and learn all relevant details along the way. Instead of spending so much time on reading endless papers at the beginning of my PhD, I was very fortunate to have started working on a particular research problem under his supervision, and by the time I was done with my first project I was surprised how much I had learned from the process of solving the problem.

I am grateful to my advisors, Professor Paul Shellard and Dr Blake Sherwin, for their invaluable advice and support. I am very fortunate to have collaborated with Blake Sherwin on two exciting projects. It has been a great learning experience working with him; I am very inspired by his insights and ability to ask great questions. I appreciate his passion for cosmology and his overall positivity. I am also very grateful to him for his generous support towards my fourth year PhD funding from his ERC grant.

I am genuinely thankful to the Cambridge Commonwealth Trust and the Pakistan Higher Education Commission for generous support during four years of my PhD. I also appreciate the support from the Cambridge Centre for Theoretical Cosmology, St Edmund's College (for travel grants and support towards the fourth year), Postgraduate Lundgren Award (support towards the fourth year) and Santandar Award (at the beginning of my PhD). I would also like to mention Dr Ishrat Hussain, who personally wrote to Sir Anwar Pervez on my behalf.

On his recommendation, Sir Anwar Pervez gave me generous relocation awards twice (for my Masters in 2015 and PhD in 2016) via his Bestway Foundation. I am also thankful to the National Centre for Physics, Islamabad, Pakistan, for their hospitality and for inviting me to present my PhD research there. The numerical part of this thesis was performed using the DiRAC COSMOS supercomputer and greatly benefited from the support of K. Kornet.

I am grateful to my other collaborators: Omar Darwish, Simon Foreman, and Daan Meerburg. I enjoyed working with them on the density reconstruction project - it was such a great collaboration. I have also enjoyed many useful discussions about cosmology, physics, data science and much more with my office mate and a great fiend, Oliver Leitch. Oliver has a great understanding of many difficult concepts, and I have learned so much from our discussions in our office and during the HEP/GR coffee breaks. I also thank my other office mate, Josh Kirklin, for useful discussions about physics. I appreciate his passion for research and his great sense of humour.

I am, as always, much thankful to Professor Fernando Quevedo for his endless support and his genuine belief in me. I consider Professor Fernando as my biggest inspiration. I have had quite interesting discussions about physics, research and life in general with him over all these years. Due to his brilliant advice and guidance, I was able to do well in my Part III Mathematical Tripos exams and also in the PhD entrance exam. He strongly suggested me to choose Dr Tobias Baldauf as my PhD advisor, and I would say it was a great suggestion. I remember when I started my PhD, one day, he told me: the key to success and being happy is to be always humble. I am genuinely grateful for all his help and support.

I cannot thank enough to my college Tutor, Dr Michele Gamelos, for her support and help. She is one of the most beautiful persons I have met in my life. I am glad she has been my Tutor since my masters year. Whenever I had some problems (academic-related or personal), she was always available to help. Everyone who has had her as their Tutor is very fortunate. I wish her all the best for her new role as Senior Tutor at Murray Edwards College.

I have many friends in Cambridge who have made my life experience here very exciting and memorable. I cannot mainly thanks to everyone, but I would like to say a few sentences about a few very special people. I will start with the most fantastic friend SengBeng Goh. I met him during my masters year in 2015 at St Edmund's college when he started his Mathematical Tripos. We used to discuss mathematics, physics, philosophy and much more. Our discussions have helped us improve overall as a human being (better ones). We both have helped each other during difficult Cambridge lives. He has continuously

supported me in my life, have shared with my valuable lessons of his life and continuously pushed me to do excellent PhD. Talking to him during the pandemic and during my thesis writing times gave me so much positive energy to do well. I am glad I have met such a fantastic friend in Cambridge; our friendship will be alive forever.

Another most beautiful person I want to thank is Khayam Javed. I have learned so much from Khayam. Khayam is one of the most intelligent and disciplined people I have met. He has made my Cambridge life exciting, and I am fortunate to be his friend. His constant support and motivation towards my PhD research cannot be appreciated enough. Whenever I felt down, or a bit depressed, his sense of humour always cheered me up. With Khayam, I would like to mention his lovely wife Saher Khayam and their beautiful, the most adorable baby, Omar Khayam. I lived with them during the year of my PhD (also during COVID-19 pandemic). I think I would not have been able to focus on my PhD research and finish my thesis on time without them being around and without their support. I wish them the happiest life together.

Thanks to my friend Dr Tashfeen S Ali. I met him at the beginning of my third year of PhD when he came to Cambridge for studies and to work at Addenbrooke's hospital. What a fantastic person he is - full of positive energy and wisdom! We had great times together at Carlos BBQ, where we used to have endless discussions about so many exciting topics. Thanks to him for encouraging me and being one of my best friends with whom I can share anything. His sense of humour has never let me down. I also want to thank my friend Gunther Klobe. We both met on the 24th of April, 2016, at the Cambridge Trust annual scholars event and became friends. The most impressive highlight is that we both share the same birthday (& year) and we met on our birthday, that is the 24th of April. Gunther is one of the happiest persons I know. He has taught me the 'art of being happy'. The lessons I have learned from Gunther have made me happier than ever before.

I am also truly grateful to my amazing friend, Elizabeth Riley. I am so thankful to her and her mother for reading my thesis and for their kind remarks. I cannot thank Elizabeth enough for encouraging me during my thesis writing times and for listening to my random useless stories (well, some were exciting). Our friendship will always flourish. I wish her best for her PhD research at Cambridge University.

In Cambridge, there are many exciting friends I made who have consistently supported me during all these five years here. Special thanks to Daniel Kornum, Taarika Singh, Safwan Khan (special thanks for proof reading my thesis), Viona Deconinck, Conor McGlynn, Maria Khan, Ahmed Zaidi, Arif Naveed, Raman Singh, Aman Singh (meeting with Aman and



Raman's parents in Cambridge for dinner and exciting discussion about cosmology with them is one of the sweetest memories I have), Megan Smith, Shujaat Abbas, Radhika Gupta, Aadil Shah, Arqum Anwar, Abdullah Athar, Minaam Abbas, Aliya Khalid, Muhammad Rabah, Alyoysius Ng, Ian Mak, Jonathan Rawlinson, Becky Whitman (I wish Jonathan and Becky a very happy marriage life together, I am so glad they introduced me to Parkruns), Frank Qu, Philip Clarke, Boryana Hadzhiyska, Maharashi, Girish Nivarti, Mussarrat (for delicious food in Cambridge and for her hospitality during my academic visits in Lahore), Ahsan Murtaza, Aleena Haider, Benjamine and Siddharth Soni (for being fantastic housemates), Ammar Khan (for great advice at the beginning of my PhD and for all other useful discussions), Leong Khim Wong, Amelia Louise, Theodore Bjorkmo, Alexandra (we took a course together on Venture Capital in Innovation Economy), all my St Edmund's college friends over the last five years and amazing people I met and had great discussions in the dining hall, Cora Uhlemann (for her constant encouragement and great advice for research), James Ferguson, Jonathan Hung (for his excellent advice on different occasions during my PhD research and also introducing me to CUBA integral packages), all fantastic people I have interacted at the Centre for Mathematical Sciences (CMS) and specially during the HEP/GR coffee sessions, tutorial office at St Edmund's college, graduate and undergraduate admissions office at CMS, and the University counselling service.

I would also like to thank my family for their love and endless support all my life. Finishing my PhD at the University of Cambridge would not have been possible without their help. Thanks to Saba Naz Abidi, Hina Zehra Abidi, Sara Qamar Abidi, Mazhar Hasnain Abidi, Raza Abidi. All of them helped me and given me so much love, especially after my parents' death. I want to especially thank my younger sibling, my best friend, and the wisest person - Mojiz Mehdi Abidi. Since my mother died in 2013, he has been pushing me and encouraging me towards achieving my goals. Although he had been having a hard time himself, he has always made sure that we all are happy. I would like to mention that Mojiz never liked or understood physics, but still before I came to Cambridge, he used to listen to me talking about physics for hours. I am amazed by his patience and support. All of that had motivated me to keep my interest in physics alive. My journey from Pakistan to Cambridge University and finishing a PhD here is mostly because of his encouragements.

Finally, I am grateful to my late parents, Qamar Hasnain Abidi and Tasneem Fatima Rizvi, for their unconditional love, support, sacrifices and constant guidance. The last memory of my father I have is when I had a Skype call with him, and I showed my Part III General Relativity notes for the first time. He looked at them and smiled in silence; his smile said everything. After a month, three days before my PhD entrance exam, he passed away. I wish I fulfil all his dreams and became a wise and amazing human being like him. My passion for

education came from my father, and my passion for mathematics came from my mother. My mother taught me how to do mathematics; she also taught me how to be kind and humble. They will always be alive in my sweet memories.

# Table of contents

<b>List of figures</b>	<b>xv</b>
<b>List of tables</b>	<b>xxv</b>
<b>1 Introduction</b>	<b>3</b>
1.1 Thesis Outline . . . . .	4
<b>2 Standard Model of Cosmology</b>	<b>7</b>
2.1 Metric . . . . .	7
2.2 Dynamics . . . . .	8
2.3 Kinematics . . . . .	11
2.4 Redshift . . . . .	12
2.5 Hubble's law . . . . .	13
2.6 $\Lambda$ CDM . . . . .	14
2.7 Cosmic Inflation . . . . .	15
2.7.1 Horizon Problem . . . . .	16
2.7.2 Conditions for Inflation . . . . .	17
2.7.3 The Physics of Inflation . . . . .	19
2.7.4 Slow-Roll Inflation . . . . .	20
2.7.5 Metric Perturbations . . . . .	22
2.7.6 Statistics of Scalar Perturbations . . . . .	23
<b>3 Large-Scale Structure of the Universe</b>	<b>26</b>
3.1 Standard Perturbation Theory (SPT) . . . . .	27
3.1.1 Linearized Equations . . . . .	29
3.1.2 Fluid Equations in Fourier Space . . . . .	30

---

3.1.3	Perturbative Solutions . . . . .	31
3.1.4	Feynman Rules . . . . .	33
3.1.5	Power Spectrum . . . . .	34
3.1.6	Bispectrum . . . . .	38
3.1.7	Shortcomings of Standard Perturbation Theory . . . . .	40
3.2	Effective Field Theory of Large-Scale Structure . . . . .	40
3.2.1	Coarse-grained Equations of Motion . . . . .	42
3.2.2	Integrating out UV Physics . . . . .	43
3.2.3	EFT and Perturbation Theory . . . . .	44
3.3	Lagrangian Perturbation Theory (LPT) . . . . .	46
3.3.1	Zeldovich Approximation (ZA) . . . . .	47
3.3.2	Second Order Lagrangian Perturbation Theory . . . . .	48
3.3.3	Generalised $n$ th Order Solution . . . . .	49
3.4	Biased Tracers . . . . .	49
3.4.1	Spherical Collapse . . . . .	50
3.4.2	Press-Schechter Mass Function . . . . .	52
3.4.3	Peak-background Split . . . . .	54
3.4.4	Effective Theory of Bias . . . . .	55
3.4.5	Halo Statistics . . . . .	57
3.5	$N$ -body Codes . . . . .	59
<b>4</b>	<b>Cubic Halo Bias in Eulerian and Lagrangian Space</b>	<b>62</b>
4.1	Introduction . . . . .	62
4.2	Halo Bias . . . . .	66
4.2.1	Eulerian Bias Model . . . . .	66
4.2.2	Lagrangian Bias Model . . . . .	68
4.2.3	Time Evolution of the Lagrangian Bias . . . . .	69
4.2.4	Co-evolution of Dark Matter and Halos . . . . .	71
4.2.5	Bias Predictions . . . . .	72
4.3	Quadratic and Cubic Fields . . . . .	73
4.3.1	Quadratic Fields . . . . .	74
4.3.2	Cubic Fields . . . . .	75
4.3.3	Bispectrum and Trispectrum Estimators . . . . .	78
4.3.4	Removing the UV Sensitive Diagrams . . . . .	78
4.3.5	Counter Term: Taylor Expansion Around $R_h$ . . . . .	79
4.4	Methodology . . . . .	80
4.4.1	Numerical Simulations . . . . .	80
4.4.2	Parameter Estimation . . . . .	81

---

4.5	Results . . . . .	82
4.5.1	Some Preliminary Checks . . . . .	82
4.5.2	Bias Constraints . . . . .	84
4.5.3	Lagrangian Bias from Protohalos . . . . .	85
4.5.4	Eulerian Bias from the Late-time Halo Field . . . . .	86
4.5.5	Constraints on Lagrangian Bias Parameters from Different Models . . . . .	88
4.5.6	Application: One-loop Halo-Matter Power Spectrum . . . . .	89
4.6	Summary & Conclusions . . . . .	91
<b>5</b>	<b>Density Field Reconstruction from Biased Tracers and Constraining local <math>f_{\text{NL}}</math></b>	<b>102</b>
5.1	Introduction . . . . .	102
5.2	Density Field Reconstruction - theory . . . . .	106
5.2.1	Quadratic Estimators . . . . .	106
5.2.2	Bias Expansion with non-Gaussianity . . . . .	110
5.2.3	Noise and Contamination . . . . .	112
5.2.4	Bias-Hardening Case: Why doesn't it Work? . . . . .	113
5.2.5	Shot Noise . . . . .	114
5.3	$N$ -body Simulations . . . . .	119
5.3.1	Setup . . . . .	119
5.3.2	Generation of Quadratic Estimators . . . . .	120
5.3.3	Simulations Checks with the Linear Field . . . . .	121
5.3.4	Cross-Correlation of Quadratic Estimators with the Linear Density Field . . . . .	124
5.3.5	Auto- and Cross-Correlations of Quadratic Estimators . . . . .	125
5.3.6	Visualisation of Reconstructed Field . . . . .	128
5.4	Fisher Forecasts for Local $f_{\text{NL}}$ . . . . .	129
5.4.1	Multi-tracer Analysis . . . . .	129
5.4.2	Scales . . . . .	131
5.4.3	Galaxy Surveys . . . . .	133
5.4.4	Results . . . . .	133
5.5	Conclusion . . . . .	135
<b>6</b>	<b>Constraining Nonlinear Galaxy Bias from CMB-LSS Cross Correlations</b>	<b>138</b>
6.1	Introduction . . . . .	138
6.2	Theory . . . . .	142
6.2.1	2D Projections . . . . .	142
6.2.2	CMB Lensing . . . . .	143
6.2.3	Biased Tracers . . . . .	146

---

6.2.4	Quadratic Fields in Projected Space . . . . .	148
6.2.5	Projected Bispectrum Estimator . . . . .	151
6.2.6	Cross-Correlations of Quadratic Fields . . . . .	152
6.2.7	Shot Noise . . . . .	153
6.2.8	Covariances . . . . .	155
6.2.9	Redshift Space Distortions . . . . .	158
6.3	<i>N</i> -body Simulations . . . . .	161
6.4	Fisher Forecasts . . . . .	163
6.4.1	Setup . . . . .	163
6.4.2	Results . . . . .	167
6.5	Conclusions . . . . .	170
<b>7</b>	<b>Conclusion</b> . . . . .	<b>172</b>
7.1	Summary . . . . .	172
7.1.1	Cubic Halo Bias in Eulerian and Lagrangian Space . . . . .	173
7.1.2	Density Field Reconstruction from Biased Tracers . . . . .	174
7.1.3	Constraints on Non-Linear Bias Parameters . . . . .	175
7.2	Future Outlooks . . . . .	176
	<b>References</b> . . . . .	<b>177</b>
	<b>Appendix A EFT Counterterms</b> . . . . .	<b>193</b>
A.1	Basis . . . . .	193
A.2	UV-sensitivity and EFT Counterterms . . . . .	193
A.2.1	$R_h$ -dependence of Quadratic and Cubic Correlations . . . . .	193
A.2.2	Quadratic EFT Counterterms . . . . .	195
A.2.3	Cubic EFT Counterterms . . . . .	197
	<b>Appendix B Fisher Information Matrix</b> . . . . .	<b>199</b>
	<b>Appendix C Limber Approximation</b> . . . . .	<b>202</b>

## List of figures

- 2.1 Temperature fluctuations from the Cosmic Microwave Background (CMB) mapped by the Planck Satellite experiment [162]. The mean temperature is 2.7K and the blue and red spots correspond to over-dense and under-dense regions respectively. . . . . 8
- 2.2 Hubble's law plot for type IA supernova. In this plot  $\mu$  is proportional to  $\log(d)$ . The figure is taken from [84]. . . . . 14
- 2.3 The illustration shows the horizon problem. If the observer  $\mathcal{O}$ , observes two points,  $p$  and  $q$ , in the opposite direction in the sky, then these seem not to be in causal contact in the past. This means that the light cones do not overlap before the singularity, yet these points seem to share the same information. This illustration is taken from [33]. . . . . 16
- 2.4 This illustration, taken from [33], shows the solution of the horizon problem provided by the theory of cosmic inflation. This shows that the singularity of the conventional Big Bang model is replaced by the the time when inflation ended. Before that time the Universe went through a phase of accelerated expansion. This shows that all points we observe today, which appear not to have been in causal contact in the Big Bang model, now seem to be in causal contact during the inflationary period. . . . . 18
- 2.5 Potential in the slow-roll inflation. The inflaton (in red) rolls down the potential, causing inflation. The shaded regions describe the regions where inflation happens. When the potential energy converts into kinetic energy at the end of the potential, inflation ends. The figure is adapted from [33]. . . 21

2.6	Illustration of the evolution of curvature perturbations $\zeta$ . On super-horizon scales, modes $k \ll \mathcal{H}$ , exit the horizon due to shrinking Hubble sphere, and got frozen. These frozen modes re-enter the horizon at late-times after reheating and have significant impact on the temperature fluctuations of the CMB. The figure is adapted from [34]. . . . .	24
2.7	The illustration shows three triangle configurations of bispectrum. The figure is adapted from [120]. . . . .	25
3.1	The Feynman diagrams in this figure represent the linear power spectrum $P_{\text{lin}}$ (left) and one-loop terms, that is $P_{22}$ (middle) and $P_{13}$ (right). . . . .	34
3.2	Various contributions to the matter power spectrum up to one-loop in perturbation theory. The blue curve represents the linear power spectrum. Blue and red curves represent $P_{22}$ and $ P_{13} $ respectively. The one-loop contribution to the matter power spectrum is plotted in Orange, and the total (linear + one-loop) is plotted in Black. . . . .	35
3.3	The high- $k$ and low- $k$ limits of $P_{13}$ and $P_{22}$ . . . . .	36
3.4	The Feynman diagrams for various two-loop terms of the matter power spectrum. . . . .	38
3.5	The tree-level and the one-loop bispectrum terms are plotted for equilateral configurations ( $k_1 = k_2 = k_3$ ). . . . .	39
3.6	This illustration describes the hierarchy of scales in perturbation theory and effective field theory. The EFT description is valid for $\Lambda < k_{\text{NL}}$ . The figure is adapted from [35]. . . . .	42
3.7	Time evolution of background density, as well as linear and non-linear evolution of spherical overdensities [24]. . . . .	51
3.8	Peak-background split. The long-wavelength modes modulates short-modes. The regions which exceed the threshold value, $\delta_c$ , collapse to form dark matter halos as shown in this figure. . . . .	54
4.1	Theoretical predictions of bias parameters are obtained from the co-evolution of the Local Lagrangian Bias model (LLB) and the co-evolution of the Lagrangian bias model with the non-zero tidal term $b_{s2}^L$ at second order. The mass dependence of the initial Lagrangian bias is defined in Eq. (4.62). . .	72
4.2	Diagrammatic representation of $\langle \mathcal{D}_2(\mathbf{k})   \delta^{(2)}(\mathbf{k}') \rangle'$ . . . . .	75



- 4.3 Perturbative expressions for one-loop, and two-loop irreducible and two-loop reducible terms of  $\langle \mathcal{D}_3(\mathbf{k}) | \delta_{\text{NL}}(\mathbf{k}') \rangle$  are shown in diagrammatic form. The propagators are represented by linear power spectra  $P_{\text{lin}}$ , the cubic field kernel  $\mathcal{D}_3$  is represented by the hatched square. Finally, empty squares correspond to the gravitational kernel  $F_3$ . Loops correspond to integrals over all wavenumbers  $\mathbf{q}$  or  $\mathbf{p}$  and arrows represent the flow of momentum. . . . . 77
- 4.4 Diagrams contributing to the correlation of cubic fields with the halo field in Eq. (4.49). The triangles represent the linear, quadratic and cubic bias kernels. The straight lines are used to describe the density field, whereas halo fields are described by wiggly lines. The Feynman rules are discussed in detail in [18]. . . . . 77
- 4.5 Cross-correlations of cubic fields with the orthogonalized fields contain only the two-loop irreducible diagram. The figure shows PT diagrams for  $\langle D_3 | \tilde{F}_3 \rangle$  (left) and  $\langle D_3 | \tilde{\mathcal{O}}_3^j \rangle$  (right). . . . . 79
- 4.6 Ratio of the cross-correlations of cubic fields with the orthogonalized non-linear matter field as measured in simulations and predicted in perturbation theory. The cubic fields are smoothed with  $R_f = 20h^{-1}$  Mpc. As discussed in the text, these cross correlations are described by the two-loop irreducible diagram in PT. The vertical dotted line is drawn at  $k = 0.1h$  Mpc $^{-1}$  to separate the region of validity of the PT. For  $k > 0.1h$  Mpc $^{-1}$  PT results can not be trusted. To ensure convergence of PT, we have chosen the maximum wavenumber  $k_{\text{max}} = 0.057h$  Mpc $^{-1}$  for parameter estimation. . . . . 83
- 4.7 Irreducible parts of the cross-spectra of cubic fields. The solid lines are the numerical evaluation of the perturbation theory loop integrals in Eq. (4.48), while the dots with errorbars show simulation data. The cubic fields from left to right are smoothed with  $R_h = 4h^{-1}$  Mpc, while fields from top to bottom are smoothed with the fiducial halo smoothing scale  $R_f = 20h^{-1}$  Mpc. 84

- 4.8 Constraints on bias parameters from the protohalo statistics. The solid lines are the predictions of the local Lagrangian model calculated from the ST mass function. The dashed line is a fit to the observed non-zero Lagrangian tidal parameter given in Eq. (4.62). We are plotting two cases. The fit leading to the red points includes the counter term  $dR$ , which is just the Taylor expansion coefficient around our fiducial choice of smoothing scale  $R_h$ , while the blue points are without a counter term. The employed fiducial  $R_h = 4h^{-1}\text{Mpc}$  does not reflect the correct Lagrangian scale for all mass bins. Thus, we are more confident in the measurements with the counter term. We also overplot the fitting functions for  $b_{s,2}$  given in Eq.(22) of [147] (rescaled to Lagrangian space, shown by the dashed-green line), which contrary to our findings indicates a positive tidal bias for low masses and a stronger effect for large masses. . . . . 93
- 4.9 Constraints on Eulerian bias parameters from seven and eight parameter fits to the late-time halo field. The red points depict the fits with an eight parameter model including the counterterm  $dR$ , whereas the green points show the results from a seven parameter model without the counterterm. The black dashed lines show the co-evolution prediction based on a local Lagrangian bias model and the black lines arise from a local Lagrangian model extended by a non-vanishing tidal term whose amplitude was fitted in Lagrangian space and is given by Eq. (4.62). Green points show constraints on linear and quadratic biases obtained from a fit to  $\chi_{\text{lin}}^2 + \chi_{\text{quad}}^2$ . The constraints are in perfect agreement with the results from the full fits, which supports the consistency of our model and fitting procedure. The fitting function of [147] for  $b_{s,2}$  is shown by the brown dashed curve. . . . . 94
- 4.10 Co-evolution Check: Difference of Eulerian and Lagrangian constraints on the local and non-local cubic bias parameters. We overplot the predictions of the local Lagrangian bias model (shown by solid black curves) and the Lagrangian model with an initial tidal field (LLB+ $b_{s,2}^L$  shown by black dotted lines). At low mass the bias generally shows the trends of local Lagrangian bias, but at the high mass end there are deviations especially for  $b_{\Gamma_3}$  and  $b_{\mathcal{G}_3}$ . 95
- 4.11 Measurements of the Eulerian bias parameter as a function of maximum wavenumber  $k_{\text{max}}$ . The horizontal blue-dashed lines are the best-fit values evaluated at  $k_{\text{max}} = 0.057h \text{ Mpc}^{-1}$  (vertical dotted line). . . . . 96

- 4.12 Non-local bias constraints plotted against the linear Lagrangian bias and quadratic local Lagrangian bias. As stated in Eq. (4.32) the non-local bias parameters are predicted to follow a linear relation with the Lagrangian bias parameters shown as the black line. The data points show a preference for the model in which the LLB is extended by a Lagrangian tidal tensor contribution leading to the predictions in Eq. (4.33) (dashed curve). We also overplot the fitting function for  $b_{s,2}$  given in Eq. (22) of [147] (shown by the dashed-green line). Our measurements for  $b_{s,2}$  are clearly not consistent with their fitting function. . . . . 97
- 4.13 Direct five parameter measurements of the Lagrangian bias parameters using the template Eq. (4.27) for the final halo field and reconstruction of the Lagrangian bias parameters from the full eight parameter fits of the final field described above. We also show direct measurements of the Lagrangian bias parameters from a five and eight parameter fit to the protohalo field. The solid lines are predictions of the ST bias function. The dashed curve for  $b_{s,2}^L$  is our best-fit defined in Eq. (4.62). . . . . 98
- 4.14 Marginalized posteriors of Lagrangian bias constraints for mass bin III obtained from the late-time halo field. The counterterm  $dR$  is shown in units of  $1 h^{-1}\text{Mpc}$ . The dark and light regions represent 64.1 % and 95.4 % confidence regions respectively. We clearly see detection of Lagrangian tidal bias and a deviation from the fiducial smoothing scale  $R_h = 4h^{-1} \text{Mpc}$ . There are some mild degeneracies between the counterterm  $dR$  and the local cubic and quadratic tidal tensor bias. . . . . 99
- 4.15 Cross correlation of the final halo field with the linear density field (propagator), normalized by the linear power spectrum. The red and blue lines show one-loop predictions with and without  $k^2$  corrections. The shaded red region shows the effects of the bias errorbars on the predictions. . . . . 100
- 4.16 Ratio of halo-matter cross power spectrum and linear power spectrum. The red and blue lines show one loop predictions with and without the  $k^2$  corrections. The shaded red region represents the uncertainty arising from the error on the cubic bias parameters (without the error on the  $k^2$  term). We also show the predictions without quadratic and cubic bias reflected by the black dotted lines. . . . . 101
- 5.1 The illustration shows how reconstruction of density field works. We reconstruct large scale modes from non-linear small scale modes of biased tracer field. The scales used in this diagram are defined in section 5.4.2. . . . . 108

- 5.2 Noise and contamination for a DESI-like survey, with a mean redshift  $\bar{z} = 1$ . LEFT PANEL: we plot noise curves  $N_{\alpha\alpha}$  where  $\alpha \in \{g, s, t, \phi\phi, c11\}$  and compare them with shot noise  $\bar{n}^{-1}$  and linear power spectrum  $P_{\text{lin}}$ . We do not plot noise corresponding to other remaining mode-couplings  $c_{01}$  and  $c_{02}$  because their amplitude is too large. RIGHT PANEL: Contamination by bias parameters to the growth estimator. The dashed curves represent negative contribution and the black solid line is the total contamination. The contribution by three  $f_{\text{NL}}$  terms ( $\phi\phi$ , 11, and 02) clearly show  $k^{-2}$  behaviour. 113
- 5.3 Bias hardened and unbiased-hardened variance for growth (left) and shift (right) estimators for  $k_{\text{max}} = 0.1h \text{ Mpc}^{-1}$ ,  $0.25h \text{ Mpc}^{-1}$ , and  $0.5h \text{ Mpc}^{-1}$ . The unbiased-hardened curves are plotted in solid curves, while bias-hardened curves are plotted in dotted curves. We also plot the shot noise (orange solid curve) and the linear power spectrum (black solid curve) to compare the overall noise with the signal. The bias hardening increases the reconstruction noise a lot. The effect is more severe in the shift estimator. . . . . 114
- 5.4 Shot noise contributions to the power spectrum, bispectrum and trispectrum for  $k_{\text{max}} = 0.1h \text{ Mpc}^{-1}$  (left) and  $k_{\text{max}} = 0.25h \text{ Mpc}^{-1}$  (right). We used the growth estimator for density reconstruction. The bias parameters  $b_1$  and  $c_\alpha$  we used for the lowest mass bin I from simulations are defined in Table 5.2. The Poisson shot noise  $P_{\text{gg,shot}} = 1500h^{-3} \text{ Mpc}^3$  corresponding to halo number density  $\bar{n} = 675 \times 10^{-6}h^3 \text{ Mpc}^3$ . . . . . 119
- 5.5 Schematic diagram for showing how we generate a quadratic estimator in simulations. We only show the growth (G) estimator here. IFT and FT are inverse Fourier transform and Fourier transform respectively. . . . . 121
- 5.6 Auto- and cross-correlations of  $\hat{\Delta}_\alpha^{\text{G}}$  for two different smoothing scales,  $R = 20h^{-1} \text{ Mpc}$  and  $R = 4h^{-1} \text{ Mpc}$ . Theoretical predictions (solids curves) agree with simulations for three quadratic fields corresponding to the growth, shift and the tidal terms. The purpose of these tests is to check the correct implementation of the kernels of the quadratic estimators in simulations. . . 123
- 5.7 Cross-correlation coefficients between two  $\hat{\Delta}_\alpha^{\text{G}}$ 's for two different smoothing scales  $R = 20h^{-1} \text{ Mpc}$  and  $R = 4h^{-1}$ . Theoretical predictions agree with simulations, verifying that the kernels of quadratic estimators and Wiener filter are correctly implemented in simulations. . . . . 124

- 5.8 Cross correlations of estimators  $\hat{\Delta}_\alpha$  corresponding to the growth, shift, and tidal mode-couplings with the linear density field  $\delta_1$ . We compare theory predictions (lines) with simulations (points) for three different smoothing scales,  $R = 20h^{-1}$  Mpc,  $R = 10h^{-1}$  Mpc and  $R = 4h^{-1}$  Mpc, corresponding to maximum wavenumbers  $k_{\max}$  of  $0.05h$  Mpc $^{-1}$ ,  $0.1h$  Mpc $^{-1}$ , and  $0.25h$  Mpc $^{-1}$  respectively. In this figure, we plot  $\langle \hat{\Delta}_\alpha \delta_1 \rangle / N_{\alpha\alpha}$ , which is the directly measurable quantity. In contrast to what is defined in Eq. (5.9), in simulations we define the estimators  $\hat{\Delta}_\alpha$  without a prefactor  $N_{\alpha\alpha}$ . We find very good agreement for the growth estimator for all smoothing scales, and also reasonably good agreement for other estimators. . . . . 125
- 5.9 Auto-correlations of the quadratic estimators  $\hat{\Delta}_\alpha$ , for the same smoothing scales shown in Fig. 5.8. The predictions for the growth estimator agree with simulations for all smoothing scales. However, for other estimators predictions agree with simulations for large smoothing scales but for the low smoothing scales, the predictions fail as higher-order terms become more important. . . . . 126
- 5.10 Comparison of the auto power spectrum of the growth estimator  $\hat{\Delta}_G$ , normalised by  $N_{GG}$  computed from theory, with the signal part which is defined as  $(\langle \hat{\Delta}_G \delta_1 \rangle)^2 / P_{\text{lin}}$ . We compare simulation results with theory predictions for the same smoothing scales as Figs. 5.8 and 5.9. We again find excellent agreement between simulations and theory. In the bottom right figure we plot the cross-correlation coefficient  $r_{G\delta_1}$  between the growth estimator and the linear density field for 3 smoothing scales. We see that  $r_{G\delta_1} > 0.9$  for  $R = 4h^{-1}$  Mpc which is why in the bottom left figure  $\langle \hat{\Delta}_G \hat{\Delta}_G \rangle$  is signal dominated. . . . . 127
- 5.11 Probability distribution functions of the initial density field and the reconstructed field in  $N$ -body simulations. The right panel shows the probability distribution of the reconstructed field the  $k_{\min} = 0.05h$  Mpc $^{-1}$ , means that we do not include modes  $k < 0.05h$  Mpc $^{-1}$  in the reconstruction. In the left we use a lower  $k_{\min} = 0.005h$  Mpc $^{-1}$ . The PDFs of both are scaled and shifted around mean 0. . . . . 128
- 5.12 2D slices of a 3D linear density field (left panel) and growth estimator  $\hat{\Delta}_G$  (right panel). For the growth estimator we used  $R = 4h^{-1}$  Mpc smoothing which corresponds to  $k_{\max} = 0.25h$  Mpc $^{-1}$ . We apply an external smoothing of  $R = 20h^{-1}$  Mpc to both linear and reconstructed fields. As expected, we find that the reconstruction reproduces many of the large-scale features in the linear density field. . . . . 130

- 5.13 This illustration shows scales we use for our Fisher analysis in this work. For the reconstruction of large-scale density modes we use wavenumbers  $k_{\min} < K < k_{\max}$  (shown in blue). For  $f_{\text{NL}}$  forecasts, however, we use very large scale modes  $K_{\min} < K < K_{\max}$  (shown in red) for  $\delta_{\text{g}} + \delta_{\text{r}}$  combined analysis (shown in red) and  $K_{\text{f}} < K < K_{\min}$  for  $\delta_{\text{r}}$ -only (shown in green), where  $K_{\text{f}}$  is the lowest wavenumber we can measure in the galaxy survey. . . . . 132
- 5.14 DESI:  $\sigma(f_{\text{NL}})$  constraints for a DESI-like survey for a range of redshift  $0.6 < z < 1.6$ . LEFT PANEL:  $\sigma(f_{\text{NL}})$  obtained from  $\delta_{\text{g}}$  only (dotted red) and  $\delta_{\text{g}} + \delta_{\text{r}}$  (solid red). We also include constraints from  $\delta_{\text{r}}$ -only in combined analysis for modes  $0.002 < K < K_{\min}$ . RIGHT PANEL: We plot ratio of constraints from combined analysis and galaxy-only. We also plot ratio without modes  $0.002 < K < K_{\min}$ . . . . . 134
- 5.15 MegaMapper low- $z$ :  $\sigma(f_{\text{NL}})$  constraints for a MegaMapper-like survey for low  $z$ ,  $2 < z < 2.5$ . LEFT PANEL:  $\sigma(f_{\text{NL}})$  obtained from  $\delta_{\text{g}}$  only (dotted red) and  $\delta_{\text{g}} + \delta_{\text{r}}$  (solid red). RIGHT PANEL: We plot ratio of constraints from combined analysis and galaxy-only. . . . . 135
- 5.16 MegaMapper high- $z$  bin:  $\sigma(f_{\text{NL}})$  constraints for a MegaMapper-like survey for high  $z$ ,  $4.5 < z < 5$ . LEFT PANEL:  $\sigma(f_{\text{NL}})$  obtained from  $\delta_{\text{g}}$  only (dotted red) and  $\delta_{\text{g}} + \delta_{\text{r}}$  (solid red). RIGHT PANEL: We plot ratio of constraints from combined analysis and galaxy-only. . . . . 137
- 6.1 An illustration of the projection along the line-of-sight. . . . . 141
- 6.2 Projected linear power spectrum  $P_{2\text{D}}$  using the Gaussian and the top-hat filters. The projection length used is  $R_{\text{p}} = 100h^{-1}$  Mpc. For comparison, the 3D linear power spectrum is shown with dashed-green curve (with units  $h^{-3} \text{ Mpc}^3$ ). . . . . 143
- 6.3 The CMB lensing kernel (solid blue) and galaxies kernels as function of redshift  $z$ . For galaxies we plot a Gaussian kernel and kernel for LSST galaxies peaked at around redshift  $z = 0.7$ . The kernels are normalised to a maximum value of 1. . . . . 144
- 6.4 The illustration shows how one can construct a quadratic field  $\mathcal{Q}_2[\delta_{\text{p}}]$  from a projected field  $\delta_{\text{p}}$ . The first step is to project a 3D density field  $\delta_{3\text{D}}$  using a Gaussian or a top-hat filter. The next step is to apply a smoothing function to the projected field in Fourier space with the smoothing scale  $R_{\text{f}}$ . Then we generate the quadratic field with a combination of Fourier and inverse Fourier transforms. . . . . 149

- 6.5 Auto- cross correlations of quadratic fields in projected space using two different window functions: Gaussian and top-hat, with a projection scale  $R_p = 100h^{-1}\text{Mpc}$ . For a reference we also show the auto spectra of  $\delta^2$  in 3D (red curve). . . . . 151
- 6.6 Projected shot noise contributions at the power spectrum and the bispectrum level using quadratic field  $\mathcal{D}_2$  corresponding to the growth, shift and the tidal terms. We use the constant 3D galaxy number density  $n_0 = 10^{-2}h^3 \text{Mpc}^{-3}$  and show the results for two galaxy redshift bins centered at  $z_m = 1.75$  and  $z_m = 0.15$ . . . . . 155
- 6.7 Projected bispectrum shot noise corresponding to the growth field for 8 redshift bins. To show how the galaxy number density impacts bispectrum shotnoise terms, in the left panel we show the results for  $n_0 = 10^{-3}h^3 \text{Mpc}^{-3}$  and in the right panel for  $n_0 = 10^{-2}h^3 \text{Mpc}^{-3}$ . . . . . 156
- 6.8 The ratio of the projected matter power spectrum in redshift space  $P_s$  and in real space  $P_{\text{real}}$ . We compare theory with simulations. We show three theory curves for modelling of RSD effects using the Kaiser formula (black) and Kaiser+FoG (blue). The projection length used is  $R_p = 100h^{-1} \text{Mpc}$  and the 1D velocity dispersion  $\sigma_v = 4h^{-1}\text{Mpc}$ . . . . . 160
- 6.9 Projection of a 3D density field onto a 3D grid along the  $\hat{z}$  axis in simulations. The finite sized slices are summed up along the  $\hat{z}$  axis to get the projected field  $\delta_p$ . In the end, the projected field  $\delta_p$  should be properly normalised before using it for cross-correlations. . . . . 161
- 6.10 Auto- and Cross correlations of quadratic fields in projected space. Theoretical predictions (solid curves) agree with simulation results (dots). We show the results for quadratic fields corresponding to the growth, shift and the tidal terms. . . . . 162
- 6.11 Here we plot auto- and cross-correlations of galaxy and CMB lensing for the redshift bin  $1.5 < z < 2$ . In the left panel we show lensing-galaxy and galaxy-galaxy power spectra as well as projected galaxy shot noise. In the right panel we show lensing auto power spectrum and lensing reconstruction noise. We show lensing reconstruction noise from Planck and Simons Observatory (SO) experiments obtained in  $k$ -space from  $l$ -space (multipoles) using the Limber approximation [133]. . . . . 164
- 6.12 Constraints on  $b_1$  and  $A_s$  as function of  $k_{\text{max}}$  using the combined 2-point functions of galaxy/lensing auto- and cross-correlations; 3-point functions; and combined, 2- and 3-point functions. The constraints are shown for one redshift bin  $1 < z < 1.5$ . We can see that 2-point functions tightly constraints  $b_1$  and  $A_s$ . The 3-point functions only started to dominate at very high  $k_{\text{max}}$ . 167

---

6.13	Correlation coefficients between $b_1$ and amplitude of fluctuations $A_s$ for six redshift ranges. We plot correlation coefficients using 2-point functions, 3-point functions and combined 2- and 3-point functions. These plots show that adding 3-point functions, as well as going to higher redshift, indeed break the degeneracy between $b_1$ and $A_s$ compare to just using 2-point functions. . . . .	168
6.14	Constraints on bias parameters as well as the relative amplitude of fluctuations from combined 2- and 3-point functions analysis for different redshift bins. We show the constraints as function of maximum wavenumber $k_{\max}$ in our model. The constraints get better as we go to higher wavenumber, which make sense because we are including more modes and hence more information. . . . .	169
6.15	Correlation coefficients between bias parameters and $A_s$ for one redshift slice, $0.3 < z < 0.6$ . . . . .	170
B.1	Constraints on $b_1$ and $A_s$ using combined galaxy-lensing 2-point functions. We show results Fisher analysis at the power spectrum level, given by Eq. (B.12), and at the fields level, given by Eq. (B.11). . . . .	201



## List of tables

1	List of abbreviations used in this thesis . . . . .	1
2	List of symbols and notations used in this thesis . . . . .	2
2.1	The cosmic inventory. The table is reproduced from [84] . . . . .	11
3.1	Convergence properties of one-loop power spectrum terms based on different values of the initial conditions. . . . .	37
4.1	Bias parameter estimation from $N$ -point functions. The tree-level power spectrum, bispectrum and trispectrum are natural statistics to obtain cleanest (and non-degenerate) constraints on the linear, quadratic and cubic bias parameters respectively. On the other hand the constraints on the derivative bias can be obtained from the loop statistics once the other bias parameters have been fixed from the tree-level statistics. The terms in Orange are quartic bias parameters which are beyond the scope of this chapter. A similar table is also given in [11]. . . . .	65
4.2	Halo mass bins employed in this study. We quote the mean mass of the sample and the number density of halos. . . . .	81
4.3	Overview of reduced $\chi^2$ models considered. We have studied six different models which are summarized in the table. First, we note that the Eulerian and Lagrangian models with the counterterm $dR$ are statistically preferable compare to the ones without the counterterm. Second, we note that for both Eulerian and Lagrangian models, for mass bin I and II, five parameter fits are statistically preferable. However, for mass bins III, IV, and V the full model with eight parameters gives a lower reduced $\chi^2$ and is therefore preferable. This implies that low mass halos are in a better agreement with the co-evolution predictions of LLB+ $b_{s^2}$ . . . . .	88

4.4	Best-fit values for the $k^2$ bias coefficients for five mass bins obtained from the one-loop halo-matter statistics after fixing all other bias parameters. The maximum wavenumber used is $k_{\max} = 0.08h \text{ Mpc}^{-1}$ . The quoted values are in units of $h^{-2} \text{ Mpc}^2$ , i.e. inverse length-squared. The error bars are dominated by the uncertainty of $b_{s^2} + 2/5b_{\Gamma_3}$ . . . . .	90
5.1	Summary of mode couplings, $f_{\text{NL}}$ components ( $\phi\phi, 01, 11$ , and $02$ ), their respective biases $c_\alpha$ and quadratic coupling kernels $F_\alpha$ . . . . .	110
5.2	Halo mass bin employed in this study. We quote the mean mass of the sample, the number density of halos $n_h$ , and the linear bias $b_1$ for the lowest halo mass bin in the simulation. . . . .	120
5.3	Survey characteristics used for our main forecasts. The DESI-like survey is based on the expected DESI emission-line galaxy sample and the MegaMapper-like survey is a next-generation survey targeting high-redshift “dropout” galaxies. . . . .	132
A.1	Quadratic fields: Relative change in the amplitude of cross-correlations of quadratic fields with the quadratic bias operators at $k = 0.042h \text{ Mpc}^{-1}$ as we change the halo smoothing scale from $R_h = 4h^{-1} \text{ Mpc}$ to $R_h = 6h^{-1} \text{ Mpc}$ . . . . .	194
A.2	Irreducible: Relative change in the amplitude of irreducible diagrams of the cross-correlations of cubic fields at $k = 0.042h \text{ Mpc}^{-1}$ as we change the halo smoothing scale from $R_h = 4h^{-1} \text{ Mpc}$ and $R_h = 6h^{-1} \text{ Mpc}$ . . . . .	194
A.3	Reducible: Relative change in the amplitude of reducible diagrams of the cross-correlations of cubic fields at $k = 0.042h \text{ Mpc}^{-1}$ as we change the halo smoothing scale from $R_h = 4h^{-1} \text{ Mpc}$ to $R_h = 6h^{-1} \text{ Mpc}$ . . . . .	195
A.4	Full theory: Relative change in the amplitude full cross-correlations of cubic fields (reducible + irreducible) at $k = 0.042h \text{ Mpc}^{-1}$ as we change the halo smoothing scale from $R_h = 4h^{-1} \text{ Mpc}$ to $R_h = 6h^{-1} \text{ Mpc}$ . . . . .	195

CMB	Cosmic Microwave Background
LSS	Large-scale structure
PT	Perturbation theory
SPT	Standard perturbation theory
LPT	Lagrangian perturbation theory
2LPT	Second-order Lagrangian perturbation theory
EFTofLSS	Effective field theory of large-scale structure
EdS	Einstein-de Sitter (flat, matter dominated Universe)
$\Lambda$ CDM	$\Lambda$ cold dark matter
FoF	Friends-of-friends algorithm
SO	Spherical overdensity
LO	Leading order (tree-level)
NLO	Next-to-leading order (one-loop)
NNLO	Next-to-next-to-leading order (two-loop)
PBS	Peak-background split
PNG	Primordial non-Gaussianity
RSD	Redshift-space distortions
LLB	Local Lagrangian bias
LIMD	Local in matter density
UV	Ultraviolet
IR	Infrared
MCMC	Monte-Carlo Markov Chain
LSST	Large Synoptic Survey Telescope
DES	Dark Energy Survey
WFIRST	WideField Infrared Survey Telescope
WMAP	Wilkinson Microwave Anisotropy Probe
tSZ	thermal Sunyaev-Zel'dovich
FoG	Finger-of-God
FFTW	Fast Fourier Transform in the West (software library)
FT	Fourier Transform
IFT	Inverse Fourier Transform
CIC	Cloud in cell

*Table 1* List of abbreviations used in this thesis

Quantity	Symbol	Definition/defined in
Conformal time	$\tau$	$d\tau \equiv dt/a$
Time derivative	$\dot{x}$	$\dot{x} \equiv dx/dt$
Hubble rate	$H$	$H \equiv \dot{a}/a$
Conformal Hubble rate	$\mathcal{H}$	$\mathcal{H} \equiv a^{-1}da/d\tau = aH$
Dirac delta function in 3D	$\delta_{\text{D}}(\mathbf{k})$	—
Eulerian comoving coordintes	$x$	—
Wavenumbers	$\mathbf{k}, \mathbf{q}, \text{etc.}$	—
Amplitude of local primordial non-Gaussianity	$f_{\text{NL}}$	—
Factor relating primordial potential and $\delta_1$	$M(k, z)$	—
Linear matter overdensity	$\delta_1$	—
Linear matter power spectrum	$P_{\text{lin}}(k, z)$	—
Tracer overdensity	$\delta_{\text{g}}$	—
Second-order mode-coupling	$F_{\alpha}(\mathbf{k}_1, \mathbf{k}_2)$	Chapter 5
Second-order response of small-scale power spectrum to long mode	$f_{\alpha}(\mathbf{k}_1, \mathbf{k}_2, z)$	Chapter 5
Coefficient of $F_{\alpha}$ in second-order bias model for $\delta_{\text{g}}$	$c_{\alpha}$	Chapter 5
Linear tracer bias	$b_1$	—
Quadratic tracer bias	$b_2$	—
Quadratic tidal bias	$b_{s,2}$	—
Other second-order bias parameters	$b_{s,2}^E, b_{01}^E, \dots$	—
Quadratic estimator for mode with wavenumber $\mathbf{K}$	$\hat{\Delta}_{\alpha}(\mathbf{K})$	Chapter 5
Weight function in $\hat{\Delta}_{\alpha}(\mathbf{K})$	$g_{\alpha}(\mathbf{k}_1, \mathbf{k}_2)$	Chapter 5
Normalization/noise of $\hat{\Delta}_{\alpha}(\mathbf{K})$	$N_{\alpha\beta}(\mathbf{K})$	Chapter 5
Mode reconstructed with growth-coupling estimator $\hat{\Delta}_{\text{G}}(\mathbf{K}, z)$	$\hat{\delta}_{\text{r}}(\mathbf{k}, z)$	Chapter 5
Power spectrum of $\delta_{\text{g}}$ , ignoring shot noise contribution	$P_{\text{gg}}$	Chapter 5
Sum of $P_{\text{gg}}$ and shot noise contribution	$P_{\text{tot}}$	Chapter 5
Cross power spectrum between $\delta_{\text{g}}$ and $\hat{\delta}_{\text{r}}$ , ignoring shot noise contribution	$P_{\text{gr}}$	Chapter 5
Power spectrum of $\hat{\delta}_{\text{r}}$ , ignoring shot noise contribution	$P_{\text{rr}}$	Chapter 5
Shot noise contribution to $\delta_{\text{g}}$ power spectrum	$P_{\text{gg,shot}}$	Chapter 5
Shot noise contribution to $\delta_{\text{g}}$ - $\hat{\delta}_{\text{r}}$ cross power spectrum	$P_{\text{gr,shot}}$	Chapter 5
Shot noise contribution to $\hat{\delta}_{\text{r}}$ power spectrum	$P_{\text{rr,shot}}$	Chapter 5
Lowest wavenumber within survey volume	$K_{\text{f}}$	Chapter 5
Wavenumber below which we assume $\delta_{\text{g}}$ cannot be measured	$K_{\text{min}}$	Chapter 5
Maximum wavenumber used for $f_{\text{NL}}$ constraints	$K_{\text{max}}$	Chapter 5
Maximum wavenumber used in quadratic estimator for reconstructed modes	$k_{\text{max}}$	Chapter 5
Relative amplitude of matter fluctuations	$A_{\text{s}}$	Chapter 6
Wavenumber parallel to the line-of-sight	$k_{\parallel}$	Chapter 6
Wavenumber perpendicular to the line-of-sight	$\mathbf{k}_{\perp}$	Chapter 6
projected matter density	$\hat{\delta}_{\text{p}}$	Chapter 6
projected galaxy density	$\hat{\delta}_{\text{g,p}}$	Chapter 6
CMB lensing convergence	$\kappa$	Chapter 6
Galaxy-galaxy power spectrum in 2D	$P_{\text{gg}}(\mathbf{k}_{\perp})$	Chapter 6
Galaxy-lensing power spectrum in 2D	$P_{\text{g}\kappa}(\mathbf{k}_{\perp})$	Chapter 6
Lensing power spectrum	$P_{\kappa\kappa}(\mathbf{k}_{\perp})$	Chapter 6
Projection length	$R_{\text{p}}$	Chapter 6
Galaxy projection window kernel in Fourier space	$W_{\text{g}}(k_{\parallel})$	Chapter 6
CMB Lensing projection kernel in Fourier space	$W_{\kappa}(k_{\parallel})$	Chapter 6
Quadratic field constructed from the projected field $\hat{\delta}_{\text{p}}$ in 2D	$\mathcal{D}_2[\hat{\delta}_{\text{p}}]$	Chapter 6
Projected quadratic field (quadratic bias operators) in 2D	$\mathcal{O}[\hat{\delta}]_{\text{p}}$	Chapter 6
Quadratic bias operators in 3D	$\mathcal{O}[\delta]$	Chapter 6
Kernel of quadratic bias operators in Fourier space in 3D	$\mathcal{O}_2(\mathbf{k}_1, \mathbf{k}_2)$	Chapter 6
Kernel of 2D quadratic field $\mathcal{D}_2$ in Fourier space	$\mathcal{H}_{\mathcal{D}_2}(\mathbf{k}_{\perp 1}, \mathbf{k}_{\perp 2})$	Chapter 6
Second-order gravitational kernel in redshift space	$Z_2(\mathbf{k}_1, \mathbf{k}_2)$	Chapter 6

Table 2 List of symbols and notations used in this thesis

## Introduction

Over the last few decades, there have been tremendous theoretical and observational advancements in cosmology that have greatly improved our current understanding of the Universe. However, there are still many fundamental questions that need to be answered. For instance, why is the universe accelerating? What is the nature of Dark Energy and Dark Matter that dominate the Universe? What is the physical origin of inflation which provided the seeds for the formation of large scale structure (LSS)? Is Einstein theory of general relativity a correct description of gravity or does it need to be modified on large scales? So far the Cosmic Microwave Background (CMB) observables have been the dominant source of information about some of these questions. However, given that the CMB is a two-dimensional survey and the amount of information that could be extracted from the CMB analysis is limited mainly due to foreground contamination as well as Silk-damping.

On the other hand, current and on-going future LSS surveys have great potential to answer these questions and put stricter bounds on the cosmological parameters and the models of inflation. One way to see this is the following: Contrary to the CMB, where the number of modes scales as  $N_{\text{CMB}} \sim l_{\text{max}}^2$ , the number of modes accessible in LSS survey depends on the cube of the maximum wavenumber  $N_{\text{LSS}} \sim (k_{\text{max}}/k_{\text{min}})^3$ . The signal-to-noise ratio in LSS depends on the volume of the survey and  $\sqrt{N_{\text{LSS}}}$ . Increasing the survey volume is an observational challenge but theoretically, increasing the number of modes depends on careful modelling of LSS observables. By pushing the theoretical and observational limits in LSS, we can significantly increase the amount of useful information about the Universe. One of the main challenges in modelling LSS observables are late-time non-linearities. There are three main sources of non-linearities that can affect late-time observables. The first one are the non-linearities due to gravity in matter clustering. Effective Field Theory of Large-Scale Structure (EFTofLSS) [46] provides a powerful framework to understand non-linearity due to gravity in matter clustering.

## 1.1 Thesis Outline

In this thesis, we make advances in the understanding of higher-order couplings in biased tracers of large-scale structures. The general outline of this thesis is outlined as follows.

### Chapter 2

In Chapter 2, we introduce the standard model of cosmology. We present Einstein's general theory of relativity and derive Friedman's equations. We discuss the basic concept in cosmology and introduce the  $\Lambda$ CDM model of cosmology, which states that the Universe is flat and dominated by dark energy  $\Lambda$  and cold dark matter. Finally, we discuss cosmic inflation, an early phase of accelerated expansion, which provides seeds to structure formation at late-times.

### Chapter 3

In Chapter 3, we review large-scale structure cosmology. To calculate the statistics of the non-linear matter density field, we introduce the framework of the standard perturbation theory (SPT). We show that SPT is not stable against corrections from higher order mode couplings and a correct way to make accurate predictions is by using EFTofLSS. The framework of EFTofLSS not only provides accurate predictions, but it can also give us insights into the physics of small scales. Finally, we discuss biased tracers and develop the statistics of biased tracers.

### Chapter 4

Chapter 4 is based on our paper "Cubic halo bias in Eulerian and Lagrangian space" [2]. In this chapter, we present our work on halo (or galaxy) bias parameters up to cubic order. We present a novel method to constrain quadratic and cubic bias parameters in dark matter simulations. Predictions of the next-to-leading order, i.e. one-loop, halo power spectra, depending on local and non-local bias parameters up to cubic order. The linear bias parameter can be estimated from the large scale limit of the halo-matter power spectrum, and the second-order bias parameters from the large scale, tree-level bispectrum. Cubic operators would naturally be quantified using the tree-level trispectrum. As the latter is computationally expensive, we extend the quadratic field method proposed in Schmittfull et al. 2014 to cubic fields, to estimate cubic bias parameters. We cross-correlate a basis set of cubic bias operators with the halo field and express the result in terms of the cross-spectra of these operators, to cancel cosmic variance. We obtain significant detections of local and non-local cubic bias parameters, which are partially in tension with predictions based on

local Lagrangian bias schemes. We directly measure the Lagrangian bias parameters of the protohaloes associated with our halo sample and detect a non-local quadratic term in Lagrangian space. We do not find a clear detection of non-local cubic Lagrangian terms for low mass bins, but there is some mild evidence for their presence for the highest mass bin. While the method presented here focuses on cubic bias parameters, the approach could also be applied to quantifications of cubic primordial non-Gaussianity.

## Chapter 5

Chapter 5 is based on our paper "Density reconstruction from biased tracers and its applications to primordial non-Gaussianity" [59]. In this chapter, we develop a formalism to reconstruct large-scale Fourier modes of the density field from the biased tracer field. We use the quadratic estimator method, similar to the one used by the CMB lensing reconstruction, and incorporate non-linearities from gravity, non-linear biasing and primordial non-Gaussianity. First, we derive a generic formula for quadratic estimators  $\hat{\Delta}_\alpha$  corresponding to non-linear quadratic mode couplings in the biased tracer field, where  $\alpha$  represents one of the seven mode couplings present in the galaxy field at quadratic order. Following this approach, we show that an unbiased estimator for the density field can be derived from the shift term  $\Psi \cdot \nabla \delta$  using a linear combination of all mode-coupling (traditionally known as bias-hardening). The challenge is to ensure that the variance does not blow up. In comparison, an estimator corresponding to the growth term  $\delta^2$  has the lowest variance and therefore we use it to reconstruct the large-scale modes of the density field. Second, using cosmological  $N$ -body simulations, we verify that our estimators give the expected results. We check our predictions not only for the growth estimator but also for the shift and the tidal estimators. We use 3 different smoothing scales  $R = 20h^{-1}$  Mpc,  $R = 10h^{-1}$  Mpc, and  $R = 4h^{-1}$  Mpc corresponding to  $k_{\max} \approx 0.05h$  Mpc $^{-1}$ ,  $k_{\max} \approx 0.1h$  Mpc $^{-1}$ , and  $k_{\max} \approx 0.25h$  Mpc $^{-1}$ . We find that the reconstruction works very well for the growth estimators up to  $k_{\max} \approx 0.25h$  Mpc $^{-1}$  at redshift  $z = 0$ , where we can find the cross-correlation coefficient of the estimator with the initial field is  $r_{G\delta_1} > 0.9$ . For the other two estimators, we also find reasonably good agreement for lower  $k_{\max}$ . Upon close inspection, we can still see some deviations at higher  $k_{\max}$  between theoretical predictions and simulations. These deviations are mainly because of higher-order terms which we neglect in this work. Finally, we carry out forecasts for some future galaxy surveys to constrain local-type of primordial non-Gaussianity. It has been shown that the galaxy field has unique imprints from inflation on large scales which has  $1/k^2$  behaviour [57, 64, 175, 135]. We show that the reconstructed large-scale modes from our quadratic estimator method have the same  $1/k^2$  contributions on large scales from the local non-Gaussianity. This motivates us to use the reconstructed field alongside the galaxy field to do multi-tracer analysis of local  $f_{\text{NL}}$ . We show that constraints

on local  $f_{\text{NL}}$  get improved by tens of percents compared to only using a single galaxy field. Therefore, this method enables us to do multi-tracer analysis using a single tracer.

## Chapter 6

In Chapter 6, we develop a novel method to measure non-linear galaxy bias parameters using the 2- and 3-point functions of the projected galaxy clustering in correlation with the CMB lensing. We bring the method presented in chapter 4 closer to data analysis. We develop the quadratic field method for the projected fields to circumvent the problem of non-linear redshift space distortions. We carry our Fisher forecasts for linear and quadratic bias parameters ( $b_1$ ,  $b_2$  and  $b_{s,2}$ ) as well as relative amplitude of matter fluctuations  $A_s$  for 8 different redshift slices ranging from  $z = 0.1$  to  $z = 4$ . Finally, we perform  $N$ -body simulations and show that, first, our methods indeed agree with simulations, and second, the projections indeed reduce the impact of non-linear finger-of-god effects from redshift space distortions.

## Conclusion

Finally we summarise our results in this thesis and discuss possible future outlooks.



## Standard Model of Cosmology

In this chapter we review the standard cosmological model to understand the concepts used in this thesis. In this chapter, we use the signature  $(-, + + +)$  for the metric. To represent 4-spacetime we use  $(\mu, \nu, \dots)$  and for 3-space the indices will be Latin  $(i, j, \dots)$ . We choose natural units such that the speed of light and the Planck's constant are set to unity ( $c = \hbar = 1$ ). This chapter is mostly based on [32, 109, 84].

### 2.1 Metric

On large scales ( $\geq 100$  Mpc) we assume that the Universe is homogeneous, isotropic and the General theory of relativity is the correct description of the gravity on such scales. The homogeneity and isotropy imply translational and rotational invariance respectively. These two assumptions have very strong support from the measurements of the temperature fluctuations in the Cosmic Microwave Background (CMB) which is uniform up to one part in 100,000. The temperature fluctuations in CMB are statistically homogeneous and isotropic. The assumption that the GR is the correct theory of gravity is very well tested on solar system scales and even larger scales [154]. These three assumptions allow us to define the following spacetime metric:

$$ds^2 = g_{\mu\nu} dx^\mu dx^\nu = -dt^2 + a(t)^2 dl^2. \quad (2.1)$$

where  $dl^2 = \gamma_{ij} dx^i dx^j$  is a 3-metric with a constant curvature. This 3-metric can be rewritten as (see [84] for explicit calculations)

$$dl^2 = R^2 \left[ \frac{dr^2}{1 - Kr^2} + r^2 (d\theta^2 + \sin^2 \theta d\phi^2) \right] \quad (2.2)$$

where  $K$  is the comoving curvature and  $R$  is the radius of curvature.  $K$  can take three values  $K \in \{-1, 0, 1\}$  on three different types of geometries. For  $K = -1$ , the underlying geometry

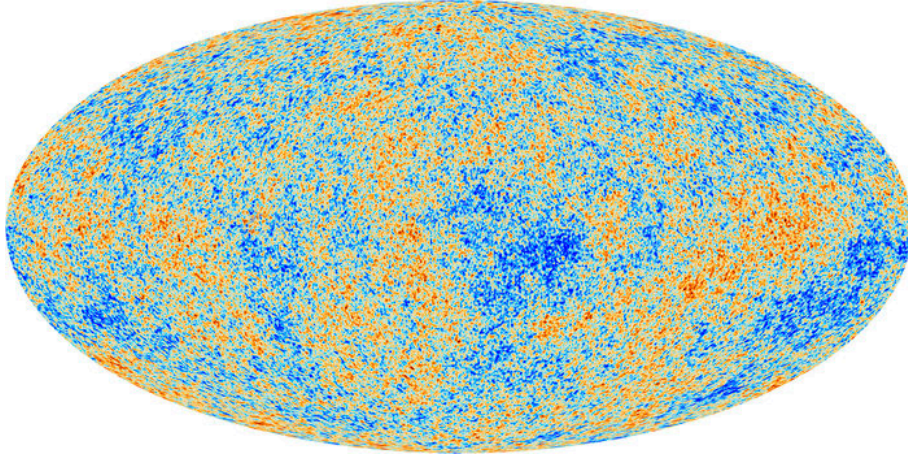


*Fig. 2.1* Temperature fluctuations from the Cosmic Microwave Background (CMB) mapped by the Planck Satellite experiment [162]. The mean temperature is 2.7K and the blue and red spots correspond to over-dense and under-dense regions respectively.

is hyperbolic  $\mathbf{H}^3$ ; for  $K = 0$  it is non-Euclidean geometry  $\mathbf{E}^3$ ; and  $K = 1$  for spherical geometry  $\mathbf{S}^3$ . We now substitute Eq. (2.2) in Eq. (2.1) and can absorb the radius of curvature  $R$  in the scale factor  $a(t)$  by  $a(t)R \rightarrow a(t)$  to obtain the Friedmann-Lemaitre-Robertson-Walker (FLRW) metric [170, 89, 124]:

$$ds^2 = -dt^2 + a^2(t) \left[ \frac{dr^2}{1 - Kr^2} + r^2 (d\theta^2 + \sin^2 \theta d\phi^2) \right]. \quad (2.3)$$

## 2.2 Dynamics

To study the evolution of the metric and to derive cosmological field equations, we need the Einstein equations. In 1915, Albert Einstein introduced the general theory of gravity and wrote down the gravitational field equations [76]. In 1917 he modified his equations by adding the cosmological constant  $\Lambda$  in his field equations [75]. The famous equations of Einstein's theory of gravity take the following form:

$$G_{\mu\nu} = 8\pi G T_{\mu\nu} - \Lambda g_{\mu\nu}, \quad (2.4)$$

where  $G_{\mu\nu}$  is the Einstein tensor which depends on the geometry of spacetime,  $G$  is the Newtonian gravitational constant,  $T_{\mu\nu}$  is the energy-momentum tensor and  $g_{\mu\nu}$  is the 4-metric. Einstein's theory predicts different states of the Universe depending on the geometry of spacetime as well as the initial conditions. To counter the effect of gravity in the predictions, Einstein introduced a counter-gravity term which he called the gravitational constant,  $\Lambda$ , in his equations. To understand Einstein's equations we need to define the Einstein's tensor

$G_{\mu\nu}$  in terms of the spacetime metric of a Riemannian manifold. The unique torsion-free and metric-compatible connections on a Riemannian manifold are described by the Levi-Civita connection. The connection coefficients are described by the Christoffel symbols:

$$\Gamma_{\mu\nu}^{\rho} = \frac{1}{2}g^{\rho\sigma}(\partial_{\mu}g_{\sigma\nu} + \partial_{\nu}g_{\mu\sigma} - \partial_{\sigma}g_{\mu\nu}). \quad (2.5)$$

From Eq. (2.5) we can define the Riemann curvature tensor

$$R_{\mu\nu\sigma}^{\rho} = \partial_{\mu}\Gamma_{\nu\sigma}^{\rho} + \partial_{\nu}\Gamma_{\mu\sigma}^{\rho} + \Gamma_{\mu\sigma}^{\tau}\Gamma_{\nu\tau}^{\rho} - \Gamma_{\nu\sigma}^{\tau}\Gamma_{\mu\tau}^{\rho}, \quad (2.6)$$

its contractions such as the Ricci tensor,  $R_{\mu\nu}$ ,

$$R_{\mu\nu} \equiv R_{\mu\sigma\nu}^{\sigma} = -\partial_{\mu}\Gamma_{\sigma\nu}^{\sigma} + \partial_{\sigma}\Gamma_{\mu\nu}^{\sigma} + \Gamma_{\mu\nu}^{\tau}\Gamma_{\sigma\tau}^{\sigma} - \Gamma_{\sigma\nu}^{\tau}\Gamma_{\mu\tau}^{\sigma}, \quad (2.7)$$

and finally the Ricci scalar,  $R$ ,

$$R \equiv R_{\mu}^{\mu}. \quad (2.8)$$

In terms of these derived quantities, the Einstein tensor can be described as

$$G_{\mu\nu} \equiv R_{\mu\nu} - \frac{1}{2}Rg_{\mu\nu}. \quad (2.9)$$

With the choice of the metric defined in Eq.(2.3), the non-vanishing terms of the Ricci tensor and the Ricci scalar using Eq.(2.6) and Eq.(2.8) respectively are given as follows:

$$R_{00} = -3\frac{\ddot{a}}{a}, \quad (2.10)$$

$$R_{ij} = \left[ \frac{\ddot{a}}{a} + 2\left(\frac{\dot{a}}{a}\right)^2 + 2\frac{K}{a^2} \right] g_{ij}, \quad (2.11)$$

$$R = 6 \left[ \frac{\ddot{a}}{a} + \left(\frac{\dot{a}}{a}\right)^2 + \frac{K}{a^2} \right]. \quad (2.12)$$

Using Eq.(2.10), Eq.(2.11) and Eq.(2.12) it is straightforward to calculate respective non-vanishing terms of the Einstein tensor:

$$G_{00} = 3 \left[ \left(\frac{\dot{a}}{a}\right)^2 + \frac{K}{a^2} \right] \quad (2.13)$$

and

$$G_{ij} = - \left[ 2\left(\frac{\ddot{a}}{a}\right) + \left(\frac{\dot{a}}{a}\right)^2 + \frac{K}{a^2} \right] g_{ij}. \quad (2.14)$$

Now we focus on the right hand side of Eq.(2.4). The energy-momentum tensor  $T_{\mu\nu}$  is defined qualitatively as

$$T_{\mu\nu} = \begin{pmatrix} \text{Energy Density} & \text{Energy Flux} \\ \text{Momentum Density} & \text{Stress Tensor} \end{pmatrix}. \quad (2.15)$$

On large scales, homogeneity and isotropy allow us to model all matter as perfect fluids, parametrised by density  $\rho(t)$  and pressure  $P(t)$ . The energy-momentum tensor,  $T_{\mu\nu}$ , of the perfect fluid is described by

$$T_{\mu\nu} = (\rho + P)U_\mu U_\nu + P g_{\mu\nu}, \quad (2.16)$$

where  $U_\mu$  is the 4-velocity of the perfect fluid. The energy-momentum tensor is conserved, that is

$$\nabla_\mu T_\nu^\mu = \partial_\mu T_\nu^\mu + \Gamma_{\mu\lambda}^\mu T^\lambda_\nu - \Gamma_{\mu\nu}^\lambda T_\lambda^\mu = 0. \quad (2.17)$$

This implies the continuity equation (or the first Friedman equation) for the fluid:

$$\dot{\rho} + 3\frac{\dot{a}}{a}(\rho + P) = 0. \quad (2.18)$$

This equation can be written as

$$\frac{d(\rho a^3)}{dt} = -P \frac{d(a)^3}{dt} \quad (2.19)$$

which is nothing but the first law of thermodynamics. Assuming a constant equation of state,  $P = \omega\rho$ , allows us to write Eq. (2.18) as

$$\frac{\dot{\rho}}{\rho} = -3(1 + \omega)\frac{\dot{a}}{a} \implies \rho = \rho_0 \left(\frac{a}{a_0}\right)^{-3(1+\omega)}. \quad (2.20)$$

The equations of state for matter ( $m$ ), radiation ( $r$ ) and dark energy ( $\Lambda$ ) are described in Tab. 2.1. The other two famous Friedmann equations can be derived from Einstein's equations which are described as

$$\left(\frac{\dot{a}}{a}\right)^2 = H^2 = \frac{8\pi G}{3}\rho - \frac{K}{a^2}, \quad (2.21)$$

$$\frac{\ddot{a}}{a} = -\frac{4\pi G}{3}(\rho + 3P), \quad (2.22)$$

Component	Contributions	Equation of state	Energy density
Matter ( $m$ )	- Cold Dark Matter ( $c$ ) - Baryons ( $b$ )	$\omega = 0$	$\rho \propto a^{-3}$
Radiation ( $r$ )	- Photons - Neutrinos ( $\nu$ ) - Gravitons ( $g$ )	$\omega = \frac{1}{3}$	$\rho \propto a^{-4}$
Dark Energy ( $\Lambda$ )	- Vacuum Energy - Modified Gravity?	$\omega = -1$	$\rho \propto a^0$

Table 2.1 The cosmic inventory. The table is reproduced from [84]

where  $H \equiv \dot{a}/a$  is the Hubble parameter. If we assume the conformal time defined as  $d\tau = dt/a(t)$  then the conformal Hubble parameter  $\mathcal{H}$  is defined as

$$\mathcal{H} = \frac{a'}{a} = aH. \quad (2.23)$$

## 2.3 Kinematics

All observations in cosmology are based on various forms of light. Due to expansion of the Universe and the fact that sources have intrinsic movement in the sky, the photons we observe are *redshifted*. Due to gravity, photons or any massive particle move along a geodesic. To understand this further we first need to derive the geodesic equations. The relativistic action,  $S$ , of a particle with mass  $m$  moving along a path  $x^\mu(\lambda)$ , where  $\lambda$  is some parameter, can be defined as

$$S = \int ds = \int \sqrt{g_{\mu\nu} \dot{x}^\mu \dot{x}^\nu} d\lambda \equiv \int \mathcal{L}(\lambda, x, \dot{x}) d\lambda \quad (2.24)$$

where  $\dot{x}$  means the differentiation with respect to  $\lambda$  and  $\mathcal{L}$  is the Lagrangian. The Euler-Lagrange equations can be obtained by maximizing the action, such that we get

$$\frac{\partial \mathcal{L}}{\partial x^\mu} - \frac{d}{d\lambda} \left( \frac{\partial \mathcal{L}}{\partial \dot{x}^\mu} \right) = 0, \quad (2.25)$$

which can be written as (see [109, 84]) as

$$\ddot{x}^\mu + \frac{1}{2} g^{\mu\nu} \left( \partial_\rho g_{\nu\sigma} + \partial_\sigma g_{\rho\nu} - \partial_\nu g_{\rho\sigma} \right) \dot{x}^\rho \dot{x}^\sigma = \frac{\ddot{s}}{\dot{s}} \dot{x}^\mu. \quad (2.26)$$

The second term in the left hand side of this equation is nothing but the Christoffel symbols defined in Eq. (2.5). The right hand side arises because the parameter  $\lambda$  is general. However if we consider it as an affine parameter such that  $s = a\lambda + b$ , where  $a$  and  $b$  are some

parameters, the right hand side vanishes. If we define the 4-momentum of the particle as  $P^\mu = \dot{x}^\mu$  then we can write the geodesic equation as

$$\frac{dP^\mu}{d\lambda} + \Gamma_{\nu\sigma}^\mu P^\nu P^\sigma = 0 \quad (2.27)$$

This geodesic equation is derived for a massive particle, but this also applies to massless particles like photons which follows null-geodesics. To further simplify this equation, let us re-write the derivative term as

$$\frac{dP^\mu}{d\lambda} = \frac{dx^\nu}{d\lambda} \frac{\partial P^\mu}{\partial x^\nu} = P^\nu \frac{\partial P^\mu}{\partial x^\nu}. \quad (2.28)$$

Homogeneity and isotropy demand that  $\partial_i P^0 = 0$  and so the geodesic equation in Eq. (2.27) becomes

$$P^0 \frac{\partial P^\mu}{\partial t} = - \left( 2\Gamma_{0j}^\mu P^0 + \Gamma_{ij}^\mu P^i \right) P^j. \quad (2.29)$$

Let us discuss some special cases. First, if we assume  $P^i = 0$  then the above geodesic equation implies that  $\partial P^i / \partial t = 0$ . This means that a particle at rest will remain at rest. Now lets consider a general 4-momentum  $p^\mu = (p, \mathbf{p})$  for a photon where  $p$  is the magnitude of the 3-momentum. The geodesic equation for  $\mu = 0$  in Eq. (2.29) can be written as

$$\frac{\dot{p}}{p} = -\frac{\dot{a}}{a} \implies p \propto \frac{1}{a}. \quad (2.30)$$

This result shows that for a massless particle, such as a photon, the physical momentum decays with the expansion of the Universe. This result can be generalised to massive particles too. For a massive particle with mass  $m$  the physical momentum can be written as  $p = mv / \sqrt{1 - v^2}$ , where  $v$  is the peculiar velocity, and so the peculiar velocity decays with the expansion of the Universe. This whole phenomenon is called as redshift effect, as the low frequency of light appears to be red.

## 2.4 Redshift

We now define the redshift parameter  $z$  here. We know for a photon the wavelength  $\lambda$  is related to the physical momentum  $p$  as  $\lambda = h/p$ , where  $h$  is the Planck's constant. From Eq. (2.30) we know the  $p \propto 1/a$  and so  $\lambda \propto a$ . If a photon with the wavelength  $\lambda_1$  get emitted at time  $t_1$  from a far away distance, and observed by us at time  $t_0$  with the wavelength  $\lambda_0$ , then we can define the redshift parameter  $z$  as the change in the wavelength as

$$z \equiv \frac{\lambda_0 - \lambda_1}{\lambda_1} = \frac{a(t_0)}{a(t_1)} - 1. \quad (2.31)$$

It is conventional to define at the scale factor at the current time  $t_0$  as  $a(t_0) = 1$  and so we rewrite the above equation as

$$z + 1 = \frac{1}{a(t_1)}. \quad (2.32)$$

We know that the scale factor increase with time and so redshift parameter  $z$  is a monotonically decreasing function of time. Because of this property it is conventional to use it to describe past events and also the position of galaxies in the sky. The photon from galaxies are redshifted and so by noticing the redshift we can infer the distance of the galaxy. In galaxy surveys, galaxies are often described by angular distance as well as by the redshift.

## 2.5 Hubble's law

The scale factor can be expanded using the Taylor expansion for nearby sources as:

$$a(t) \approx a(t_0) [1 + (t - t_0)H_0 + \dots] \quad (2.33)$$

where  $H_0$  which is the Hubble's parameter defined at the present time and is described as

$$H_0 \equiv \frac{1}{a(t_0)} \frac{da}{dt}. \quad (2.34)$$

Substituting Eq. (2.33) in Eq. (2.32) we get

$$z = H_0(t_0 - t_1) + \dots = H_0 d + \dots \quad (2.35)$$

For nearby objects,  $t_0 - t_1$  is the proper distance  $d$ . This is the famous Hubble's law which states that the redshift of galaxies are proportional to the proper distances. Georges Lemaitre [124] and Edwin Hubble [108] did pioneering work on the measurements of the Hubble's constant. Their work established that the universe really is expanding which was a remarkable discovery at that time. The Hubble constant at present time is defined as

$$H_0 \equiv 100h \text{ km s}^{-1} \text{ Mpc}^{-1}, \quad (2.36)$$

where  $h$  is the dimensionless parameter. The current value of  $h$  as measured by the Planck Collaboration [160] is

$$h = 67.66 \pm 0.42. \quad (2.37)$$

Historically, the measurement of the Hubble constant was based on the Universe's local expansion history. However, the Planck's measurement of  $H_0$  relies on the CMB physics as well as whole expansion history of the Universe. The current measurements of the Hubble

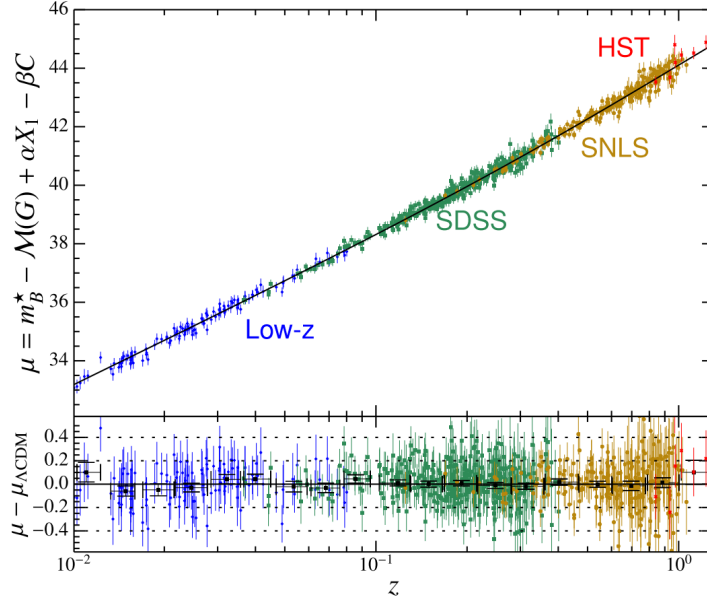


Fig. 2.2 Hubble's law plot for type IA supernova. In this plot  $\mu$  is proportional to  $\log(d)$ . The figure is taken from [84].

parameter using the local expansion history of the Universe at late-times come from the Supernova H0 for the Equation of States (SHoES) collaboration [168]. This cosmological survey makes use of the properties of the Type Ia supernovae explosions. The current measurement of the Hubble parameter by SHoES is  $h = 74.03 \pm 1.42$  which is clearly in tension with the Planck's measurement to more than  $4\sigma$  [169]. This Hubble's parameter tension between the two experiments is one of the most interesting paradoxes in modern cosmology. This might relate to the inherent differences of the Planck and SHoES; the former is based on the early universe physics and the later is based on the late-time measurements. Moreover, both used the same equation of state for Dark energy and so if there are no systematic errors in any of the experiments then one proposal could be that Dark energy is not constant. This would require to modify the standard model of cosmology (see for example [71, 70]). Future experiments will shed more light on how to resolve this paradox.

## 2.6 $\Lambda$ CDM

The latest model of cosmology is the  $\Lambda$ CDM model which states that the universe is flat and dominated by dark energy  $\Lambda$  and cold dark matter. We summarise this model in this section. The critical density parameter  $\rho_{c,0}$  at the present time is defined as

$$\rho_{c,0} \equiv \frac{3H_0^2}{8\pi G} = 1.878 \times 10^{-26} h^2 \text{ kg m}^{-3}. \quad (2.38)$$



We define the dimensionless density parameter for each cosmological component which we denote as  $I$ :

$$\Omega_I \equiv \frac{\rho_{I,0}}{\rho_{c,0}}. \quad (2.39)$$

The Friedman's equation can be expressed as

$$\frac{H^2}{H_0^2} = \Omega_r a^{-4} + \Omega_m a^{-3} + \Omega_k a^{-2} + \Omega_\Lambda \quad (2.40)$$

where  $\Omega_k \equiv -k/(a_0 H_0)^2$  is the curvature density parameter. The precise measurement of the black-body temperature of CMB we got from the COBE experiment is  $T = 2.72548 \pm 0.00057$  K [87] which gives the value of the radiation density  $\Omega_r = 9.140 \times 10^{-5}$ . Other density parameters  $\Omega_m$ ,  $\Omega_k$ , and  $\Omega_\Lambda$  as measured by the Planck collaboration are given as follows [164]:

$$\Omega_m = 0.3111 \pm 0.0056, \quad \Omega_k = 0.0007 \pm 0.0037, \quad \Omega_\Lambda = 0.6889 \pm 0.0056. \quad (2.41)$$

The matter density parameter  $\Omega_m$  is the sum of the cold dark matter density  $\Omega_c = 0.2607$  and the baryon density  $\Omega_b = 0.04897$ . The curvature density is consistent with 0, which means that the Universe is flat. During the matter and the radiation dominated era, any deviation from flatness grows with time. However, the fact that we do not observe any deviation in curvature from flatness shows that the fundamental physics parameters in the early universe physics were finely tuned. This problem is called the *flatness problem* [72]. In order to solve this problem, and some other shortcomings of the basic Big Bang model of cosmology, we describe the theory of cosmic inflation in the next section.

## 2.7 Cosmic Inflation

In this section, we discuss the theory of cosmic inflation (for a useful review, please see [33, 84]). In Sec. 2.6, we described the *flatness problem* in the Big Bang model of cosmology. Another problem is called the *Horizon problem* which is explained as follows. On very large scales, the Universe is homogeneous and isotropic. We observe that the causally disconnected regions now in the Universe seem to have the same temperature and densities. How can these regions, beyond the horizon, are correlated with each other and contains the same information. The theory of cosmic inflation provides a reasonable explanation for these problems. It proposes that given any general initial conditions, an early phase of accelerated expansion pushed the Universe towards the state of homogeneity and isotropy,

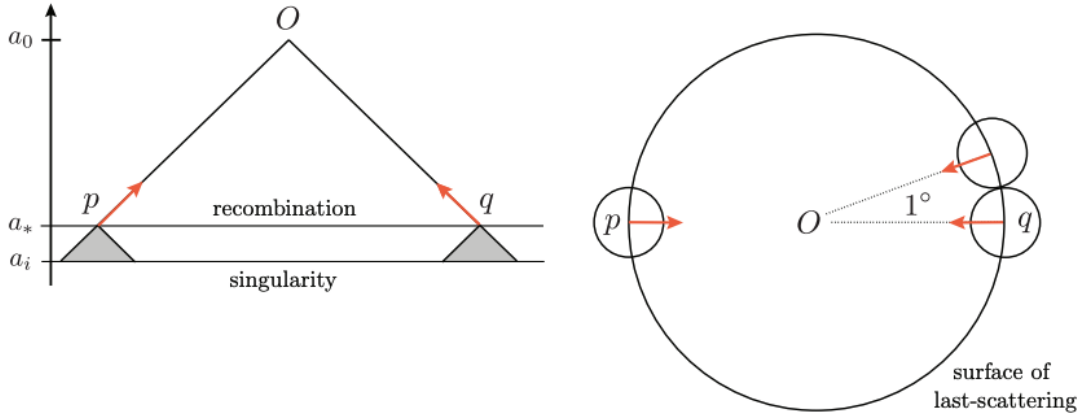


Fig. 2.3 The illustration shows the horizon problem. If the observer  $\mathcal{O}$ , observes two points,  $p$  and  $q$ , in the opposite direction in the sky, then these seem not to be in causal contact in the past. This means that the light cones do not overlap before the singularity, yet these points seem to share the same information. This illustration is taken from [33].

and thus provides an excellent explanation to the flatness and the horizon problems [100, 33].

Cosmic inflation is the leading theory that succinctly describes the formation and evolution of density fluctuations. It predicts an early phase of accelerated expansion during which the quantum fluctuations  $\delta\phi$  in the scalar field  $\phi$ , responsible for driving inflation, were stretched out and became the seeds to the growth of large scale structures. Understanding the exact mechanism of inflation could tell us a lot about fundamental physics. The energy scale of inflation is roughly  $10^{14}$  GeV, which is much higher than the energy scales that we can ever think of achieving in particle colliders. This energy scale is also very close to that of Grand Unified Theories. In this sense, we can think of inflation as a gigantic collider that can be used to extract information about fundamental physics. From particle colliders, we obtain the information of particles interactions at different energy scales, which helps us to identify the Lagrangian of the fundamental physics beyond the standard model. We can extract the same information by studying the mechanism of inflation: the field(s) and types of interactions that were present during the time of inflation, and whether we should expect new particles. Identifying the right model of inflation and understanding its mechanism, therefore, will significantly enhance our understanding of the fundamental physics at high energies.

### 2.7.1 Horizon Problem

Let us introduce the concept of the horizon. The *particle horizon* is the maximum distance that light can travel between an initial time  $\tau_i$  and the final time  $\tau_f$ . This means that the

maximum distance that the current observer could have been influenced by the regions in the past light cone. We define the particle horizon  $\chi_{\text{ph}}$  as

$$\chi_{\text{ph}} = \tau - \tau_i = \int_{\tau_i}^{\tau} \frac{dt}{a(t)} = \int_{\ln a_i}^{\ln a} (\tilde{a}H)^{-1} d \ln \tilde{a} \quad (2.42)$$

where  $(aH)^{-1} = \mathcal{H}^{-1}$  is the *Hubble horizon*. The Hubble horizon is the maximum comoving distance that particles will be able to move in one Hubble time. The Hubble time is defined as  $t_H \equiv H^{-1} = dt/d \ln a$ . For completeness, we can also define the *event horizon*. It is the maximum distance in the future light cone that we can influence. We define it as

$$\chi_{\text{ev}} = \tau_f - \tau = \int_{\tau}^{\tau_f} \frac{dt}{a(t)}. \quad (2.43)$$

In the FRW background, the expression for the particle horizon and the Hubble horizon is the same; however, they differ from each other intuitively. If we say two particles are at a distance  $l$  apart, then if  $l > \chi_{\text{ph}}$  they could never be in causal contact with each other. Whereas if  $l > \mathcal{H}^{-1}$  they can never be able to communicate. In the standard Big Bang cosmology, the Hubble horizon always increases. Inflation solves the Horizon problem by introducing an early phase where the Hubble horizon shrinks. We discuss this in detail in the next subsections.

## 2.7.2 Conditions for Inflation

One solution to the horizon problem is to introduce a period of time in the early Universe when the Hubble sphere shrinks, that is

$$\frac{d}{dt}(\mathcal{H})^{-1} < 0. \quad (2.44)$$

Using this period the comoving horizon is shrinking and the regions which are casually connected exit the horizon. Later when they re-enter the horizon they seem to be casually connected. The initial time  $\tau_i$  can be expressed as

$$\tau_i = \frac{2H_0^{-1}}{1+3w} a_i^{(1+3w)/2}, \quad (2.45)$$

and from Eq. (2.44) implies  $(1+3w) < 0$ , which means  $\tau_i \rightarrow \infty$  as  $a_i \rightarrow 0$ . Fig. 2.4 shows the extended spacetime region due to this condition. There are other popular ideas for describing inflation which are all equivalent. We describe them as [33]:

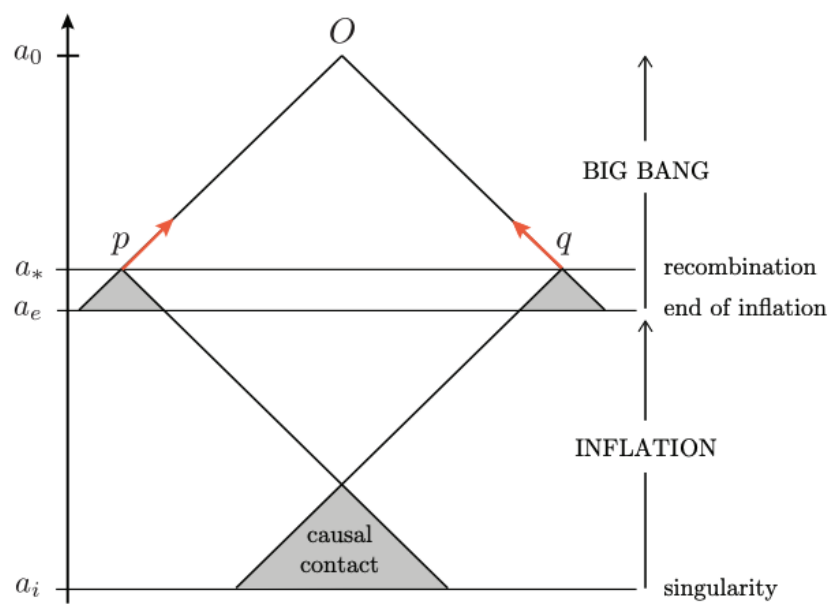


*Fig. 2.4* This illustration, taken from [33], shows the solution of the horizon problem provided by the theory of cosmic inflation. This shows that the singularity of the conventional Big Bang model is replaced by the time when inflation ended. Before that time the Universe went through a phase of accelerated expansion. This shows that all points we observe today, which appear not to have been in causal contact in the Big Bang model, now seem to be in causal contact during the inflationary period.

- **Period of acceleration:** The shrinking Hubble radius implies the accelerated expansion. This is described as

$$\frac{d}{dt}(\mathcal{H})^{-1} = \frac{d}{dt}(\dot{a})^{-1} = -\frac{\ddot{a}}{(\dot{a})^2}. \quad (2.46)$$

Using Eq. (2.44) we get  $\ddot{a} > 0$ .

- **Slowly varying Hubble parameter:** We can also write the condition as

$$\frac{d}{dt}(aH)^{-1} = -\frac{\dot{a}H + a\dot{H}}{(aH)^2} = -\frac{1}{a}(1 - \varepsilon), \quad \text{where} \quad \varepsilon \equiv -\frac{\dot{H}}{H^2} \quad (2.47)$$

The shrinking Hubble radius implies that  $\varepsilon < 1$ .

- **Negative Pressure:** For a perfect fluid with pressure  $P$  and density  $\rho$ , the Friedman equations imply

$$\dot{H} + H^2 = -\frac{1}{M_{\text{pl}}^2}(\rho + 3P) = -\frac{H^2}{2} \left( 1 + \frac{3P}{\rho} \right). \quad (2.48)$$

Using this we write

$$\varepsilon = -\frac{\dot{H}}{H^2} = \frac{3}{2} \left( 1 + \frac{P}{\rho} \right) < 1 \implies w < -\frac{1}{3}, \quad (2.49)$$

where  $w = P/\rho$ . This shows that negative pressure causes inflation.

- **Constant density:** If we combine the continuity equation with Eq. (2.48) we get

$$\left| \frac{d \ln \rho}{d \ln a} \right| = 2\varepsilon < 1. \quad (2.50)$$

This shows that for small  $\varepsilon$ , which is required for inflation, we need the constant energy density, unlike the ordinary matter which energy density dilutes with the expansion of the Universe.

### 2.7.3 The Physics of Inflation

We discussed that for inflation to occur we need

$$\varepsilon \equiv -\frac{\dot{H}}{H^2} = -\frac{d \ln H}{dN} < 1. \quad (2.51)$$

Once the inflation has occurred. We need a condition for it to last for at least 60-*e*-folds. We define  $dN \equiv d \ln a = H dt$  which measures the number of *e*-folds  $N$  of inflationary expansion. To solve the horizon problem we need inflation to last for a long time and therefore we need  $N$  to be within the range of 40 to 60 *e*-folds. This condition is parametersied by

$$\eta \equiv \frac{\dot{\epsilon}}{H\epsilon} = \frac{d \ln \epsilon}{d \ln a} < 1. \quad (2.52)$$

This shows that if the fractional change of  $\epsilon$  per Hubble time is small then inflation lasts. These two parameters,  $\epsilon$  and  $\eta$ , are know as slow-roll parameters. The conditions for inflation can be summarised by  $\epsilon < 1$  and  $\eta < 1$ .

### 2.7.4 Slow-Roll Inflation

In this subsection we discuss the microscopic origin of the physics of inflation. The simple single field slow-roll inflation model depends on a scalar field  $\phi(t, \mathbf{x})$ , called the *inflaton field*, coupled with the gravity. This field contains a potential energy  $V(\phi)$ ; the shape of the potential is described as shown in Fig. 2.5. The most general action, without specifying the form of the potential, is

$$S = \int d^4x \sqrt{-g} \left[ \frac{M_{pl}^2}{2} R - \frac{1}{2} \partial_\mu \phi \partial^\mu \phi - V(\phi) \right]. \quad (2.53)$$

The background is described by the flat FRW metric

$$ds^2 = g_{\mu\nu} dx^\mu dx^\nu = -dt^2 + a^2(t) \delta_{ij} dx^i dx^j, \quad (2.54)$$

where  $a(t)$  represents the scale factor describing the expansion of the universe and  $x^i$  are the comoving spatial coordinates. We can split  $\phi(t, \mathbf{x})$  into the background field  $\bar{\phi}(t)$ , which only depends on time, and perturbations  $\delta\phi(t, \mathbf{x})$ , which depend both on time and space. Let us introduce the background stress-energy tensor:

$$T_{\mu\nu} = -\frac{2}{\sqrt{-g}} \frac{\delta S}{\delta g^{\mu\nu}} = \partial_\mu \phi \partial_\nu \phi - g_{\mu\nu} \left( \frac{1}{2} \partial^\sigma \phi \partial_\sigma \phi + V(\phi) \right), \quad (2.55)$$

where

$$\begin{aligned} T_0^0 = -\rho &\Rightarrow \text{Energy density: } \rho = \frac{1}{2} \dot{\bar{\phi}}^2 + V(\bar{\phi}), \\ T_j^i = P \delta_j^i &\Rightarrow \text{Pressure: } P = \frac{1}{2} \dot{\bar{\phi}}^2 - V(\bar{\phi}). \end{aligned} \quad (2.56)$$

Given this stress-energy tensor, the Friedman equations become:

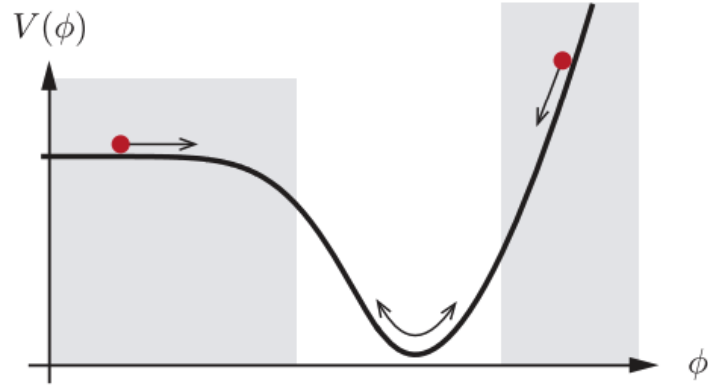


*Fig. 2.5* Potential in the slow-roll inflation. The inflaton (in red) rolls down the potential, causing inflation. The shaded regions describe the regions where inflation happens. When the potential energy converts into kinetic energy at the end of the potential, inflation ends. The figure is adapted from [33].

$$H^2 = \frac{\rho}{3M_{pl}^2} = \frac{1}{3M_{pl}^2} \left( \frac{1}{2} \dot{\phi}^2 + V(\bar{\phi}) \right) \quad (2.57)$$

$$\dot{H} = \frac{1}{2M_{pl}^2} (\rho + P) = -\frac{\dot{\phi}^2}{2M_{pl}^2}, \quad (2.58)$$

where  $M_{pl} \equiv (8\pi G)^{-1/2}$  is the reduced Planck mass. By taking the time derivative of the first Friedman equation and using the second give us the Klein Gordon equation of the inflaton in the unperturbed FRW background:

$$\ddot{\phi} + 3H\dot{\phi} + V'(\bar{\phi}) = 0 \quad (2.59)$$

where  $H = \dot{a}/a$  is the Hubble's parameter and  $V' = dV/d\phi$ . We see the expansion of the universe introduces the friction term which slows down the rolling inflaton. Substituting Eq. (2.58) in Eq. (2.51) we get

$$\epsilon = -\frac{\dot{H}}{H} = \frac{\dot{\phi}^2}{2M_{pl}^2 H^2} < 1. \quad (2.60)$$

For inflation to occur the kinetic term of the scalar field should be small. We define now the dimensionless acceleration per Hubble time as

$$\delta \equiv -\frac{\ddot{\phi}}{H\dot{\phi}} \quad (2.61)$$

For inflation to persist  $\delta$  should be small too. Taking the time derivative of  $\varepsilon$  we write  $\eta$  as

$$\eta = \frac{\dot{\varepsilon}}{H\varepsilon} = 2\frac{\ddot{\phi}}{H\dot{\phi}} - 2\frac{\dot{H}}{H^2} = 2(\varepsilon - \delta). \quad (2.62)$$

This shows that  $\varepsilon < 1$  and  $\delta < 1$  implies  $\eta < 1$ . Using these *slow-roll approximation* we can simplify the Friedman and Klein-Gordon equations. The condition that  $\varepsilon < 1$  implies the Friedman equation to simplify as

$$H^2 \approx \frac{V}{3M_{\text{pl}}^2}. \quad (2.63)$$

and the condition  $\delta < 1$  simplifies the Klein-Gordon equation to become

$$3H\dot{\phi} \approx -V'. \quad (2.64)$$

using these simplified equations we can describe the relation between the gradient of the potential and the kinetic energy of the inflaton. The  $\varepsilon$  can be written as

$$\varepsilon = \frac{\dot{\phi}^2}{2M_{\text{pl}}^2 H^2} \approx \frac{M_{\text{pl}}^2}{2} \left( \frac{V'}{V} \right)^2. \quad (2.65)$$

and also with some computation we can get

$$\delta + \varepsilon = -\frac{\ddot{\phi}}{H\dot{\phi}} - \frac{\dot{H}}{H^2} \approx M_{\text{pl}}^2 \frac{V''}{V}. \quad (2.66)$$

These results show that one another way to describe the *slow-roll parameters* are in terms of potential:

$$\varepsilon_V \equiv \frac{M_{\text{pl}}^2}{2} \left( \frac{V'}{V} \right)^2, \quad |\eta_V| \equiv \frac{\dot{H}}{H^2} \approx M_{\text{pl}}^2 \frac{V''}{V}. \quad (2.67)$$

Another way to describe the conditions for inflation are:  $\varepsilon_V \ll 1$  and  $|\eta_V| \ll 1$ . One can see that for a nearly flat potential the slow-roll conditions satisfy and inflation happens as shown in Fig. 2.5.

### 2.7.5 Metric Perturbations

To test the predictions of inflationary models against observations we have to compute the statistical properties of the field's fluctuations. The most convenient variable to use is the comoving curvature perturbation denoted by  $\zeta$ . Simple inflationary models predict that the curvature perturbations for adiabatic primordial fluctuations are conserved on super-horizon



scales, i.e.  $k \ll \mathcal{H}$ . This means that these modes got frozen when they exit the horizon during inflation but re-enter the horizon at late-times. Because of this property they contain useful information about the inflationary mechanism (see Fig. 2.6). To study the statistics of  $\zeta$ , let's first start with the perturbed FLRW metric:

$$ds^2 = a^2(\tau) \left[ - (1 + 2A)d\tau^2 + 2B_i d\tau dx^i + (\delta_{ij} + h_{ij}) dx^i dx^j \right]. \quad (2.68)$$

These perturbations can be decomposed into scalar, vector and tensor parts. The vector part  $B_i$  can be further decomposed into a scalar part  $\delta_i B$  and a divergence-free vector which satisfies  $\delta^i \hat{B}_i = 0$ . Since the vector perturbations do not have any source it decays with expansion and so can be ignored. The tensor part  $h_{ij}$  can further be decomposed into a scalar part,  $2C\delta_{ij} + 2\delta_{(i}\delta_{j)}E$ , a divergence-free vector part,  $2\delta_{(i}\hat{E}_{j)}$ , and a traceless tensor  $2\hat{E}_{ij}$ . We introduce some notations and to explain them we define:

$$\partial_{(i}\partial_{j)}E \equiv \left( \partial_i\partial_j - \frac{1}{3}\delta_{ij}\nabla^2 \right) E, \quad (2.69)$$

$$\partial_{(i}\hat{E}_{j)} \equiv \frac{1}{2} \left( \partial_i\hat{E}_j + \partial_j\hat{E}_i \right). \quad (2.70)$$

All these comprises of 10 degrees of freedom, and not all are physical. In the GR, a general choice of coordinate system can introduce non-physical degrees of freedom which can be eliminated either by using a different coordinate system or by fixing a gauge. We can also work with quantities which are gauge-invariant and do not depends on any choice of coordinate system. Let us choose a general coordinate transformation, i.e.  $x^\mu \rightarrow \tilde{x}^\mu = x^\mu + \eta^\mu$ . We apply the SVT decomposition using  $\zeta^\mu = (\zeta^0, \partial_i\zeta + \hat{\zeta}_i)$ . Using this we can eliminate 2 scalar degrees of freedom and 2 vector degrees of freedom. In a *spatially-flat* gauge, where  $C = E = 0$ , we can see that scalar perturbations  $\delta\phi$  is related to the curvature perturbations  $\zeta$  by

$$\zeta = -\frac{aH}{\dot{\phi}} \delta\phi. \quad (2.71)$$

### 2.7.6 Statistics of Scalar Perturbations

To check the predictions of the inflationary models against observations, we have to compute statistical properties of  $\zeta$ . The one-point function, which is simply the ensemble mean of the field, is considered to be zero, i.e.  $\langle \zeta \rangle = 0$ . The power spectrum, which is simply the two-point correlation function in Fourier space, is defined as

$$\langle \zeta(\mathbf{k})\zeta(\mathbf{k}') \rangle = (2\pi)^3 \delta_{\mathbf{D}}(\mathbf{k} + \mathbf{k}') P_\zeta(k). \quad (2.72)$$

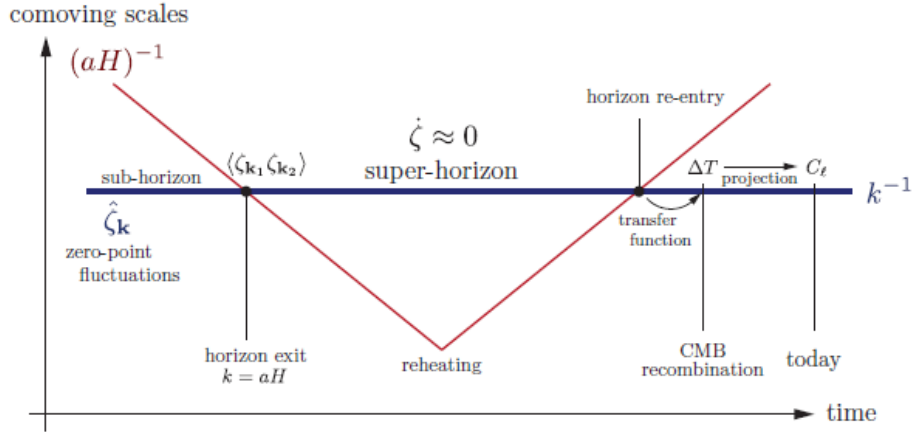


Fig. 2.6 Illustration of the evolution of curvature perturbations  $\zeta$ . On super-horizon scales, modes  $k \ll \mathcal{H}$ , exit the horizon due to shrinking Hubble sphere, and got frozen. These frozen modes re-enter the horizon at late-times after reheating and have significant impact on the temperature fluctuations of the CMB. The figure is adapted from [34].

Due to the delta function, the power spectrum only depends on the magnitude of the Fourier mode. As inflation predicts a scale invariant spectrum, it is convenient to introduce the dimension-less power spectrum defined as

$$\Delta_{\zeta}^2(k) \equiv \frac{k^3}{2\pi^2} P_{\zeta}(k). \quad (2.73)$$

It is convenient to change the variable from  $\delta\phi$  to  $\zeta$  at the time of horizon crossing when  $k = aH$ . We can use Eq.(2.71) to write Eq.(2.73) as

$$\Delta_{\zeta}^2(k) = \left( \frac{aH}{\dot{\phi}} \right)^2 \Delta_{\delta\phi}^2 \Big|_{k=aH} = \frac{1}{2\varepsilon M_{\text{pl}}^2} \Delta_{\delta\phi}^2 \Big|_{k=aH} \quad (2.74)$$

where  $\varepsilon$  is the slow-roll parameter. For single-field slow-roll inflation the power spectrum of  $\delta\phi$  in the super-horizon limit is  $\Delta_{\delta\phi}^2 = (H/2\pi)^2$  [109]. This means that  $\Delta_{\zeta}^2$  depends on  $H$  and  $\varepsilon$  which are slowly varying variables during inflation. As we are evaluating  $\Delta_{\zeta}^2$  at the time of horizon crossing it remains scale invariant such that we can define it as

$$\Delta_{\zeta}^2(k) \equiv A_s \left( \frac{k}{k_*} \right)^{n_s-1} \quad (2.75)$$

where  $A_s$  is the amplitude of fluctuations measured at the reference wavenumber  $k_*$  and  $n_s$  is the spectral tilt of the power spectrum. For single-field slow-roll inflation we define the

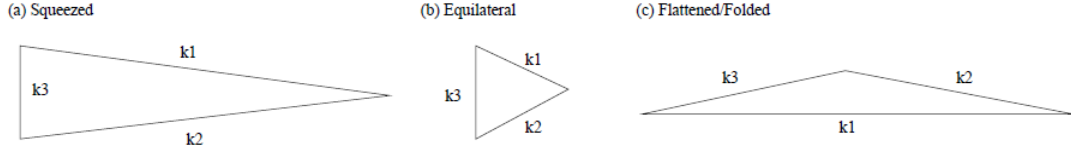


Fig. 2.7 The illustration shows three triangle configurations of bispectrum. The figure is adapted from [120].

spectral tilt as

$$n_s - 1 \equiv \frac{d \ln \Delta_\zeta^2}{d \ln k} = -2\varepsilon - \eta. \quad (2.76)$$

This result shows that inflation predicts a small deviation from the exact scale invariance of the power spectrum. If the primordial scalar perturbations are Gaussian then the statistical properties are defined only by the power spectrum. However, if the primordial fluctuations are not Gaussian then more interesting information is given by the higher point functions. The lowest order statistics which contains the non-Gaussianity information is the bispectrum, which is simply the three-point correlation functions in Fourier space:

$$\langle \zeta(\mathbf{k}_1) \zeta(\mathbf{k}_2) \zeta(\mathbf{k}_3) \rangle = (2\pi)^3 \delta_{\mathbf{D}}(\mathbf{k}_1 + \mathbf{k}_2 + \mathbf{k}_3) B_\zeta(k_1, k_2, k_3) \quad (2.77)$$

where the Dirac delta function imposes the restriction that the three Fourier modes should form a triangle, i.e.  $\mathbf{k}_1 + \mathbf{k}_2 + \mathbf{k}_3 = 0$ . Three particular configurations of triangles are given in Fig. 2.7. We define the shape of the bispectrum as

$$S(k_1, k_2, k_3) = \frac{B(k_1, k_2, k_3)}{\Delta_\zeta^2} (k_1 k_2 k_3)^2. \quad (2.78)$$

Moreover, we define the amplitude of the bispectrum,  $f_{\text{NL}}$ , in the equilateral configuration as [119]

$$f_{\text{NL}} = \frac{k^6}{\Delta_\zeta^2} B(k, k, k), \quad (2.79)$$

where all three  $k_i$  are equal. An important type of non-Gaussianity, which we are also going to discuss later in this thesis is the local-type. If we assume the perturbation to Gaussianity is local in real space we can Taylor expand the non-Gaussian local field as

$$\zeta_{\text{local}}(\mathbf{x}) = \zeta_{\text{G}}(\mathbf{x}) + \frac{3}{5} f_{\text{NL}}^{\text{loc}} (\zeta_{\text{G}}^2(\mathbf{x}) - \langle \zeta_{\text{G}}^2 \rangle). \quad (2.80)$$

It has been shown that local-type non-Gaussianity has unique  $1/k^2$  type imprint on late-time observables [153] which we will discuss in Chapter 5.

## Large-Scale Structure of the Universe

In the previous chapter, we discussed that inflation created the initial conditions for the Universe. These initial conditions are defined by primordial curvature perturbations which then evolved into other cosmological observables at late times. The evolution of primordial perturbations is non-trivial as it depends on several factors and also on the fact that modes enter the horizon at different times. The Transfer function, defined by  $T(k, z)$ , captures this information at least at the linear order. This function relates the linear matter density  $\delta_{\text{lin}}$  with the primordial density field  $\delta_{\text{p}}$  at high redshift  $z$ :  $\delta_{\text{lin}}(\mathbf{k}, z) = T(k, z)\delta_{\text{p}}(\mathbf{k})$ . The linear power spectrum can be written as

$$P_{\text{lin}}(k, z) = T^2(k, z)P_{\text{p}}(k) \quad (3.1)$$

where the primordial power spectrum  $P_{\text{p}} \propto k^{n_s}$  for slow-roll single-field inflation. The transfer function can be calculated numerically using packages such as CAMB [127], CMBFast [186], and CLASS [125]. A general idea to calculate the transfer function numerically is by tracing the interactions of matter and radiation during the radiation domination era and then by evolution of linear density field in the matter domination era [109].

The two important late-time observables in cosmology are CMB temperature anisotropies defined by  $\Theta = \nabla T/T$  and the matter overdensity field which defined in real space as

$$\delta(\mathbf{x}) = \frac{\Delta\rho(\mathbf{x})}{\bar{\rho}} \quad (3.2)$$

where  $\bar{\rho}$  is the background matter density field. The matter density field is considered as a continuous field which interacts with other matter through gravity. The gravitational evolution of matter induces nonlinearities in the matter field at late-times. So even if there are no non-linearities in the initial conditions, the gravitational evolution introduces non-linearities in the dark matter distribution at late-times. The clustering dark matter forms gravitationally-bound, virialised dark matter halos, and inside those halos galaxies

are formed. The dark matter halo field  $\delta_h$  is a discrete field defined in term of the halo centres. The galaxies are born inside dark matter halos and therefore provide a way to trace the distribution of dark matter. The clustering of halos or galaxies (defined by  $\delta_h$  or  $\delta_g$  respectively) is not the same as the clustering of dark matter, instead, it is biased compare to that of matter. We define the overdensity of galaxy field in terms of the number density  $n(x)$ :

$$\delta_g(\mathbf{x}) = \frac{\Delta n(\mathbf{x})}{\bar{n}} \quad (3.3)$$

where  $n$  is the number density of the discrete tracer. We study the biasing relation of the discrete tracers of the matter density field in this thesis. As we mentioned that gravitational evolution induces non-linearities in the matter density field, so even if the initial conditions are Gaussian, the matter density field will have a non-vanishing bispectrum. In Fourier space the matter bispectrum is defined as

$$\langle \delta(\mathbf{k}_1)\delta(\mathbf{k}_2)\delta(\mathbf{k}_3) \rangle = (2\pi)^3 \delta_D(\mathbf{k}_1 + \mathbf{k}_2 + \mathbf{k}_3) B_\delta(k_1, k_2, k_3). \quad (3.4)$$

In this chapter, to calculate the statistics of the clustering of the late-time matter density field and discrete tracer fields, we develop the framework of cosmological perturbation theory. We introduce the standard perturbation theory (SPT) which provides a framework to study non-linear dynamics of matter fields. We introduce Eulerian and Lagrangian Perturbation Theory. Lagrangian Perturbation Theory (LPT) is useful to generate the initial conditions in  $N$ -body simulations. We shall discuss the shortcoming of SPT and introduce the framework of Effective Field Theory of Large-Scale Structure (EFTofLSS). We also discuss biased tracers and the statistics of biased tracers.

### 3.1 Standard Perturbation Theory (SPT)

In this section, we derive the equations of motion and discuss the standard perturbation theory (SPT) following [12, 37, 109]. First, let us consider the Newtonian limit, that is small distance  $x \ll H^{-1}$  and small velocities  $v \ll 1$ . In the Newtonian limit, we can write the equation of motion for a particle as

$$\ddot{\mathbf{r}} = -\nabla_{\mathbf{r}}\Phi \quad (3.5)$$

where  $\mathbf{r}$  is the physical position defined as  $\mathbf{r} = a\mathbf{x}$  and  $\Phi$  is the gravitational potential. The derivative of the physical position with respect to the physical time can be expressed in terms

of the comoving position  $\mathbf{x}$  as  $\dot{\mathbf{r}} = \mathcal{H}\mathbf{x} + \mathbf{x}'$ . The eq. (3.5) can now be written as

$$\dot{\mathbf{r}} = \frac{1}{a} \left( \mathcal{H}'\mathbf{x} + \mathcal{H}\mathbf{x}' + \mathbf{x}'' \right) = \frac{1}{a} \nabla \Phi. \quad (3.6)$$

We identify  $\mathbf{u} = \mathbf{x}'$  as the peculiar velocity and define the peculiar potential as

$$\Phi = -\frac{1}{2} \mathcal{H}' x^2 + \phi, \quad (3.7)$$

where the derivative of the Hubble parameter is defined as  $\mathcal{H}' = -4\pi G a \rho / 3$ . We can write the equation of motion as

$$\mathbf{u}' + \mathcal{H}\mathbf{u} = -\nabla \phi. \quad (3.8)$$

This is a good approximation as the Universe now is  $\Lambda$ -dominated and most of the structure formation takes place in the matter-dominated era. We write the Poisson equation in terms of the comoving quantities as

$$\nabla^2 \phi = 4\pi G a^2 \bar{\rho} \delta = \frac{3}{2} \mathcal{H}^2 \Omega_m(\tau) \delta_m, \quad (3.9)$$

where we assume that perturbations are sourced by matter only. From this equation we can see that the peculiar potential is sourced by the density fluctuations  $\delta$ .

Now we discuss the Vlasov equation. The distribution function  $f(\mathbf{x}, \mathbf{p}, \tau)$  of particles in the phase space is a function of conjugate momentum  $\mathbf{p}$  and position  $\mathbf{x}$ . The conjugate momentum is defined as  $\mathbf{p} = am\mathbf{u}$ . The total number of particles in the volume  $d^3x$  having the momentum distribution  $d^3p$  is given by  $dN = f(\mathbf{x}, \mathbf{p}, \tau) d^3x d^3p$ . The Liouville theorem asserts that the distribution function along the phase space trajectory of collision less particles is constant. This leads us to the Vlasov equation defined as

$$\begin{aligned} \frac{df}{d\tau} &= \frac{\partial f}{\partial \tau} + \frac{d\mathbf{x}}{d\tau} \cdot \frac{\partial f}{\partial \mathbf{x}} + \frac{d\mathbf{p}}{d\tau} \cdot \frac{\partial f}{\partial \mathbf{p}} \\ &= \frac{\partial f}{\partial \tau} + \frac{\mathbf{p}}{ma} \cdot \nabla f - am \nabla \Phi \cdot \frac{\partial f}{\partial \mathbf{p}} = 0. \end{aligned} \quad (3.10)$$

This Vlasov equation is very complicated to deal with because it is a non-linear partial differential equation. Non-linearity comes from the gravitational potential. We take the moments of the distribution function and the Vlasov equation to obtain the set of equations in position space. The zeroth-, first- and second moments of  $f(\mathbf{x}, \mathbf{p}, \tau)$  describe the energy

density  $\rho$ , the peculiar velocity flow  $u_i$  and stress tensor  $\sigma_{ij}$  in the following way:

$$\rho(\mathbf{x}, \tau) \equiv \frac{m}{a^3} \int d^3\mathbf{p} f(\mathbf{x}, \mathbf{p}, \tau), \quad (3.11)$$

$$u_i(\mathbf{x}, \tau) \equiv \frac{m}{\rho(\mathbf{x}, \tau)a^3} \int d^3\mathbf{p} \frac{p_i}{am} f(\mathbf{x}, \mathbf{p}, \tau), \quad (3.12)$$

$$\sigma_{ij}(\mathbf{x}, \tau) \equiv \frac{m}{\rho(\mathbf{x}, \tau)a^3} \int d^3\mathbf{p} \frac{p_i p_j}{a^2 m^2} f(\mathbf{x}, \mathbf{p}, \tau) - u_i u_j \quad (3.13)$$

The zeroth order moment of eq. (3.10) gives us the continuity equation

$$\delta'(\mathbf{x}, \tau) + \nabla \cdot \left[ (1 + \delta)\mathbf{u}(\mathbf{x}, \tau) \right] = 0 \quad (3.14)$$

and the second order moment gives rise to the Euler equation (or the conservation of momentum)

$$\mathbf{u}'(\mathbf{x}, \tau) + \mathcal{H}\mathbf{u}(\mathbf{x}, \tau) + \mathbf{u}(\mathbf{x}, \tau) \cdot \nabla \mathbf{u}(\mathbf{x}, \tau) + \nabla \Phi(\mathbf{x}, \tau) + \frac{1}{\rho} \nabla_j (\rho \sigma_{ij}) = 0. \quad (3.15)$$

In principle we can achieve a hierarchy of equations by taking higher moments, which will couple the equation of motion for the  $n$ -th order moment of the Vlasov equation to the  $n + 1$ -th moment. However for pressureless cold dark matter we can make a good assumption that all moments higher than velocity vanish. This is a good assumption in the linear regime and for the late-time (non-linear regime) it should be validated using numerical simulations. We set  $\sigma_{ij} = 0$  and write  $\mathbf{u}$  in terms of a divergence term  $\theta = \nabla \cdot \mathbf{u}$  and curl  $\mathbf{w} = \nabla \times \mathbf{u}$ . The equation corresponding to the curl can be ignored in the absence of any anisotropic stress and primordial velocity.

### 3.1.1 Linearized Equations

It is interesting to see the solution to the linearized equations. Let us neglect the quadratic terms in the continuity and Euler equations:

$$\delta' + \theta = 0 \quad (3.16)$$

$$\mathbf{u}' + \mathcal{H}\mathbf{u} = -\nabla\phi. \quad (3.17)$$

In terms of divergence and the velocity vorticity we can write the Euler equation as

$$\theta' + \mathcal{H}\theta = -\Delta\phi \quad (3.18)$$

$$\mathbf{w}' + \mathcal{H}\mathbf{w} = 0. \quad (3.19)$$

It is straightforward to solve the vorticity equation. The solution is  $\mathbf{w} \propto a^{-1}$ , this means that vorticity decay at linear level with the scale factor. To solve Eq. (3.18) we take the time derivative of Eq.(3.16) and replace  $\theta'$  with Eq. (3.18). Also using the Poisson equation in the resulting equation we get the second order differential equation:

$$\delta''(\mathbf{k}, \tau) + \mathcal{H} \delta'(\mathbf{k}, \tau) - \frac{3}{2} \Omega_m(\tau) \mathcal{H}^2 \delta(\mathbf{k}, \tau) = 0. \quad (3.20)$$

This equation has two solutions: one is a decaying mode solution  $D_-(\tau) \delta_-(\mathbf{k})$  and another is a growing mode solution  $D_+(\tau) \delta_+(\mathbf{k})$ . The full solution is the combination of both:  $\delta(\mathbf{k}, \tau) = D_-(\tau) \delta_-(\mathbf{k}) + D_+(\tau) \delta_+(\mathbf{k})$ . The decaying mode factor is defined as  $D_-(\tau) = \mathcal{H}/a$  and the growing modes factor, which is also called the growth factor, is described by

$$D_+(\tau) = D_{+,0} H(\tau) \int_0^{a(\tau)} \frac{da'}{\mathcal{H}^3(a')}, \quad (3.21)$$

where  $D_{+,0}$  is a normalisation factor. We can use the normalisation factor to fix  $D_+(a=1) = 1$ . For an EdS Universe, we can get the exact form solutions as:  $D_+ = a$  and  $D_- = a^{-3/2}$ . This shows that in matter-only Universe the growth scales as the scale factor. Unlike EdS, in the  $\Lambda$ CDM Universe, the structure grows initially but at late times the growth stops as the Universe become dominated by the dark energy. From now on we represent the growth factor as  $D$ . Sometimes we see logarithmic growth factor, which is defined as

$$f = \frac{d \ln D}{d \ln a}. \quad (3.22)$$

### 3.1.2 Fluid Equations in Fourier Space

We have discussed solutions of the fluid equations in the linear regime. Our goal is to solve full fluid equations. It is convenient to work in Fourier space instead of real space because we can consider the evolution of each Fourier mode. In Fourier space the continuity and Euler equations can be written as

$$\frac{\partial \delta}{\partial \tau}(\mathbf{k}, \tau) + \theta(\mathbf{k}, \tau) = - \int \frac{d^3 \mathbf{k}_1}{(2\pi)^3} \frac{d^3 \mathbf{k}_2}{(2\pi)^3} \delta_D(\mathbf{k}_1 + \mathbf{k}_2 - \mathbf{k}) \frac{(\mathbf{k}_1 + \mathbf{k}_2) \cdot \mathbf{k}_1}{k_1^2} \theta(\mathbf{k}_1, \tau) \delta(\mathbf{k}_2, \tau), \quad (3.23)$$

$$\begin{aligned} \frac{\partial \theta}{\partial \tau}(\mathbf{k}, \tau) + \mathcal{H} \theta(\mathbf{k}, \tau) + \frac{3}{2} \Omega_m \mathcal{H}^2 \delta(\mathbf{k}, \tau) = & - \int \frac{d^3 \mathbf{k}_1}{(2\pi)^3} \frac{d^3 \mathbf{k}_2}{(2\pi)^3} \delta_D(\mathbf{k}_1 + \mathbf{k}_2 - \mathbf{k}) \frac{(\mathbf{k}_1 + \mathbf{k}_2)^2 (\mathbf{k}_1 \cdot \mathbf{k}_2)}{2k_1^2 k_2^2} \\ & \times \theta(\mathbf{k}_1, \tau) \theta(\mathbf{k}_2, \tau). \end{aligned} \quad (3.24)$$



The quadratic terms have introduced mode coupling terms in the Fourier-space field equations. These mode coupling terms encode all information about non-linear dynamics. It is conventional to call them  $\alpha(\mathbf{k}_1, \mathbf{k}_2)$  and  $\beta(\mathbf{k}_1, \mathbf{k}_2)$ :

$$\alpha(\mathbf{k}_1, \mathbf{k}_2) \equiv \frac{\mathbf{k}_1 \cdot (\mathbf{k}_1 + \mathbf{k}_2)}{k_1^2}, \quad (3.25)$$

$$\beta(\mathbf{k}_1, \mathbf{k}_2) \equiv \frac{1}{2}(\mathbf{k}_1 + \mathbf{k}_2)^2 \frac{\mathbf{k}_1 \cdot \mathbf{k}_2}{k_1^2 k_2^2} = \frac{1}{2} \frac{\mathbf{k}_1 \cdot \mathbf{k}_2}{k_1 k_2} \left( \frac{k_2}{k_1} + \frac{k_1}{k_2} \right) + \frac{(\mathbf{k}_1 \cdot \mathbf{k}_2)^2}{k_1^2 k_2^2}. \quad (3.26)$$

### 3.1.3 Perturbative Solutions

Eq. (3.23) and Eq. (3.24) are coupled differential equation and so the general solution does not exist. However we can solve them using Perturbation Theory. In an EdS Universe the growing mode factor is  $D = a$  and so solve those equations perturbatively we use the following ansatz:

$$\delta(\mathbf{k}, \tau) = \sum_{n=1}^{\infty} a^n(\tau) \delta^{(n)}(\mathbf{k}) \quad \text{and} \quad \theta(\mathbf{k}, \tau) = -\mathcal{H}(\tau) \sum_{n=1}^{\infty} a^n(\tau) \theta^{(n)}(\mathbf{k}). \quad (3.27)$$

We can write the  $n$ th order solutions for  $\delta_n$  and  $\theta_n$  as convolutions of  $n$  linear density fields:

$$\delta^{(n)}(\mathbf{k}) = \prod_{i=1}^n \left\{ \int \frac{d^3 q_i}{(2\pi)^3} \delta^{(1)}(\mathbf{q}_i) \right\} (2\pi)^3 \delta_{\mathbf{D}}(\mathbf{k} - \mathbf{q}_{1\dots n}) F_n(\mathbf{q}_1, \dots, \mathbf{q}_n) \quad (3.28)$$

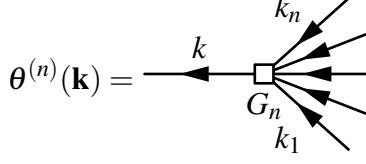
$$\theta^{(n)}(\mathbf{k}) = \prod_{i=1}^n \left\{ \int \frac{d^3 q_i}{(2\pi)^3} \delta^{(1)}(\mathbf{q}_i) \right\} (2\pi)^3 \delta_{\mathbf{D}}(\mathbf{k} - \mathbf{q}_{1\dots n}) G_n(\mathbf{q}_1, \dots, \mathbf{q}_n) \quad (3.29)$$

where  $\mathbf{q}_{1\dots n} \equiv \mathbf{q}_1 + \dots + \mathbf{q}_n$  while  $F_n$  and  $G_n$  are gravitational coupling kernels, defined explicitly using the following iterative expressions:

$$F_n(\mathbf{q}_1, \dots, \mathbf{q}_n) = \sum_{m=1}^{n-1} \frac{G_m(\mathbf{q}_1, \dots, \mathbf{q}_m)}{(2n+3)(n-1)} \left[ (2n+1)\alpha(\mathbf{q}_{1\dots i}, \mathbf{q}_{i+1\dots n}) F_{n-m}(\mathbf{q}_{m+1}, \dots, \mathbf{q}_n) + \right. \\ \left. 2\beta(\mathbf{q}_{1\dots i}, \mathbf{q}_{i+1\dots n}) G_{n-m}(\mathbf{q}_{m+1}, \dots, \mathbf{q}_n) \right], \quad (3.30)$$

$$G_n(\mathbf{q}_1, \dots, \mathbf{q}_n) = \sum_{m=1}^{n-1} \frac{G_m(\mathbf{q}_1, \dots, \mathbf{q}_m)}{(2n+3)(n-1)} \left[ 3\alpha(\mathbf{q}_{1\dots i}, \mathbf{q}_{i+1\dots n}) F_{n-m}(\mathbf{q}_{m+1}, \dots, \mathbf{q}_n) + \right. \\ \left. 2n\beta(\mathbf{q}_{1\dots i}, \mathbf{q}_{i+1\dots n}) G_{n-m}(\mathbf{q}_{m+1}, \dots, \mathbf{q}_n) \right]. \quad (3.31)$$





$$\theta^{(n)}(\mathbf{k}) = \text{---} k \text{---} \square_{G_n} \text{---} k_1, k_2, \dots, k_n \text{---} = (2\pi)^3 \delta^{(D)}(\mathbf{k}_1 + \dots + \mathbf{k}_n - \mathbf{k}) G_n(\mathbf{k}_1, \dots, \mathbf{k}_n). \quad (3.38)$$

The coupling kernels have interesting UV and IR properties. For example when the total momentum  $\mathbf{k} = \mathbf{k}_1 + \mathbf{k}_2 \dots$  goes to zero, but individual momenta  $\mathbf{k}_i$  do not go to zero then  $F_n^{(s)} \rightarrow k^2$ . Similarly, when one of the momenta becomes very large, the kernels obey the scaling law such as

$$\lim_{q \rightarrow \infty} F_n(\mathbf{k}_1, \dots, \mathbf{k}_{n-2}, \mathbf{q}, -\mathbf{q}) \propto \frac{k^2}{q^2} \quad (3.39)$$

and similarly for  $G_n^{(s)}$ .

We have discussed the solutions in the EdS universe. Since the difference between the results derived above for an EdS Universe and a  $\Lambda$ CDM Universe are small, one can easily generalise these results to any cosmological model by replacing  $a(\tau)$  by the general growth factor  $D(\tau)$  which depends on  $\Omega_m$  and  $\Omega_\Lambda$  (see [37, 183, 203] for more details). Therefore, for  $\Lambda$ CDM cosmology, the series solutions in eq. (3.27) can be generalised to

$$\delta(\mathbf{k}, \tau) = \sum_{n=1}^{\infty} D^n(\tau) \delta^{(n)}(\mathbf{k}) \quad \text{and} \quad \theta(\mathbf{k}, \tau) = -\mathcal{H}(\tau) f(\tau) \sum_{n=1}^{\infty} D^n(\tau) \theta^{(n)}(\mathbf{k}). \quad (3.40)$$

where  $f(\tau)$  is the logarithmic growth factor.

### 3.1.4 Feynman Rules

It is quite convenient to define Feynman rules to compute  $N$ -point correlation functions of density fields. The Feynman rules for computing the  $n$ -spectra are defined explicitly in [18]. For calculating the  $i^{\text{th}}$  order diagram for the  $n$ -spectrum we follow the following rules. First, draw all possible connected diagrams with  $n$  external legs and assign each vertex the factors defined in eq. (3.30) and eq. (3.31) depending if we are computing correlation functions of  $\delta$  or  $\theta$  respectively. We follow:

1. For each vertex with ingoing momenta  $\mathbf{k}_i$  and outgoing momenta  $\mathbf{k}$  we assign a delta function  $(2\pi)^3 \delta_D(\mathbf{k} - \sum_i \mathbf{k}_i)$  and a coupling kernel  $F_n(\mathbf{k}_1, \dots, \mathbf{k}_n)$  (or  $G_n$  or any another coupling - for instance, later in this thesis we will talk about quadratic and cubic galaxy bias couplings.)
2. For each vertex with outgoing momenta  $\mathbf{k}$  and  $\mathbf{k}'$  we assign a linear power spectrum  $(2\pi)^3 \delta_D(\mathbf{k} + \mathbf{k}') P_{\text{lin}}(k)$

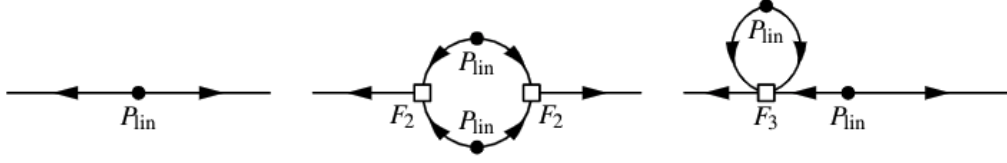


Fig. 3.1 The Feynman diagrams in this figure represent the linear power spectrum  $P_{\text{lin}}$  (left) and one-loop terms, that is  $P_{22}$  (middle) and  $P_{13}$  (right).

3. Integrate over each loop momenta  $\int d^3k_i/(2\pi)^3$
4. To take into account the different permutations multiply the factors by the symmetry factor  $n!$ , where  $n$  is the number of external legs.
5. Sum over all labels of the external lines.

Finally we add up all the contributions from all diagrams.

### 3.1.5 Power Spectrum

So far we know that the non-linear density or velocity field can be expressed as product of  $n$  linear density fields. If we want to compute the  $n$ -spectra we have to cross correlate these non-linear fields. The cross correlation of two non-linear density fields give rise to power spectrum in Fourier space. The leading-order term in power spectrum is the second-order term in the linear density field. The next-to-leading order terms are fourth order in the linear density field by Wick theorem. Since the linear density field is a Gaussian random field the odd correlators always vanish and so there is no term in the power spectrum which is third order in density fields. The next-to-leading order terms are also called *one-loop* terms and contain one inner momentum to integrate over. There are two distinct power spectrum diagrams at the *one-loop* level. One is obtained by cross-correlating the second-order density field by another second order density field. The other diagram is obtained by cross-correlating the linear density field with the third order density field. We write the power spectrum at *one-loop* as

$$\langle \delta(\mathbf{k})\delta(\mathbf{k}') \rangle = \langle \delta^{(1)}(\mathbf{k})\delta^{(1)}(\mathbf{k}') \rangle + 2\langle \delta^{(1)}(\mathbf{k})\delta^{(3)}(\mathbf{k}') \rangle + \langle \delta^{(2)}(\mathbf{k})\delta^{(2)}(\mathbf{k}') \rangle + \dots \quad (3.41)$$

This gives rise to

$$P(k) = P_{\text{lin}}(k) + 2P_{13}(k) + P_{22}(k) + \dots \quad (3.42)$$

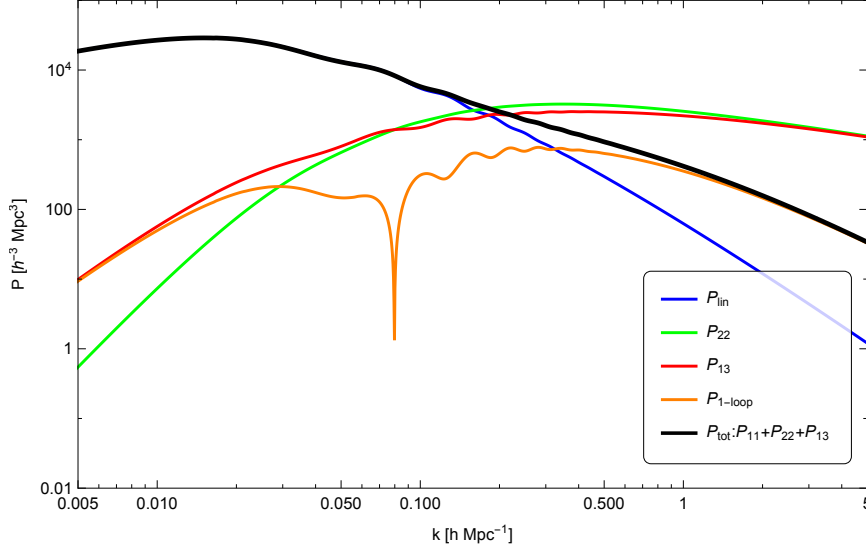


Fig. 3.2 Various contributions to the matter power spectrum up to one-loop in perturbation theory. The blue curve represents the linear power spectrum. Blue and red curves represent  $P_{22}$  and  $|P_{13}|$  respectively. The one-loop contribution to the matter power spectrum is plotted in Orange, and the total (linear + one-loop) is plotted in Black.

where

$$P_{22}(k) = 2 \int \frac{d^3q}{(2\pi)^3} P_{\text{lin}}(|\mathbf{k} - \mathbf{q}|) P_{\text{lin}}(q) \left[ F_2^{(s)}(\mathbf{q}, \mathbf{k} - \mathbf{q}) \right]^2, \quad (3.43)$$

$$P_{13}(k) = 3 \int \frac{d^3q}{(2\pi)^3} P_{\text{lin}}(k) P_{\text{lin}}(q) F_3^{(s)}(\mathbf{k}, -\mathbf{q}, \mathbf{q}). \quad (3.44)$$

The diagrammatic representations of linear and one-loop power spectrum terms are given in Fig. 3.1. In Fig. 3.2 we plot the linear power spectrum and the loop terms.

### IR and UV behaviour of *one-loop* terms

Previously we discussed the high- $k$  and low- $k$  limits of the mode coupling kernels. It will be interesting to see how the loop terms behave in the limit of very large and very low external momenta. In the low- $k$  limit (which corresponds to large scales),  $P_{13}$  behaves as

$$\lim_{k \ll q} P_{13}(k) = -\frac{1}{3} \int \frac{d^3q}{(2\pi)^3} \frac{P_{\text{lin}}(q)}{q^2} \left( \frac{16}{210} - \frac{2}{35} \frac{k^2}{q^2} + \dots \right) = -\frac{61}{210} k^2 P_{\text{lin}}(k) \sigma_{\text{d}}^2(k) \quad (3.45)$$

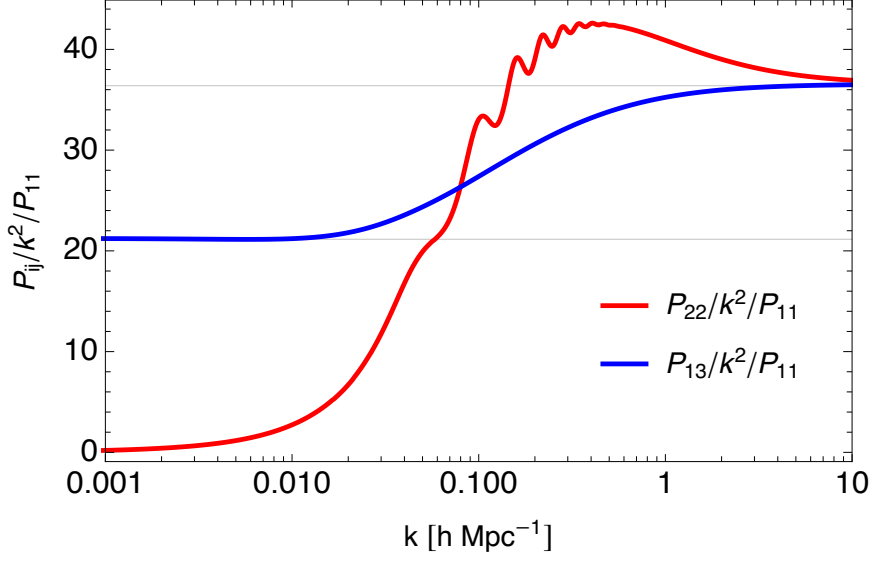


Fig. 3.3 The high- $k$  and low- $k$  limits of  $P_{13}$  and  $P_{22}$ .

where  $\sigma_d^2 = (1/3) \int d^3q / (2\pi)^3 P_{\text{lin}}(q) / q^2$ . The high- $k$  limit (or short scales) of  $P_{13}$  is given by

$$\lim_{k \gg q} P_{13}(k) = -\frac{1}{3} \int \frac{d^3q}{(2\pi)^3} \frac{P_{\text{lin}}(q)}{q^2} \left( 1 - \frac{116 q^2}{105 k^2} + \frac{188 q^4}{245 k^4} + \dots \right) = -\frac{1}{2} k^2 P_{\text{lin}}(k) \sigma_d^2(k). \quad (3.46)$$

Similarly we can look at the low- $k$  and high- $k$  limits of the  $P_{22}$  integral. In the low- $k$  limit, the  $P_{22}$  term behaves as

$$\lim_{k \ll q} P_{22}(k) \propto \frac{9}{98} k^4 \int \frac{d^3q}{(2\pi)^3} \frac{P_{\text{lin}}^2(q)}{q^4}. \quad (3.47)$$

Finally, in the high- $k$  limit the  $P_{22}$  term behaves as

$$\begin{aligned} \lim_{k \gg q} P_{22}(k) &\propto \left( \frac{569}{735} P_{\text{lin}}(k) - \frac{47}{105} k \frac{dP}{dk} + \frac{1}{10} k^2 \frac{d^2P}{dk^2} \right) \int \frac{d^3q}{(2\pi)^3} P_{\text{lin}}(q) + \frac{1}{3} k^2 P_{\text{lin}}(q) \int \frac{d^3q}{(2\pi)^3} \frac{P_{\text{lin}}(q)}{q^2} \\ &= \left( \frac{569}{735} P_{\text{lin}}(k) - \frac{47}{105} k \frac{dP}{dk} + \frac{1}{10} k^2 \frac{d^2P}{dk^2} \right) \sigma_d^2(k) + k^2 P_{\text{lin}}(k) \sigma_d^2(k) \end{aligned} \quad (3.48)$$

We see from eq. (3.46) and eq. (3.48) that in the high- $k$  limit the positive contribution from  $P_{22}$  is cancelled by the negative  $2P_{13}$  contribution. We plot  $P_{22}/k^2/P_{\text{lin}}$  and  $P_{13}/k^2/P_{\text{lin}}$  in Fig. 3.3 to understand high- $k$  and low- $k$  limits. In the high- $k$  limit both terms asymptotes to  $\sigma_d^2$ .

One of the problems is that based on the initial conditions, that is for a scaling universe when  $P_{\text{lin}} \propto k^n$ , the loop terms are either UV or IR divergent based on the value of  $n$  as given in Table 3.1. These loop divergences are one of the shortcomings of SPT and we will discuss in the next section how Effective Field Theory of LSS deals with such problems. We can see that when the internal momenta goes to zero, that is  $q \rightarrow 0$ , both terms  $P_{13}$  and  $P_{22}$  have IR divergences. The term  $P_{22}$  has another IR divergence when  $q \rightarrow k$ . We can get rid of these divergences either by having an IR cut-off or by computing the loop terms together using a single integral as discussed in [44]. The *one-loop* IR-safe integral is defined as

$$\begin{aligned}
P_{1\text{-loop IR-safe}}(k) &= \int \frac{d^3q}{(2\pi)^3} \left\{ P_{13}(q) + P_{22}(q)\Theta(|\mathbf{k}-\mathbf{q}|-q) + P_{22}(-q)\Theta(|\mathbf{k}+\mathbf{q}|-q) \right\} \\
&= \int \frac{d^3q}{(2\pi)^3} \left\{ 6P_{\text{lin}}(k)P_{\text{lin}}(q)F_3^{(s)}(\mathbf{k}, \mathbf{q}, -\mathbf{q}) \right. \\
&\quad + P_{\text{lin}}(q)P_{\text{lin}}(|\mathbf{k}-\mathbf{q}|)[F_2^{(2)}(\mathbf{q}, \mathbf{k}-\mathbf{q})]^2\Theta(|\mathbf{k}+\mathbf{q}|-q) \\
&\quad \left. + P_{\text{lin}}(q)P_{\text{lin}}(|\mathbf{k}+\mathbf{q}|)[F_2^{(2)}(-\mathbf{q}, \mathbf{k}+\mathbf{q})]^2\Theta(|\mathbf{k}+\mathbf{q}|-q) \right\}. \tag{3.49}
\end{aligned}$$

	UV-divergent	IR-divergent
$P_{22}$	$n \geq 1/2$	$n \leq -1$
$P_{13}$	$n \geq -1$	$n \leq -1$
$P_{1\text{-loop}}$	$n \geq -1$	$n \leq -3$

Table 3.1 Convergence properties of one-loop power spectrum terms based on different values of the initial conditions.

### Two-loop Power Spectrum

The next-to-next-to-leading order contributions are called *two-loop* terms. There are four distinct terms at this level. These terms contain two loop integrals. The full power spectrum up to sixth order in density fields is given by

$$\begin{aligned}
\langle \delta(\mathbf{k})\delta(\mathbf{k}') \rangle &= \langle \delta^{(1)}(\mathbf{k})\delta^{(1)}(\mathbf{k}') \rangle + 2\langle \delta^{(1)}(\mathbf{k})\delta^{(3)}(\mathbf{k}') \rangle + \langle \delta^{(2)}(\mathbf{k})\delta^{(2)}(\mathbf{k}') \rangle \\
&\quad + 2\langle \delta^{(1)}(\mathbf{k})\delta^{(5)}(\mathbf{k}') \rangle + \langle \delta^{(3)}(\mathbf{k})\delta^{(3)}(\mathbf{k}') \rangle + 2\langle \delta^{(2)}(\mathbf{k})\delta^{(4)}(\mathbf{k}') \rangle \tag{3.50}
\end{aligned}$$

which leads to

$$P(k) = P_{\text{lin}}(k) + P_{1\text{-loop}}(k) + P_{2\text{-loop}}(k) \tag{3.51}$$

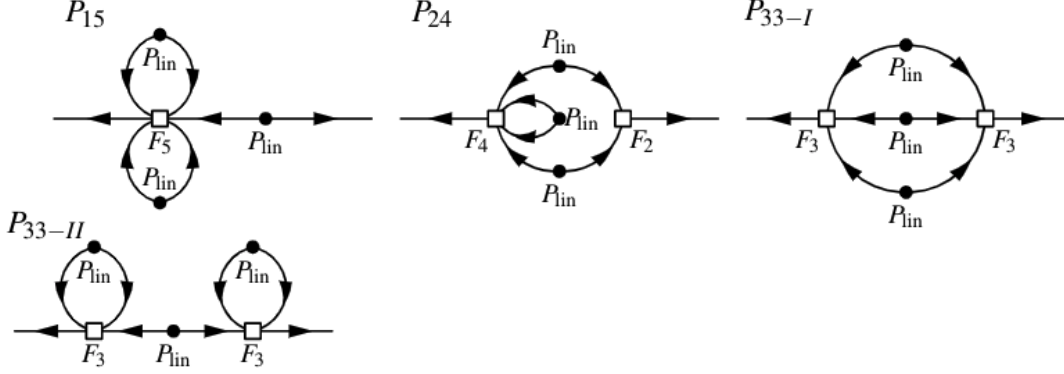


Fig. 3.4 The Feynman diagrams for various two-loop terms of the matter power spectrum.

where the *two-loop* power spectrum consists of four distinct terms:

$$P_{2\text{-loop}}(k) = P_{15}(k) + P_{24}(k) + P_{33}^I(k) + P_{33}^{II}(k). \quad (3.52)$$

These four *two-loop* terms are explicitly defined as

$$P_{24}(k) = 12 \int_{\mathbf{q}_1} \int_{\mathbf{q}_2} F_2^{(s)}(-\mathbf{q}_2, -\mathbf{k} + \mathbf{q}_2) F_4^{(s)}(\mathbf{q}_1, -\mathbf{q}_1, \mathbf{q}_2, \mathbf{k} - \mathbf{q}_2) P_{\text{lin}}(q_1) P_{\text{lin}}(q_2) P_{\text{lin}}(|\mathbf{k} - \mathbf{q}_2|), \quad (3.53)$$

$$P_{15}(k) = 15 \int_{\mathbf{q}_1} \int_{\mathbf{q}_2} P_{\text{lin}}(q_1) P_{\text{lin}}(q_2) F_5^{(s)}(\mathbf{k}, \mathbf{q}_1, -\mathbf{q}_1, \mathbf{q}_2, \mathbf{q}_2), \quad (3.54)$$

$$P_{33}^I(k) = 6 \int_{\mathbf{q}_1} \int_{\mathbf{q}_2} P_{\text{lin}}(q_1) P_{\text{lin}}(q_2) P_{\text{lin}}(|\mathbf{k} - \mathbf{q}_1 - \mathbf{q}_2|) \left[ F_3^{(s)}(\mathbf{q}_1, \mathbf{q}_2, \mathbf{k} - \mathbf{q}_1 - \mathbf{q}_2) \right]^2, \quad (3.55)$$

$$P_{33}^{II}(k) = P_{\text{lin}}(k) \left[ 3 \int_{\mathbf{q}_1} F_3^{(s)}(\mathbf{q}_1, -\mathbf{q}_1, \mathbf{k}) P_{\text{lin}}(q_1) \right]^2 = \frac{P_{13}^2(k)}{P_{\text{lin}}(k)}. \quad (3.56)$$

Diagrammatically these terms are described in Fig. 3.4. For more details about properties of *two-loop* terms we refer to [44, 17]

### 3.1.6 Bispectrum

The initial density field is a Gaussian random field and so the odd correlators vanish. However, the late-time gravitational instability induce non-Gaussianity in non-linear density field. This non-Gaussianity contribution can be studied by 3-point correlation function or bispectrum in Fourier space. The correlation of three non-linear density fields are defined as



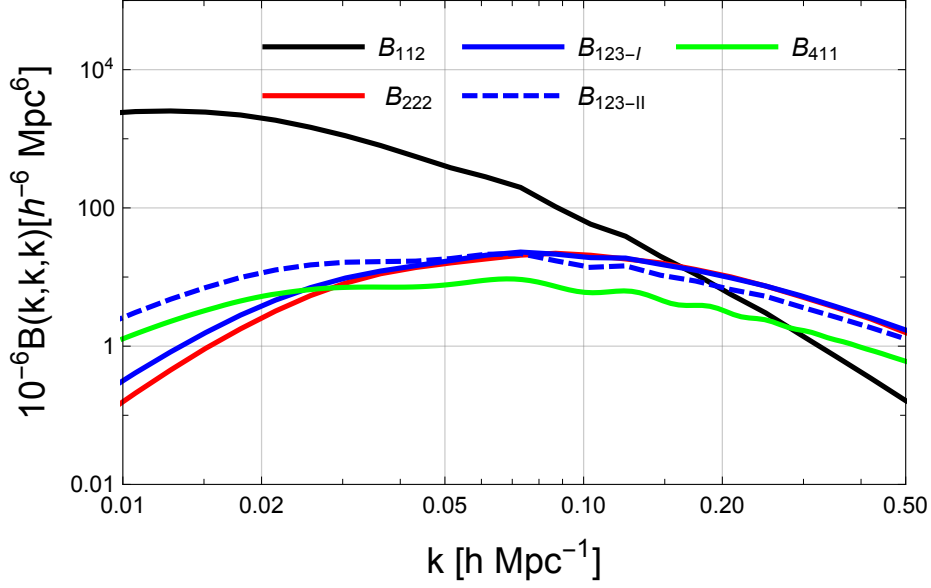


Fig. 3.5 The tree-level and the one-loop bispectrum terms are plotted for equilateral configurations ( $k_1 = k_2 = k_3$ ).

$$\begin{aligned} \langle \delta(\mathbf{k}_1) \delta(\mathbf{k}_2) \delta(\mathbf{k}_3) \rangle &= \langle \delta^{(1)}(\mathbf{k}_1) \delta^{(1)}(\mathbf{k}_2) \delta^{(2)}(\mathbf{k}_3) \rangle + 2 \text{ cyc} + \dots \\ &= (2\pi)^3 \delta_{\text{D}}(\mathbf{k}_1 + \mathbf{k}_2 + \mathbf{k}_3) B(\mathbf{k}_1, \mathbf{k}_2, \mathbf{k}_3) \end{aligned} \quad (3.57)$$

where the leading order bispectrum is defined as

$$B(\mathbf{k}_1, \mathbf{k}_2, \mathbf{k}_3) = 2F_2(\mathbf{k}_1, \mathbf{k}_2) P_{\text{lin}}(k_1) P_{\text{lin}}(k_2) + 2 \text{ cyc}. \quad (3.58)$$

The leading order bispectrum is fourth order in the initial density field and so we can represent it as  $B_{112}$ . The delta function in Eq. (3.57) imposes  $\mathbf{k}_1 + \mathbf{k}_2 + \mathbf{k}_3 = 0$  in order to have a non-vanishing correlator.

### One-loop Bispectrum

The next-to-leading order, or *one-loop*, bispectrum is sixth order in density field. There are four distinct bispectrum terms possible at the *one-loop* level (for more details see [26]). The SPT bispectrum at the one-loop level is defined as

$$B_{1\text{-loop}}(k_1, k_2, k_3) = B_{222} + B_{321}^I + B_{321}^{II} + B_{411} \quad (3.59)$$

where these four terms can be defined explicitly as

$$B_{222} = 8 \int_{\mathbf{q}} F_2(-\mathbf{q}, \mathbf{q}, \mathbf{k}_1) F_2(\mathbf{q} + \mathbf{k}_1, -\mathbf{q} + \mathbf{k}_2) F_2(\mathbf{k}_2, -\mathbf{q}, \mathbf{q}) P_{\text{lin}}(q) P_{\text{lin}}(|\mathbf{q} + \mathbf{k}_1|) P_{\text{lin}}(|\mathbf{q} - \mathbf{k}_2|), \quad (3.60)$$

$$B_{321}^I = 6 P_{\text{lin}}(k_3) \int_{\mathbf{q}} F_3(-\mathbf{q}, \mathbf{q} - \mathbf{k}_2, -\mathbf{k}_3) F_2(\mathbf{q}, \mathbf{k}_2 - \mathbf{q}) P_{\text{lin}}(q) P_{\text{lin}}(|\mathbf{q} - \mathbf{k}_2|), \quad (3.61)$$

$$B_{321}^{II} = 6 F_2(\mathbf{k}_2, \mathbf{k}_3) P_{\text{lin}}(k_2) P_{\text{lin}}(k_3) \int_{\mathbf{q}} F_3(\mathbf{k}_3, \mathbf{q}, -\mathbf{q}) P_{\text{lin}}(q) + 5 \text{ perm}, \quad (3.62)$$

$$B_{411} = 12 P_{\text{lin}}(k_2) P_{\text{lin}}(k_3) \int_{\mathbf{q}} F_4(\mathbf{q}, -\mathbf{q}, -\mathbf{k}_2, -\mathbf{k}_3) P_{\text{lin}}(q) + 2 \text{ cyc. perm.} \quad (3.63)$$

For equilateral configurations, we plot the tree-level and one-loop bispectrum terms in Fig. 3.5.

### 3.1.7 Shortcomings of Standard Perturbation Theory

Although SPT provides a basis for the solutions of fluid equations to explain matter inhomogeneities, it has several shortcomings:

- The density contrast is not small on all scales and so we do not have a clear expansion parameter.
- We assume perfect pressureless fluid, however any deviation from a perfect pressureless fluid is not explained by the SPT framework.
- For generic initial conditions the loop corrections can be UV divergent and require a UV cut-off that means the SPT predictions are all UV cut-off dependent, which is clearly unphysical.

In sec. 3.2 we introduce the Effective Field Theory of Large Scale Structure (EFTofLSS). The EFTofLSS provides answers to these shortcomings and provides physical, cut-off independent predictions.

## 3.2 Effective Field Theory of Large-Scale Structure

Note: *The EFTofLSS review is closely adapted from [12]; for more detailed discussion we refer the reader to that review.*

Let us review what we have understood so far. The late-time structure formation in the Universe is highly non-linear. One of the main non-linearities is non-linear matter clustering due to gravity. We can model it by a perfect pressure-less fluid, the equations

of motion of which could be obtained by solving the Boltzmann, Euler and continuity equations. The equations of motion are highly complex but can be solved numerically. To make analytical predictions, however, we can solve them perturbatively using the standard perturbation theory (SPT). On large scales, which correspond to low wavenumbers  $k$ , where non-linearities are not present the SPT describes the statistics of LSS very well. However, the predictions of SPT start to deviate beyond the linear order where non-linearities become important. Moreover the loop corrections are UV divergent and require a UV cut-off  $\Lambda$ . Let's understand it a bit more specifically and consider the variance of modes below a cut-off  $k < \Lambda$ :

$$\sigma_{\Lambda}^2 = \frac{1}{2\pi^2} \int_0^{\Lambda} d\ln q q^3 P_{\text{lin}}(q) \approx \frac{\Lambda^3 P_{\text{lin}}(\Lambda)}{2\pi^2} \quad (3.64)$$

This variance is a growing function of  $\Lambda$ . Later we in this section we use the non-linear wavenumber  $k_{\text{NL}}$  which is defined as the scale around which the perturbation theory breaks down.

Fortunately, the framework of the Effective Field Theory of Large Scale Structures (EFTofLSS) provides a powerful framework to expand the scope of SPT [15, 28, 35, 44, 46, 157]. The underlying idea of the EFTofLSS is that it integrates out the short scale modes and takes into account their effects on the large scale dynamics. The physical effects of short scale modes are to introduce non-linearities in the perfect cosmological fluid description by adding terms corresponding to *speed-of-sound*, *dissipative corrections*, and *the stochastic noise*. These terms respect the symmetries of the equations of motion and have the same form to cancel the UV divergences that emerge from the PT loop integrals.

The EFTofLSS not only provides a powerful theoretical framework which can be used to make good predictions, it also provides a systematic way to model theoretical uncertainties. Usually, theoretical uncertainties are neglected when analyzing data, even though they could have a significant impact on constraining the cosmological parameters. Imagine, if the signal of some new physics is within the theoretical uncertainties of the model then no matter how state of the art the experiments are, we will never be able to detect that signal. The significance of theoretical uncertainties in forecasting is discussed in detail in [25].

It has been shown that the EFTofLSS prediction for the two-loop dark matter power spectrum agrees with 1% precision with the N-body simulations up to  $k_{\text{max}} \approx 0.3h \text{ Mpc}^{-1}$  [15, 44] and the one-loop bispectrum up to  $k_{\text{max}} \approx 0.22h \text{ Mpc}^{-1}$  at redshift  $z = 0$  [28]. In contrast to SPT prediction where the power spectrum starts to deviate from the simulation data at  $k \sim 0.1h \text{ Mpc}^{-1}$ , the EFTofLSS has shown that it can increase the number of modes 27 times compared to the SPT:

$$N_{\text{LSS}}^{\text{SPT}} \sim \left( \frac{0.1h \text{ Mpc}^{-1}}{k_{\text{min}}} \right)^3, \quad N_{\text{LSS}}^{\text{EFT}} \sim \left( \frac{0.3h \text{ Mpc}^{-1}}{k_{\text{min}}} \right)^3 \Rightarrow \frac{N_{\text{LSS}}^{\text{EFT}}}{N_{\text{LSS}}^{\text{SPT}}} \sim 27 \quad (3.65)$$

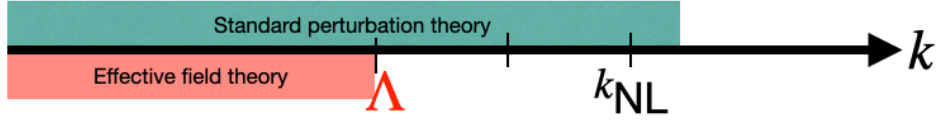


Fig. 3.6 This illustration describes the hierarchy of scales in perturbation theory and effective field theory. The EFT description is valid for  $\Lambda < k_{\text{NL}}$ . The figure is adapted from [35].

where  $N_{\text{LSS}}^{\text{SPT}}$  and  $N_{\text{LSS}}^{\text{EFT}}$  are the number of modes in LSS predicted by SPT and EFTofLSS respectively. The signal-to-noise ratio in LSS depends on the volume of the survey and  $\sqrt{N_{\text{LSS}}}$ . Since the signal-to-noise ratio depends on  $k_{\text{max}}$ , achieving even a slight improvement in the  $k_{\text{max}}$  can make a huge difference. In Fig. 3.6 we define the hierarchy of scales involved in SPT and EFTofLSS. In the rest of this section we discuss the basics of EFTofLSS following [12, 44].

### 3.2.1 Coarse-grained Equations of Motion

The equations of motion of an effective fluid can be obtained by smoothing the Vlasov equations and by taking its corresponding moments. This process can remove modes above a cut-off, that is scales  $k > \Lambda$  which correspond to small wavelengths  $\lambda < 1/\Lambda$ . The cut-off is taken as  $\Lambda < k_{\text{NL}}$ . The smoothing function is not important but we use the Gaussian smoothing defined in real and Fourier space as

$$W_{\Lambda}(\mathbf{x}) = \left(\frac{\Lambda}{\sqrt{2\pi}}\right)^3 \exp\left(-\frac{1}{2}\Lambda^2 x^2\right) \quad \text{and} \quad W_{\Lambda}(\mathbf{k}) = \exp\left(-\frac{1}{2}\frac{k^2}{\Lambda^2}\right). \quad (3.66)$$

respectively. In particular, if  $\mathcal{O}(\mathbf{x}, t)$  is a cosmological field that depends on both long and short modes, we can regularise it by applying the smoothing function so that at the end it only depends on the long-wavelength modes. The smoothing can be done in real space as

$$\mathcal{O}_l = [\mathcal{O}]_{\Lambda}(\mathbf{x}) = \int d^3x' W_{\Lambda}(\mathbf{x} - \mathbf{x}', \Lambda) \mathcal{O}(\mathbf{x}). \quad (3.67)$$

We can define the short wavelentgh part as  $\mathcal{O}_s = \mathcal{O} - \mathcal{O}_l$ . The effective fluid equations can be derived by taking the moments of the smoothed Vlasov equation:

$$\int d^3\mathbf{p} p^i p^j \dots p^{i_n} \left[\frac{Df}{D\tau}\right]_{\Lambda}(\mathbf{x}, \mathbf{p}) = 0 \quad (3.68)$$

where the smoothed Boltzmann equation is written as

$$\left[ \frac{Df}{D\tau} \right]_{\Lambda}(\mathbf{x}, \mathbf{p}) = \frac{\partial f_l}{\partial \tau} + \frac{\mathbf{p}}{ma^2} \cdot \nabla f_l - m \sum_{\bar{n} \neq n} \int d^3 \mathbf{x}' W_{\Lambda}(\mathbf{x} - \mathbf{x}') \nabla \phi_n \cdot \frac{\partial f_n}{\partial \mathbf{p}}. \quad (3.69)$$

Following our definition here we define  $f_l$  as the smoothed distribution function. Similarly, we define the coarse-grained density and momentum as

$$\rho_l = \int d^3 p f_l(\mathbf{x}, \mathbf{p}, \tau) \quad (3.70)$$

$$\pi_l = \rho_l \mathbf{v}_l = \frac{m^3}{a^3} \int d^3 p \frac{\mathbf{p}}{ma} f_l(\mathbf{x}, \mathbf{p}, \tau). \quad (3.71)$$

Finally, the continuity and Euler equations that we obtain are

$$\delta'_l + \partial_j [(1 + \delta_l) v_{l,j}] = 0, \quad (3.72)$$

$$v'_{l,i} + \mathcal{H} v_{l,i} + \partial_i \phi_l + v_{l,j} \partial_j v_{l,i} = -\frac{1}{\rho} \partial_j [\tau_{ij}]_{\Lambda}. \quad (3.73)$$

where  $\tau_{ij}$  is the effective stress tensor induced by the short wavelength fluctuations. This non-vanishing stress tensor arises due to the fact that coarse-grained products of fluctuations produce products of long wavelength modes plus correction which depends on the products of short wavelength modes. The stress tensor arises from the microscopic stress tensor  $\sigma_{ij}$  and the products of short modes:

$$\tau_{ij} = \rho \sigma_{ij} + \rho v_i^s v_j^s - \frac{\phi_{,k}^s \phi_{,k}^s \delta_{ij} - 2\phi_{,i}^s \phi_{,j}^s}{8\pi G}. \quad (3.74)$$

### 3.2.2 Integrating out UV Physics

The stress tensor that arises from the coarse-graining depends on the short wavelength fluctuations. The short modes are strongly coupled and cannot be explained with the effective theory. Correlation functions of long wavelength fluctuations are expectation values. Since we do not observe the short modes we can take their expectation values. These expectation values will depend on the long wavelength modes. In quantum field theory this operation is referred to as *integrating out the UV degrees of freedom*. This effective theory will depend only on long wavelength modes. Since the long wavelength fluctuations are small we can Taylor expand the expectation values as background response:

$$\langle [\tau^{ij}]_{\Lambda} \rangle_{\delta_l} = \langle [\tau^{ij}]_{\Lambda} \rangle_0 + \left. \frac{\partial \langle [\tau^{ij}]_{\Lambda} \rangle}{\partial \delta_l} \right|_{\delta_l=0} \delta_l + \dots \quad (3.75)$$

Using the symmetries of the equations of motion, the effective stress tensor takes the following form:

$$\langle [\tau^{ij}]_{\Lambda} \rangle_{\delta_l} = p\delta^{ij} + \bar{\rho}c_s^2\delta_l\delta^{ij} - \bar{\rho}\frac{c_{b,v}^2}{\mathcal{H}}\delta^{ij}\partial_k v_l^k - \frac{3}{4}\bar{\rho}\frac{c_{s,v}^2}{\mathcal{H}}\left[\partial^j v_l^i + \partial^i v_l^j - \frac{2}{3}\delta^{ij}\partial_k v_l^k\right] + \Delta\tau^{ij} \quad (3.76)$$

where  $p$  is the background pressure,  $c_s^2$  is the speed of sound of the fluctuations,  $c_{b,v}^2$  is the coefficient of the bulk-viscosity,  $c_{s,v}^2$  is the coefficient of the shear-viscosity, and finally  $\Delta\tau^{ij}$  is the stochastic term which can be determined by taking the difference between the actual value of  $\tau^{ij}$  and its expectation value. By taking two spatial derivatives of the stress tensor we get the source term of the Euler equation for the velocity divergence defined as

$$\begin{aligned} \tau_{\theta} = \partial_i\partial_j\tau_{ij} &= \bar{\rho}\left[c_s^2\partial^2\delta_l - \frac{c_{v,b}^2}{\mathcal{H}}\partial^2\theta - \frac{3}{4}\frac{c_{v,s}^2}{\mathcal{H}}\partial^2\theta\right] + \Delta J \\ &= \bar{\rho}\left[c_s^2\partial^2\delta_l - \frac{c_v^2}{\mathcal{H}}\partial^2\theta\right] + \Delta J \end{aligned} \quad (3.77)$$

where  $\Delta J = \partial_i\partial_j\tau_{ij}$  and  $c_v^2 = c_{v,b}^2 + (2/3)c_{v,s}^2$ . The EFT parameters are either measured in  $N$ -body simulations or fit directly to the data.

### 3.2.3 EFT and Perturbation Theory

The perturbation theory (PT) within the framework of EFT is quite similar to the SPT in a sense that the set of equations that we have to solve perturbatively are the same except now we have to add new terms in the Euler equation. To solve the new equations using the new source terms we need to solve using the Green function method for the coupled system given by

$$\mathcal{H}^2\left\{-a^2\partial_a^2 + \frac{3}{2}(\Omega_m(a) - 2)a\partial_a + \frac{3}{2}\Omega_m(a)\right\}\delta = S_{\beta} - \mathcal{H}\partial_a(aS_{\alpha}) \quad (3.78)$$

$$\mathcal{H}\left\{a^2\partial_a^2 + \left(4 - \frac{3}{2}\Omega_m(a)\right)a\partial_a + (2 - 3\Omega_m(a))\right\}\delta = \partial_a(aS_{\beta}) - \frac{3}{2}\mathcal{H}\Omega_m(a)S_{\alpha} \quad (3.79)$$

where

$$S_{\alpha}(\mathbf{k}, \tau) = -\int \frac{d^3q}{(2\pi)^3}\alpha(\mathbf{q}, \mathbf{k} - \mathbf{q})\theta(\mathbf{q}, \tau)\delta(\mathbf{k} - \mathbf{q}, \tau), \quad (3.80)$$

$$S_{\beta}(\mathbf{k}, \tau) = -\int \frac{d^3q}{(2\pi)^3}\beta(\mathbf{q}, \mathbf{k} - \mathbf{q})\theta(\mathbf{q}, \tau)\theta(\mathbf{k} - \mathbf{q}, \tau) + \tau_{\theta}(\mathbf{k}, \tau). \quad (3.81)$$

The solution for  $\delta$  can be obtained using the Green's function as

$$c_s^2 k^2 \delta^{(1)}(\mathbf{k}) = \int da G_\delta(a, a') k^2 \left[ c_s^2(a') + c_v^2(a') \right] \delta^{(1)}(\mathbf{k}, a') \quad (3.82)$$

Finally we can write the density field in the EFTofLSS as

$$\delta(\mathbf{k}, \tau) = \delta^{(1)}(\mathbf{k}, \tau) + \delta^{(2)}(\mathbf{k}, \tau) + \delta^{(3)}(\mathbf{k}, \tau) - k^2 c_s^2(\tau) \delta^{(1)}(\mathbf{k}, \tau) + \delta_J(\mathbf{k}, \tau). \quad (3.83)$$

On the right hand side of this equation, the first three terms corresponds to the first-order, second-order and third-order matter density fields respectively; the fourth term is the linear-order counterterm and  $\delta_J$  is the stochastic term. We can now compute the power spectrum up to *one-loop* in the EFTofLSS as

$$P(k) = P_{\text{lin}}(k) + 2P_{13,\Lambda}(k) + P_{22,\Lambda}(k) - 2c_{s,\Lambda}^2 k^2 P_{\text{lin}}(k) + P_{JJ,\Lambda}(k) \quad (3.84)$$

where  $P_{13,\Lambda}$  and  $P_{22,\Lambda}$  depend on the UV cut-off  $\Lambda$ . The last two terms in eq. (3.84) are the counterterms as the UV divergent terms in  $P_{13}$  and  $P_{22}$  are exactly cancelled out by *speed of the sound* and *stochastic* counterterms. In short these terms regularize the theory. To see this explicitly, let us us split the integral in  $P_{13}$  at the cut-off  $\Lambda$

$$\begin{aligned} P_{13,\infty}(k) &= 3P_{\text{lin}}(k) \int_0^\Lambda \frac{d^3 q}{(2\pi)^3} F_3(\mathbf{k}, \mathbf{q}, -\mathbf{q}) P_{\text{lin}}(q) + 3P_{\text{lin}}(k) \int_\Lambda^\infty \frac{d^3 q}{(2\pi)^3} F_3(\mathbf{k}, \mathbf{q}, -\mathbf{q}) P_{\text{lin}}(q) \\ &= P_{13,\Lambda}(k) - k^2 P_{\text{lin}}(k) \frac{61}{210} \frac{1}{6\pi^2} \int_\Lambda^\infty dq P_{\text{lin}}(q). \end{aligned} \quad (3.85)$$

The counterterm in eq. (3.84) has the exact form to cancel out the UV divergence of the loop integrals. If we substitute eq. (3.85) in eq. (3.84) we can define a new speed of the sound parameter as

$$c_{s,\infty}^2 = c_{s,\Lambda}^2 - \frac{61}{210} \frac{1}{6\pi^2} \int_\Lambda^\infty dq P_{\text{lin}}(q). \quad (3.86)$$

This defines the cut-off independent result as:

$$P_{13,\Lambda}(k) - c_{s,\Lambda}^2 k^2 P_{\text{lin}}(k) = P_{13,\infty}(k) - c_{s,\infty}^2 k^2 P_{\text{lin}}(k). \quad (3.87)$$

Similarly the UV cut-off dependence in  $P_{22}$  is exactly cancelled by the stochastic counterterm (for details see [12, 44]) and therefore we can write

$$P_{22,\Lambda}(k) + P_{JJ,\Lambda}(k) = P_{22,\infty}(k) + P_{JJ,\infty}(k). \quad (3.88)$$

Using eq. (3.87) and eq. (3.88) in eq.(3.84) we can finally get the UV independent power spectrum up to one-loop in the EFTofLSS:

$$P(k) = P_{\text{lin}}(k) + 2P_{13}(k) + P_{22}(k) - 2c_{s,\infty}^2 k^2 P_{\text{lin}}(k) + P_{JJ,\infty}(k) \quad (3.89)$$

where we define  $P_{13,\infty}$  and  $P_{22,\infty}$  as  $P_{13}$  and  $P_{22}$  respectively. This completely solves one of the problems faced by SPT. Given any initial conditions the divergences of the loop integrals will be fully captured by the last two terms in eq. (3.89) and the final result will always remain finite.

### 3.3 Lagrangian Perturbation Theory (LPT)

In this section we introduced another variant of the perturbation theory called the Lagrangian Perturbation Theory (LPT). LPT is particularly useful to generate initial conditions in  $N$ -body simulations. In this thesis, in our simulation work we use the initial conditions generated by the second-order Lagrangian Perturbation Theory (2LPT). Therefore, it is useful to discuss LPT briefly here. The derivations in this section are closely adapted from [12, 37, 109, 111].

In LPT, the main focus is on the displacement field  $\psi(\mathbf{q}, \tau)$ . The particles start from the initial unperturbed Lagrangian position  $\mathbf{q}$  and follow their trajectories to the final Eulerian position  $\mathbf{x}$ . We can define the mapping between the Eulerian and Lagrangian coordinates as

$$\mathbf{x}(\tau) = \mathbf{q} + \psi(\mathbf{q}, \tau). \quad (3.90)$$

The conservation of mass allows us to write

$$1 + \delta(\mathbf{x}, \tau) = \left| \frac{\partial \mathbf{q}}{\partial \mathbf{x}} \right| \equiv \frac{1}{J(\mathbf{q}, \tau)} \quad (3.91)$$

where  $J(\mathbf{q}, \tau) = \det(\delta_{ij} + \psi_{i,j}(\mathbf{q}, \tau))$  is the Jacobian of the transformation from Eulerian to Lagrangian coordinates. Note that  $\psi_{i,j}$  represents the derivative with respect to Lagrangian coordinate  $q_j$ . From eq. (3.6) we know that the equations of motion for particles in an expanding universe is given by

$$\frac{d^2 \mathbf{x}}{d\tau^2} + \mathcal{H}(\tau) \frac{d\mathbf{x}}{d\tau} = -\nabla \Phi. \quad (3.92)$$

Taking the divergence of eq. (3.92) and the Poisson equation we get

$$J\nabla \cdot \left[ \frac{d^2 \mathbf{x}}{d\tau^2} + \mathcal{H} \frac{d\mathbf{x}}{d\tau} \right] = \frac{3}{2} \mathcal{H}^2 \Omega_m (J - 1). \quad (3.93)$$



Substituting eq. (3.90) in eq. (3.93) we arrive at

$$(\delta_{ij} + \psi_{i,j})^{-1} \left[ \frac{d^2 \psi_{i,j}}{d\tau} + \mathcal{H} \frac{d\psi_{i,j}}{d\tau} \right] = \frac{3}{2} \mathcal{H}^2 \Omega_m \frac{(J-1)}{J} \quad (3.94)$$

$(\delta_{ij} + \psi_{i,j})^{-1}$  is the transformation matrix from  $\nabla_{\mathbf{x}} \rightarrow \nabla_{\mathbf{q}}$ . For EdS Universe, the above equation can be solved perturbatively using the ansatz

$$\boldsymbol{\psi} = \sum_{n=1}^{\infty} D_1^n(\tau) \boldsymbol{\psi}^{(n)}(\mathbf{q}) = \sum_{n=1}^{\infty} a^n(\tau) \boldsymbol{\psi}^{(n)}(\mathbf{q}), \quad (3.95)$$

where the scale factor  $a \propto \tau^2$  and so we can write eq. (3.92) as

$$J(\delta_{ij} + \psi_{i,j})^{-1} \left( n^2 + \frac{n}{2} \right) \mathcal{H}^2 \psi_{i,j}^{(n)} = \frac{3}{2} \mathcal{H}^2 (J-1). \quad (3.96)$$

Similar to the displacement field, we expand the Jacobian as

$$J = 1 + J^{(1)} + J^{(2)} + J^{(3)} + \dots \quad (3.97)$$

where the perturbations are defined in terms of the displacement field as:

$$J^{(1)} = \mathcal{L}^{(1)} = \sum_i \psi_{i,i}^{(1)}, \quad (3.98)$$

$$J^{(2)} = \mathcal{L}^{(2)} + \mathcal{K}^{(2)} = \sum_i \psi_{i,i}^{(2)} + \frac{1}{2} \sum_{i \neq j} \left[ \psi_{i,i}^{(1)} \psi_{j,j}^{(1)} - \psi_{i,j}^{(1)} \psi_{j,i}^{(1)} \right], \quad (3.99)$$

$$J^{(3)} = \mathcal{L}^{(3)} + \mathcal{K}^{(3)} + \mathcal{M}^{(3)} = \sum_i \psi_{i,i}^{(3)} + \sum_{i \neq j} \left[ \psi_{i,i}^{(2)} \psi_{j,j}^{(1)} - \psi_{i,j}^{(2)} \psi_{j,i}^{(1)} \right] + \det \psi_{i,j}^{(1)}, \quad (3.100)$$

where  $\mathcal{L}$ ,  $\mathcal{K}$ , and  $\mathcal{M}$  are scalar invariants of the deformation tensors.

### 3.3.1 Zeldovich Approximation (ZA)

The linear order approximation in LPT is commonly called the Zeldovich approximation (ZA) [208]. At the linear order in perturbation, the transformation matrix becomes

$$(\delta_{ij} + \psi_{i,j})^{-1} = \delta_{ij} - a \psi_{i,j}. \quad (3.101)$$

Using eq. (3.101) and eq. (3.98) and the continuity equation we can obtain the first order solution as

$$\delta^{(1)}(\mathbf{q}, \tau) = -\nabla_{\mathbf{q}} \cdot \boldsymbol{\psi}^{(1)}(\mathbf{q}, \tau) \implies \boldsymbol{\psi}^{(1)}(\mathbf{k}, \tau) = i \frac{\mathbf{k}}{k^2} \delta^{(1)}(\mathbf{k}) a(\tau). \quad (3.102)$$

### 3.3.2 Second Order Lagrangian Perturbation Theory

To obtain a second order solution we need to expand the Jacobian up to second order

$$J = 1 + a\psi_{i,i}^{(1)} + a^2\psi_{i,i}^{(2)} + \frac{a^2}{2} \left( \psi_{i,i}^{(1)}\psi_{j,j}^{(1)} - \psi_{i,j}^{(1)}\psi_{j,i}^{(1)} \right) \quad (3.103)$$

and the transformation matrix to only first order. We can now simplify eq. (3.96) as

$$\begin{aligned} & \left[ \frac{d^2(a^2\psi_{i,i}^{(2)})}{d\tau^2} + \mathcal{H} \frac{d(a^2\psi_{i,i}^{(2)})}{d\tau} \right] - a\psi_{i,j}^{(1)} \left[ \frac{d^2(a^2\psi_{i,j}^{(1)})}{d\tau^2} + \mathcal{H} \frac{d(a^2\psi_{i,j}^{(1)})}{d\tau} \right] \\ &= \frac{3}{2} \mathcal{H}^2 a^2 \left[ \psi_{i,i}^{(2)} - \psi_{i,i}^{(1)}\psi_{j,j}^{(1)} + \frac{1}{2} \left( \psi_{i,i}^{(1)}\psi_{j,j}^{(1)} - \psi_{i,j}^{(1)}\psi_{j,i}^{(1)} \right) \right] \end{aligned} \quad (3.104)$$

We separate the first and second order  $\psi$  terms to obtain

$$\frac{d^2(a^2\psi_{i,i}^{(2)})}{d\tau^2} + \mathcal{H} \frac{d(a^2\psi_{i,i}^{(2)})}{d\tau} - \frac{3}{2} \mathcal{H}^2 a^2 \psi_{i,i}^{(2)} = -\frac{3}{4} \mathcal{H}^2 a^2 \left( \psi_{i,i}^{(1)}\psi_{j,j}^{(1)} - \psi_{i,j}^{(1)}\psi_{j,i}^{(1)} \right). \quad (3.105)$$

This lead us to

$$\psi_{i,i}^{(2)} = -\frac{3}{7} \sum_{i>j} \left( \psi_{i,i}^{(1)}\psi_{j,j}^{(1)} - \psi_{i,j}^{(1)}\psi_{j,i}^{(1)} \right). \quad (3.106)$$

This can also be written as  $\mathcal{H}^{(2)} = -3/7\mathcal{L}^{(2)}$ . The Fourier transform of  $\psi_{i,j}^{(1)}(\mathbf{q})$  as

$$\psi_{i,j}^{(1)}(\mathbf{k}) = ik_j\psi_i^{(1)}(\mathbf{k}) = -\frac{k_i k_j}{k^2} \delta^{(1)}(\mathbf{k}), \quad (3.107)$$

and the density field  $\delta(\mathbf{k})$  is defined as

$$\delta(\mathbf{k}) = \int d^3x e^{i\mathbf{k}\cdot\mathbf{x}} \delta(\mathbf{x}) = \int d^3x e^{i\mathbf{k}\cdot\mathbf{x}} (1 + \delta(\mathbf{x})) - \int d^3q e^{i\mathbf{k}\cdot\mathbf{q}} = \int d^3q e^{i\mathbf{k}\cdot\mathbf{q}} (e^{i\mathbf{k}\cdot\psi(\mathbf{q})} - 1) \quad (3.108)$$

Using eq. (3.107) and eq. (3.108), we can Fourier transform eq. (3.106) to find the following:

$$\begin{aligned} i\mathbf{k} \cdot \psi^{(2)}(\mathbf{k}) &= -\frac{3}{14} \int d^3q \left[ (\delta^{(1)})^2(\mathbf{q}) - (\psi_{i,j}^{(1)})^2(\mathbf{q}) \right] e^{i\mathbf{k}\cdot\mathbf{q}} \\ &= -\frac{3}{14} \int \frac{d^3k_1}{(2\pi)^3} \frac{d^3k_2}{(2\pi)^3} \left[ \delta^{(1)}(\mathbf{k}_1)\delta^{(1)}(\mathbf{k}_2) - \psi_{i,j}^{(1)}(\mathbf{k}_1)\psi_{i,j}^{(1)}(\mathbf{k}_2) \right] \delta_D(\mathbf{k} - \mathbf{k}_1 - \mathbf{k}_2) \\ &= -\frac{3}{14} \int \frac{d^3k_1}{(2\pi)^3} \frac{d^3k_2}{(2\pi)^3} \left[ \delta^{(1)}(\mathbf{k}_1)\delta^{(1)}(\mathbf{k}_2) - \frac{(\mathbf{k}_1 \cdot \mathbf{k}_2)^2}{k_1^2 k_2^2} \delta^{(1)}(\mathbf{k}_1)\delta^{(1)}(\mathbf{k}_2) \right] \delta_D(\mathbf{k} - \mathbf{k}_1 - \mathbf{k}_2) \\ &= -\frac{3}{14} \int \frac{d^3k_1}{(2\pi)^3} \frac{d^3k_2}{(2\pi)^3} \delta^{(1)}(\mathbf{k}_1)\delta^{(1)}(\mathbf{k}_2) \left[ 1 - \frac{(\mathbf{k}_1 \cdot \mathbf{k}_2)^2}{k_1 k_2} \right] \delta_D(\mathbf{k} - \mathbf{k}_1 - \mathbf{k}_2). \end{aligned} \quad (3.109)$$

### 3.3.3 Generalised $n$ th Order Solution

In Fourier space we can write the  $n$ th order solution for the displacement field as convolution of  $n$  linear density field and kernels  $L_n$  which account for the coupling:

$$\psi^{(n)}(\mathbf{k}) = \frac{i}{n!} \prod_{i=1}^n \left\{ \int \frac{d^3 k_i}{(2\pi)^3} \delta^{(1)}(\mathbf{k}_i) \right\} L_n(\mathbf{k}_1, \dots, \mathbf{k}_n) (2\pi)^3 \delta_D(\mathbf{k} - \mathbf{k}_1 \dots \mathbf{k}_n). \quad (3.110)$$

The first order kernel is  $L_1(\mathbf{k}) = 1$  and the second coupling kernel is

$$L_2 = \frac{3}{7} \frac{\mathbf{k}}{k^2} \left[ 1 - \frac{(\mathbf{k}_1 \cdot \mathbf{k}_2)^2}{k_1^2 k_2^2} \right]. \quad (3.111)$$

Expanding eq. (3.108) in the density field one can see that LPT and SPT are equivalent order by order.

## 3.4 Biased Tracers

The distribution of matter in the Universe could tell us a lot about fundamental physics, but more importantly, it has a significant potential to constrain the early universe models [19]. The initial conditions of the Universe have a unique imprint on the matter distribution. The real challenge is that we can not observe the dark matter distribution, except in the weak lensing surveys. However, we know that galaxies are indirect and imperfect tracers of the matter distribution. Understanding the relationship between the distribution of the tracers and the dark matter distribution is an important theoretical challenge before we can use the future LSS survey data to put constraints on the early universe physics.

To understand non-linearities coming from the non-Gaussian initial conditions, we should understand the sources of non-linearities in the late-time observables. The galaxy bias (or halo bias) is one of the most important secondary sources of the non-linearities. We should understand it properly and quantify the terms in the galaxy bias relation with high precision if we want to put tighter constraints on models of inflation. Since we know that galaxies are formed inside gravitationally bound, virialized lumps of dark matter called halos, the first step is to understand the clustering of dark matter halos. This is called the *halo bias*. Here we study the halo bias relation.

In this section, we study how matter collapses to form gravitational bound stable objects and how we can calculate the distribution of galaxies or how many galaxies we can see at some particular mass scale. We will describe the spherical collapse dynamics and how we

can use it to predict mass function. Later we will describe the effective theory of bias and halo statistics.

### 3.4.1 Spherical Collapse

The initial matter density field has peaks and troughs and due to gravitational evolution it evolves to forms complex structures at late-times. These structures form a cosmic web and consist of halos of dark matter, filaments and voids. To study the evolution of matter overdensities and get some intuition on how structures are formed, we make some assumptions. First, we assume a matter dominated Universe. Second, we assume that the overdensity  $\delta_0$  is spherical so we can use Newton's Shell theorem such that all spherical overdensities evolve independently. This simplified model is called *spherical collapse* model.

We consider a matter-dominated universe with the mean background density  $\rho_b$ . Consider a ball of radius  $R_{b,0}$  and let us shrink it to the sphere of radius  $R_0$  with the density  $\rho$ . The background Universe evolves with the scale factor  $a_b = R_b/R_{b,0} = (3/2H_{b,0}t)^{2/3}$  (the subscript  $b$  is for background). The evolution of the overdense region is given by the Friedmann equation

$$H^2 = \frac{8\pi G\rho}{3a^3} - \frac{K}{a^2} = H_0^2 \left[ \Omega_{m,0}a^{-3} + (1 - \Omega_{m,0})a^{-2} \right], \quad (3.112)$$

where we define the scale factor  $a = R/R_0$  and using the conservation of mass we have  $R_0^3\rho = R_{b,0}^3\rho_b$ . The parametric solutions of the evolution of the perturbations are given by

$$a \equiv \frac{R}{R_0} = A(1 - \cos \theta), \quad (3.113)$$

$$t = B(\theta - \sin \theta), \quad (3.114)$$

where the parameter  $\theta$  runs from 0 to  $2\pi$ , and time runs from 0 to  $t_{\text{coll}} = 2\pi B$ . The coefficients  $A$  and  $B$  are given by

$$A = \frac{4\pi G\rho}{3K} = \frac{\Omega_{m,0}}{2(\Omega_{m,0} - 1)}, \quad (3.115)$$

$$B = \frac{4\pi G\rho}{3K^{3/2}} = \frac{\Omega_{m,0}}{2H_0(\Omega_{m,0} - 1)^{3/2}}. \quad (3.116)$$

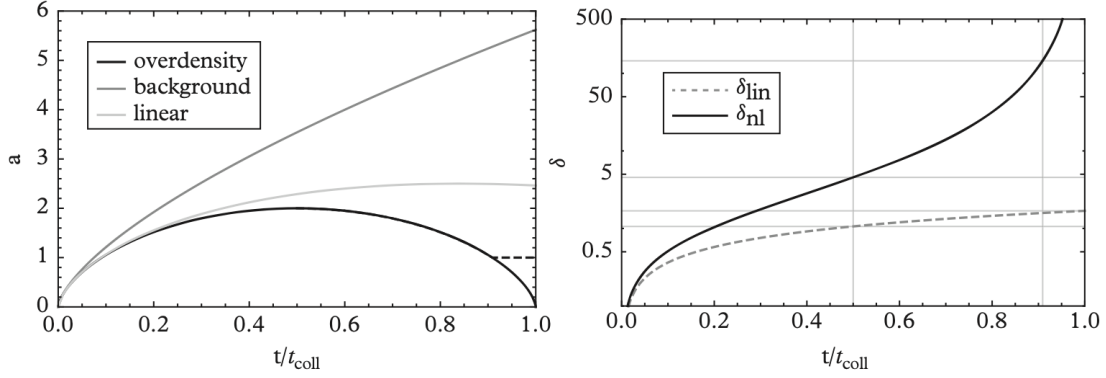


Fig. 3.7 Time evolution of background density, as well as linear and non-linear evolution of spherical overdensities [24].

We can expand Eq. (3.113) and Eq.(3.114) to get

$$a(t) = A \left( \frac{\theta^2}{2} \right) \left( 1 - \frac{\theta^2}{12} \right), \quad (3.117)$$

$$t = B \left( \frac{\theta^3}{6} \right) \left( 1 - \frac{\theta^2}{20} \right). \quad (3.118)$$

The linear order solutions are given by  $t = B\theta^3/6$  and  $a = (2/3H_{b,0}t)^{2/3}\Omega_{m,0}^{1/3} \propto a_b$ . The leading order solution of the scale factor is the same as for the background evolution. The corrections to the leading order solution to the scale factor can be obtained from Eq. (3.117):

$$a = \frac{R(t)}{R_0} \approx \frac{A}{2} \left( \frac{6t}{B} \right)^{2/3} \left[ 1 - \frac{1}{2} \left( \frac{6t}{B} \right)^{2/3} \right]. \quad (3.119)$$

The linear density contrast is given by

$$\delta_{\text{lin}} = \frac{R_b^3}{R_0^3} - 1 = \frac{3}{20} \left( \frac{6t}{B} \right)^{2/3} \quad (3.120)$$

An important event happens at  $t_{\text{turn}} = \pi B$  or  $\theta = \pi$  called the *turnaround* when the overdensity stops expanding and starts to collapse. At this moment the linear density contrast is

$$\delta_{\text{lin}}^{\text{turn}} = \frac{3}{20} (6\pi)^{2/3} \approx 1.06. \quad (3.121)$$

The collapse happens at  $\theta = 2\pi B$  or  $t_{\text{coll}} = 2\pi B$  when the linear density contrast becomes

$$\delta_{\text{lin}}^{\text{turn}} = \frac{3}{20} (12\pi)^{2/3} \approx 1.686. \quad (3.122)$$

This is the critical threshold density for dark matter halos that are collapsing now. This means that for halos which have collapsed completely today, we expect their linear density to have exceeded the critical threshold of  $\delta_c = 1.686$ . This is a good approximation for realistic models of cosmology including  $\Omega_\Lambda$  and  $\Omega_m$  [146]. There are, however, some shortcomings to this model. First, is that realistically the collapse is not completely spherical due to the presence of initial tidal forces [2]. Second, the overdensity never collapses to a point. At some point during the collapse the random motion of dark matter particles balances the gravitational pull and the overdense region becomes stable. This process is called virialisation. After the virialisation happens the total kinetic energy  $T_{\text{vir}}$  and the potential energy  $V_{\text{vir}}$  satisfies  $V_{\text{vir}} + 2T_{\text{vir}}=0$ . We know that when turnaround happens, the kinetic energy becomes zero and the total energy  $E$  becomes equal to the potential energy. We call the maximum potential energy as  $V_{\text{max}}$ . After the virialisation we can write this relation as  $E = V_{\text{vir}} + T_{\text{vir}} = 1/2V_{\text{vir}}$ . Using the conservation of energy we can deduce that the radius at the time of virialisation is actually half the size of the radius at the time of turnaround, that is  $R_{\text{vir}} = R_{\text{max}}/2$ . This means that the overdensity grows by a factor of 8. Also from the turnaround to collapse the background density shrinks by four times. The non-linear density at the time of turn around can be deduced from Eq.(3.117) which is  $1 + \delta^{\text{turn}} \approx 5.55$ . Using all information about virialisation, the non-linear density at the time of the virialisation can be estimated as

$$1 + \delta^{\text{vir}} \approx 5.55 \times 8 \times 4 = 178. \quad (3.123)$$

This is a simple yet a powerful result. This shows that if the linear density field exceeds the threshold of 1.686 then we expect a halo to form with the non-linear density of almost 200 times the background density. The evolution of the background density as well as linear and non-linear densities are shown in Fig. 3.7

### 3.4.2 Press-Schechter Mass Function

The spherical collapse dynamics tells us that if we have a region with overdensity exceeding the critical overdensity  $\delta_c$  then we expect that region to collapse to form a dark matter halo. If the radius of the spherical region is  $R$  then the mass of the halo formed will be

$$M = \frac{4\pi}{3} R^3 \rho \quad (3.124)$$

The variance of fluctuations at the scale  $R$  (or mass  $M$ ), smoothed with a filter is defined as

$$\sigma^2(M) = \int \frac{d^3q}{(2\pi)^3} P(q) W_{\text{TH}}^2[kR(M)] \quad (3.125)$$

where  $R(M) \propto M^{1/3}$  and the Top-Hat smoothing function in Fourier space is defined as

$$W_{\text{TH}}(kR) = \frac{3}{(kR)^3} \left( \sin(kR) - (kR) \cos(kR) \right). \quad (3.126)$$

We now define the probability of finding regions with an overdensity  $\delta$  in a Gaussian random field. This probability function is defined as

$$\mathcal{P}(\delta|M) = \frac{1}{\sqrt{2\pi\sigma^2(M)}} \exp\left(-\frac{1}{2} \frac{\delta^2}{\sigma^2(M)}\right). \quad (3.127)$$

The probability of finding the regions whose overdensity exceed a given threshold  $\delta_c$  can be found by integrating eq. (3.127) as

$$\mathcal{P}( > \delta|M) = \int_{\delta_c}^{\infty} d\delta \mathcal{P}(\delta|M) = \int_v^{\infty} dx \exp\left(-\frac{x^2}{2}\right) \quad (3.128)$$

where we have introduced a new variable  $v = \delta_c/\sigma$  which is called the *peak height* or *significance*. For a model of the Universe the variance of fluctuations  $\sigma^2$  decreases with the Mass scale. This implies that since the small-scale inhomogeneities have larger variance, they cross the critical threshold first and form structures. The small-scale objects collapse first and merge to form larger objects. In the Universe filled by hot dark matter, the structure formation is top to bottom, which means that large objects collapse first and then disintegrate into smaller objects [24].

We want to find the total number of halos of mass  $M$ . The smaller objects which exceed the critical threshold form halos first and then merge to form larger halos. Because of this we assume that halos of mass  $M$  are part of massive halos of mass  $M + dM$  which also exceed the critical threshold. taking into account this we define the probability of the fraction of halos of  $M$  as

$$\mathcal{P}( > \delta_c|[M, M + dM]) \approx -\frac{d\mathcal{P}}{dM} = -\frac{d\mathcal{P}}{dv} \frac{dv}{d\sigma} \frac{d\sigma}{dM} - \frac{1}{\sqrt{2\pi}} \frac{\delta_c}{\sigma^2} \exp\left(-\frac{\delta_c^2}{2\sigma^2}\right) \frac{d\sigma}{dM} \quad (3.129)$$

Eq. (3.129) takes into account only half of the mass in the Universe because the underdense regions do not collapse. Integrating Eq. (3.129) over  $\sigma$  yields 1/2. Press-Schechter introduced a factor 2 in Eq. (3.129) to take into account that information. Furthermore, to calculate the mass function we need to multiply Eq. (3.129) by the maximum number of regions of mass  $M$  in a given volume  $V$  with the total mass  $M_{\text{total}}$ :  $N_{\text{total}} = M_{\text{total}}/M$ . The

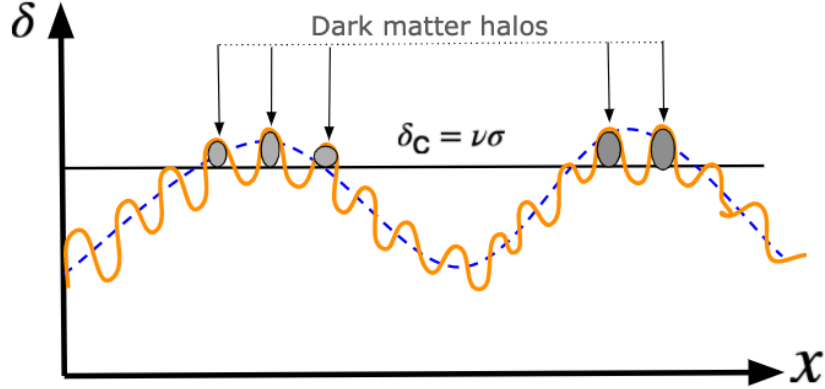


*Fig. 3.8* Peak-background split. The long-wavelength modes modulates short-modes. The regions which exceed the threshold value,  $\delta_c$ , collapse to form dark matter halos as shown in this figure.

maximum number density thus given by  $n_{\max} = \rho/M$ . After a little bit of rearranging we get

$$n(M) = n_{\max} \mathcal{P}( > \delta_c | [M, M + dM] ) = -\sqrt{\frac{2}{\pi}} \frac{\bar{\rho}}{M^2} v \exp\left(-\frac{v^2}{2}\right) \frac{d \ln \sigma}{d \ln M}. \quad (3.130)$$

This is the famous Press-Schechter mass function [166].

### 3.4.3 Peak-background Split

Using the mass function we can define the biasing between the clustering of dark matter halos and dark matter. To derive the clustering relation we use the framework of the peak-background split formulated in [31, 53, 113, 145, 190]. Here the smoothing of linear density field at scale  $R$  is different than in EFTofLSS. In EFofLSS the smoothing scale is not physical while here  $R$  is the physical scale corresponding to the scale of dark matter halos. The long wavelength fluctuations of the density field, which correspond to the wavenumbers  $k < R^{-1}$ , determines the large scale clustering of halos. Furthermore, the long wavelength mode modulates the short modes so they can easily cross the critical threshold  $\delta_c$  and collapse to form massive objects such as halos. Fig. 3.8 illustrate this process clearly. This means that the long wavelength modes shift the critical threshold and so the peak height becomes

$$v = \frac{\delta_c}{\sigma} \rightarrow \tilde{v} = \frac{\delta_c - \delta_l}{\sigma} \quad (3.131)$$



The mass function has now become a function of new shifted peak height  $\tilde{v}$ . We Taylor expand around the background value to get

$$n(\tilde{v}) = n(v) + \frac{\partial n(\tilde{v})}{\partial \delta_l} \delta_l + \frac{1}{2} \frac{\partial^2 n(\tilde{v})}{\partial \delta_l^2} \delta_l^2 + \dots \quad (3.132)$$

In general we are interested in halo (or galaxy) overdensity not directly in the number density. The overdensity of halos are therefore defined in Lagrangian coordinates,  $\mathbf{q}$ , as

$$\delta_h(\mathbf{q}) = \frac{n}{\bar{n}} - 1 = b_1^{(L)} \delta_1(\mathbf{q}) + \frac{b_2^{(L)}}{2} \delta_1^2(\mathbf{q}) + \frac{b_3^{(L)}}{3!} \delta_1^3(\mathbf{q}) + \dots, \quad (3.133)$$

where  $b_i^{(L)} = (1/\bar{n})(\partial^i n / \partial \delta_l^i)$  are called Lagrangian bias parameters. For the Press-Schechter mass function defined in Eq. (3.130) the first two Lagrangian bias parameters are explicitly defined as

$$b_1^{(L)} = \frac{v^2 - 1}{\delta_c}, \quad b_2^{(L)} = \frac{v^2(v^2 - 3)}{\delta_c^2}. \quad (3.134)$$

We will discuss the Lagrangian bias model in detail in Chapter 4.

### 3.4.4 Effective Theory of Bias

Here we discuss the effective theory of galaxy (or halo) bias (for good review see [10, 66, 140]). We know that that the clustering of dark matter halos are biased. The simplest bias model is the linear model where halo density field is linearly depend on the matter density:  $\delta_h(\mathbf{x}) = b_1 \delta(\mathbf{x})$ , where  $b_1$  is called the linear bias parameter. This model works well on very large scales ( $k \ll 0.1h^{-1}$  Mpc), however it fails on small scales where non-linearities start to kick in. Beyond the linear model, the halo density field can be Taylor expanded in terms of the dark matter density  $\delta$  which to give the *local Eulerian* bias model [90]:

$$\delta_h(\mathbf{x}, \tau) = \sum_{n=0}^{\infty} \frac{b_n}{n!} \delta^n(\mathbf{x}, \tau). \quad (3.135)$$

where  $b_n$  are non-linear local Eulerian bias parameters. This local bias model has been used in data-analysis of galaxy surveys [81, 93, 94, 137, 181, 207]. We know that the local bias model is incomplete and requires essential non-local terms too [20, 50, 141]. Gravitational evolution induces non-local terms at late-times [2, 20, 50]. Another reason is the symmetries of equations of motion which allow to include a set of local and non-local terms at each order and define an effective theory of bias. Taking into account symmetries we write the

most general bias model as [10, 140]

$$\delta_{\text{h}}(\mathbf{x}, \tau) = \sum_{\mathcal{O}} b_{\mathcal{O}}^{\text{R}}[\mathcal{O}](\mathbf{x}, \tau) \quad (3.136)$$

where  $b_{\mathcal{O}}^{\text{R}}$  are renormalised bias parameters and  $[\mathcal{O}]$  are renormalised bias operators.

We now discuss what operators are allowed by symmetries as follows. Under a homogeneous boost, the gravitational potential  $\Phi_{\text{g}}$  and the velocity potential  $\Phi_{\text{v}}$  shift by a vector. If the initial conditions are also invariant under these transformations, the counterterms can be chosen to be scalar under these transformations. The operators should depend on  $\nabla_i \nabla_j \Phi$ . If we also consider rotational invariance then we should contract the indices as well. Taking into account all symmetries of dark matter equations of motion we arrive at the following set of allowed operators at different order in perturbation theory: At the **leading order** only allowed bias operator is  $\delta = \nabla^2 \Phi_{\text{g}}^{(1)}$ . At the **second order** in PT we have three allowed operators given by

$$\mathcal{O}_2 \in \left\{ \delta, \delta^2, \mathcal{G}_2(\Phi_{\text{g}}) \right\} \quad (3.137)$$

where second order Galilean operator is defined by  $\mathcal{G}_2(\Phi_{\text{g}}) = (\nabla_i \nabla_j \Phi_{\text{g}})^2 - (\nabla^2 \Phi_{\text{g}})^2$ . Finally, at the **cubic order** in PT there are seven allowed operators:

$$\mathcal{O}_3 \in \left\{ \delta, \delta^2, \delta^3, \mathcal{G}_2(\Phi_{\text{g}}), \mathcal{G}_2(\Phi_{\text{g}})\delta, \mathcal{G}_3(\Phi_{\text{g}}), \Gamma_3(\Phi_{\text{g}}, \Phi_{\text{v}}) \right\} \quad (3.138)$$

where  $\mathcal{G}_3$  is the third order Galilean operator defined as

$$\mathcal{G}_3(\Phi_{\text{g}}) = -\frac{1}{2} \left[ (\nabla^2 \Phi_{\text{g}})^3 + 2 \nabla_i \nabla_j \Phi_{\text{g}} \nabla^j \nabla^k \Phi_{\text{g}} \nabla_k \nabla_i \Phi_{\text{g}} - 3 (\nabla_i \nabla_j \Phi_{\text{g}})^2 \nabla^2 \Phi_{\text{g}} \right] \quad (3.139)$$

and  $\Gamma_3$  is the velocity tidal tensor which explicitly depends on the velocity potential:

$$\Gamma_3(\Phi_{\text{v}}, \Phi_{\text{g}}) = \mathcal{G}_2^{(3)}(\Phi_{\text{g}}) - \mathcal{G}_2^{(3)}(\Phi_{\text{v}}) \quad (3.140)$$

with

$$\mathcal{G}_2^{(3)}(\Phi) = 2 \left( \nabla_i \nabla_j \Phi^{(1)} \nabla^i \nabla^j \Phi^{(2)} - \nabla^2 \Phi^{(1)} \nabla^2 \Phi^{(2)} \right). \quad (3.141)$$

We can estimate how each of these operators scale. The scaling of operators in EFTofLSS are studied in [157, 44]. If we consider a scaling law initial conditions, the power spectrum scales as  $(q/k_{\text{NL}})^{3+n}$  where  $n \approx -2.1$  near the non-linear scale at redshift  $z = 0$ . If we assume that the effective theory is valid on scales larger than  $\Lambda_*^{-1}$  and if this scale is roughly assumed to be  $\Lambda_* \sim k_{\text{NL}}$  then power counting of each bias operator in the effective theory is

given by the following general formula:

$$\{[\mathcal{O}_{(\alpha,\beta)}]\} \equiv \left\{ \frac{[\nabla^{2\alpha}(\nabla^2\Phi_g)^\beta]}{\Lambda_*^{2\alpha}} \right\} \sim \left( \frac{q}{k_{\text{NL}}} \right)^{2\alpha + \frac{1}{2}\beta}. \quad (3.142)$$

Using this formula we write the scaling of bias operators at the leading order in derivative as

$$q^{1/2} : \quad \mathcal{O}_{(0,1)} = \{\delta\}, \quad (3.143)$$

$$q^1 : \quad \mathcal{O}_{(0,2)} = \{\delta^2, \mathcal{G}_2\}, \quad (3.144)$$

$$q^{3/2} : \quad \mathcal{O}_{(0,3)} = \{\delta^3, \mathcal{G}_3, \mathcal{G}_2\delta, \Gamma_3\}. \quad (3.145)$$

The derivative operators are actually more suppressed than the scaling defined in eq. (3.142).

### 3.4.5 Halo Statistics

Here we discuss the halo statistics, that is the halo power spectrum, the halo bispectrum and the halo triepctrum. These statistics depend on the bias operators. The higher order bias operators become important at higher point functions or higher order loop corrections. We define these statistics below.

#### Halo Power Spectrum

The halo-matter and halo-halo power spectra are defined through the 2-point function in Fourier space:

$$\langle \delta_m(\mathbf{k}) \delta_h(\mathbf{k}') \rangle = (2\pi)^3 \delta_D^{(3)}(\mathbf{k} + \mathbf{k}') P_{\text{hm}}(k) \quad (3.146)$$

$$\langle \delta_h(\mathbf{k}) \delta_h(\mathbf{k}') \rangle = (2\pi)^3 \delta_D^{(3)}(\mathbf{k} + \mathbf{k}') P_{\text{hh}}(k). \quad (3.147)$$

The expression for one-loop halo-matter and halo-halo power spectra are given by [10, 138]

$$P_{\text{hm}}(k) = b_1 \left( P_{\text{lin}}(k) + P_{13}(k) + P_{22}(k) \right) + \left( \frac{b_2}{2} - \frac{4}{5} b_{\mathcal{G}_2} \right) \mathcal{F}(q) \\ + \left( b_{\mathcal{G}_2} + \frac{2}{5} b_{\Gamma_3} \right) \mathcal{F}(q) - b_{\nabla^2\delta} k^2 P_{\text{lin}}(k) \quad (3.148)$$

$$\begin{aligned}
P_{\text{hh}}(k) = & b_1 \left[ b_1 \left( P_{\text{lin}}(k) + P_{13}(k) + P_{22}(k) \right) + 2 \left( \frac{b_2}{2} - \frac{4}{5} b_{\mathcal{G}_2} \right) \mathcal{I}(q) + 2 \left( b_{\mathcal{G}_2} + \frac{2}{5} b_{\Gamma_3} \right) \mathcal{F}(q) \right] \\
& + \sum_{\mathcal{O}, \mathcal{O}'} b_{\mathcal{O}_2} b_{\mathcal{O}'_2} \langle \mathcal{O}_2 \mathcal{O}'_2 \rangle' + \text{higher derivative terms}
\end{aligned} \tag{3.149}$$

where  $\mathcal{I}(k)$ ,  $\mathcal{F}(k)$ , and  $\langle \mathcal{O}_2 \mathcal{O}'_2 \rangle'$  are defined as

$$\mathcal{I}(k) = 2 \int_{\mathbf{q}} F_2(\mathbf{k} - \mathbf{q}, \mathbf{q}) P_{\text{lin}}(q) P_{\text{lin}}(|\mathbf{k} - \mathbf{q}|) \tag{3.150}$$

$$\mathcal{F}(k) = 4 P_{\text{lin}}(k) \int_{\mathbf{q}} \sigma^2(\mathbf{q}, \mathbf{k} - \mathbf{q}) F_2(\mathbf{k}, -\mathbf{q}) P_{\text{lin}}(q) \tag{3.151}$$

$$\langle \mathcal{O}_2 \mathcal{O}'_2 \rangle' = 2 \int_{\mathbf{q}} \mathcal{O}_2(\mathbf{q}, \mathbf{k} - \mathbf{q}) \mathcal{O}'_2(\mathbf{q}, \mathbf{k} - \mathbf{q}) P_{\text{lin}}(q) P_{\text{lin}}(|\mathbf{k} - \mathbf{q}|) \tag{3.152}$$

where  $\sigma^2(\mathbf{q}_1, \mathbf{q}_2) = \left( (\mathbf{q}_1 \cdot \mathbf{q}_2)^2 / q_1^2 q_2^2 \right) - 1$  and  $\mathcal{O}_2$  are quadratic bias operators.

### Halo Bispectrum

The bispectrum is the three point function in the Fourier space. For example, the halo-matter-matter correlator is defined as

$$\langle \delta_{\text{m}}(\mathbf{k}_1) \delta_{\text{m}}(\mathbf{k}_2) \delta_{\text{h}}(\mathbf{k}_3) \rangle = (2\pi)^3 \delta_{\text{D}}^{(3)}(\mathbf{k}_1 + \mathbf{k}_2 + \mathbf{k}_3) B_{\text{hmm}} \tag{3.153}$$

The expression for the tree level bispectrum  $B_{\text{hmm}}$  is given by

$$\begin{aligned}
B_{\text{hmm}}(\mathbf{k}_1, \mathbf{k}_2, \mathbf{k}_3) = & b_1 \left( 2 P_{\text{lin}}(k_1) P_{\text{lin}}(k_2) F_2(\mathbf{k}_1, \mathbf{k}_2) + \text{cyc} \right) \\
& + 2 \left[ b_2 + b_{s,2} \left( \frac{(\mathbf{k}_1 \cdot \mathbf{k}_2)^2}{k_1^2 k_2^2} - \frac{1}{3} \right) \right] P_{\text{lin}}(k_1) P_{\text{lin}}(k_2) + \text{cyc}
\end{aligned} \tag{3.154}$$

We use the halo bispectrum statistics to put constraints on the quadratic bias parameters.

### Halo Trispectrum

Similarly, the trispectrum is defined from the four-point function described by

$$\langle \delta_{\text{m}}(\mathbf{k}_1) \delta_{\text{m}}(\mathbf{k}_2) \delta_{\text{m}}(\mathbf{k}_3) \delta_{\text{h}}(\mathbf{k}_4) \rangle = (2\pi)^3 \delta_{\text{D}}^{(3)}(\mathbf{k}_1 + \mathbf{k}_2 + \mathbf{k}_3 + \mathbf{k}_4) T_{\text{hmmm}} \tag{3.155}$$

The leading order halo trispectrum depends on the cubic bias operators and hence is the natural statistics to constrain cubic bias parameters. The tree-level trispectrum expression is

given by

$$T_{\text{hmmm}} = b_1 T_{\text{mmmm}} + \sum_{\mathcal{O}_2} b_{\mathcal{O}_2} \langle \delta^{(1)} \delta^{(1)} \delta^{(2)} \mathcal{O}_2 \rangle' + \sum_{\mathcal{O}_3} b_{\mathcal{O}_3} \langle \delta^{(1)} \delta^{(1)} \delta^{(1)} \mathcal{O}_3 \rangle' \quad (3.156)$$

where  $\mathcal{O}_2 \in \{\delta^2, s^2\}$  and  $\mathcal{O}_3 \in \{\delta^3, \mathcal{G} - 2\delta, \mathcal{O}_3, \Gamma_3\}$ . Moreover,  $b_{\delta^2}$  and  $b_{\delta^3}$  are related to our parameters  $b_2$  and  $b_3$  as:  $b_{\delta^2} = b_2/2$  and  $b_{\delta^3} = b_3/6$ .

Measuring the bispectrum and the trispectrum in  $N$ -body simulations is computationally quite expensive, but we will show in the next chapter that we can in fact write these statistics in terms of the cross spectra of quadratic and cubic fields with the halo density fields respectively. This method is optimal and more efficient than the traditional bispectrum and trispectrum estimation [2, 176].

### 3.5 $N$ -body Codes

Cosmological  $N$ -body simulations are a great tool to understand the large-scale structure and non-linear dynamics. Theoretical models are tested against simulations before they can be applied directly to analyse data from cosmological surveys. In this section, we discuss the  $N$ -body simulation codes employed in this thesis. A useful review on cosmological numerical simulations are given in [38, 41].

Collisionless dark matter obeys the Vlasov equation for the distribution in phase space in the limit when the number of particles is large (i.e.  $N \gg 1$ ). Numerical simulations solve this equation by partitioning phase space into smaller fundamental volumes. These fundamental volumes, referred to as "particles", have position and velocities in phase space. These particles are evolved under the influence of gravity. Each particle carries a smooth density profile, which can be thought of as a cloud, the size of which depends on the mass of the particle, i.e.  $\epsilon_i \propto m_i^{1/3}$ , where  $\epsilon_i$  refers to the softening parameter. This parameter softens the interaction between nearby particles and fixes the spatial resolution of the numerical simulation. The number of particles fixes the mass resolution which depends on the volume times density divided by the number of particles. The necessary steps to perform  $N$ -body simulations are: (1) Implement the initial conditions on a cubic grid [74, 40]; (2) calculate forces between particles [198, 42, 105]; (3) update positions and velocities of particles using a time integrator [196, 105]; (4) test that the energy and momentum remain conserved [38].

The initial positions and velocities of particles can be generated from the density field using the Lagrangian perturbation theory. Using the Zeldovich approximation, the small displacement  $\mathbf{q}$  and the velocity are given by

$$\mathbf{x}(\mathbf{q}, t) = \mathbf{q} + D(t)\Psi_0(\mathbf{q}), \quad \frac{d\mathbf{x}}{dt} = \frac{d\Psi(\mathbf{q}, t)}{dt}. \quad (3.157)$$

For linear perturbations we can separate the displacement field into the time independent component and the spatial component. The displacement field relates to the density perturbations by

$$\frac{\delta\rho}{\rho} = -\nabla \cdot \Psi, \quad \nabla \times \Psi = 0. \quad (3.158)$$

The displacement field can be obtained from Eq. (3.158) using Fourier transforms. In summary, the steps to generate the initial conditions are: (1) generate Gaussian random field on a cubic grid; (2) compute the displacement field from Eq. (3.158) using the Fast Fourier Transforms<sup>1</sup> (FFTs); and (3) update positions and velocities using Eq. (3.157). In this thesis work we use **2LPT** code [182] to generate initial conditions. This code using the second-order Lagrangian perturbation theory instead of the linear-order Zeldovich approximation described in Eq. (3.157). We use **Gadget-2** code [196] to evolve the initial conditions on the cubic grid. Gadget-2 is a parallel TreeSPH code, which follows the dynamic of dark matter particles using the  $N$ -body method. We are only interested in the large-scale effects and not the gas dynamics part. To calculate forces between particles in numerical  $N$ -body simulations requires  $\mathcal{O}(N^2)$  operations. **Gadget-2** reduces this complexity to  $\mathcal{O}(N \log N)$  by using efficient methods. The code uses a pure Tree code to calculate the gravitational forces on small scales by computing hierarchical multipole expansion of the gravitational field. On large scales it uses FFTs to speed up the process.

Positions and velocities of particles can be updated using the Leapfrog integrator [105]. This integrator shifts positions and velocities by half a time-steps. The time integrators are symplectic to make sure that the phase space volume is preserved.

Finally, we make sure that we use an appropriate periodic boundary conditions. We define the periodic boundary conditions on a cubic grid of length  $L$  as

$$\delta(x + iL, y + jL, z + kL) = \delta(x, y, z) \quad i, j, k \in \mathbf{Z}. \quad (3.159)$$

At the end when the simulation is completed we get the non-linear dark matter density field. Once we have the dark matter field, we investigate the clustering of dark matter. The basic building blocks of large-scale structure are gravitationally-bound objects called dark matter halos. In the dark matter field, according to the spherical collapse model, the dark matter halos are formed with overdensity  $\delta \approx 180$ . To identify these structures in simulations we run the **Friends-of-Friends** (FoF) algorithm [118]. This algorithm has a linking parameter  $l$ . Particles which have separation distance less than  $l$  are identified as friends. A dark matter halo is identified with particles that are connected by at-least one friendship, that is friends-of-friends. The linking length  $l$  depends on a certain threshold  $\rho$  above which a halo is formed. If  $M_p$  is the average particle mass then we can define a sphere of radius  $l$  which

---

<sup>1</sup>we use FFTW library

exceed the threshold density. The radius is defined by

$$l = \left( \frac{2M_p}{4/3\pi\rho} \right)^{1/3} \quad (3.160)$$

The FoF algorithm also depends on the minimum number  $N_{\min}$  of particles per halo to reject spurious halos which are not gravitationally bound objects. In our simulations we use the linking length  $l = 0.2$  and  $N_{\min} = 20$ .

## Cubic Halo Bias in Eulerian and Lagrangian Space

*Note: This chapter is my original work (done under the supervision of Tobias Baldauf) and is based on my first-authored published paper "Cubic Halo Bias in Eulerian and Lagrangian Space" [2].*

### 4.1 Introduction

The Large Scale Structure (LSS) of the Universe contains a wealth of information about the origin, composition, and evolution of the Universe. In order to extract this information from on-going and future LSS surveys, we have to understand various sources of non-linearities present in the late-time LSS observables. In general, there are three main sources of non-linearities:

- non-linear matter clustering due to gravity
- non-linear biasing: the relation between the distribution of tracers and dark matter
- primordial non-Gaussianity (PNG), which induces non-linearities on the initial conditions

Recently, the powerful framework of the Effective Field Theory of Large Scale Structure (EFTofLSS) [36, 45, 165, 188, 27, 7, 16, 39, 158], which is an extension and correction of Standard Perturbation Theory [37], has provided a valuable insight into the non-linear nature of matter clustering due to gravity. It has been shown that the EFTofLSS prediction for the two-loop dark matter power spectrum agrees to 1% precision both with the  $N$ -body simulations up to  $k_{\max} \approx 0.3h \text{ Mpc}^{-1}$  [47, 16] and with the one-loop bispectrum up to  $k_{\max} \approx 0.22h \text{ Mpc}^{-1}$  at redshift  $z = 0$  [7, 27]. However, to provide a consistent model for the statistics of biased tracers using the framework of the EFTofLSS, we need to understand



the non-linearities due to biasing between the distribution of the tracers (halos or galaxies) and the matter distribution.

The predictions of the next-to-leading order, that is one-loop halo power spectra and halo-matter cross spectra, depend on the bias parameters up to cubic order [11, 142, 187]. The one-loop halo bispectra, on the other hand, depend on the bias parameters up to quartic order [11]. Therefore, quantifying the higher order bias parameters precisely is a crucial step towards the modeling of the statistics of biased tracers. As we will describe in more detail in Sec. 4.5.6, the halo-matter cross power spectrum depends on a particular combination of two cubic bias parameters. Study [172] attempted to measure this combination of bias parameters by fitting the scale dependence of the halo-matter power spectrum. However, the authors neglected the presence of derivative (or  $k^2$ ) bias parameters, which are degenerate with the effect of the cubic bias operators. Their constraints are likely to be biased.

In this chapter, we focus on the biasing problem and the measurements of halo bias parameters up to cubic order. There are two ways to study the halo bias: one is called the *Eulerian bias model* and the other is known as the *Lagrangian bias model*. In the Eulerian bias model, the halo overdensity field  $\delta_{\text{h}}(\mathbf{x}, \tau)$  is described in terms of co-moving coordinates  $\mathbf{x}$  as

$$\delta_{\text{h}}(\mathbf{x}, \tau) = \sum_{\mathcal{O}} b_{\mathcal{O}} \mathcal{O}(\mathbf{x}, \tau), \quad (4.1)$$

where  $b_{\mathcal{O}}$  are the bias parameters and  $\mathcal{O}(\mathbf{x})$  are bias operators that are functionals of matter density  $\delta(\mathbf{x})$ . Eulerian biasing beyond linear order was first studied by [91] who introduced the local Eulerian bias model, where  $\mathcal{O}(\mathbf{x})$  are local functions of  $\delta(\mathbf{x})$  expanded into a Taylor series. However, based on symmetry arguments, it was shown in [142, 11, 51] that the local Eulerian model is incomplete, making it important to include non-local terms at quadratic and cubic order. Numerical evidence for the presence of a quadratic non-local term in the Eulerian bias model in  $N$ -body simulations was given by [51, 21]. In principle, the halo field contains a typical scale, for instance the Eulerian or Lagrangian extent of a halo. For this and for numerical reasons, we will evaluate the operators in the right hand side of Eq. (4.1) smoothed on  $R_{\text{h}}$ . Physical bias models, based on the notion of halos being formed from a patch of size  $R_{\text{h}} \propto M$  in Lagrangian space which exceeds the critical collapse density, have a physical scale built in. This scale can be fitted from the actual halos, as in [14], as a function of mass, but we will rather pick a fixed value independent of mass and account for the residual uncertainty.

On the other hand, in a *Lagrangian bias model* we identify protohalos, the regions in the initial density field that collapse and form halos at late-time, and describe the relation of the protohalo density field  $\delta_{\text{h}}(\mathbf{q})$  and the initial density field  $\delta_{\text{G}}(\mathbf{q})$  in Lagrangian coordinates  $\mathbf{q}$ . Writing the biasing relation in Lagrangian space is very useful, because it separates the non-linearities due to biasing from the non-linearities generated from gravitational instabilities.

The most studied Lagrangian bias model so far is the local Lagrangian Bias (LLB) model. However, some evidence for the presence of a non-local tidal term in the Lagrangian model has been found recently in [147]. The time evolution of Lagrangian protohalos can be studied in the framework of co-evolution of a halo fluid coupled to the dynamically dominant dark matter component through its gravitational potential, as we will describe in the next section.

One of the aims of this chapter is to constrain the bias parameters up to cubic order in Eulerian and Lagrangian spaces. The linear bias parameter can be estimated from the large scale halo-matter cross power spectrum and the second order bias parameters from the large scale, tree-level, bispectrum. Furthermore, the natural statistic to constrain cubic bias parameters is the large-scale, tree-level trispectrum. We summarize the N-point functions and relevant bias parameters in Tab. 4.1. Estimating the bispectrum and trispectrum is computationally expensive, so we use the quadratic field method proposed in [177] to estimate the quadratic bias and extend the method to cubic fields to estimate cubic bias parameters.

The key idea is to cross-correlate a basis of cubic bias operators (i.e. a weighted sum of three smoothed Gaussian fields) with the protohalo field and the late-time halo field, and to express the results in terms of the cross-spectra of cubic operators with themselves. The smoothing on the scale  $R_f$  serves as a high- $k$  cutoff in our analysis. In perturbation theory (PT), the cross correlation of cubic fields with themselves can be expressed in terms of two-loop power spectrum diagrams. These diagrams contain one UV-sensitive reducible two-loop diagram and one two-loop irreducible diagram. Because of our ignorance of the exact scale of halos, the UV-sensitive diagrams might affect the measurements, of the bias parameters depending on which fiducial halo smoothing scale (cutoff) we choose. In our approach, we remove the strongly UV-sensitive diagrams by removing the part of the field that correlates with the linear density field. We will refer to this procedure as *orthogonalization*. The quadratic correlators do not contain this sort of UV-sensitive diagrams, so there is no need to orthogonalize them.

The two-loop irreducible diagrams contain two cut-off scales. One scale is the artificially induced  $R_f$ , which we choose to be  $20h^{-1}$  Mpc, and the other is the fiducial halo smoothing scale  $R_h$ . The smoothing scale  $R_f$  corresponds to the  $1/k_{\text{max}}$  in a bispectrum or trispectrum analysis. Even though the irreducible diagrams at quadratic field and cubic field level are not highly UV-sensitive, they are still affected by the choice of  $R_h$  and this dependency can affect the bias measurements. To make our measurements of the bias parameters independent of the halo smoothing scale, we Taylor-expand the cross-spectra around  $R_h = 4h^{-1}$  Mpc and introduce a one parameter counterterm  $dR$  for both quadratic and cubic statistics. This pragmatic approach is introduced in order to avoid dealing with a large number  $\mathcal{O}(20)$  of EFT counterterms.

We find clear detection of the presence of cubic local and non-local terms in Eulerian space. On the other hand, we find clear evidence of a non-local Lagrangian tidal field. In addition, we do not find a clear detection of Lagrangian cubic non-local terms for low mass bins; however, for the highest mass bin we do find some presence of cubic non-local Lagrangian terms. Furthermore, we find that the mass dependence of the Eulerian cubic non-local bias terms prefer a co-evolution prediction of the Lagrangian bias model with a non-zero tidal field and no cubic fields. We also find that the presence of the Lagrangian tidal field does not induce new cubic bias operators at late-times; rather it merely changes the amplitude of cubic bias operators, which has been previously discussed in [51, 144, 66].

This chapter is organized as follows. In Section 4.2, we discuss the bias models in Eulerian and Lagrangian space, as well as the co-evolution of the dark matter halos and dark matter. We present both the general definitions of the cubic operators and the co-evolution predictions for cubic bias parameters in the presence of the Lagrangian tidal field. In Section 4.3, we discuss the quadratic and cubic field methods, and discuss how to remove UV-sensitive diagrams. In Section 4.4, we describe our methodology to measure bias parameter from  $N$ -body simulations. In Section 4.5, we present our results. We conclude in Section 4.6.

	Tree-level	One-loop
Power Spectrum $P_{\text{hm}}$	$b_1$	$b_1, b_2, b_{s^2}, b_{\Gamma_3}$ derivative bias ( $b_{\nabla^2\delta} \dots$ )
Bispectrum $B_{\text{hmm}}$	$b_1, b_2, b_{s^2}$	$b_1, b_2, b_{s^2},$ $b_{\Gamma_3}, b_{\mathcal{G}_3}, b_{\mathcal{G}_2\delta}, b_3,$ $b_{\Gamma_4}, b_{\Delta_4}, b_{\Gamma_3\delta}, b_{\bar{\Gamma}_4},$ derivative bias ( $b_{\nabla^2\delta} \dots$ )
Trispectrum $T_{\text{hmmm}}$	$b_1, b_2, b_{s^2},$ $b_{\Gamma_3}, b_{\mathcal{G}_3}, b_{\mathcal{G}_2\delta}, b_3$	many bias terms...

*Table 4.1* Bias parameter estimation from  $N$ -point functions. The tree-level power spectrum, bispectrum and trispectrum are natural statistics to obtain cleanest (and non-degenerate) constraints on the linear, quadratic and cubic bias parameters respectively. On the other hand the constraints on the derivative bias can be obtained from the loop statistics once the other bias parameters have been fixed from the tree-level statistics. The terms in Orange are quartic bias parameters which are beyond the scope of this chapter. A similar table is also given in [11].

## 4.2 Halo Bias

There are two ways to write down the halo bias relation: (1) in evolved Eulerian space and (2) in initial Lagrangian space. We will discuss both viewpoints in this Section.

### 4.2.1 Eulerian Bias Model

Following [142, 11, 187], without loss of generality the bias relation in Eulerian space given in Eq. (4.1) can be written up to cubic order as

$$\begin{aligned}
\delta_{\text{h}}(\mathbf{x}) = & b_1 \left( \delta^{(1)}(\mathbf{x}) + \delta^{(2)}(\mathbf{x}) + \delta^{(3)}(\mathbf{x}) \right) + \frac{b_2}{2!} \left( \delta^2(\mathbf{x}) - \langle \delta^2(\mathbf{x}) \rangle \right) + b_2 \left( \delta^{(1)}(\mathbf{x}) \delta^{(2)}(\mathbf{x}) - \langle \delta^{(1)} \delta^{(2)} \rangle \right) \\
& + b_{s^2} \left( s^2(\mathbf{x}) - \langle s^2(\mathbf{x}) \rangle \right) + 2b_{s^2} \left( s_{ij}^{(1)}(\mathbf{x}) s_{ij}^{(2)}(\mathbf{x}) - \langle s_{ij}^{(1)} s_{ij}^{(2)} \rangle \right) + b_{\delta^3} \left( \delta^3(\mathbf{x}) - 3\delta(\mathbf{x}) \langle \delta^2(\mathbf{x}) \rangle \right) \\
& + b_{\mathcal{G}_3} \mathcal{G}_3(\mathbf{x}) + b_{\mathcal{G}_2 \delta} \left( \mathcal{G}_2 \delta(\mathbf{x}) - \langle \mathcal{G}_2 \delta(\mathbf{x}) \rangle \right) + b_{\Gamma_3} \left( \Gamma_3(\mathbf{x}) - \langle \Gamma_3(\mathbf{x}) \rangle \right) \\
& + b_{\nabla^2 \delta} \nabla^2 \delta(\mathbf{x}) + \dots
\end{aligned} \tag{4.2}$$

Here,  $s_{ij}^{(1)}(\mathbf{x}) s_{ij}^{(2)}(\mathbf{x})$  describes the tidal bias contribution propagated to cubic order and  $\delta^{(1)}(\mathbf{x}) \delta^{(2)}(\mathbf{x})$  quadratic bias contribution propagated to third order. The quadratic tidal field  $s^2(\mathbf{x}) = s_{ij}(\mathbf{x}) s_{ij}(\mathbf{x})$  is given as the trace of the square of the tidal tensor

$$s_{ij}(\mathbf{x}) = \left( \frac{\nabla_i \nabla_j}{\nabla^2} - \frac{1}{3} \delta_{ij}^{(K)} \right) \delta(\mathbf{x}), \tag{4.3}$$

where  $\delta_{ij}^{(K)}$  is the Kronecker delta function. For simplicity, from now onwards we adopt the notation  $s^{(3)}(\mathbf{x})$  for  $s_{ij}^{(1)}(\mathbf{x}) s_{ij}^{(2)}(\mathbf{x})$ . The remaining operators will be introduced in detail later. We remove the variance of the quadratic fields in order to ensure a mean zero halo overdensity  $\langle \delta_{\text{h}} \rangle = 0$  and subtract contributions proportional to  $\sigma^2 \delta$  from the cubic terms, to avoid a renormalization [139] of the low- $k$  limit of the halo-matter power spectrum. The bias parameters appearing in Eq. (4.2) are thus renormalized and physical bias parameters. Evaluating the one point moments  $\sigma^2 = \langle \delta_{\text{G}}^2 \rangle = \int_{\mathbf{q}} P_{\text{in}}(\mathbf{q})$  in Eq. (4.2) yields

$$\begin{aligned}
\delta_{\text{h}}(\mathbf{x}) = & b_1 \left( \delta^{(1)}(\mathbf{x}) + \delta^{(2)}(\mathbf{x}) + \delta^{(3)}(\mathbf{x}) \right) + \frac{b_2}{2!} \left( \delta^2(\mathbf{x}) - \sigma^2 \right) + b_2 \left( \delta^{(1)} \delta^{(2)}(\mathbf{x}) - \frac{68}{21} \sigma^2 \delta(\mathbf{x}) \right) \\
& + b_{s^2} \left( s^2(\mathbf{x}) - \frac{2}{3} \sigma^2 \right) + 2b_{s^2} \left( s^{(3)}(\mathbf{x}) - \frac{136}{63} \delta(\mathbf{x}) \sigma^2 \right) + b_{\delta^3} \left( \delta^3(\mathbf{x}) - 3\delta(\mathbf{x}) \sigma^2 \right) \\
& + b_{\mathcal{G}_3} \mathcal{G}_3(\mathbf{x}) + b_{\mathcal{G}_2 \delta} \left( \mathcal{G}_2 \delta(\mathbf{x}) + 4\delta(\mathbf{x}) \sigma^2 \right) + b_{\Gamma_3} \left( \Gamma_3(\mathbf{x}) + \frac{32}{35} \delta(\mathbf{x}) \sigma^2 \right) \\
& + b_{\nabla^2 \delta} \nabla^2 \delta(\mathbf{x}) + \dots
\end{aligned} \tag{4.4}$$

The second order terms  $\delta^{(2)}$ ,  $\delta^2$  and  $s^2$  are the second order density field, the density-squared, and the square of the tidal tensor terms respectively, and form a basis of the quadratic bias operators  $\mathcal{O}_2$ . There are seven distinct bias operators at cubic order, corresponding to seven bias parameters in general. Among seven bias operators at cubic order, four correspond to four new bias parameters: the coefficients of  $\delta^3$ ,  $\mathcal{G}_3$ ,  $\mathcal{G}_2\delta$  and  $\Gamma_3$ . These are the most general operators made up of the second derivatives of the gravitational and velocity potentials,  $\Phi_{g,v}$ , which are invariant under the symmetries of the equations of motion. At second order, there is no distinction between the gravitational and velocity potentials, because the contributions arise from squares of the linear potentials and at this order  $\delta^{(1)} = -\theta^{(1)}$ . However, the velocity potential becomes an independent degree of freedom at cubic order [11]. In fact,  $\Gamma_3$  depends on the gravitational as well as velocity potentials explicitly. The Galileon operators and  $\Gamma_3$  are defined as follows [51, 11]:

$$\begin{aligned}\mathcal{G}_1(\Phi_g) &= \nabla^2\Phi_g = \delta \\ \mathcal{G}_2(\Phi_g) &= (\nabla_i\nabla_j\Phi_g)^2 - (\nabla^2\Phi_g)^2 \\ \mathcal{G}_3(\Phi_g) &= -\frac{1}{2}\left[(\nabla^2\Phi_g)^3 + 2\nabla_i\nabla_j\Phi_g\nabla^j\nabla^k\Phi_g\nabla_k\nabla_i\Phi_g - 3(\nabla_i\nabla_j\Phi_g)^2\nabla^2\Phi_g\right]\end{aligned}\quad (4.5)$$

and

$$\Gamma_3(\Phi_v, \Phi_g) = \mathcal{G}_2^{(3)}(\Phi_g) - \mathcal{G}_2^{(3)}(\Phi_v) \quad (4.6)$$

where  $\mathcal{G}_2^{(3)}$  is given by

$$\mathcal{G}_2^{(3)}(\Phi) = 2\left(\nabla_i\nabla_j\Phi^{(1)}\nabla^i\nabla^j\Phi^{(2)} - \nabla^2\Phi^{(1)}\nabla^2\Phi^{(2)}\right). \quad (4.7)$$

The second order potential  $\Phi_{g,v}^{(2)}$  depends on the second order density  $\delta^{(2)}$  or velocity divergence  $\theta^{(2)}$ . We define our basis of quadratic bias operators  $\mathcal{O}_2$  and cubic bias operators  $\mathcal{O}_3$  in Eulerian space as:

$$\mathcal{O}_2 \in \left\{ \delta^{(2)}(\mathbf{x}), \delta^2(\mathbf{x}), s^2(\mathbf{x}) \right\} \quad (4.8)$$

$$\mathcal{O}_3 \in \left\{ \delta^{(3)}(\mathbf{x}), \delta^{(1)}\delta^{(2)}(\mathbf{x}), s^{(3)}(\mathbf{x}), \delta^3(\mathbf{x}), \mathcal{G}_3(\mathbf{x}) + \frac{1}{9}\delta^3(\mathbf{x}), \mathcal{G}_2\delta(\mathbf{x}) + \frac{2}{3}\delta^3(\mathbf{x}), \Gamma_3(\mathbf{x}) + \frac{16}{63}\delta^3(\mathbf{x}) \right\}. \quad (4.9)$$

In order to reduce degeneracies in the fitting and to make the results more aligned with the usual notion of local cubic bias  $b_3$ , we removed  $\delta^3$  contributions from the non-local bias operators  $\Gamma_3$ ,  $\mathcal{G}_2\delta$  and  $\mathcal{G}_3$ . In Appendix A, we show how this basis can be mapped to the

basis employed in [6, 92]. Our full basis of Eulerian bias parameters is given by<sup>1</sup>

$$\mathcal{B} \in \left\{ b_1, b_2, b_{s^2}, b_3, b_{\mathcal{G}_3}, b_{\mathcal{G}_2\delta}, b_{\Gamma_3} \right\}. \quad (4.11)$$

## 4.2.2 Lagrangian Bias Model

In Lagrangian space, all gravitational coupling kernels  $F_n$  (for  $n > 1$ ) are zero, so matter field equals the linear Gaussian field. We write the Lagrangian bias model with local and non-local terms up to cubic order as

$$\begin{aligned} \delta_{\text{h}}(\mathbf{q}) = & b_1^{\text{L}} \delta_{\text{G}}(\mathbf{q}) + \frac{b_2^{\text{L}}}{2!} \left( \delta_{\text{G}}^2(\mathbf{q}) - \sigma^2 \right) + \frac{b_3^{\text{L}}}{3!} \left( \delta_{\text{G}}^3(\mathbf{q}) - 3\sigma^2 \delta_{\text{G}}(\mathbf{q}) \right) + b_{s^2}^{\text{L}} \left( s^2(\mathbf{q}) - \frac{2}{3} \sigma^2 \right) \\ & + b_{\mathcal{G}_3}^{\text{L}} \mathcal{G}_3(\mathbf{q}) + b_{\mathcal{G}_2\delta}^{\text{L}} \left( \mathcal{G}_2 \delta(\mathbf{q}) + 4\sigma^2 \delta_{\text{G}}(\mathbf{q}) \right) + b_{\Gamma_3}^{\text{L}} \left( \Gamma_3(\mathbf{q}) + \frac{32}{35} \sigma^2 \delta_{\text{G}}(\mathbf{q}) \right) + b_{\nabla^2\delta} \nabla^2 \delta_{\text{G}}(\mathbf{q}) + \dots \end{aligned} \quad (4.12)$$

where  $\mathbf{q}$  is the Lagrangian coordinate of protohalos,  $b_i^{\text{L}}$  are the Lagrangian bias parameters, and  $\delta_{\text{h}}(\mathbf{q})$  is the protohalo density field. This expansion in Hermite polynomials ensures that there is no renormalization of the bias parameters in the correlators [202, 85]. Thus, the bias parameters in the model are the physical bias parameters occurring in the low- $k$  limit of  $n$ -point functions. Our basis of quadratic bias operator  $\mathcal{O}_2^{\text{L}}$  and cubic bias operators  $\mathcal{O}_3^{\text{L}}$  in Lagrangian space are defined as:

$$\mathcal{O}_2^{\text{L}} \in \left\{ \delta_{\text{G}}^2(\mathbf{q}), s^2(\mathbf{q}) \right\} \quad \text{and} \quad \mathcal{O}_3^{\text{L}} \in \left\{ \delta_{\text{G}}^3(\mathbf{q}), \mathcal{G}_3(\mathbf{q}) + \frac{1}{9} \delta_{\text{G}}^3(\mathbf{q}), \mathcal{G}_2 \delta(\mathbf{q}) + \frac{2}{3} \delta_{\text{G}}^3(\mathbf{q}), \Gamma_3(\mathbf{q}) + \frac{16}{63} \delta_{\text{G}}^3(\mathbf{q}) \right\}. \quad (4.13)$$

Similar to Eulerian bias parameters, we define a basis of the cubic Lagrangian bias parameters as

$$\mathcal{B}^{\text{L}} \in \left\{ b_1^{\text{L}}, b_2^{\text{L}}, b_{s^2}^{\text{L}}, b_3^{\text{L}}, b_{\mathcal{G}_3}^{\text{L}}, b_{\mathcal{G}_2\delta}^{\text{L}}, b_{\Gamma_3}^{\text{L}} \right\}. \quad (4.14)$$

<sup>1</sup>Note that corresponding to the cubic bias operators defined in eq.(4.9), the local cubic bias parameter has changed to  $b_3$ , which is the coefficient of  $\delta^3$  as predicted by the spherical collapse model. However, in a naive expansion in terms of the cubic bias operators, the coefficient becomes

$$b_{\delta^3} = b_3 + \frac{1}{9} b_{\mathcal{G}_3} + \frac{2}{3} b_{\mathcal{G}_2\delta} + \frac{16}{63} b_{\Gamma_3}. \quad (4.10)$$

as shown in Eqs (4.2) and (4.4).

### 4.2.3 Time Evolution of the Lagrangian Bias

For simplicity, we consider the local Lagrangian bias model and study its time evolution. At some initial time  $\tau_i$  we define the protohalo density field with only local terms as

$$\delta_h(\mathbf{q}, \tau_i) = b_1^L(\tau_i) \delta_G(\mathbf{q}, \tau_i) + \frac{b_2^L(\tau_i)}{2!} \left( \delta_G^2(\mathbf{q}, \tau_i) - \sigma^2 \right) + \frac{b_3^L(\tau_i)}{3!} \left( \delta_G^3(\mathbf{q}, \tau_i) - 3\delta_G(\mathbf{q}, \tau_i) \sigma^2 \right) + \dots \quad (4.15)$$

The time dependence of bias parameters  $b_n^L(\tau)$  and the linear density field  $\delta_G(\mathbf{q}, \tau)$  are defined as

$$b_n^L(\tau) = \left( \frac{D(\tau_i)}{D(\tau)} \right)^n b_n^L(\tau_i) \quad \text{and} \quad \delta_G(\mathbf{q}, \tau) = \frac{D(\tau)}{D(\tau_i)} \delta_G(\mathbf{q}, \tau_i), \quad (4.16)$$

where  $\tau$  is the conformal time and  $D(\tau)$  is the linear growth factor. From now onwards, we will choose  $\tau_i = 0$ .<sup>2</sup> We now transform the fields from Lagrangian to Eulerian coordinates. The Eulerian comoving coordinates  $\mathbf{x}$  and Lagrangian coordinates  $\mathbf{q}$  are related through the displacement field vector  $\Psi(\mathbf{q}, \tau)$  as

$$\mathbf{x}(\mathbf{q}, \tau) = \mathbf{q} + \Psi(\mathbf{q}, \tau). \quad (4.17)$$

We can use this relation and expand the Lagrangian density field up to third order by expressing the Lagrangian coordinates in the Eulerian coordinates as

$$\delta_G(\mathbf{q}, \tau) = \delta_G(\mathbf{x}, \tau) - \underbrace{\Psi(\mathbf{q}, \tau) \cdot \nabla \delta_G(\mathbf{q}, \tau) + \frac{1}{2} \Psi_i(\mathbf{q}, \tau) \Psi_j(\mathbf{q}, \tau) \nabla_i \nabla_j \delta_G(\mathbf{q}, \tau) + \dots}_{\text{shift terms}} \quad (4.18)$$

The second and third term in Eq. (4.18) describe the shift terms. We define the second and third order shift terms in the Eulerian coordinates as  $H^{(2)}(\mathbf{x}, \tau)$  and  $H^{(3)}(\mathbf{x}, \tau)$  respectively as below:

$$\begin{aligned} H^{(2)}(\mathbf{x}, \tau) &= \Psi^{(1)}(\mathbf{x}, \tau) \cdot \nabla \delta_G(\mathbf{x}, \tau), \\ H^{(3)}(\mathbf{x}, \tau) &= \Psi^{(2)}(\mathbf{x}, \tau) \cdot \nabla \delta_G(\mathbf{x}, \tau) - \frac{1}{2} \Psi_i^{(1)}(\mathbf{x}, \tau) \Psi_j^{(1)}(\mathbf{x}, \tau) \nabla_i \nabla_j \delta_G(\mathbf{x}, \tau) \\ &\quad - \Psi_i^{(1)}(\mathbf{x}, \tau) \left( \nabla_i \Psi_j^{(1)}(\mathbf{x}, \tau) \right) \nabla_j \delta_G(\mathbf{x}, \tau), \end{aligned} \quad (4.19)$$

where  $\Psi^{(1)}$  and  $\Psi^{(2)}$  are the first and second order displacement fields in Lagrangian Perturbation Theory (LPT) (see [136] for more details). In order to transform the halo density field in eq. (4.15) from Lagrangian to Eulerian coordinates, we have to use the

<sup>2</sup>To avoid confusion, we use  $\delta_h(\mathbf{q}) \equiv \delta_h(\mathbf{q}, \tau_i = 0)$  to represent the halo density field in the Lagrangian coordinates at the initial time  $\tau_i = 0$  and  $\delta_h(\mathbf{x}, \tau)$  as the evolved halo density field in the Eulerian coordinates

continuity equations for halos and dark matter given by

$$[1 + \delta_h(\mathbf{x}, \tau)]d^3\mathbf{x} = [1 + \delta_h(\mathbf{q})]d^3\mathbf{q} \quad \text{and} \quad [1 + \delta(\mathbf{x}, \tau)]d^3\mathbf{x} = d^3\mathbf{q}, \quad (4.20)$$

which lead to

$$\delta_h(\mathbf{x}, \tau) = \delta_h(\mathbf{q}) + \delta(\mathbf{x}, \tau) + \delta_h(\mathbf{q})\delta(\mathbf{x}, \tau). \quad (4.21)$$

In Eq. (4.21),  $\delta(\mathbf{x}, \tau)$  represents the fully evolved non-linear matter field at late time  $\tau$ . Using Eqs. (4.15), (4.17), (4.19), and (4.21) the second order halo field in Eulerian space is written as

$$\delta_h^{(2)}(\mathbf{x}, \tau) = \left(1 + b_1^L(\tau)\right)\delta^{(2)}(\mathbf{x}, \tau) + \left(\frac{1}{2}b_2^L(\tau) + \frac{4}{21}b_1^L(\tau)\right)\delta^2(\mathbf{x}, \tau) - \frac{2}{7}b_1^L s^2(\mathbf{x}, \tau) \quad (4.22)$$

In deriving the above expression, we use the relation

$$\delta^{(2)}(\mathbf{x}, \tau) = \frac{17}{21}\delta^2(\mathbf{x}, \tau) - H^{(2)}(\mathbf{x}, \tau) + \frac{2}{7}s^2(\mathbf{x}, \tau). \quad (4.23)$$

The third order solution contains many terms, and it is not convenient to write the full expression here. Instead we compare the final expression with our Eulerian cubic basis defined in Eq. (4.9). The full expression of the cubic halo density field can then be obtained by multiplying the basis with the coefficient vector

$$\left\{1, \frac{4}{21}, -\frac{2}{7}, 0, -\frac{22}{63}, 0, \frac{23}{42}\right\} b_1^L + \left\{0, \frac{1}{2}, 0, -\frac{1}{2}, 0, -\frac{2}{7}, 0\right\} b_2^L + \left\{0, 0, 0, \frac{1}{6}, 0, 0, 0\right\} b_3^L, \quad (4.24)$$

which gives

$$\begin{aligned} \delta_h^{(3)}(\mathbf{x}, \tau) = & (1 + b_1^L(\tau))\delta^{(3)}(\mathbf{x}, \tau) + \left(\frac{b_3^L(\tau)}{6} - \frac{b_2^L(\tau)}{2}\right)\delta^3(\mathbf{x}, \tau) - \frac{22}{63}b_1^L(\tau)\mathcal{G}_3(\mathbf{x}, \tau) \\ & - \frac{2}{7}b_2^L(\tau)\delta\mathcal{G}_2(\mathbf{x}, \tau) + \frac{23}{42}b_1^L(\tau)\Gamma_3(\mathbf{x}, \tau) + \left(\frac{8}{21}b_1^L(\tau) + b_2^L(\tau)\right)\delta\delta^{(2)}(\mathbf{x}, \tau) \\ & - \frac{4}{7}b_1^L s^{(3)}(\mathbf{x}, \tau). \end{aligned} \quad (4.25)$$

This time evolution of quadratic and cubic bias parameters in the Lagrangian framework has already been previously discussed in [144, 66]. If we carry out the same calculations assuming a non-zero tidal field in the initial Lagrangian bias model we get the following second and third order solutions:

$$\tilde{\delta}_h^{(2)}(\mathbf{x}, \tau) = \left(1 + b_1^L(\tau)\right)\delta^{(2)}(\mathbf{x}, \tau) + \left(\frac{1}{2}b_2^L(\tau) + \frac{4}{21}b_1^L(\tau)\right)\delta^2(\mathbf{x}, \tau) - \left(\frac{2}{7}b_1^L(\tau) - b_{s^2}^L(\tau)\right)s^2(\mathbf{x}, \tau) \quad (4.26)$$



and

$$\begin{aligned}
\tilde{\delta}_h^{(3)}(\mathbf{x}, \tau) &= (1 + b_1^L(\tau)) \delta^{(3)}(\mathbf{x}, \tau) + \left( \frac{b_3^L(\tau)}{6} - \frac{b_2^L(\tau)}{2} - \frac{2}{3} b_{s^2}^L(\tau) \right) \delta^3(\mathbf{x}, \tau) \\
&\quad - \left( \frac{22}{63} b_1^L(\tau) - 2b_{s^2}^L(\tau) \right) \mathcal{G}_3(\mathbf{x}, \tau) - \left( \frac{2}{7} b_2^L(\tau) + \frac{8}{21} b_{s^2}^L(\tau) \right) \delta \mathcal{G}_2(\mathbf{x}, \tau) \\
&\quad + \left( \frac{23}{42} b_1^L(\tau) - \frac{5}{2} b_{s^2}^L(\tau) \right) \Gamma_3(\mathbf{x}, \tau) + \left( \frac{8}{21} b_1^L(\tau) + b_2^L(\tau) \right) \delta \delta^{(2)}(\mathbf{x}, \tau) \\
&\quad - \left( \frac{4}{7} b_1^L(\tau) - 2b_{s^2}^L(\tau) \right) s^{(3)}(\mathbf{x}, \tau).
\end{aligned} \tag{4.27}$$

The Lagrangian tidal term leaks into the cubic bias parameters, but does not change the Eulerian basis.

#### 4.2.4 Co-evolution of Dark Matter and Halos

Gravity naturally introduces non-local terms in the bias relation. To see this we do the following. Under the assumptions of no velocity bias (that is the velocity of halos traces the velocity of dark matter) and the conservation of halos, one can solve the coupled equations of motion for dark matter and dark matter halos. The continuity and Euler equations are given by

$$\begin{aligned}
\delta'_m(\mathbf{k}, \tau) + \theta_m(\mathbf{k}, \tau) &= - \int_{\mathbf{q}} \alpha(\mathbf{q}, \mathbf{k} - \mathbf{q}) \theta_m(\mathbf{q}, \tau) \delta_m(\mathbf{k} - \mathbf{q}, \tau), \\
\theta'_m(\mathbf{k}, \tau) + \mathcal{H} \theta_m(\mathbf{k}, \tau) + \frac{3}{2} \mathcal{H}^2 \Omega_m \delta_m(\mathbf{k}, \tau) &= - \int_{\mathbf{q}} \beta(\mathbf{q}, \mathbf{k} - \mathbf{q}) \theta_m(\mathbf{q}, \tau) \theta_m(\mathbf{k} - \mathbf{q}, \tau), \\
\delta'_h(\mathbf{k}, \tau) + \theta_h(\mathbf{k}, \tau) &= - \int_{\mathbf{q}} \alpha(\mathbf{q}, \mathbf{k} - \mathbf{q}) \theta_h(\mathbf{q}, \tau) \delta_h(\mathbf{k} - \mathbf{q}, \tau), \\
\theta'_h(\mathbf{k}, \tau) + \mathcal{H} \theta_h(\mathbf{k}, \tau) + \frac{3}{2} \mathcal{H}^2 \Omega_m \delta_h(\mathbf{k}, \tau) &= - \int_{\mathbf{q}} \beta(\mathbf{q}, \mathbf{k} - \mathbf{q}) \theta_h(\mathbf{q}, \tau) \theta_h(\mathbf{k} - \mathbf{q}, \tau),
\end{aligned} \tag{4.28}$$

where  $\int_{\mathbf{q}} = \int d^3\mathbf{q}/(2\pi)^3$ . If we assume that the Eulerian bias model was completely local at some initial time  $\tau_i$ , then the second and third order solutions of the coupled system of equations described above can tell us how much non-locality is induced by gravity in the late-time bias relation. For a detailed discussion/calculations of the co-evolution of dark matter and dark matter halos we refer to [51, 21, 172]. The second order solution is

$$\begin{aligned}
\delta_h^{(2)}(\mathbf{k}, \tau) &= \delta_h^{(2)}(\mathbf{k}, \tau_i) + (b_1^L(\tau) + 1) \int_{\mathbf{q}} F_2(\mathbf{q}, \mathbf{k} - \mathbf{q}) \delta_G(\mathbf{q}, \tau) \delta_G(\mathbf{k} - \mathbf{q}, \tau) \\
&\quad + \frac{4}{21} b_1^L(\tau) \int_{\mathbf{q}} \delta_G(\mathbf{q}, \tau) \delta_G(\mathbf{k} - \mathbf{q}, \tau) - \frac{2}{7} b_1^L(\tau) \int_{\mathbf{q}} S_2(\mathbf{q}, \mathbf{k} - \mathbf{q}) \delta_G(\mathbf{q}, \tau) \delta_G(\mathbf{k} - \mathbf{q}, \tau)
\end{aligned} \tag{4.29}$$

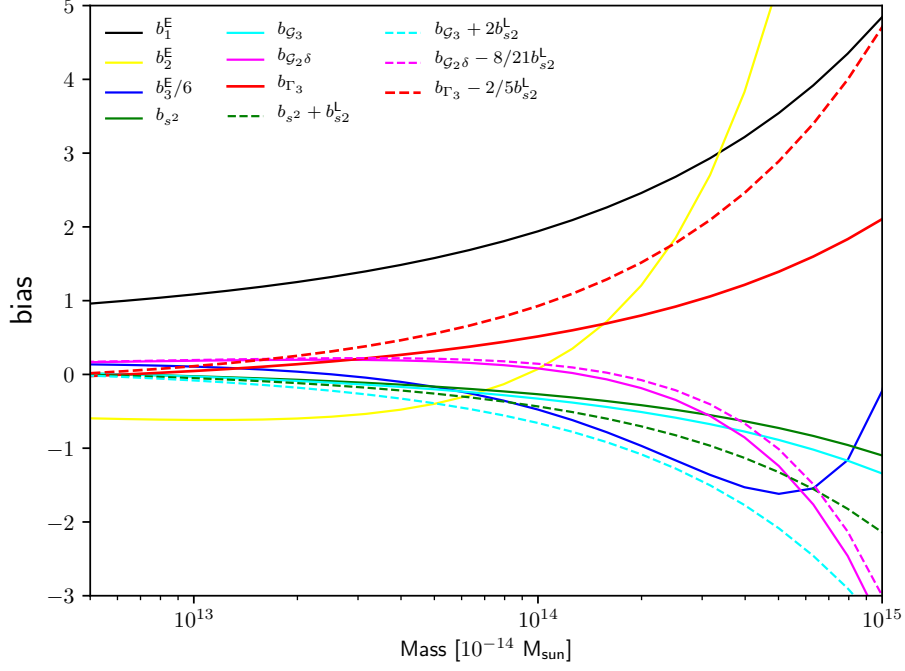


*Fig. 4.1* Theoretical predictions of bias parameters are obtained from the co-evolution of the Local Lagrangian Bias model (LLB) and the co-evolution of the Lagrangian bias model with the non-zero tidal term  $b_{s2}^L$  at second order. The mass dependence of the initial Lagrangian bias is defined in Eq. (4.62).

and the third order solution is given in [172] and previously in different notation in [51]:

$$\delta_h^{(3)}(\mathbf{k}, \tau) = \int_{\mathbf{q}_1} \int_{\mathbf{q}_2} \mathcal{K}_3(\mathbf{q}_1, \mathbf{q}_2, \mathbf{k} - \mathbf{q}_1 - \mathbf{q}_2; \tau) \delta_G(\mathbf{q}_1, \tau) \delta_G(\mathbf{q}_2, \tau) \delta_G(\mathbf{k} - \mathbf{q}_1 - \mathbf{q}_2, \tau), \quad (4.30)$$

where

$$\begin{aligned} \mathcal{K}_3 = & \frac{1}{3} b_3^L(\tau) + \frac{1}{3} G_3(\mathbf{q}_1, \mathbf{q}_2, \mathbf{k} - \mathbf{q}_1 - \mathbf{q}_2) + \left( \frac{1}{2} b_1^L(\tau) + \frac{1}{3} \right) \alpha(\mathbf{q}_1, \mathbf{q}_2 + \mathbf{q}_3) F_2(\mathbf{q}_2, \mathbf{q}_3) \\ & + \left( \frac{1}{2} b_2^L(\tau) + \frac{2}{21} b_1^L(\tau) \right) \alpha(\mathbf{q}_1, \mathbf{q}_2 + \mathbf{q}_3) + \frac{1}{14} b_1^L(\tau) \alpha(\mathbf{q}_1, \mathbf{q}_2 + \mathbf{q}_3) S_2(\mathbf{q}_2, \mathbf{q}_3) \\ & + \left( \frac{1}{2} b_1^L(\tau) + \frac{1}{3} \right) \alpha(\mathbf{q}_1, \mathbf{q}_2 + \mathbf{q}_3) G_2(\mathbf{q}_2, \mathbf{q}_3). \end{aligned} \quad (4.31)$$

Eqs. (4.30) and (4.31) agree with Eqs. (4.24) and (4.25) respectively.

## 4.2.5 Bias Predictions

Let us summarize the predictions for the coefficients of our basis Eq. (4.9). We study two cases:

### Local Lagrangian Bias Model

Under the assumption of a local Lagrangian bias model all non-local terms in the late-time bias model are generated from gravitational instability. The late-time bias parameters are then given by:

$$\begin{aligned}
b_1 &= b_1^L + 1; & b_2 &= \frac{4}{21}b_1^L + \frac{1}{2}b_2^L \\
b_{s^2} &= -\frac{2}{7}b_1^L; & b_{\delta^3} &= -\frac{1}{2}b_2^L + \frac{1}{6}b_3^L \\
b_{\mathcal{G}_3} &= -\frac{22}{63}b_1^L; & b_{\mathcal{G}_2\delta} &= -\frac{2}{7}b_2^L; \\
b_{\Gamma_3} &= \frac{23}{42}b_1^L; & b_3 &= -\frac{398}{3969}b_1^L - \frac{13}{42}b_2^L + \frac{1}{6}b_3^L.
\end{aligned} \tag{4.32}$$

### Local Lagrangian Bias Model + $b_{s^2}^L$

We extend the local Lagrangian model and include a non-local tidal term at second order. Such a term would arise in ellipsoidal collapse models [49, 147]. Propagating the additional contribution through the co-evolution calculation, we obtain the following prediction for late-time bias parameters:

$$\begin{aligned}
b_1 &= b_1^L + 1; & b_2 &= \frac{4}{21}b_1^L + \frac{1}{2}b_2^L \\
b_{s^2} &= -\frac{2}{7}b_1^L + b_{s^2}^L; & b_{\delta^3} &= -\frac{1}{2}b_2^L + \frac{1}{6}b_3^L - \frac{2}{3}b_{s^2}^L \\
b_{\mathcal{G}_3} &= -\frac{22}{63}b_1^L + 2b_{s^2}^L; & b_{\mathcal{G}_2\delta} &= -\frac{2}{7}b_2^L - \frac{8}{21}b_{s^2}^L; \\
b_{\Gamma_3} &= \frac{23}{42}b_1^L - \frac{5}{2}b_{s^2}^L; & b_3 &= -\frac{398}{3969}b_1^L - \frac{13}{42}b_2^L + \frac{1}{6}b_3^L.
\end{aligned} \tag{4.33}$$

Fig. 4.1 shows the co-evolution bias predictions with and without the Lagrangian tidal field  $b_{s^2}^L$  based on local bias parameters derived from a Sheth-Tormen (ST) mass function [191]. The initial Lagrangian tidal bias used in this plot is motivated by our observations and given in Eq. (4.62).

## 4.3 Quadratic and Cubic Fields

In this section we discuss the quadratic field method proposed in [177] and extend it to cubic fields. First, we discuss the quadratic fields and describe the PT expressions for the cross-correlation of quadratic fields with the density fields. Then, we describe our full basis of cubic fields and the cross correlation with the non-linear matter field and halo field. The cross-

spectra with cubic fields contain diagrams that are highly UV-sensitive. To remove these diagrams from our model, we describe a procedure that we denote *orthogonalization*. Finally, we discuss why including the counter terms is essential for making the bias measurements insensitive to our ignorance of the halo smoothing scale  $R_h$ .

### 4.3.1 Quadratic Fields

As proposed in [177] we consider three quadratic fields: the density-squared  $\delta^2(\mathbf{x})$ , the shift  $\Psi(\mathbf{x}) \cdot \nabla \delta(\mathbf{x})$ , and the square of the tidal tensor  $s^2(\mathbf{x})$ . In Fourier space, these fields are defined as

$$\mathcal{D}_2[\delta](\mathbf{k}) = \int_{\mathbf{q}} \delta_G(\mathbf{q}) \delta_G(\mathbf{k} - \mathbf{q}) \mathcal{K}_{D_2}(\mathbf{q}, \mathbf{k} - \mathbf{q}) W_{R_f}(\mathbf{q}) W_{R_f}(\mathbf{k} - \mathbf{q}), \quad (4.34)$$

where  $\mathcal{D}_2[\delta] \in \{\delta^2, -\Psi \cdot \nabla \delta, s^2\}$  and  $\mathcal{K}_{D_2} \in \{1, H_2, S_2\}$  with  $H_2$  and  $S_2$  defined as

$$H_2(\mathbf{q}_1, \mathbf{q}_2) = -\frac{1}{2}(\mathbf{q}_1 \cdot \mathbf{q}_2) \left( \frac{q_1}{q_2} + \frac{q_2}{q_1} \right) \quad \text{and} \quad S_2(\mathbf{q}_1, \mathbf{q}_2) = \frac{(\mathbf{q}_1 \cdot \mathbf{q}_2)^2}{q_1^2 q_2^2} - \frac{1}{3}. \quad (4.35)$$

The density squared and  $s^2$  correspond to the bias parameters  $b_2$  and  $b_{s^2}$  respectively. Due to the equivalence principle, there is no separate bias parameter corresponding to the shift term.

Due to the convolution integrals, Eq. (4.34) receives contributions from all modes. To restrict to large scale modes, we implement a cut-off by smoothing the density field:  $\delta_G(\mathbf{k}) \rightarrow W_{R_f}(\mathbf{k}) \delta_G(\mathbf{k})$ . For definiteness, we choose a Gaussian filter  $W_{R_f}(k) = \exp(-k^2 R_f^2/2)$  with a fiducial  $R_f = 20h^{-1}$  Mpc, corresponding to a  $k_{\max} \approx 1/R_f$  cutoff. This cutoff  $k_{\max} \approx 0.05h$  Mpc $^{-1}$  is the maximum wavenumber contributing to the quadratic and cubic field integrals. This choice of smoothing can be motivated from the fact that one-loop PT is typically valid for wavenumbers  $k < 0.1h$  Mpc $^{-1}$  [16]. The cross-correlation of the smoothed quadratic fields with the halo density  $\delta_h$  can be expanded as

$$\langle \mathcal{D}_2[\delta](\mathbf{k}) | \delta_h(\mathbf{k}') \rangle = b_1 \langle \mathcal{D}_2[\delta](\mathbf{k}) | \delta^{(2)}(\mathbf{k}') \rangle + \frac{b_2}{2} \langle \mathcal{D}_2[\delta](\mathbf{k}) | \delta^2(\mathbf{k}') \rangle + b_{s^2} \langle \mathcal{D}_2[\delta](\mathbf{k}) | s^2(\mathbf{k}') \rangle. \quad (4.36)$$

In the above equation, each term can be expressed as a one-loop PT integral as<sup>3</sup>

$$\begin{aligned} \langle \mathcal{D}_2[\delta](\mathbf{k}) | \mathcal{O}_2(\mathbf{k}') \rangle' &= 2 \int_{\mathbf{q}} W_{R_f}(\mathbf{q}) W_{R_f}(\mathbf{k} - \mathbf{q}) W_{R_h}(\mathbf{q}) W_{R_h}(\mathbf{k} - \mathbf{q}) P_{\text{lin}}(q) P_{\text{lin}}(|\mathbf{k} - \mathbf{q}|) \\ &\quad \times \mathcal{K}_{D_2}(\mathbf{q}, \mathbf{k} - \mathbf{q}) \mathcal{K}_{\mathcal{O}_2}(\mathbf{q}, \mathbf{k} - \mathbf{q}), \end{aligned} \quad (4.37)$$

<sup>3</sup>The prime on the correlator signifies that the Fourier space expectation value is equal to the power spectrum, i.e.,  $\langle \delta(\mathbf{k}) \delta(\mathbf{k}') \rangle' = P(k)$  as opposed to  $\langle \delta(\mathbf{k}) \delta(\mathbf{k}') \rangle = (2\pi)^3 \delta_{\text{D}}^3(\mathbf{k} + \mathbf{k}') P(k)$ .

where  $\mathcal{O}_2(\mathbf{k})$  is defined in Eq. (4.8) and  $\mathcal{H}_{\mathcal{O}_2}(\mathbf{q}_1, \mathbf{q}_2) \in \{F_2(\mathbf{q}_1, \mathbf{q}_2), 1, S_2(\mathbf{q}_1, \mathbf{q}_2)\}$  respectively. The diagrammatic representation of (4.37) is shown in Fig. 4.2, for  $\mathcal{H}_{\mathcal{O}_2} = F_2$ .

There are two different smoothing scales in Eq. (4.37). The halo smoothing scale  $R_h$  has a physical meaning and corresponds to the size of the Lagrangian patch collapsing into the halo. However, since we don't know  $R_h$  a priori, we will have to take into account our ignorance of this fact while constraining the physical bias parameters. In general, the cut-offs are not physical and should not appear in the model. One has to add appropriate counter terms to remove the cut-off dependence. We will discuss our choice of the counter term in a later section. The external smoothing scale  $R_f$  is an analysis cutoff avoiding high- $k$  contributions to the estimator. As long as this requirement is satisfied the results will not depend on the choice of  $R_f$  since it is consistently implemented.

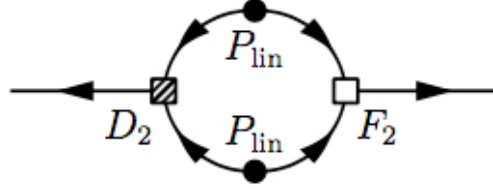


Fig. 4.2 Diagrammatic representation of  $\langle \mathcal{D}_2(\mathbf{k}) | \delta^{(2)}(\mathbf{k}') \rangle'$ .

### 4.3.2 Cubic Fields

The definition of cubic fields follows straightforwardly from the above considerations concerning quadratic fields. We define a smoothed cubic field in Fourier space as

$$\begin{aligned} \mathcal{D}_3[\delta](\mathbf{k}) = & \int_{\mathbf{q}_1} \int_{\mathbf{q}_2} \delta_G(\mathbf{q}_1) \delta_G(\mathbf{q}_2) \delta_G(\mathbf{k} - \mathbf{q}_1 - \mathbf{q}_2) W_{R_f}(\mathbf{q}_1) W_{R_f}(\mathbf{q}_2) \\ & \times W_{R_f}(\mathbf{k} - \mathbf{q}_1 - \mathbf{q}_2) \mathcal{K}_{D_3}(\mathbf{q}_1, \mathbf{q}_2, \mathbf{k} - \mathbf{q}_1 - \mathbf{q}_2) \end{aligned} \quad (4.38)$$

where  $\mathcal{K}_{D_3}$  is cubic kernels after symmetrization. In our model, there are seven cubic bias fields as described in Eq. (4.9). The unsymmetrized cubic kernels are defined as

$$\mathcal{K}_{\mathcal{G}_2\delta}(\mathbf{q}_1, \mathbf{q}_2, \mathbf{q}_3) = \left( \frac{(\mathbf{q}_1 \cdot \mathbf{q}_2)^2}{q_1^2 q_2^2} - 1 \right), \quad (4.39)$$

$$\mathcal{K}_{\mathcal{G}_3}(\mathbf{q}_1, \mathbf{q}_2, \mathbf{q}_3) = -\frac{1}{2} \left[ \frac{(\mathbf{q}_1 \cdot \mathbf{q}_2)(\mathbf{q}_1 \cdot \mathbf{q}_3)(\mathbf{q}_2 \cdot \mathbf{q}_3)}{q_1^2 q_2^2 q_3^2} - \frac{(\mathbf{q}_1 \cdot \mathbf{q}_2)^2}{q_1^2 q_2^2} - \frac{(\mathbf{q}_1 \cdot \mathbf{q}_3)^2}{q_1^2 q_3^2} - \frac{(\mathbf{q}_2 \cdot \mathbf{q}_3)^2}{q_2^2 q_3^2} \right], \quad (4.40)$$

$$\mathcal{K}_{\Gamma_3}(\mathbf{q}_1, \mathbf{q}_2, \mathbf{q}_3) = 2 \left( \frac{(\mathbf{q}_1 \cdot (\mathbf{q}_2 + \mathbf{q}_3))^2}{q_1^2 (\mathbf{q}_2 + \mathbf{q}_3)^2} - 1 \right) \left( F_2(\mathbf{q}_2, \mathbf{q}_3) - G_2(\mathbf{q}_2, \mathbf{q}_3) \right), \quad (4.41)$$

$$\mathcal{K}_{s^{(3)}}(\mathbf{q}_1, \mathbf{q}_2, \mathbf{q}_3) = 2S_2(\mathbf{q}_1, \mathbf{q}_2 + \mathbf{q}_3)F_2(\mathbf{q}_2, \mathbf{q}_3), \quad (4.42)$$

$$\mathcal{K}_{\delta^{(1)}\delta^{(2)}}(\mathbf{q}_1, \mathbf{q}_2, \mathbf{q}_3) = 2F_2(\mathbf{q}_2, \mathbf{q}_3), \quad (4.43)$$

$$\mathcal{K}_{\delta^{(3)}}(\mathbf{q}_1, \mathbf{q}_2, \mathbf{q}_3) = F_3(\mathbf{q}_1, \mathbf{q}_2, \mathbf{q}_3). \quad (4.44)$$

We cross correlate these cubic fields with the halo density field. The cubic fields are of order  $\mathcal{O}(\delta^3)$  and they correlate only with the linear and cubic operators in  $\delta_{\text{h}}$ . The cross-correlation of the cubic fields with the quadratic fields are five-point functions which vanish in an infinite volume universe and hence do not contribute to the signal. However, for finite ensembles, these five-point functions do contribute to the noise. In order to make more precise measurements, we remove them to reduce the noise.

We provide a step by step explanation as things get more elaborate at cubic level. First, we describe the cubic correlations with the non-linear density field  $\delta_{\text{NL}}$  up to order  $\mathcal{O}(\delta^6)$ :

$$\langle \mathcal{D}_3[\delta](\mathbf{k}) | \delta_{\text{NL}}(\mathbf{k}') \rangle' = \langle \mathcal{D}_3[\delta](\mathbf{k}) | \delta^{(1)}(\mathbf{k}') \rangle' + \langle \mathcal{D}_3[\delta](\mathbf{k}) | \delta^{(3)}(\mathbf{k}') \rangle'. \quad (4.45)$$

The first term is the one-loop term and the second is the two-loop term. The two-loop term consists of an irreducible part and a reducible part, where the latter can be written as the product of two one-loop diagrams. The diagrammatic representation of these terms is shown in Fig. 4.3 and the PT expressions are given as follows:

$$\text{One-Loop} \Rightarrow 3W_{\text{Rf}}(\mathbf{k})P_{\text{lin}}(k) \int_{\mathbf{q}} P_{\text{lin}}(q) \mathcal{K}_{D_3}(\mathbf{k}, \mathbf{q}, -\mathbf{q}) W_{\text{Rf}}(\mathbf{q})^2 \quad (4.46)$$

$$\begin{aligned} \text{Two-Loop Reducible} \Rightarrow 9W_{\text{Rf}}(\mathbf{k})P_{\text{lin}}(k) \int_{\mathbf{q}_1} P_{\text{lin}}(q_1) W_{\text{Rf}}(\mathbf{q}_1) \mathcal{K}_{D_3}(\mathbf{k}, \mathbf{q}_1, -\mathbf{q}_1) \times \\ \int_{\mathbf{q}_2} P_{\text{lin}}(q_2) W_{\text{Rf}}(\mathbf{q}_2) F_3(\mathbf{k}, \mathbf{q}_2, -\mathbf{q}_2) \end{aligned} \quad (4.47)$$

$$\begin{aligned} \text{Two-Loop Irreducible} \Rightarrow 6 \int_{\mathbf{q}_1} \int_{\mathbf{q}_2} P_{\text{lin}}(|\mathbf{k} - \mathbf{q}_1 - \mathbf{q}_2|) P_{\text{lin}}(q_1) P_{\text{lin}}(q_2) W_{\text{Rf}}(\mathbf{q}_1) W_{\text{Rf}}(\mathbf{q}_2) \\ \times W_{\text{Rf}}(\mathbf{k} - \mathbf{q}_1 - \mathbf{q}_2) \mathcal{K}_{D_3}(\mathbf{k} - \mathbf{q}_1 - \mathbf{q}_2, \mathbf{q}_1, \mathbf{q}_2) F_3(\mathbf{k} - \mathbf{q}_1 - \mathbf{q}_2, \mathbf{q}_1, \mathbf{q}_2) \end{aligned} \quad (4.48)$$

Basically, the PT expressions and diagrams are similar in all cubic correlations up to order  $\mathcal{O}(\delta^6)$ . We can write the cubic correlations with the halo density field as

$$\begin{aligned} \langle \mathcal{D}_3[\delta](\mathbf{k}) | \delta_{\text{h}}(\mathbf{k}') \rangle' = b_1 \langle \mathcal{D}_3[\delta](\mathbf{k}) | \delta^{(1)}(\mathbf{k}') \rangle' + b_1 \langle \mathcal{D}_3[\delta](\mathbf{k}) | \delta^{(3)}(\mathbf{k}') \rangle' + \frac{b_3}{3!} \langle \mathcal{D}_3[\delta](\mathbf{k}) | \delta^3(\mathbf{k}') \rangle' \\ + b_{\mathcal{G}_2\delta} \langle \mathcal{D}_3[\delta](\mathbf{k}) | \mathcal{G}_2\delta(\mathbf{k}') \rangle' + b_{\mathcal{G}_3} \langle \mathcal{D}_3[\delta](\mathbf{k}) | \mathcal{G}_3(\mathbf{k}') \rangle' + b_{\Gamma_3} \langle \mathcal{D}_3[\delta](\mathbf{k}) | \Gamma_3(\mathbf{k}') \rangle' \\ + b_2 \langle \mathcal{D}_3[\delta](\mathbf{k}) | \delta\delta^{(2)}(\mathbf{k}') \rangle' + 2b_{s^2} \langle \mathcal{D}_3[\delta](\mathbf{k}) | s^{(3)}(\mathbf{k}') \rangle' + \dots \end{aligned} \quad (4.49)$$

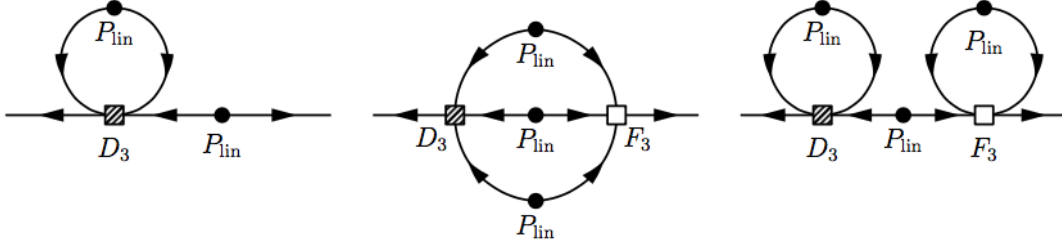


*Fig. 4.3* Perturbative expressions for one-loop, and two-loop irreducible and two-loop reducible terms of  $\langle \mathcal{D}_3(\mathbf{k}) | \delta_{\text{NL}}(\mathbf{k}') \rangle$  are shown in diagrammatic form. The propagators are represented by linear power spectra  $P_{\text{lin}}$ , the cubic field kernel  $\mathcal{D}_3$  is represented by the hatched square. Finally, empty squares correspond to the gravitational kernel  $F_3$ . Loops correspond to integrals over all wavenumbers  $\mathbf{q}$  or  $\mathbf{p}$  and arrows represent the flow of momentum.

The first two terms are the same as Eqs. (4.46), (4.47), and (4.48), except here they are multiplied by the linear bias  $b_1$ . The other terms in Eq. (4.49) are two-loop terms which again consist of a reducible and an irreducible diagram. The PT expressions are the same as Eqs. (4.47) and (4.48) except the  $F_3$  kernel is replaced by the cubic kernels from  $\mathcal{O}_3$  in Eq. (4.9) and we have to add extra smoothing functions corresponding to the intrinsic halo smoothing scale  $R_h$ . The diagrams are shown in Fig. 4.4.

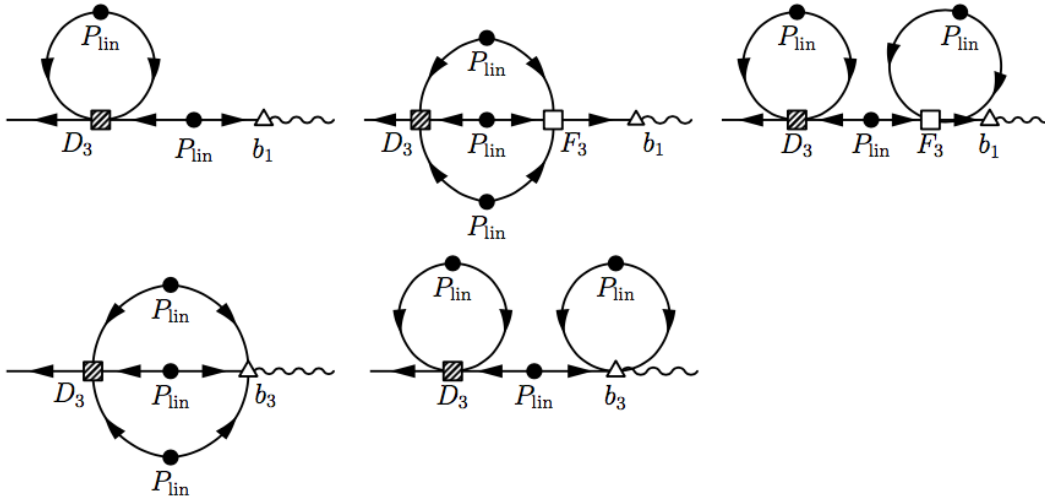


*Fig. 4.4* Diagrams contributing to the correlation of cubic fields with the halo field in Eq. (4.49). The triangles represent the linear, quadratic and cubic bias kernels. The straight lines are used to describe the density field, whereas halo fields are described by wiggly lines. The Feynman rules are discussed in detail in [18].

### 4.3.3 Bispectrum and Trispectrum Estimators

The cross-spectra between quadratic fields and the halo field are nothing but the integrated bispectra:

$$\langle \mathcal{D}_2[\delta](\mathbf{k}) | \delta_h(\mathbf{k}') \rangle' = \int_{\mathbf{q}} \mathcal{K}_{D_2}(\mathbf{q}, \mathbf{k} - \mathbf{q}) B_{\text{hmm}}(\mathbf{k}', \mathbf{q}, \mathbf{k} - \mathbf{q}) W_{R_f}(\mathbf{q}) W_{R_f}(\mathbf{k} - \mathbf{q}), \quad (4.50)$$

where all of the matter fields in the bispectrum are Gaussian fields. Similarly, the cross power spectra between a cubic field and the halo field can be written as integrated trispectra

$$\begin{aligned} \langle \mathcal{D}_3[\delta](\mathbf{k}) | \delta_h(\mathbf{k}') \rangle' &= \int_{\mathbf{q}} \int_{\mathbf{p}} \mathcal{K}_{D_3}(\mathbf{k} - \mathbf{q} - \mathbf{p}, \mathbf{q}, \mathbf{p}) T_{\text{hmmm}}(\mathbf{k}', \mathbf{p}, \mathbf{k} - \mathbf{q} - \mathbf{p}, \mathbf{q}) \\ &\quad \times W_{R_f}(\mathbf{q}) W_{R_f}(\mathbf{p}) W_{R_f}(\mathbf{k} - \mathbf{q} - \mathbf{p}). \end{aligned} \quad (4.51)$$

The estimators defined in Eqs. (4.50) and (4.51) contain bispectrum and trispectrum information (see [177]). We will use these estimators to constrain quadratic and cubic bias parameters. Note that the matter fields are the Gaussian fields. An alternative way to estimate cubic bias parameters is to calculate the bispectrum of the Gaussian field, a squared field operator and the orthogonalized halo field  $\langle \delta_G \mathcal{D}_2 \delta_h \rangle$ . This measurement probes the trispectrum in terms of a one-loop bispectrum rather than a two-loop power spectrum. This measurement retains additional external configuration dependence, but a detailed exploration of the performance of this estimator exceeds the scope of this paper.

### 4.3.4 Removing the UV Sensitive Diagrams

The reducible diagrams introduced above contain a loop with two counteraligned momenta entering into a cubic kernel. These diagrams are highly cutoff or smoothing dependent. For instance, if we consider  $\mathcal{O}_3 = \delta^3$ , the integral yields the variance of the field smoothed on scale  $R_h$ . As we describe in more detail in Appendix A.2, a change of halo smoothing from  $R_h = 4h^{-1} \text{Mpc}$  to  $R_h = 6h^{-1} \text{Mpc}$  can lead to a order unity relative change in the amplitude of these contributions. Such a massive change in the template would lead to an equally significant change in the prefactors and thus bias the constraint on the bias parameters. In contrast the amplitude of the irreducible diagrams changes by a much smaller magnitude on the order of a few percent. We thus consider it important to remove the highly UV-sensitive contributions from our bias estimator. Fortunately, the reducible diagrams can be identified with the part of the halo field that correlates with the linear field. The remaining parts of  $\delta_{\text{NL}}$  and  $\delta_h$  orthogonal to the linear field are defined as

$$\tilde{\delta}_A(\mathbf{k}) = \delta_A(\mathbf{k}) - \frac{\langle \delta_G | \delta_A \rangle}{\langle \delta_G | \delta_G \rangle} \delta_G(\mathbf{k}), \quad (4.52)$$



where  $A \in \{\text{NL}, \text{h}\}$ . These residual contributions only contribute to the irreducible diagrams. The above definition can be extended to arbitrary operators  $\mathcal{O}$ . The cross-correlation of cubic operators with the orthogonal part of the halo field now only depends on the two-loop irreducible diagram. The irreducible diagram also depends on the smoothing scale; however, this dependence is less severe and if necessary can be taken into account by adding a counter term  $dR$  as discussed in the next subsection. The final expression for the cross-correlation of the cubic fields with the projected halo density field that we use to constrain cubic bias is given by

$$\langle \mathcal{D}_3[\delta](\mathbf{k}) | \tilde{\delta}_h(\mathbf{k}') \rangle' = \sum_{j=1}^{j=7} b_j \langle \mathcal{D}_3[\delta](\mathbf{k}) | \tilde{\mathcal{O}}_{3,j}(\mathbf{k}') \rangle'. \quad (4.53)$$

We diagrammatically describe the correlations of cubic fields with the orthogonalized fields in Fig. 4.5.

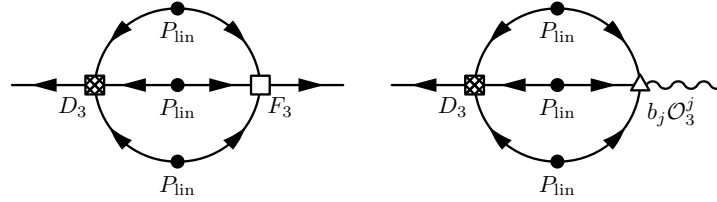


Fig. 4.5 Cross-correlations of cubic fields with the orthogonalized fields contain only the two-loop irreducible diagram. The figure shows PT diagrams for  $\langle D_3 | \tilde{F}_3 \rangle$  (left) and  $\langle D_3 | \tilde{\mathcal{O}}_3^j \rangle$  (right).

### 4.3.5 Counter Term: Taylor Expansion Around $R_h$

The models for the cross-correlations of quadratic and cubic fields with the halo fields in Eqs. (4.36) and (4.53) have some residual dependence on the halo smoothing scale  $R_h$ . For the cubic fields this is still the case after orthogonalization, but the dependence is less severe for the orthogonalized fields. In principle this cutoff or smoothing dependence would call for the inclusion of EFT inspired counterterms. The dependence of quadratic and cubic correlations on the halo smoothing scale  $R_h$  is explained in more detail in Appendix. A.2, where we explicitly quantify this effect and discuss the possibility of including EFT counter terms to remove this effect. In particular, we show that despite removing reducible diagrams and the fiducial scale being much larger than the halo scale, there are residual dependencies of the correlators on the halo smoothing scale at the several percent level.

However, the large number of necessary counterterms arising at the field level required to absorb the dependency of the results on the unknown halo smoothing scale  $R_h$  motivates a more pragmatic approach. In particular, we are considering a Taylor expansion in the

dependence on  $R_h$  around the fiducial value  $R_h = 4h^{-1}$  Mpc. The Taylor expansions of the quadratic and cubic correlations are thus given by

$$\langle \mathcal{D}_{2,i} | \mathcal{O}_{2,j} \rangle = \langle \mathcal{D}_{2,i} | \mathcal{O}_{2,j} \rangle \Big|_{R_h=4} + \frac{dR}{2} \left( \langle \mathcal{D}_{2,i} | \mathcal{O}_{2,j} \rangle \Big|_{R_h=4} - \langle \mathcal{D}_{2,i} | \mathcal{O}_{2,j} \rangle \Big|_{R_h=6} \right) \quad (4.54)$$

and

$$\langle \mathcal{D}_{3,i} | \tilde{\mathcal{O}}_{3,j} \rangle = \langle \mathcal{D}_{3,i} | \tilde{\mathcal{O}}_{3,j} \rangle \Big|_{R_h=4} + \frac{dR}{2} \left( \langle \mathcal{D}_{3,i} | \tilde{\mathcal{O}}_{3,j} \rangle \Big|_{R_h=4} - \langle \mathcal{D}_{3,i} | \tilde{\mathcal{O}}_{3,j} \rangle \Big|_{R_h=6} \right) \quad (4.55)$$

respectively. The l.h.s. of Eqs. (4.54) and (4.55) are now functions of  $dR$ . This dependency quantifies the effect of the deviation of the halo smoothing scale from its fiducial value  $R_h = 4h^{-1}$  Mpc. In the subsequent analysis, we will constrain this parameter  $dR$  along with other bias parameters.

## 4.4 Methodology

### 4.4.1 Numerical Simulations

We use a suite of 15 realisations of a cosmological  $N$ -body simulation. The initial conditions are generated with the second order Lagrangian Perturbation Theory (**2-LPT**) code [182] at the initial redshift  $z_i = 99$  and are subsequently evolved using **Gadget-2** [196]. The simulations are performed with  $N_p = 1024^3$  dark matter particles in a cubic box of length  $L = 1500h^{-1}$  Mpc with periodic boundary conditions. We assume a flat  $\Lambda$ CDM cosmology with the cosmological parameters  $\Omega_m = 0.272$ ,  $\Omega_\Lambda = 0.728$ ,  $h = 0.704$ ,  $n_s = 0.967$ .

Dark matter halos in the final  $z = 0$  density field are identified using the Friends-of-Friends (FoF) algorithm with linking length  $l = 0.2$  times the mean inter particle distance. We also trace back the halo particles to the initial conditions to define the protohalos as progenitors of gravitational collapse. We will be using these protohalos to study the evolution of bias from Lagrangian to Eulerian space. The halos are binned in mass, with each bin spanning a factor of three in mass. The mass and number density of the five halo mass bins are given in Table 5.2. Particles and halos are assigned to a regular grid using the Cloud-in-Cell (CIC) scheme. We Fourier transform the matter and halo density fields using the publicly available **FFTW** library<sup>4</sup>.

<sup>4</sup><http://www.fftw.org>

From the initial conditions we also extract the underlying Gaussian density field from which we generate the quadratic and cubic field using a sequence of multiplications with powers of the wavenumber in Fourier space, Fourier transforms and multiplications of fields in configuration space.

Mass Bin	Halo Mass [ $10^{13}h^{-1}M_{\odot}$ ]	Number Density [ $10^{-6}h^3 \text{ Mpc}^{-3}$ ]
I	0.773	627
II	2.33	216
III	6.93	66.5
IV	20.1	16.5
V	56.8	2.48

*Table 4.2* Halo mass bins employed in this study. We quote the mean mass of the sample and the number density of halos.

#### 4.4.2 Parameter Estimation

As described before, the natural statistic for estimating  $b_1$  is the tree-level halo-matter power spectrum. To estimate  $b_1$  we minimize  $\chi_{\text{lin}}^2$  defined below

$$\chi_{\text{lin}}^2 = \sum_{k_i}^{k_{\text{max}}} \left( \frac{\hat{P}_{\text{hm}}(k_i)/\hat{P}_{\text{mm}}(k_i) - b_1}{\sigma(\hat{P}_{\text{hm}}(k_i)/\hat{P}_{\text{mm}}(k_i))} \right)^2. \quad (4.56)$$

Taking the ratio of two power spectra obtained from the same initial conditions cancels out the random fluctuations, resulting in the reduction of cosmic variance and improved constraints on  $b_1$ . The maximum wavenumber is chosen to be  $k_{\text{max}} = 0.026h \text{ Mpc}^{-1}$  to ensure that we are in the regime where linear theory and scale independent bias are applicable.

To estimate the quadratic and cubic bias parameters we cross correlate three quadratic fields defined in Eq. (4.34) and a basis of cubic bias operators (4.38) with the orthogonalized halo density field. To do cosmic variance cancellation, we obtain the cross-spectra terms in Eq. (4.36) and Eq. (4.53) from N-body simulations, rather than using the PT result. The motivation is again cosmic variance cancellation. At the field level  $|P_{\text{sim}} - P_{\text{model}}|$  can be written as

$$\langle \mathcal{D}_{2,i} | \Delta \delta_{\text{h}}^{\text{quad}} \rangle = \sum_{j=1}^{j=3} \left\langle \mathcal{D}_{2,i} \left( \delta_{\text{h}} - b_1 \delta_{\text{G}} - b_j \mathcal{O}_{2,j} \right) \right\rangle \quad (4.57)$$

and

$$\langle \mathcal{P}_{3,i} | \Delta \tilde{\delta}_h^{\text{cubic}} \rangle = \sum_{j=1}^{j=7} \left\langle \mathcal{P}_{3,i} \left| \left( \tilde{\delta}_h - b_j \tilde{\mathcal{O}}_{3,j} - b_1 \tilde{\delta}^{(2)} - b_2 \tilde{\delta}^2 - b_{s^2} \tilde{s}^2 \right) \right. \right\rangle \quad (4.58)$$

for quadratic and cubic statistics respectively<sup>5</sup>. The tilde stands for orthogonalized fields. Note that in Eq. (4.36) and Eq. (4.53) we omitted odd-correlators, that is the cross-correlations of the quadratic fields with the linear density field or cubic fields with the quadratic fields. These cross-spectra are zero in an infinite volume limit. However, in a finite simulation volume these correlations contribute to the covariance matrix. In fact, the odd cross-correlations are the leading source of noise, which can be reduced by removing these contributions at the field level in Eq. (4.57) and Eq. (4.58).

We define the  $\chi^2$  for the quadratic and cubic statistics as

$$\chi_{\text{quad}}^2 = \sum_{k_j=k_{\min}}^{k_{\max}} \sum_{i=1}^{i=3} \left( \frac{\langle \mathcal{P}_{2,i}(\mathbf{k}_j) | \Delta \delta_h^{\text{quad}}(\mathbf{k}'_j) \rangle'}{\sigma(\langle \mathcal{P}_{2,i}(\mathbf{k}_j) | \Delta \delta_h^{\text{quad}}(\mathbf{k}'_j) \rangle')} \right)^2 \quad (4.59)$$

and

$$\chi_{\text{cubic}}^2 = \sum_{k_j=k_{\min}}^{k_{\max}} \sum_{i=1}^{i=7} \left( \frac{\langle \mathcal{P}_{3,i}(\mathbf{k}_j) | \Delta \tilde{\delta}_h^{\text{cubic}}(\mathbf{k}'_j) \rangle'}{\sigma(\langle \mathcal{P}_{3,i}(\mathbf{k}_j) | \Delta \tilde{\delta}_h^{\text{cubic}}(\mathbf{k}'_j) \rangle')} \right)^2. \quad (4.60)$$

The maximum wavenumber we use in our analysis is  $k_{\max} = 0.056h \text{ Mpc}^{-1}$ . In Eq. (4.59) and Eq. (4.60) we sum over quadratic and cubic fields. After defining the chi-squared for the linear, quadratic and cubic statistics we run the MCMC chains to get the best-fit bias parameters that minimize the joint chi-squared (or joint likelihood function), which is defined as

$$\chi^2 = \chi_{\text{lin}}^2 + \chi_{\text{quad}}^2 + \chi_{\text{cubic}}^2. \quad (4.61)$$

## 4.5 Results

### 4.5.1 Some Preliminary Checks

Before discussing our main results, we describe some preliminary checks as follows:

- Measuring bias parameters from large-scale, tree-level bispectrum and trispectrum is the cleanest way to avoid the degeneracies of the bias parameters. Therefore, we want to choose the maximum wavenumber  $k_{\max}$  in our analysis such that we are in

<sup>5</sup>Here  $\mathcal{P}_2$  and  $\mathcal{P}_3$  describe the quadratic and cubic fields smoothed with  $R_f = 20h^{-1} \text{ Mpc}$ . On the other hand,  $\mathcal{O}_2$  and  $\mathcal{O}_3$  describe the quadratic and cubic basis operators smoothed with a halo smoothing scale  $R_h$

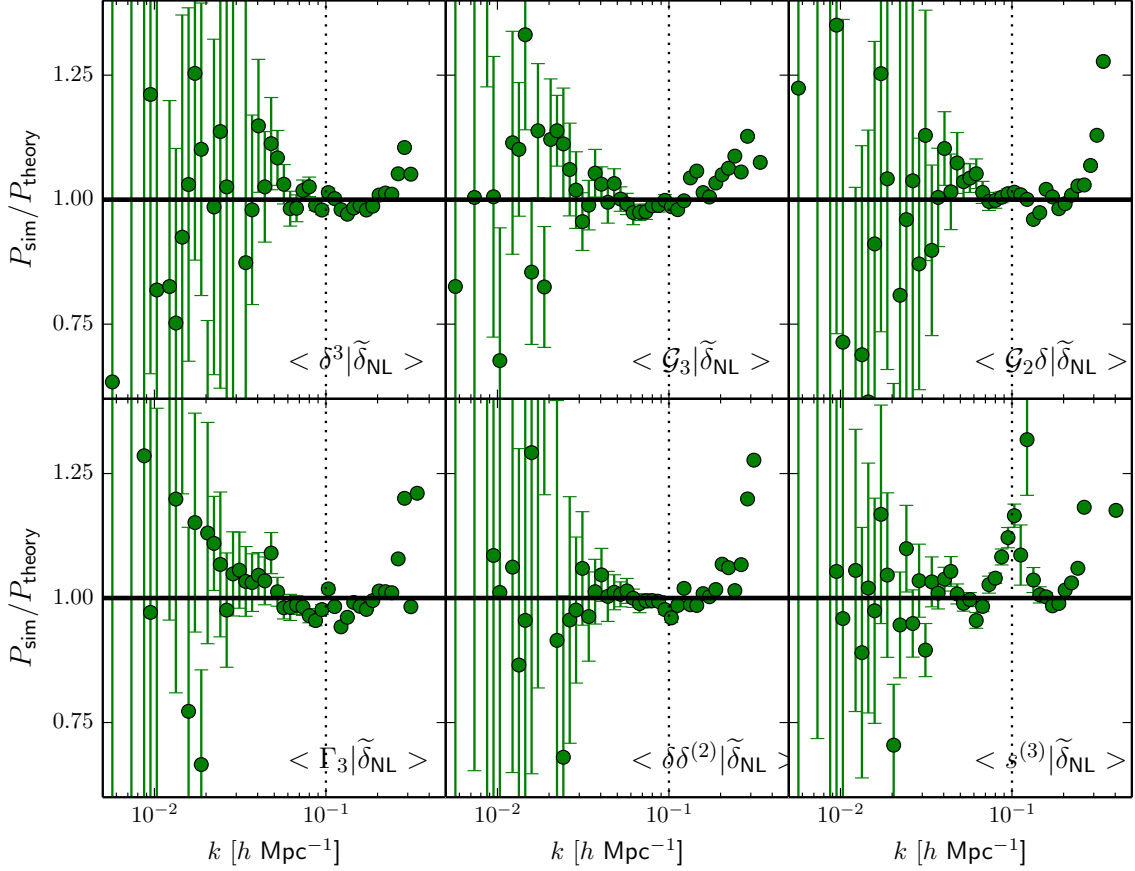


*Fig. 4.6* Ratio of the cross-correlations of cubic fields with the orthogonalized non-linear matter field as measured in simulations and predicted in perturbation theory. The cubic fields are smoothed with  $R_f = 20h^{-1}$  Mpc. As discussed in the text, these cross correlations are described by the two-loop irreducible diagram in PT. The vertical dotted line is drawn at  $k = 0.1h \text{ Mpc}^{-1}$  to separate the region of validity of the PT. For  $k > 0.1h \text{ Mpc}^{-1}$  PT results can not be trusted. To ensure convergence of PT, we have chosen the maximum wavenumber  $k_{\text{max}} = 0.057h \text{ Mpc}^{-1}$  for parameter estimation.

the regime where PT is valid. To get an idea of the regime of validity of the tree-level trispectrum, we show in Fig. 4.6 the ratio of the cross-correlations of cubic fields with the non-linear matter field as measured in simulations and predicted by perturbation theory. We see that the data points start deviating from theory around wavenumber  $k = 0.1h\text{Mpc}^{-1}$ , which means that as we go to higher  $k$ -modes, loop corrections in the  $T_{\text{hmmm}}$  trispectrum become important. We therefore make the conservative choice of  $k_{\text{max}} = 0.057h \text{ Mpc}^{-1}$  to ensure that we remain in the perturbative regime.

- To check that the orthogonalized cross-spectra of cubic fields obtained from simulations agree with a numerical evaluation of the perturbation theory integrals in Eq. (4.48), we plot the irreducible parts of cubic cross-correlations in the seven by

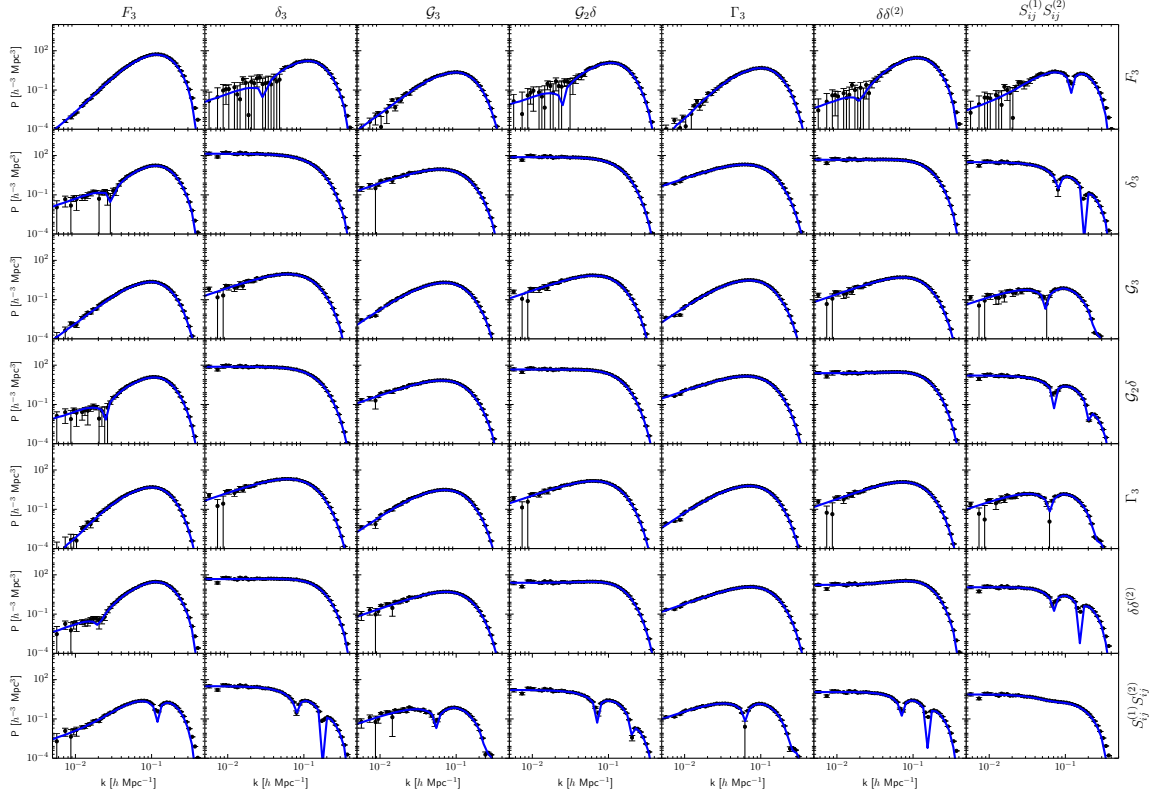


*Fig. 4.7* Irreducible parts of the cross-spectra of cubic fields. The solid lines are the numerical evaluation of the perturbation theory loop integrals in Eq. (4.48), while the dots with errorbars show simulation data. The cubic fields from left to right are smoothed with  $R_h = 4h^{-1}$  Mpc, while fields from top to bottom are smoothed with the fiducial halo smoothing scale  $R_f = 20h^{-1}$  Mpc.

seven matrix plot in Fig. 4.7. The solid lines are predictions of perturbation theory, whereas the data points with errorbars show simulation results. We see an excellent agreement between the simulations and the numerical two-loop integrals.

## 4.5.2 Bias Constraints

We are now ready to discuss our main results. We measured the bias parameters in Lagrangian and Eulerian space and compare our results with the co-evolution predictions described in Eq. (4.32) and Eq. (4.33). We then discuss Eulerian and Lagrangian models with different number of parameters.

### 4.5.3 Lagrangian Bias from Protohalos

We obtained the protohalo density field in Lagrangian space by tracing back the constituent particles and assigning the Lagrangian center of mass to the grid. In Lagrangian space all the operators involving non-linear gravitational kernels vanish and thus we discard  $\delta^{(2)}$ ,  $\delta\delta^{(2)}$  and  $s^{(1)}s^{(2)}$  as shown in Eq. (4.12). However, we still cross-correlate the full basis of three quadratic and seven cubic operators with the protohalo density field in Lagrangian space and measure all bias parameters up to cubic order. The resulting bias measurements are shown in Fig. 4.8. We have detected a clear evidence of the presence of non-local Lagrangian tidal bias, the mass dependence of which is well captured by the fitting function

$$b_{s^2}^L(M) = -\frac{1}{2} \left( \frac{M}{4 \times 10^{14} h^{-1} M_\odot} \right)^{0.8} \quad (4.62)$$

shown by the dotted black line in Fig. 4.8. This fitting function will be the basis of predictions of the LLB+ $b_{s^2}^L$  model in the rest of this chapter. The measurements of the linear Lagrangian bias  $b_1^L$  are strongly constrained by the halo-matter cross power spectrum and are in good agreement with the trends of the ST bias function, except for two highest mass bins that show slight deviation. Note that we include the ST bias predictions only as a reference to guide the eye rather than expecting perfect agreement. Similarly, the measurements of non-linear local Lagrangian bias parameters  $b_2^L$  and  $b_3^L$  qualitatively agree with the predictions of the ST bias function. However, quantitatively we see deviations which are more obvious in the case of  $b_3^L$ . The theory lines for  $b_2^L$  and  $b_3^L$  are calculated from the second and third derivatives of the mass function. The detection of non-zero Lagrangian tidal bias clearly shows the failure of the spherical collapse model, partially explaining the disagreement of the measurements of local Lagrangian bias parameters with the theory predictions. A previous attempt at measuring cubic local Lagrangian bias was presented in [147], where in agreement with our results, evidence for negative Lagrangian tidal bias at the high mass end is found. At the quantitative level however, their measurements and in particular their fitting function indicate a larger effect than what we find here. In particular, we don't find any evidence for positive  $b_{s^2}^L$  at the low-mass end. For reference, we overplot their fitting function in Fig. 4.8.

Next, we consider the non-local cubic bias parameters. We do not find significant detection of the presence of  $b_{\Gamma_3}^L$ ,  $b_{\mathcal{G}_2\delta}^L$ , and  $b_{\mathcal{G}_3}^L$  for low masses. Mass bin V, however, shows some mild evidence for non-vanishing cubic non-local Lagrangian bias. We have to caution however, that the employed smoothing and cutoff scales might be insufficient to suppress the impact of derivative bias corrections for these high mass, large radius tracers (see for instance [14, 147] for the scale dependence of Lagrangian bias).

Fig. 4.8 reveals statistically significant changes between the fits with and without the counterterm  $dR$ . Naively, one might have expected that the halo scale dependence is

insignificant due to the large fiducial smoothing scale  $R_f$ . However, as we discuss in detail in App. A.2, there is a several percent level residual dependency of the correlators on the halo smoothing scale. This sensitivity is at the same order as the relative errors on some of the bias parameters and can thus induce significant parameter shifts. At the same time, the presence of the counterterm can actually account for some of the stochasticity in the data. Thus, the constraints including the counterterm may show smaller error bars despite the larger parameter set.

#### 4.5.4 Eulerian Bias from the Late-time Halo Field

We now turn to the constraints on Eulerian bias parameters. In Fig. 4.14 we show the bias constraints for five mass bins obtained from seven and eight parameter fits to the late-time halo field. The solid lines are the predictions of the co-evolution of the local Lagrangian bias model, whereas the dashed lines are the predictions of the co-evolution of the local Lagrangian bias model extended by a non-local Lagrangian tidal term (LLB+ $b_{s2}^L$ ). We have plotted the constraints with and without the counter term  $dR$ . The measurements of the local Eulerian bias parameters  $b_1^E$ ,  $b_2^E$  and  $b_3^E$  are following the trends of the ST bias function, with slight deviations towards the high mass end. As we noted before, we don't expect perfect agreement with this particular bias function. Our measurements of the tidal bias  $b_{s2}$  fall below the prediction based on co-evolution of the local Lagrangian bias model. The reason for this is the presence of the initial Lagrangian tidal field discussed in the previous section. The measurements show a preference for the predictions of the LLB+ $b_{s2}^L$  model. To check the consistency of our model, we have also performed fits to the propagator and quadratic field correlators ( $\chi_{\text{lin}}^2 + \chi_{\text{quad}}^2$ ) using only  $b_1^E$ ,  $b_2^E$ ,  $b_{s2}^E$  and  $dR$ . We find that the constraints are in good agreement with the ones obtained from the full eight parameter fits to linear, quadratic and cubic statistics.

Even though we are fitting for bias measurements on large scales, as ensured by the cutoffs  $k_{\text{max}} = 0.057h \text{ Mpc}^{-1}$  and  $R_f = 20h^{-1} \text{ Mpc}$ , to avoid corrections from non-linear modes, the higher mass bins can already be affected by higher derivative corrections. Going beyond the (integrated) tree-level trispectrum requires additional bias parameters and the inclusion of higher derivative bias operators. In fact, it has been shown that in the framework of EFTofLSS including higher derivative bias in the model improves the model performance for massive halos [92]. In the EFTofLSS, the halo density is written in terms of the expansion in  $(k/k_{\text{NL}})$  and  $(k/k_{\text{M}})$ , where  $k_{\text{NL}}$  is the non-linear scale of the theory and  $k_{\text{M}}$  corresponds to the scale of the derivative bias. For massive halos  $k_{\text{M}}$  decreases and therefore derivative corrections become more important compared to low mass halos.

Coming back to bias measurements, we detect the presence of the non-local cubic bias in the late-time halo field at a significant level. The measurements for  $b_{\mathcal{G}_3}$ ,  $b_{\mathcal{G}_2\delta}$ , and  $b_{\Gamma_3}$ ,



however, do not follow the predictions of the co-evolution of LLB; rather, in general, they are in slightly better agreement with the predictions of the co-evolution of LLB with initial Lagrangian tidal bias.

In Fig. 4.10 we highlight the dynamical contribution to the bias parameters by showing the difference of the initial and late-time measurements, and comparing them to the co-evolution predictions of the LLB and  $\text{LLB}+b_{s^2}^{\text{L}}$ . For  $b_{\Gamma_3}$  the measurements follow the trend of the latter, except for a small deviation for mass bin III. For  $b_{\mathcal{G}_2\delta}$  and  $b_{\mathcal{G}_3}$  we see that the lowest three mass bins are in good agreement with the predictions of  $\text{LLB}+b_{s^2}^{\text{L}}$ , whereas the highest two mass bins clearly disagree from the predictions of both LLB and  $\text{LLB}+b_{s^2}^{\text{L}}$  models.

In Fig. 4.12 we plot  $b_{s^2}$ ,  $b_{\Gamma_3}$ , and  $b_{\mathcal{G}_3}$  against the linear bias and  $b_{\mathcal{G}_2\delta}$  against the non-linear local quadratic bias. In addition, we have also plotted the combination  $2/5b_{\Gamma_3} + b_{s^2} = -1/15b_1^{\text{L}}$  that appears in the predictions for the halo-matter power spectrum at one-loop (see Sec. 4.5.6 below). We see that except for the fifth mass bin, the measurements of  $b_{\mathcal{G}_3}$  are in good agreement with the predictions of both LLB and  $\text{LLB}+b_{s^2}^{\text{L}}$ . We see that  $b_{\Gamma_3}$  is increasing with the linear bias but quantitatively mass bins II and III are clearly in disagreement with the co-evolution predictions. Unfortunately the errorbars are huge and affect the predictions for the one-loop halo-matter cross power spectra which we discuss below in Sec. 4.5.6. These measurements are the best we can obtain from the cubic field method given our ensemble of simulations.

Finally, we also show the bias measurements as a function of the cutoff wavenumber  $k_{\text{max}}$  in Fig. 4.11. As one increases the maximum  $k$ -mode, non-linear modes start affecting the measurements and should be taken care of by including appropriate loop corrections in the model. The measurements are fairly consistent on large scales up to our fiducial  $k_{\text{max}}$ .

During the final stages of this study [121] presented a similar study of cubic non-local bias. These authors use the correlation of cubic operators with the halo field without orthogonalization but remove the matter non-linearities from the halo field. This leaves closed loops in the bias operators, which we remove due to their strong UV-sensitivity (as discussed in Appendix A.2). Their analysis goes to higher wavenumbers and subtracts a subset of odd correlators. They marginalize over residual  $k^2$  dependencies for each of the cubic bias parameters to capture higher derivative and higher-order perturbative corrections, while we aim to account for these effects by fitting to  $dR$ . Qualitatively we agree with their finding that the Eulerian non-local bias parameters are in tension with the predictions based on the LLB model. Both approaches show the potential of the cubic field approach and future high-precision implementations should aim to combine the respective advantages of the two methods.

### 4.5.5 Constraints on Lagrangian Bias Parameters from Different Models

Given that the final halo field shows reasonable agreement with the  $\text{LLB}+b_{s2}^{\text{L}}$  model, we consider a direct fit of the final halo field using the template in Eq. (4.27), i.e. linking the amplitude of the final cubic operators to the local Lagrangian bias and the Lagrangian tidal tensor bias. The free parameters in this fit are thus  $\{b_1^{\text{L}}, b_2^{\text{L}}, b_3^{\text{L}}, b_{s2}^{\text{L}}\}$  and  $dR$ . We perform this same fit on the protohalos as well.

We show the results of this study in Fig. 4.13, where we also show the Lagrangian bias parameters reconstructed from the eight parameter fits discussed above. In general we see a consistent picture, where all of the Lagrangian bias parameters obtained from the four different fitting procedures follow the same trend. There is some tension for the local cubic bias  $b_3^{\text{L}}$ , which is probably due to large parameter degeneracies in the protohalo fits. This might be partially due to us neglecting explicit  $k^2$  bias contributions in the protohalo field as for instance predicted by the peak model [14, 147].

Just for an example, Fig. 4.14 we plot marginalized posteriors of Lagrangian bias constraints for mass bin III obtained from the late-time halo field. We can see some mild degeneracies between the counterterm  $dR$  and the cubic local and quadratic non-local Lagrangian bias. These degeneracies are more severe in the constraints obtained from the protohalos.

Models	Bin 1	Bin 2	Bin 3	Bin 4	Bin 5
Eulerian 8 pars (with CT)	2.782	1.914	1.080	1.006	1.297
Eulerian 7 pars (without CT)	2.417	1.708	1.120	1.144	1.405
Lagrangian 8 pars (with CT)	1.975	1.303	1.168	1.373	1.454
Lagrangian 7 pars (without CT)	2.680	1.636	1.162	1.263	1.267
Lagrangian 5 pars (initial)	1.800	1.296	1.267	1.370	1.497
Lagrangian 5 pars (final)	1.216	1.203	1.162	1.023	1.190

Table 4.3 Overview of reduced  $\chi^2$  models considered. We have studied six different models which are summarized in the table. First, we note that the Eulerian and Lagrangian models with the counterterm  $dR$  are statistically preferable compare to the ones without the counterterm. Second, we note that for both Eulerian and Lagrangian models, for mass bin I and II, five parameter fits are statistically preferable. However, for mass bins III, IV, and V the full model with eight parameters gives a lower reduced  $\chi^2$  and is therefore preferable. This implies that low mass halos are in a better agreement with the co-evolution predictions of  $\text{LLB}+b_{s2}$ .

### 4.5.6 Application: One-loop Halo-Matter Power Spectrum

We are now ready to check the halo-matter cross spectrum and halo-propagator predictions. The halo-matter cross spectrum  $P_{\text{hm}}(k)$  and the halo-propagator  $P_{\text{hG}}(k)$  are defined through the two-point function in Fourier space as:

$$\langle \delta_{\text{h}}(\mathbf{k}) \delta_{\text{i}}(\mathbf{k}') \rangle = (2\pi)^3 \delta_{\text{D}}^{(3)}(\mathbf{k} + \mathbf{k}') P_{\text{hi}}(k), \quad (4.63)$$

where  $i = \text{m}$  or  $\text{G}$  correspond to the non-linear and linear density field respectively. Up to one-loop in PT and at leading order in derivatives  $P_{\text{hm}}$  and  $P_{\text{hG}}$  are given by the following expressions [142, 11]

$$P_{\text{hm}}(k) = b_1 \left( P_{\text{lin}}(k) + 2P_{13}(k) + P_{22}(k) \right) + \left( b_{s^2} + \frac{2}{5} b_{\Gamma_3} \right) \mathcal{F}(q) - b_{\nabla^2 \delta} k^2 P_{\text{lin}}(k) + \frac{1}{2} b_2 \mathcal{I}_{\delta^{(2)} \delta^2}(k) + b_{s^2} \mathcal{I}_{\delta^{(2)} s^2}(k) \quad (4.64)$$

$$P_{\text{hG}}(k) = b_1 \left( P_{\text{lin}}(k) + P_{13}(k) \right) + \left( b_{s^2} + \frac{2}{5} b_{\Gamma_3} \right) \mathcal{F}(q) - \tilde{b}_{\nabla^2 \delta} k^2 P_{\text{lin}}(k)$$

where  $\mathcal{F}(k)$ ,  $\mathcal{I}_{\delta^{(2)} \delta^2}(k)$ , and  $\mathcal{I}_{\delta^{(2)} s^2}(k)$  are defined as

$$\mathcal{F}(k) = 4P_{\text{lin}}(k) \int_{\mathbf{q}} \left( S_2(\mathbf{q}, \mathbf{k} - \mathbf{q}) F_2(\mathbf{k}, -\mathbf{q}) - \frac{34}{63} \right) P_{\text{lin}}(q), \quad (4.65)$$

$$\mathcal{I}_{\delta^{(2)} \delta^2}(k) = 2 \int_{\mathbf{q}} F_2(\mathbf{k} - \mathbf{q}, \mathbf{q}) P_{\text{lin}}(q) P_{\text{lin}}(|\mathbf{k} - \mathbf{q}|), \quad (4.66)$$

$$\mathcal{I}_{\delta^{(2)} s^2}(k) = 2 \int_{\mathbf{q}} F_2(\mathbf{k} - \mathbf{q}, \mathbf{q}) S_2(\mathbf{k} - \mathbf{q}, \mathbf{q}) P_{\text{lin}}(q) P_{\text{lin}}(|\mathbf{k} - \mathbf{q}|). \quad (4.67)$$

Note that the above expressions do not contain a smoothing scale. For explicit expressions of  $P_{13}$  and  $P_{22}$  see [37]. Note that naively, there would have been contributions proportional to  $\sigma^2 P$  in the halo-matter power spectrum and propagator, which would renormalize the linear bias prefactor of the leading  $P_{\text{lin}}$  contribution. This would cause the large scale limit to deviate from  $b_1 P_{\text{lin}}$  [139]. However, the propagation of the  $-b_2^{\text{L}}/2\sigma^2 - b_3^{\text{L}}/2\sigma^2 \delta_{\text{G}}(\mathbf{q}) - 2/3b_{s^2}^{\text{L}}\sigma^2$  contributions to Eq. (4.12) leads to a  $(-b_2^{\text{L}}/2\sigma^2 - b_3^{\text{L}}/2\sigma^2 - 2/3b_{s^2}^{\text{L}}\sigma^2)P$  contribution to the power spectrum, which exactly cancels these renormalizing terms.

Having fixed the bias parameters from our measurements described earlier in this Section, we are only left with the  $k^2$  term. The importance of  $k^2$  corrections has been discussed in the literature in the context of peak model [65, 69, 14] or symmetry arguments [142, 174]. Constraints on the  $k^2$  bias or the leading derivative bias can be obtained by comparing Eqs. (4.64) with the simulation data. We quote our best-fit values for  $b_{\nabla^2 \delta}$  and  $\tilde{b}_{\nabla^2 \delta}$  in Tab. 4.4. The large errorbars on the bias parameters  $b_{s^2} + \frac{2}{5} b_{\Gamma_3}$  do not allow for a significant detection of non-zero  $k^2$  corrections for mass bins I and V. However, we get a significant

Mass Bin	$\tilde{b}_{\nabla^2\delta}$	$\Delta\tilde{b}_{\nabla^2\delta}$	$b_{\nabla^2\delta}$	$\Delta b_{\nabla^2\delta}$
I	-2.74	6.52	-0.92	6.59
III	-20.94	8.52	-18.65	8.58
III	-35.21	15.37	-32.18	15.34
IV	26.74	19.39	32.39	19.44
V	-30.35	66.35	-16.34	67.12

*Table 4.4* Best-fit values for the  $k^2$  bias coefficients for five mass bins obtained from the one-loop halo-matter statistics after fixing all other bias parameters. The maximum wavenumber used is  $k_{\max} = 0.08h \text{ Mpc}^{-1}$ . The quoted values are in units of  $h^{-2} \text{ Mpc}^2$ , i.e. inverse length-squared. The error bars are dominated by the uncertainty of  $b_{s^2} + 2/5b_{\Gamma_3}$ .

detection of  $k^2$  corrections for mass bins II, III and IV. The constraints obtained from the propagator and equal-time halo-matter power spectrum are consistent with each other. The amplitude of the parameter is non-monotonic with mass, which could be understood in the context of the peak model, where the Eulerian  $k^2$ -bias is given by sums of positive and negative contributions with different mass dependence [13]. The difference of  $P_{\text{hm}}$  and  $P_{\text{hG}}$  has its own residual  $k^2$  correction  $\tilde{b}_{\nabla^2\delta} - b_{\nabla^2\delta} = -c_s^2$ , which is related to the EFT speed of sound in the matter power spectrum  $P_{\text{mm}}(k) = P_{\text{lin}}(k) + 2P_{13}(k) + P_{22}(k) - 2c_s^2k^2P_{\text{lin}}(k)$ . As the difference  $P_{\text{hm}}$  and  $P_{\text{hG}}$  does not contain  $\mathcal{F}$ , it is less affected by the large error bars on  $b_{s^2} + \frac{2}{5}b_{\Gamma_3}$  and allows us to put tighter constraints on  $c_s^2$  than on  $\tilde{b}_{\nabla^2\delta}$  and  $b_{\nabla^2\delta}$  individually. Within the error bars the results indeed agree with reported values in the literature [27].

In Figs. 4.15 and 4.16 we show our predictions for the one-loop halo propagator and halo-matter power spectrum. The predictions with and without  $k^2$  are represented by solid blue and red lines respectively. In addition, the shaded green region shows the uncertainty arising from the error bars on the bias measurements (without the error on the  $k^2$  correction). We see that after adding the  $k^2$  corrections the theory agrees with the data up to wavenumber  $k = 0.1h \text{ Mpc}^{-1}$ . However, precision is highly affected by the large error bars on the combination of cubic parameters  $b_{s^2} + \frac{2}{5}b_{\Gamma_3}$ .

## 4.6 Summary & Conclusions

In this chapter we have studied the measurement of bias parameters beyond leading order from cross-correlations of quadratic and cubic bias operators with halo fields in a suite of  $N$ -body simulations.

We summarize our results as follows:

- We find that we can model the final halo distribution with seven bias parameters (one linear, two second order and four third order bias parameters) with one additional parameter that accounts for the halo scale. We find clear evidence for non-zero quadratic and cubic non-local bias operators. The amplitude of the detected non-local bias deviates from the predictions of the evolved local Lagrangian model both at quadratic and cubic level.
- The distribution of protohalos in Lagrangian space in turn shows evidence for the existence of a Lagrangian quadratic tidal bias contribution, i.e., a deviation from the local Lagrangian bias model. The presence of such a term indicates that the collapse threshold for halo formation depends not only on the density but also on the shear [49, 147], and that the strength of this dependence increases with mass.
- We have not detected any cubic non-local terms in Lagrangian space for low mass bins; however, for the highest mass bin V we find some evidence for the presence of these terms. We would like to emphasize again that our smoothing and cutoff scales might be insufficient to suppress the derivative bias corrections for high mass bins. Should this hint for the existence of cubic Lagrangian bias be confirmed, the modelling of collapse thresholds for halo formation would need to be extended to cubic fields.
- The non-detection of cubic Lagrangian bias operators for low masses motivated us to consider the consequences of a Lagrangian bias model with a quadratic tidal component but no non-local cubic operators. The Lagrangian tidal bias contributes to both the quadratic and cubic non-local bias operators in Eulerian space. We were able to fit the final distribution with the simple five parameter model that contains Lagrangian local biases up to third order and a tidal Lagrangian bias.
- We see some mild degeneracies between the counterterm  $dR$  and the cubic local and quadratic non-local bias terms in Lagrangian space, which might be because of neglecting  $k^2$  terms in the protohalo field.
- Given the importance of the  $k^2$  term, we constrained it from the one-loop halo-matter cross spectra statistics for five mass bins after having fixed the other bias parameters

from our measurements. The constraints are given in Tab. 4.4. Because of large errorbars on the cubic bias parameters entering in these statistics, we have not detected the presence of non-zero  $k^2$  term for some of the mass bins. We find that the constraints from the propagator and equal time statistic are consistent and that their difference agrees with previous measurements of the dark matter speed of sound in the EFT framework.

- We plot the predictions of one-loop halo propagator and halo-matter cross spectrum in Fig. 4.15 and Fig. 4.16 respectively. Our predictions agree with the  $N$ -body simulation data up to  $k = 0.1h \text{ Mpc}^{-1}$ . However, to make more precise predictions, one has to reduce the errorbars on the combination of the cubic bias  $2/5b_{\Gamma_3} + b_{s^2}$ .

As we hinted in Sec. 4.3.3, it might be interesting to consider the bispectrum of quadratic field, linear field and halo field as an alternative means to extract bias information from the trispectrum. Furthermore, the strong filtering or derivative corrections in the protohalo statistics [16, 147] should be accounted for more directly in order to improve the reliability of the constraints on Lagrangian bias parameters. An application of the presented method to actual observations will be complicated by the nonavailability of a Gaussian reference field. This problem could potentially be alleviated by using cross correlation of squared and cubed lensing fields with the galaxy field.

The method presented here allows for straightforward extensions to quartic statistics, which will be relevant for computations of the one-loop halo or galaxy bispectrum. Furthermore, straightforward extensions of this method should allow to constrain cubic primordial non-Gaussianity such as the  $g_{\text{NL}}$  [3] local model.

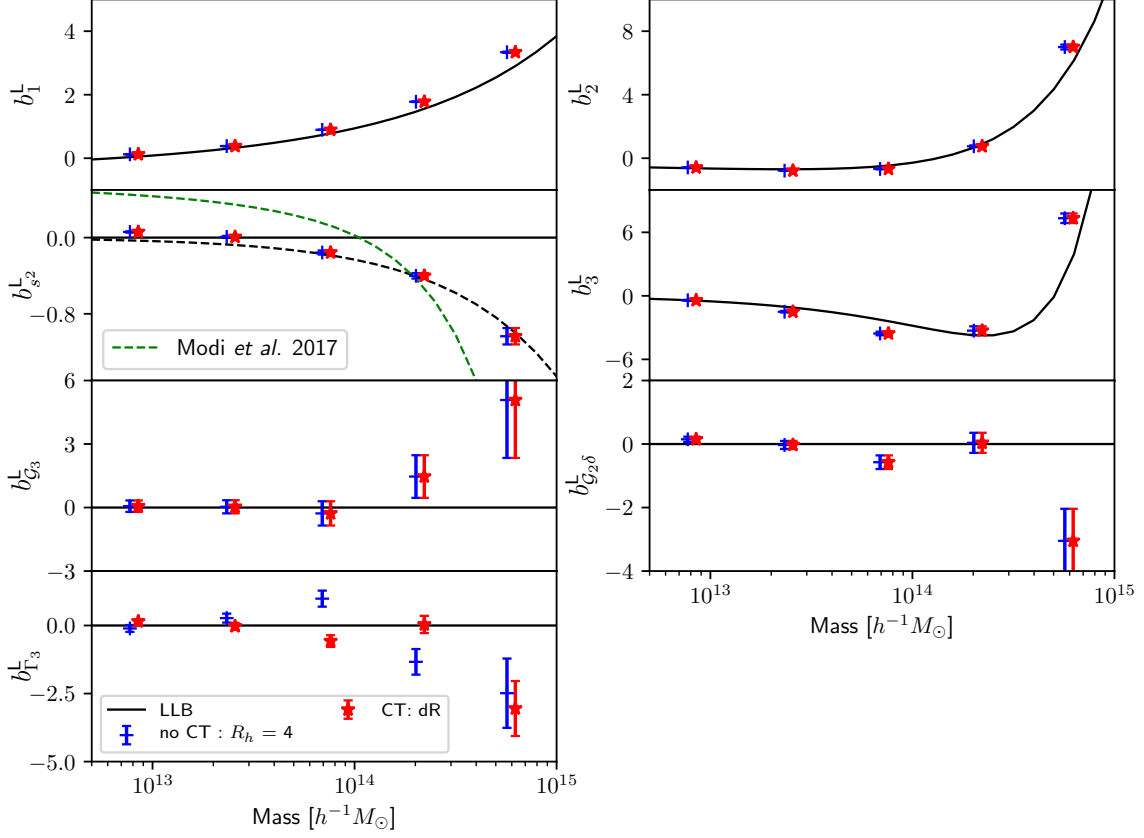


*Fig. 4.8* Constraints on bias parameters from the protohalo statistics. The solid lines are the predictions of the local Lagrangian model calculated from the ST mass function. The dashed line is a fit to the observed non-zero Lagrangian tidal parameter given in Eq. (4.62). We are plotting two cases. The fit leading to the red points includes the counter term  $dR$ , which is just the Taylor expansion coefficient around our fiducial choice of smoothing scale  $R_h$ , while the blue points are without a counter term. The employed fiducial  $R_h = 4h^{-1}\text{Mpc}$  does not reflect the correct Lagrangian scale for all mass bins. Thus, we are more confident in the measurements with the counter term. We also overplot the fitting functions for  $b_{s^2}$  given in Eq.(22) of [147] (rescaled to Lagrangian space, shown by the dashed-green line), which contrary to our findings indicates a positive tidal bias for low masses and a stronger effect for large masses.

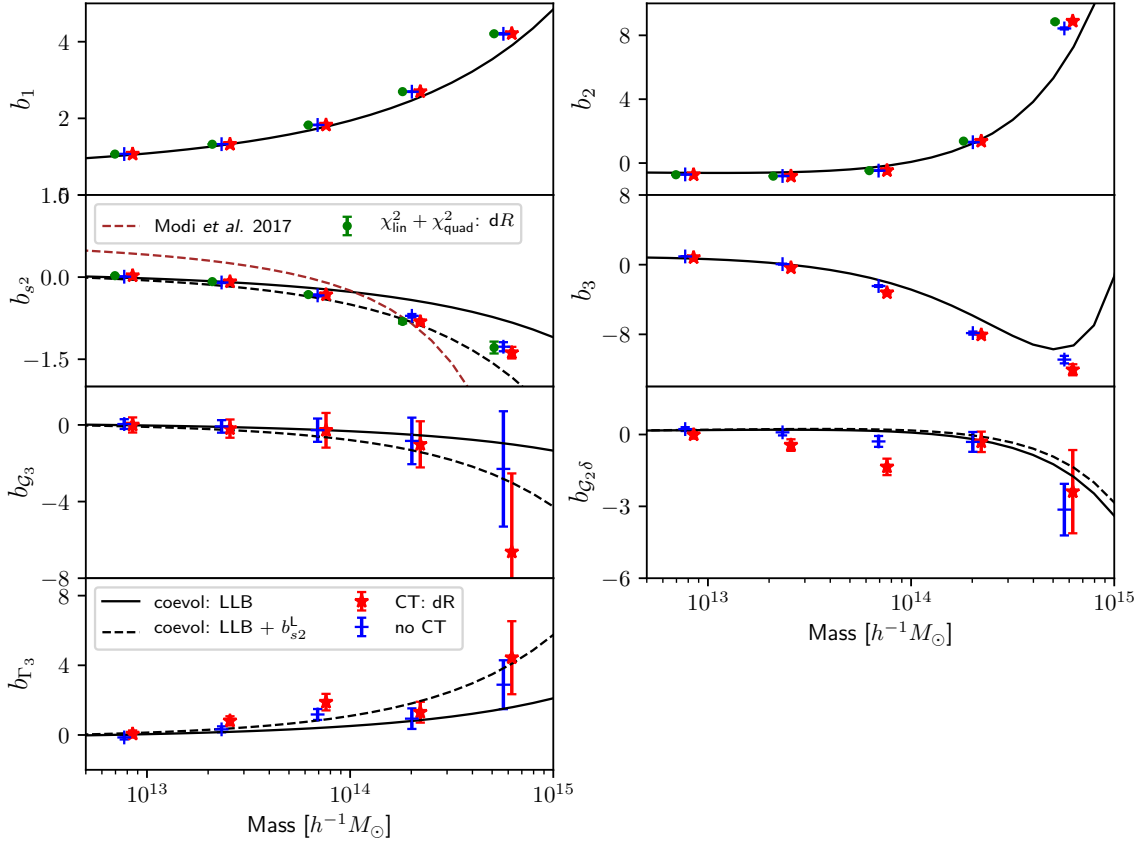


*Fig. 4.9* Constraints on Eulerian bias parameters from seven and eight parameter fits to the late-time halo field. The red points depict the fits with an eight parameter model including the counterterm  $dR$ , whereas the green points show the results from a seven parameter model without the counterterm. The black dashed lines show the co-evolution prediction based on a local Lagrangian bias model and the black lines arise from a local Lagrangian model extended by a non-vanishing tidal term whose amplitude was fitted in Lagrangian space and is given by Eq. (4.62). Green points show constraints on linear and quadratic biases obtained from a fit to  $\chi_{\text{lin}}^2 + \chi_{\text{quad}}^2$ . The constraints are in perfect agreement with the results from the full fits, which supports the consistency of our model and fitting procedure. The fitting function of [147] for  $b_{s2}$  is shown by the brown dashed curve.



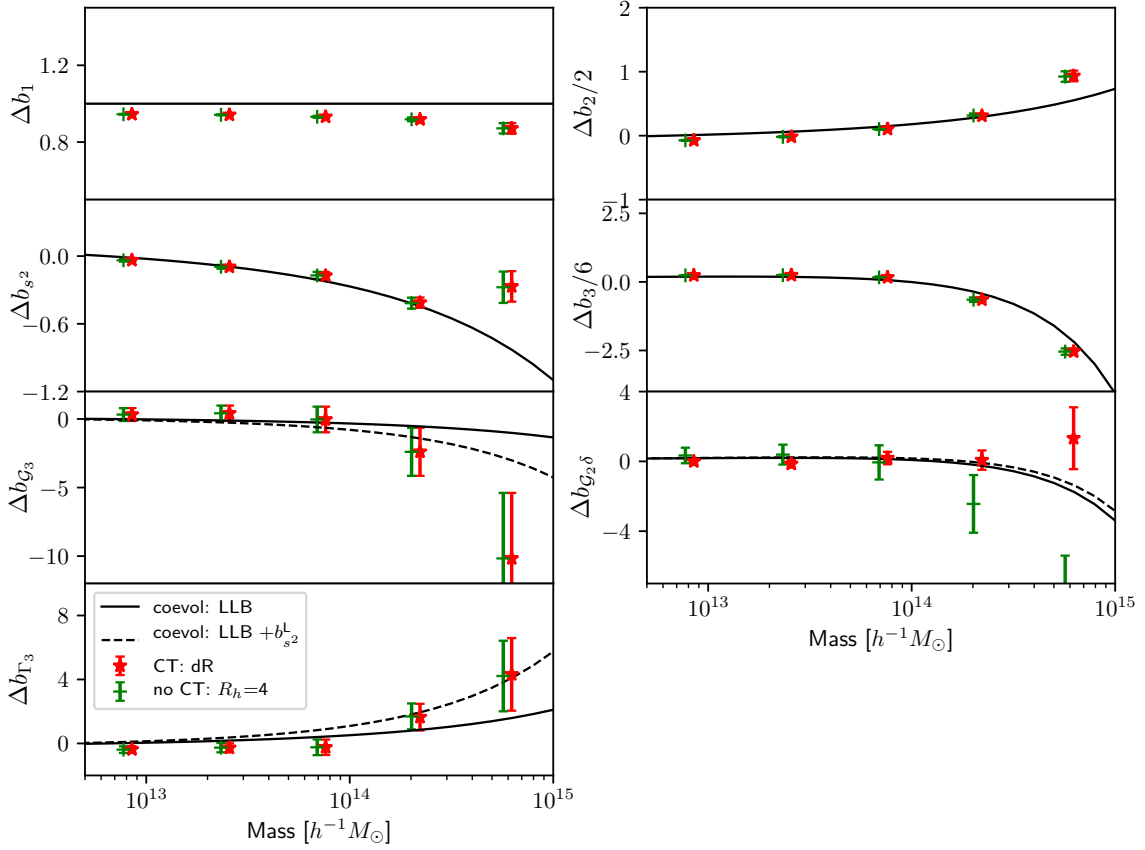


*Fig. 4.10* Co-evolution Check: Difference of Eulerian and Lagrangian constraints on the local and non-local cubic bias parameters. We overplot the predictions of the local Lagrangian bias model (shown by solid black curves) and the Lagrangian model with an initial tidal field (LLB+ $b_{s2}^L$  shown by black dotted lines). At low mass the bias generally shows the trends of local Lagrangian bias, but at the high mass end there are deviations especially for  $b_{\Gamma_3}$  and  $b_{\mathcal{G}_3}$ .

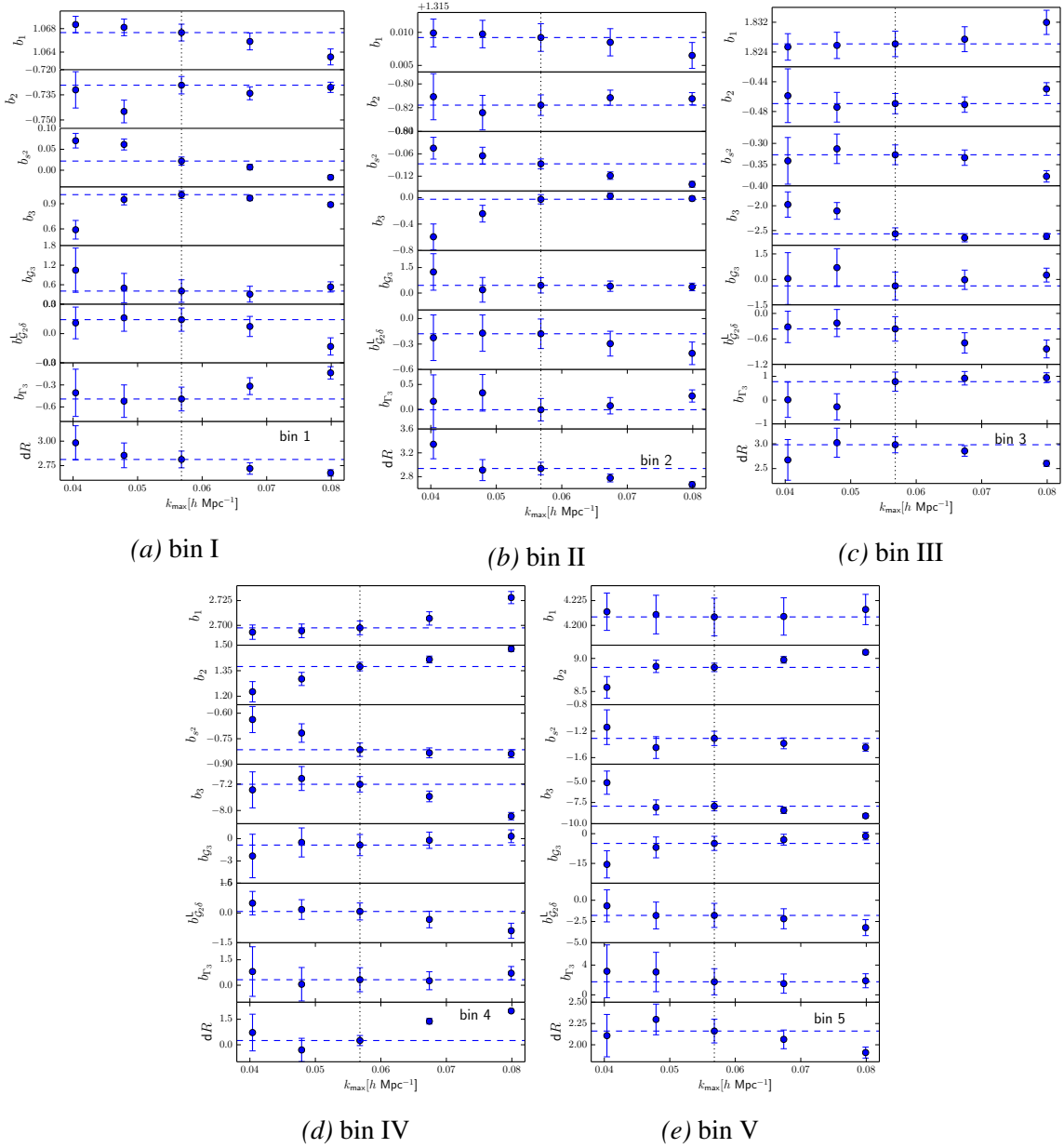
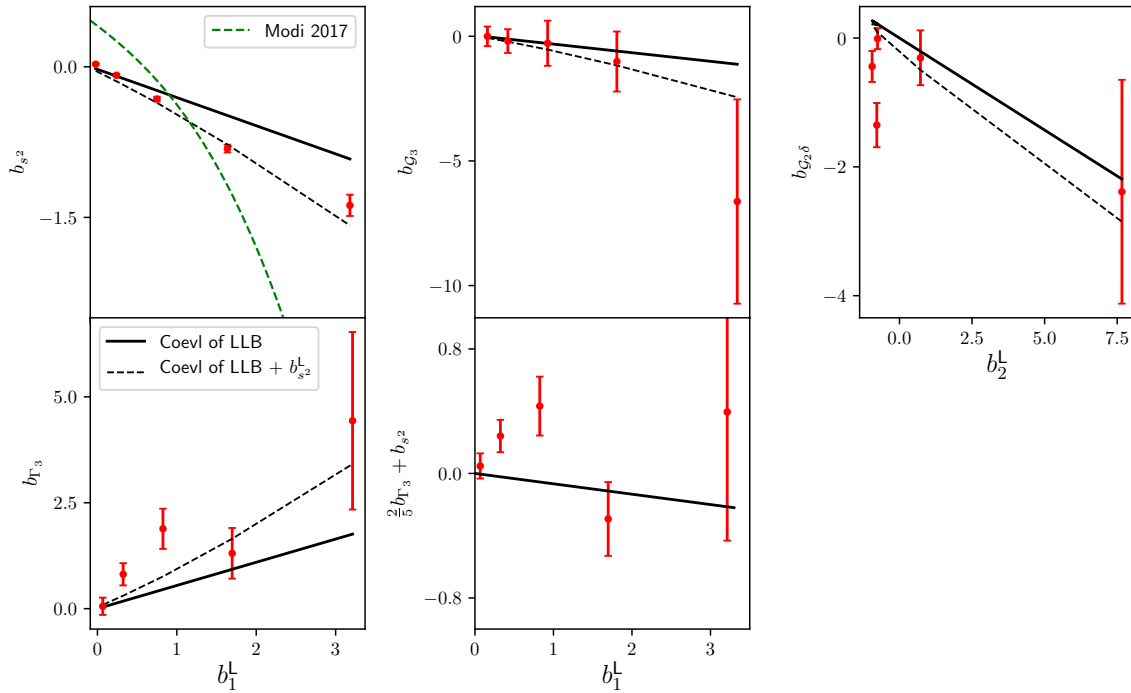
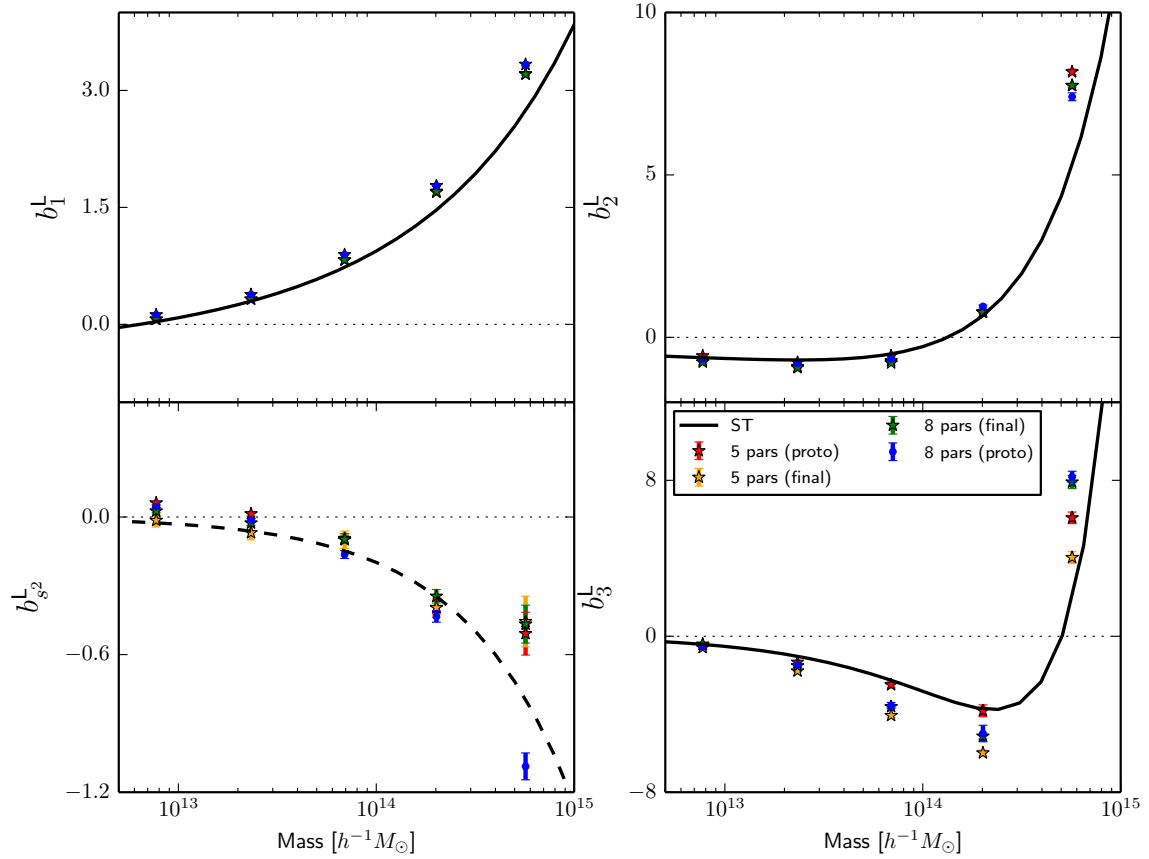


Fig. 4.11 Measurements of the Eulerian bias parameter as a function of maximum wavenumber  $k_{\max}$ . The horizontal blue-dashed lines are the best-fit values evaluated at  $k_{\max} = 0.057 h \text{ Mpc}^{-1}$  (vertical dotted line).



*Fig. 4.12* Non-local bias constraints plotted against the linear Lagrangian bias and quadratic local Lagrangian bias. As stated in Eq. (4.32) the non-local bias parameters are predicted to follow a linear relation with the Lagrangian bias parameters shown as the black line. The data points show a preference for the model in which the LLB is extended by a Lagrangian tidal tensor contribution leading to the predictions in Eq. (4.33) (dashed curve). We also overplot the fitting function for  $b_{s^2}$  given in Eq. (22) of [147] (shown by the dashed-green line). Our measurements for  $b_{s^2}$  are clearly not consistent with their fitting function.



*Fig. 4.13* Direct five parameter measurements of the Lagrangian bias parameters using the template Eq. (4.27) for the final halo field and reconstruction of the Lagrangian bias parameters from the full eight parameter fits of the final field described above. We also show direct measurements of the Lagrangian bias parameters from a five and eight parameter fit to the protohalo field. The solid lines are predictions of the ST bias function. The dashed curve for  $b_{s^2}^L$  is our best-fit defined in Eq. (4.62).

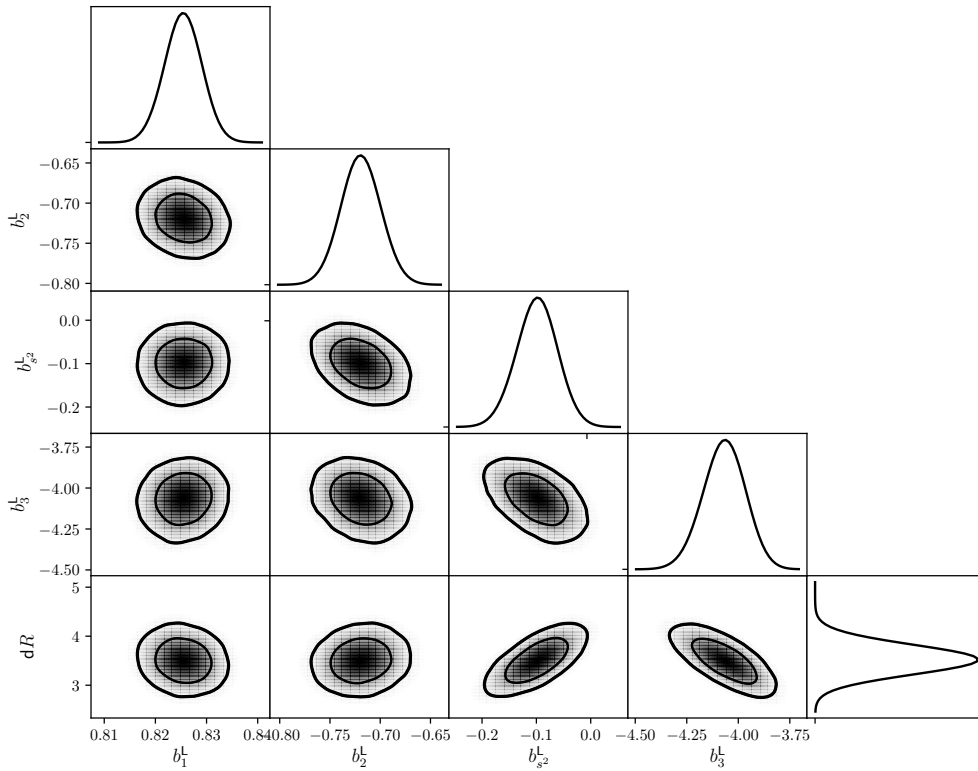


*Fig. 4.14* Marginalized posteriors of Lagrangian bias constraints for mass bin III obtained from the late-time halo field. The counterterm  $dR$  is shown in units of  $1 h^{-1} \text{Mpc}$ . The dark and light regions represent 64.1 % and 95.4 % confidence regions respectively. We clearly see detection of Lagrangian tidal bias and a deviation from the fiducial smoothing scale  $R_h = 4h^{-1} \text{Mpc}$ . There are some mild degeneracies between the counterterm  $dR$  and the local cubic and quadratic tidal tensor bias.

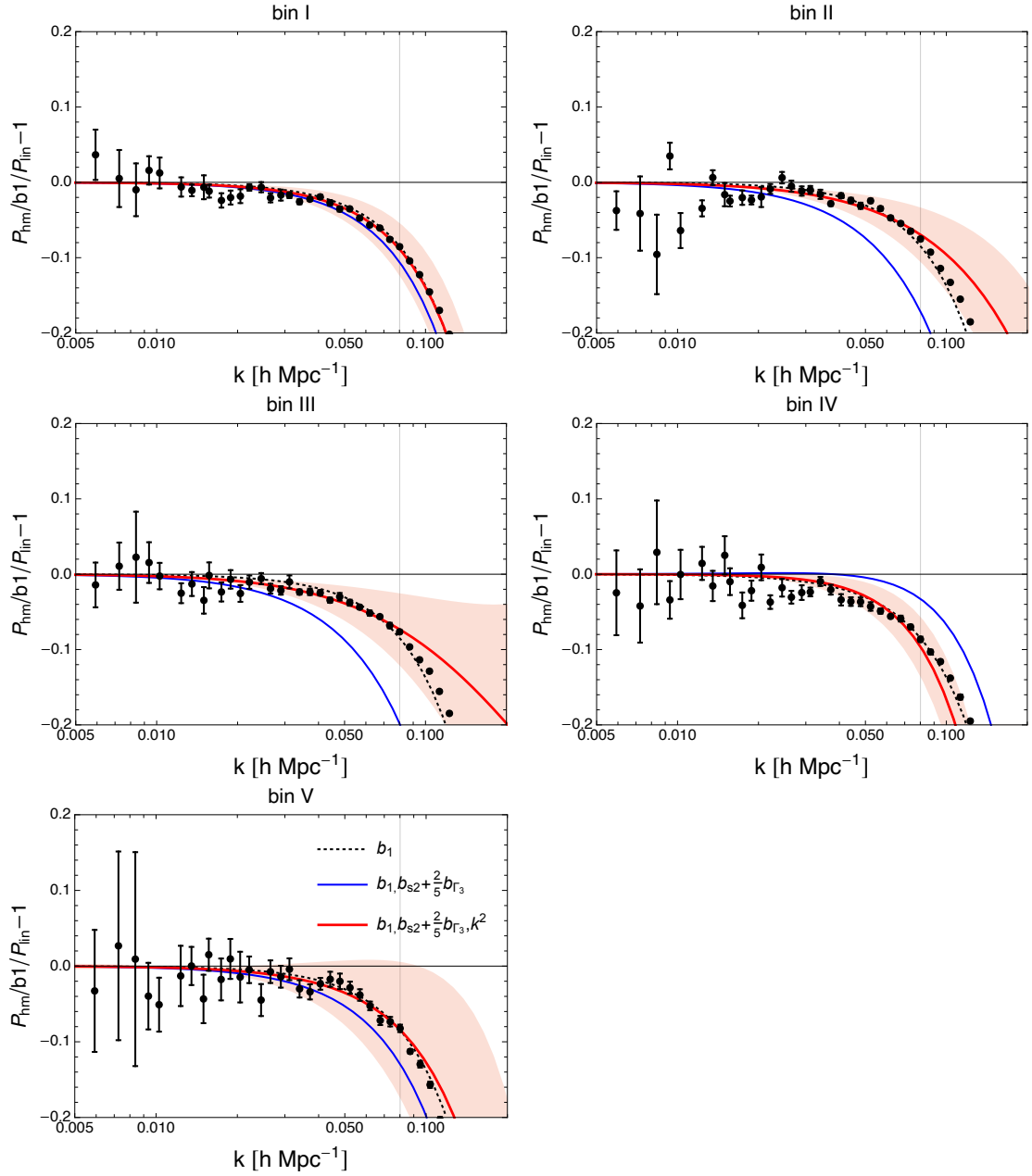


*Fig. 4.15* Cross correlation of the final halo field with the linear density field (propagator), normalized by the linear power spectrum. The red and blue lines show one-loop predictions with and without  $k^2$  corrections. The shaded red region shows the effects of the bias errorbars on the predictions.

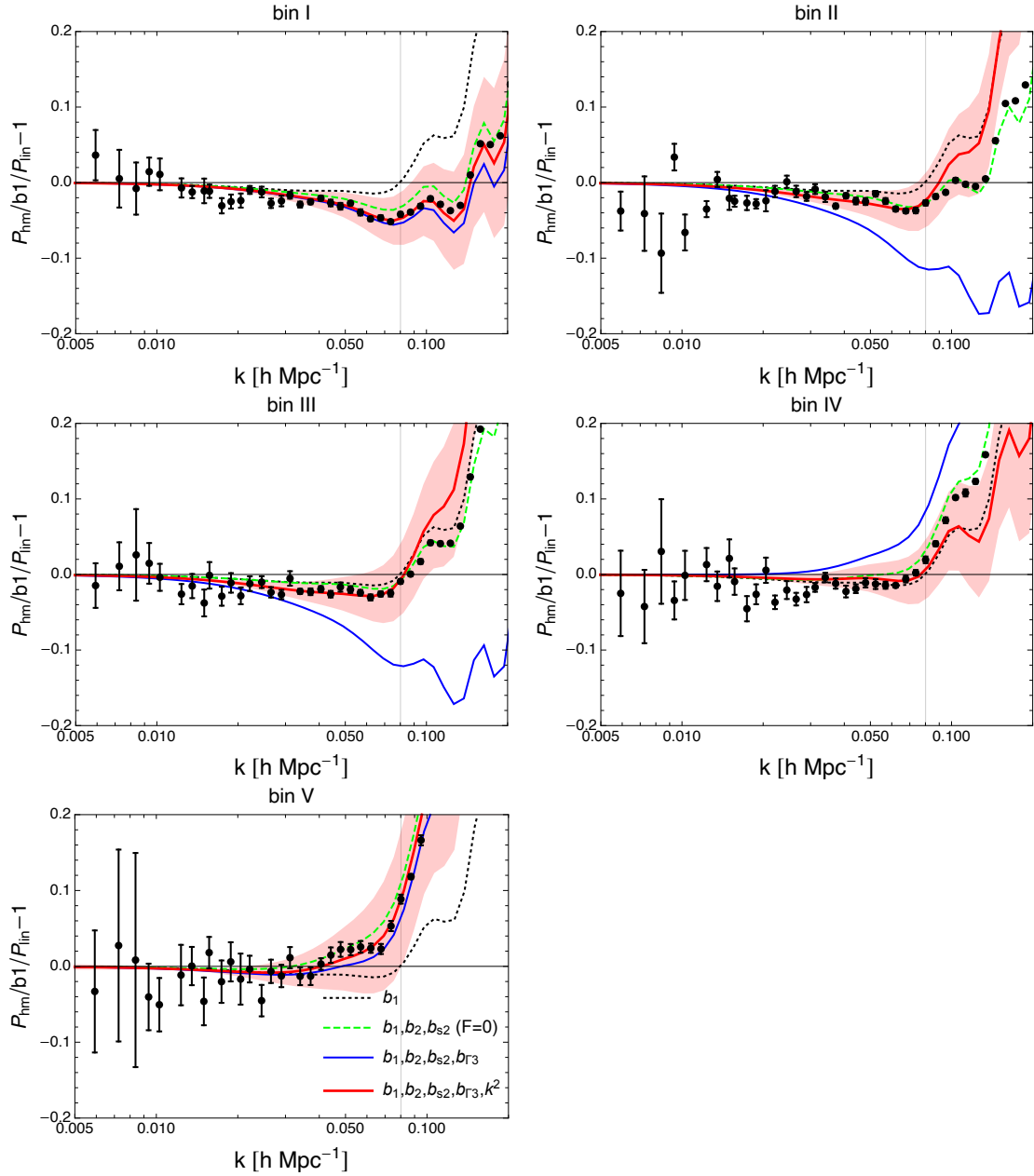


*Fig. 4.16* Ratio of halo-matter cross power spectrum and linear power spectrum. The red and blue lines show one loop predictions with and without the  $k^2$  corrections. The shaded red region represents the uncertainty arising from the error on the cubic bias parameters (without the error on the  $k^2$  term). We also show the predictions without quadratic and cubic bias reflected by the black dotted lines.

## Density Field Reconstruction from Biased Tracers and Constraining local $f_{\text{NL}}$

*Note: This chapter is based on my co-authored work, "Density reconstruction from biased tracers and its application to primordial non-Gaussianity", done in collaboration with Omar Darwish, Simon Foreman, Tobias Baldauf, Blake Sherwin, and Daan Meerburg [59]. Reconstructing the density field from dark matter halos in numerical N-body simulations and verifying all analytical predictions of cross-spectra with simulation results are my original work (done under the supervision of Tobias Baldauf). All other results and derivations in [59] were thoroughly cross-checked by my independent Mathematica code. All figures and plots in this chapter have been reproduced from my own code.*

### 5.1 Introduction

The measurements of temperature fluctuations in Cosmic Microwave Background (CMB) have improved our understanding of the Universe. The model that has emerged from these measurements is that the Universe is mostly flat and dominated by dark energy and dark matter. This model of the Universe, which is called the  $\Lambda$ CDM model, has been confirmed very well by observations [160]. However, several challenges remain that need to be solved. One of the main problems in modern cosmology is to constrain the initial conditions of the Universe and to learn more about the physics of the early Universe. The temperature fluctuations in CMB are uniform, telling us that the Universe is extremely homogeneous and isotropic on large scales, where fractional inhomogeneity present is 1 in 100 000. These CMB fluctuations are correlated and can be correctly described by the 2-point function, which in Fourier space is called the power spectrum. It is believed that the seeds for fluctuations in the CMB and structure formation in the late time universe originated from inflation, which is a period of early exponential expansion of the Universe [100, 131]. If



the initial conditions of inflation are Gaussian, then the power spectrum is the only relevant statistic to describe the data and extract all useful information accurately. All higher point functions, in this case, will add no additional information. However, in the presence of non-Gaussianity in the initial conditions, higher point statistics become essential to extract information about the early Universe, especially it will induce non-vanishing three-point function, which is called the bispectrum in Fourier space. So far, observational data shows no sign of non-Gaussianity and therefore, the most favourable model is the single field slow roll inflation model.

So far the most critical constraints on cosmological parameters, as well as on the initial conditions, come from CMB experiments [160]. While these constraints tell us that inflation did happen with a single scalar field, they do not shed light on how the inflation happened. Understanding the physics of inflation is one of the main goals of modern cosmology. The energy scale of inflation can be as large as  $10^6$  GeV, which is much higher than 10 TeV at which most particle accelerators are probing high energy physics [8]. The energy scale of inflation is much larger than any energy scale we can ever achieve in a particle accelerator. Thus, understanding the physics of inflation can tremendously improve our understanding of physics at very high energies. However, this understanding is not entirely possible from 2-point function measurements from the data. This is because if there is a presence of a small non-Gaussianity in the initial conditions, then going beyond the 2-point function or power spectrum becomes essential. These higher-point spectra probe the dynamics of inflation as they contain useful information about single or multiple scalar fields and their interactions in the early universe [143].

The primordial non-Gaussianity is quantified by non-Gaussianity parameters  $\{f_{\text{NL}}, g_{\text{NL}}, \dots\}$ . The recent Planck constraints on the local, equilateral, and orthogonal types non-Gaussianities are  $f_{\text{NL}}^{\text{loc}} = 0.8 \pm 5.0$ ,  $f_{\text{NL}}^{\text{eq}} = -4 \pm 43$ , and  $f_{\text{NL}}^{\text{orth}} = -26 \pm 21$  respectively [80]. From now onward, we use  $f_{\text{NL}}$  for local  $f_{\text{NL}}^{\text{loc}}$ . Planck sets the current constraints of  $\sigma(f_{\text{NL}}) \sim \mathcal{O}(5)$ , however, it has been shown that the compelling theoretical threshold is  $\sigma(f_{\text{NL}}) \sim 1$  [5, 25, 79, 178, 29]. This motivates us to go beyond the current limits, because if we can measure  $f_{\text{NL}} > 1$ , then it can rule out single field slow-roll inflation. Future CMB experiments [1, 192] have potential to reach  $\sigma(f_{\text{NL}}) \sim \mathcal{O}(1)$ , however, galactic and cosmological foregrounds will cause huge challenges to reach that limit. As it has been mentioned before in this thesis, that the large-scale structure (LSS) of the Universe has access to more information than CMB due to its three-dimensional nature. In LSS the constraint on  $f_{\text{NL}}$  depends on the number of modes as  $\sigma(f_{\text{NL}}) \propto [k_{\text{max}}^3 \log(k_{\text{max}}/k_{\text{min}})]^{-1/2}$ , where  $k_{\text{max}}$  is the maximum wavenumber accessible in LSS observables and  $k_{\text{min}}$  is the minimum wavenumber that depends on the survey. Although, in principle, we have access to more information due to three-dimensional nature, using LSS has different challenges. One of the challenges is that the scaling argument we just mentioned breaks down when we go to the non-linear regime

when  $k_{\max} > k_{\text{NL}}$ , where  $k_{\text{NL}}$  is the non-linear scale above which the perturbation theory fails. For current galaxy surveys,  $k_{\text{NL}} \approx 0.2h \text{ Mpc}^{-1}$  [58, 110]. Another challenge is to carefully model redshift space distortions effects [98]. Moreover, modelling of the full LSS bispectrum is also challenging because of non-Gaussian covariances of bispectrum [180, 184, 116].

To explain how measuring higher-point LSS statistics is computationally very expensive, we consider bispectrum and trispectrum. Measuring bispectrum requires that we consider the possible triangle configurations spanned by two independent Fourier modes (the third mode depends on the other two). If we divide each side of the simulation box in  $N$  independent  $k$ -bins, then the possible number of all triangle configuration scales roughly as  $\mathcal{O}(N^3)$ . The computational cost of measuring the trispectrum is even more than it is for the bispectrum. For the trispectrum, one has to check all the possible configurations of tetrahedra with four sides and two diagonals as independent degrees of freedom. It has been shown that this problem can be circumvented if we use compressed statistics [176, 83, 73, 43, 56, 167, 99]. The general idea is to write the maximum likelihood estimator for a separable bispectrum in terms of the cross-spectra of quadratic fields with the density field. This cross-spectra contains all bispectrum information optimally and is thus much more efficient because it only comes with the computational costs of simple power spectrum measurement. This method can be altered appropriately to put constraints on quadratic bias operators as well as quadratic primordial non-Gaussianity, parameterized by  $f_{\text{NL}}$ .

In LSS, local primordial non-Gaussianity can also affect the galaxy power spectrum. On large scales local primordial non-Gaussianity has a unique  $1/k^2$  imprints on the galaxy power spectrum [153, 133, 193]. Using this unique signature on large-scales, current galaxy surveys have used the galaxy power spectrum to put constraints on  $f_{\text{NL}}$  [97, 123, 48]. Unfortunately, the precision up to which we can constrain  $f_{\text{NL}}$  (or any other cosmological parameters or bias parameters on large scales) is affected by the shot noise and cosmic variance. Shot noise arises due to the discrete nature of the halo density field and the finite size of halos. On the other hand, the cosmic variance encodes the uncertainty in measuring the variance of the field from a small number of Fourier modes. We can reduce the impact of cosmic variance on measurements significantly if we also use the information present in the phases of all the modes by using multiple tracers of the underlying density field which contains different biases but the same phase [185, 141, 178]. Using multiple tracers allow us to cancel cosmic variance and therefore the measurement of the scale-dependent bias, that is  $f_{\text{NL}}$ , will depend on the number density of galaxy surveys [132, 178]. Using this method in LSS it is possible to achieve  $\sigma(f_{\text{NL}}) \sim 1$  [151, 178, 29, 192].

In this chapter, we explore a novel method of quadratic density reconstruction to access large scale modes and apply it to put constraints on local  $f_{\text{NL}}$ . Because of non-linear evolution and higher-order non-linear biasing, the long-wavelength modes are coupled with

different small-scale modes. In the presence of a fixed long-wavelength mode, the shorter modes can be averaged over in an ensemble. The correlation of two small-scale modes in the presence of a fixed long-wavelength mode also breaks the statistical homogeneity. We can write down a quadratic estimator and can estimate the long-wavelength modes using the statistical properties of small-scale modes. This method is quite similar to the method used in CMB lensing reconstruction [107]. The reconstruction using the quadratic estimator similar to the one used for the CMB lensing reconstruction was first used in [88]. Other similar examples of reconstruction methods introduced in the field are [159, 209, 210, 128, 149, 115, 130, 129]

Here we develop the quadratic estimator method for the density reconstruction from biased tracers using a full non-linear bias model for the first time. We apply this method to dark matter halos in numerical  $N$ -body simulations and demonstrate that our method performs very well according to our expectations. The simulation results agree with theoretical predictions. These results encourage us to explore applications of our reconstructions method. There are two main applications we explore in this work. First, LSS surveys are affected by observational systematics at large-scales which restrict us to observe very low- $k$  modes. For example, galaxy and quasar surveys are affected by foregrounds or galactic dust dynamics [171, 104, 114]. We define  $K_{\min}$  are the lowest wavenumber accessible from galaxy surveys. Using the quadratic reconstruction method we can, in principle, access modes which are much larger that is  $K < K_{\min}$ . In this way, we have more modes available which we can use in addition to the modes accessible from the galaxy survey only. The second application of our method is that we can constrain the local primordial non-Gaussianity,  $f_{\text{NL}}$ . We show that, like galaxy fields, the reconstructed modes also contains the unique  $1/k^2$  imprints from local primordial non-Gaussianity. This motivates us to use the reconstructed field alongside the galaxy field to do the multi-tracer analysis of local  $f_{\text{NL}}$  for some galaxy surveys. We show that from this method, we can improve  $f_{\text{NL}}$  constraints by tens of percents compared to only using a single galaxy field. In some cases, the improvement comes from cosmic variance cancellation, while in other cases the improvement comes from the fact that we are accessing additional modes  $K < K_{\min}$  from the reconstruction method which is unaffected by systematics.

The outline of this chapter is as follows. In Sec. 5.2, we discuss the theory of quadratic estimator method. We include the full non-linear bias model as well as terms introduced by primordial non-Gaussianity. We discuss reconstruction noise and contamination. We also derive higher-order shot noise terms which arise in auto- and cross-correlations of the reconstructed field and the galaxy field. In Sec. 5.3, we apply the method of density reconstruction to dark matter halos in numerical  $N$ -body simulations. We construct quadratic estimators corresponding to the growth, shift, and the tidal terms. We show that analytical predictions of cross-spectra of estimators with themselves as well as with the initial density

field agree with simulation results. In Sec. 5.4, we carry out Fisher forecasts for local  $f_{\text{NL}}$  using the multi-tracer analysis for some galaxy surveys and discuss our results. In Sec. 5.5, we conclude.

## 5.2 Density Field Reconstruction - theory

### 5.2.1 Quadratic Estimators

Our aim in this section is to derive a quadratic estimator formula for the linear density field, or large-scale density modes, from a galaxy field  $\delta_g$ . Later we will discuss that at second order  $\delta_g$  comprises of several non-linearities. These non-linearities come from gravitational clustering, galaxy biasing and primordial non-Gaussianity. We will take into account all these non-linearities to reconstruct large-scale density modes.

Derivation in this section closely follows [59, 88]. Let us consider the matter density field  $\delta$  at second order in Perturbation theory. In Fourier space, its expression is given by

$$\delta(\mathbf{k}, z) = D_1(z)\delta_1(\mathbf{k}) + D_1(z)^2 \int \frac{d^3\mathbf{q}}{(2\pi)^3} F_2(\mathbf{q}, \mathbf{k} - \mathbf{q}) \delta_1(\mathbf{q}) \delta_1(\mathbf{k} - \mathbf{q}) \quad (5.1)$$

where we define  $\delta(\mathbf{k})$  as the linear matter density at redshift  $z = 0$  and  $D_1(z)$  is the growth factor which depends on the redshift  $z$ . The second-order term is generated by gravity;  $F_2$  is the gravitational kernel defined by

$$F_2(\mathbf{k}_1, \mathbf{k}_2) = \frac{17}{21} + \frac{1}{2} \left( \frac{k_1}{k_2} + \frac{k_2}{k_1} \right) \hat{\mathbf{k}}_1 \cdot \hat{\mathbf{k}}_2 + \frac{2}{7} \left[ \left( \hat{\mathbf{k}}_1 \cdot \hat{\mathbf{k}}_2 \right)^2 - \frac{1}{3} \right]. \quad (5.2)$$

In the gravity kernel  $F_2$ , the first term corresponds to the growth term, the second corresponds to the shift, and the last term corresponds to the tidal term. For any biased tracer, such as the galaxy density field  $\delta_g$ , we can expand it up to second order in the linear density field in real space in the following way:

$$\delta_g(\mathbf{x}, z) = b_1 \delta_1(\mathbf{x}, z) + b_1 \delta^{(2)}(\mathbf{x}, z) + b_2 \delta_1^2(\mathbf{x}, z) + b_{s^2} s^2(\mathbf{x}, z) + \varepsilon(\mathbf{x}, z) \quad (5.3)$$

where  $\varepsilon$  is the shot noise term. We can rearrange different terms in Eq. (5.3) to get the following expression

$$\delta_g(\mathbf{x}, z) = b_1 \delta_1(\mathbf{x}, z) + 2b_1 \left( \frac{b_2}{b_1} + \frac{17}{21} \right) \delta_1^2(\mathbf{x}, z) + b_1 \Psi \cdot \nabla \delta_1(\mathbf{x}, z) + b_1 \left( \frac{b_{s^2}}{b_1} + \frac{2}{7} \right) s^2(\mathbf{x}, z). \quad (5.4)$$

In Fourier space we can write Eq. (5.4) as

$$\delta_g(\mathbf{k}, z) = D_1(z)b_1\delta_1(\mathbf{k}) + D_1(z)^2 \int_{\mathbf{q}} \left[ \sum_{\alpha} c_{\alpha} F_{\alpha}(\mathbf{q}, \mathbf{k} - \mathbf{q}) \right] \delta_1(\mathbf{q}) \delta_1(\mathbf{k} - \mathbf{q}) \quad (5.5)$$

where  $c_{\alpha}$  corresponds to bias parameters for growth, shift and tidal terms. We consider an ensemble average over all modes of  $\delta_1$  except those which are in a small neighborhood around some  $\mathbf{K}$ , where  $\delta_1(\mathbf{K})$  is what we want to reconstruct. We denote the ensemble average as " $\delta(\mathbf{K})$  fixed". We compute the 2-point function of Eq. (5.5) in Fourier space by fixing one mode  $\delta_1(\mathbf{K})$  in the following way:

$$\begin{aligned} \langle \delta_g(\mathbf{k}, z) \delta_g(\mathbf{K} - \mathbf{k}, z) \rangle_{\delta_1(\mathbf{k}) \text{ fixed}} &= D_1(z)^2 b_1^2 \langle \delta_1(\mathbf{k}) \delta_1(\mathbf{K} - \mathbf{k}) \rangle \\ &+ D_1(z)^3 b_1 \int_{\mathbf{q}} \sum_{\alpha} c_{\alpha} F_{\alpha}(\mathbf{q}, \mathbf{k} - \mathbf{q}) \langle \delta_1(\mathbf{q}) \delta_1(\mathbf{k} - \mathbf{q}) \delta_1(\mathbf{K} - \mathbf{k}) \rangle_{\delta_1(\mathbf{K}) \text{ fixed}} + [\mathbf{k} \leftrightarrow \mathbf{K} - \mathbf{k}]. \end{aligned} \quad (5.6)$$

In the first term we assumed that  $\mathbf{k}$  is not within the neighborhood of  $\mathbf{K}$  so the ensemble average is the same as the standard one. In the second term, if  $\mathbf{q}$  and  $\mathbf{K} - \mathbf{q}$  are not within the neighborhood then all three modes will be averaged over and the integral will be zero. If  $\mathbf{q}$  or  $\mathbf{K} - \mathbf{q}$  are in the neighborhood of  $\mathbf{K}$  then  $\delta_1(\mathbf{q})$  or  $\delta_1(\mathbf{K} - \mathbf{q})$  will be held fixed and the remaining two modes will be averaged over. The final result is

$$\langle \delta_g(\mathbf{k}, z) \delta_g(\mathbf{K} - \mathbf{k}, z) \rangle_{\delta_1(\mathbf{k}) \text{ fixed}} = D_1(z)^2 (2\pi)^3 \delta_{\mathbf{D}}(\mathbf{K}) b_1^2 P_{11}(K) + D_1(z)^3 \sum_{\alpha} b_1 c_{\alpha} f_{\alpha}(\mathbf{k}, \mathbf{K} - \mathbf{k}) \delta_1(\mathbf{K}) \quad (5.7)$$

where we can define the new kernel  $f_{\alpha}$  as

$$f_{\alpha}(\mathbf{q}_1, \mathbf{q}_2) \equiv 2 \left( F_{\alpha}(\mathbf{q}_1 + \mathbf{q}_2, -\mathbf{q}_1) P_{\text{lin}}(\mathbf{q}_1) + F_{\alpha}(\mathbf{q}_1 + \mathbf{q}_2, -\mathbf{q}_2) P_{\text{lin}}(\mathbf{q}_2) \right). \quad (5.8)$$

It can be seen in Eq. (5.7) that if we multiply two different modes of the galaxy field and then divide by the factor  $\sum_{\alpha} c_{\alpha} b_1 f_{\alpha}(\mathbf{k}, \mathbf{K} - \mathbf{k})$  then we will get an estimate of the linear density field, or the large-scale mode  $\delta_1(\mathbf{K})$ . In Eq. (5.7)  $b_1$  and  $c_{\alpha}$  are bias parameters which we do not know. If we can measure these bias parameters and use the values in this formalism then we can get unbiased estimator for the density field. However in the case when these biases are not know, we can define a biased estimator of the density field corresponding to a coupling factor  $\alpha$ . Given a quadratic mode coupling  $\alpha$ , we define a quadratic estimator as

$$\hat{\Delta}_{\alpha}(\mathbf{K}, z) = \int_{\mathbf{q}} g_{\alpha}(\mathbf{q}, \mathbf{K} - \mathbf{q}) \delta_g(\mathbf{q}, z) \delta_g(\mathbf{K} - \mathbf{q}, z) \quad (5.9)$$

where  $g_{\alpha}$  is the weight corresponding to the mode-coupling  $\alpha$  such that the estimator  $\hat{\Delta}_{\alpha}$  is optimal and unbiased. Optimal estimator means that the Gaussian contributions to the

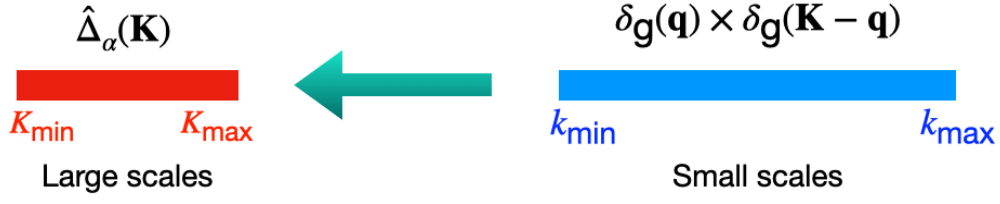


Fig. 5.1 The illustration shows how reconstruction of density field works. We reconstruct large scale modes from non-linear small scale modes of biased tracer field. The scales used in this diagram are defined in section 5.4.2.

variance of the estimator is minimum. The variance is defined as

$$\langle \hat{\Delta}_\alpha(\mathbf{K}) \hat{\Delta}_\alpha^*(\mathbf{k}') \rangle - \langle \hat{\Delta}_\alpha(\mathbf{K}) \rangle \langle \hat{\Delta}_\alpha^*(\mathbf{k}') \rangle. \quad (5.10)$$

and the unbiasedness condition is given by

$$\int \frac{d^3 \mathbf{q}}{(2\pi)^3} g_\alpha(\mathbf{q}, \mathbf{K} - \mathbf{q}) f_\alpha(\mathbf{q}, \mathbf{K} - \mathbf{q}) = 1. \quad (5.11)$$

These two conditions, unbiasedness and minimum variance, give us the following expression for the weight function  $g_\alpha$ :

$$g_\alpha(\mathbf{q}, \mathbf{K} - \mathbf{q}) = N_{\alpha\alpha}(\mathbf{K}) \frac{f_\alpha(\mathbf{q}, \mathbf{k} - \mathbf{q})}{2P_{\text{tot}}(\mathbf{q})P_{\text{tot}}(\mathbf{K} - \mathbf{q})} \quad (5.12)$$

where the normalization  $N_{\alpha\alpha}$  defines the Gaussian part of the variance of the quadratic estimator  $\hat{\Delta}_\alpha$ , also known as the reconstruction noise. The expression for the normalization is given by

$$N_{\alpha\beta}(\mathbf{K}) = \left[ \int_{\mathbf{q}} \frac{f_\alpha(\mathbf{q}, \mathbf{K} - \mathbf{q}) f_\beta(\mathbf{q}, \mathbf{K} - \mathbf{q})}{2P_{\text{tot}}(\mathbf{q})P_{\text{tot}}(\mathbf{K} - \mathbf{q})} \right]^{-1}. \quad (5.13)$$

In the presence of all three mode-coupling terms, each estimator is biased, with the expectation value given by a  $k$ -dependent factor times the initial density field:

$$\langle \hat{\Delta}_\alpha(\mathbf{K}) \rangle = b_1 \left[ c_\alpha + \sum_{\beta \neq \alpha} c_\beta \frac{N_{\alpha\alpha}(K)}{N_{\alpha\beta}(K)} \right] \delta_1(\mathbf{K}) \quad (5.14)$$

The ensemble average of the estimator is proportional to the linear density field with the scale-dependent bias factor, which depends on the bias parameters, as well as contamination arising due to mode-couplings in  $\delta_{\mathbf{g}}$ . We will discuss noise and contamination in Sec. 5.2.3. We define the matrix form of the estimators corresponding to the growth, the shift and the

tidal terms as:

$$\begin{pmatrix} \langle \hat{\Delta}_g \rangle \\ \langle \hat{\Delta}_s \rangle \\ \langle \hat{\Delta}_t \rangle \end{pmatrix} = b_1 \begin{pmatrix} 1 & \frac{N_{gg}}{N_{gs}} & \frac{N_{gg}}{N_{gt}} \\ \frac{N_{ss}}{N_{gs}} & 1 & \frac{N_{ss}}{N_{ts}} \\ \frac{N_{tt}}{N_{gt}} & \frac{N_{tt}}{N_{ts}} & 1 \end{pmatrix} \begin{pmatrix} c_g \\ c_s \\ c_t \end{pmatrix} \delta_1(\mathbf{K}). \quad (5.15)$$

In a more compact notation we can express Eq. (5.15) as  $\langle \hat{\Delta}_i(\mathbf{K}) \rangle = b_1 \sum_j c_j M_{ij}(\mathbf{K}) \delta_1(\mathbf{K})$ , where  $M_{ij}$  is the  $3 \times 3$  matrix. The covariance of two estimators  $\hat{\Delta}_\alpha$  and  $\hat{\Delta}_\beta$  is given by

$$\begin{aligned} \text{Cov}(\hat{\Delta}_\alpha(\mathbf{K}), \hat{\Delta}_\beta(\mathbf{K}')) &= \langle \hat{\Delta}_\alpha(\mathbf{K}) \hat{\Delta}_\beta(\mathbf{K}') \rangle - \langle \hat{\Delta}_\alpha(\mathbf{K}) \rangle \langle \hat{\Delta}_\beta(\mathbf{K}') \rangle \\ &= \int \int \frac{d^3 \mathbf{q}}{(2\pi)^3} \frac{d^3 \mathbf{p}}{(2\pi)^3} g_\alpha(\mathbf{q}, \mathbf{K} - \mathbf{q}) g_\beta(\mathbf{p}, \mathbf{K}' - \mathbf{p}) \left( \left\langle \delta_g(\mathbf{q}) \delta_g(\mathbf{K} - \mathbf{q}) \delta_g(\mathbf{p}) \delta_g(\mathbf{K}' - \mathbf{p}) \right\rangle \right. \\ &\quad \left. - \left\langle \delta_g(\mathbf{q}) \delta_g(\mathbf{K} - \mathbf{q}) \right\rangle \left\langle \delta_g(\mathbf{p}) \delta_g(\mathbf{K}' - \mathbf{p}) \right\rangle \right) \\ &= (2\pi)^3 \delta_D^{(3)}(\mathbf{K} + \mathbf{K}') \left[ \frac{N_{\alpha\alpha}(\mathbf{K}) N_{\beta\beta}(\mathbf{K})}{N_{\alpha\beta}(\mathbf{K})} + N_{\alpha\beta, \text{shot}}(\mathbf{K}) \right]. \end{aligned} \quad (5.16)$$

In general, the covariance depends on the Gaussian and the non-Gaussian terms. Here, we only focus on the Gaussian covariances because we are interested in large-scale modes; in Sec. 5.3.6 we discuss why this is a fairly reasonable assumption. In Eq. (5.16), the first term is the noise term which depends on the auto- and cross normalisation factors and is of the order  $\mathcal{O}(\delta^4)$ . The second term, however, is the trispectrum shot noise term and is of order  $\mathcal{O}(\delta^6)$ . The higher-order shot noise terms  $N_{\alpha\beta, \text{shot}}$  are discussed in Sec. 5.2.5. The leading order variance of  $\hat{\Delta}_\alpha$  can be described as  $\text{Var}(\hat{\Delta}_\alpha(\mathbf{K})) = N_{\alpha\alpha}(\mathbf{K})$  (after ignoring the higher-order shot noise term). This means the leading order variance is the reconstruction noise.

Similarly, the cross-correlation of the estimator with the galaxy field can be expressed as

$$\begin{aligned} \text{Cov}(\hat{\Delta}_\alpha(\mathbf{K}), \delta_g(\mathbf{K}')) &= \langle \hat{\Delta}_\alpha(\mathbf{K}) \delta_g(\mathbf{K}') \rangle - \langle \hat{\Delta}_\alpha(\mathbf{K}) \rangle \langle \delta_g(\mathbf{K}') \rangle \\ &= \int \frac{d^3 \mathbf{q}}{(2\pi)^3} g_\alpha(\mathbf{q}, \mathbf{K} - \mathbf{q}) \left( \left\langle \delta_g(\mathbf{q}) \delta_g(\mathbf{K} - \mathbf{q}) \delta_g(\mathbf{K}') \right\rangle - \left\langle \delta_g(\mathbf{q}) \delta_g(\mathbf{K} - \mathbf{q}) \right\rangle \left\langle \delta_g(\mathbf{K}') \right\rangle \right) \\ &= (2\pi)^3 \delta_D^{(3)}(\mathbf{K} + \mathbf{K}') N_{\alpha, \text{shot}}(\mathbf{K}), \end{aligned} \quad (5.17)$$

where  $N_{\alpha, \text{shot}}$  is the bispectrum shot noise term which is also discussed in Sec. 5.2.5.

mode couplings	$c_\alpha$	$F_\alpha(\mathbf{k}_1, \mathbf{k}_2)$
$g$	$b_1 + \frac{21}{17}b_2$	$\frac{17}{21}$
$s$	$b_1$	$\frac{1}{2}\left(\frac{1}{k_1^2} + \frac{1}{k_2^2}\right)(\mathbf{k}_1 \cdot \mathbf{k}_2)$
$t$	$b_1 + \frac{7}{2}b_{s^2}$	$\frac{2}{7}\left[\frac{(\mathbf{k}_1 \cdot \mathbf{k}_2)^2}{k_1^2 k_2^2} - \frac{1}{3}\right]$
$\phi\phi$	$b_1$	$\frac{M( \mathbf{k}_1 + \mathbf{k}_2 , z)}{M(\mathbf{k}_1, z)M(\mathbf{k}_2, z)}$
01	$2\delta_c(b_1 - 1)$	$\frac{1}{2}\mathbf{k}_1 \cdot \mathbf{k}_2 \left(\frac{1}{k_2^2 M(\mathbf{k}_1)} + \frac{1}{k_1^2 M(\mathbf{k}_2)}\right)$
11	$2\left(\delta_c \left[\frac{b_2 - 2(a_1 + a_2)(b_1 - 1)}{a_1}\right] - a_1[b_1 - 1]\right) + 2\delta_c(b_1 - 1)$	$\frac{1}{2}\left(\frac{1}{M(\mathbf{k}_1, z)} + \frac{1}{M(\mathbf{k}_2, z)}\right)$
02	$4\delta_c \left(\delta_c \left[\frac{b_2 - 2(a_1 + a_2)(b_1 - 1)}{a_1^2}\right] - 2[b_1 - 1]\right)$	$\frac{1}{M(\mathbf{k}_1, z)M(\mathbf{k}_2, z)}$

Table 5.1 Summary of mode couplings,  $f_{\text{NL}}$  components ( $\phi\phi$ , 01, 11, and 02), their respective biases  $c_\alpha$  and quadratic coupling kernels  $F_\alpha$ .

## 5.2.2 Bias Expansion with non-Gaussianity

In this section, we discuss galaxy biasing in the presence of primordial non-Gaussianity (see [19, 9, 96] for more detailed discussion). Considering the homogeneity and isotropy of the initial conditions, we can write the primordial Gaussian potential  $\phi_{\text{nG}}$  as

$$\phi_{\text{nG}}(\mathbf{k}) = \phi_{\text{G}}(\mathbf{k}) + f_{\text{NL}} \int \frac{d^3\mathbf{q}}{(2\pi)^3} \left[ \phi_{\text{G}}(\mathbf{q})\phi_{\text{G}}(\mathbf{q} - \mathbf{k}) - P_\phi(\mathbf{q})\hat{\delta}_{\text{D}}(\mathbf{k}) \right] + \dots \quad (5.18)$$

where  $\phi_{\text{G}}$  is a primordial Gaussian potential,  $f_{\text{NL}}$  is the parameter that quantifies the deviation from Gaussianity,  $P_\phi$  is the power spectrum of  $\phi_{\text{G}}$ , and  $\hat{\delta}_{\text{D}}$  is the Dirac delta function. In the Newtonian limit, the Poisson equation relates the primordial Gaussian potential to the primordial density perturbation  $\delta_p$  as

$$\phi_{\text{G}}(\mathbf{k}) = \frac{\delta_p(\mathbf{k}, z)}{M(k, z)}, \quad (5.19)$$

where

$$M(k, z) = \frac{2k^2 c^2 D(z) T(k)}{3H_0^2 \Omega_m} \frac{a(z=0)}{a(z=\infty)}. \quad (5.20)$$

In the above equation,  $c$  is the speed of light,  $T(k)$  is the transfer function which scales as unity on large scales,  $D(z)$  is the growth factor and  $a(z)$  is the scale factor as a function of redshift  $z$ . The Eq. (5.20) scales as  $k^2/H^2$  on large scales. At first order, the linearly evolved density perturbation depends on the Gaussian potential,  $\delta_p^{(1)}(\mathbf{k}, z) = M(k, z)\phi_{\text{G}}(\mathbf{k})$ . At higher orders, the non-Gaussian couplings of the potential introduce non-linearities in the density field. We write the matter density field in the presence of local non-Gaussianity at



second order as

$$\begin{aligned}\delta_p(\mathbf{k}, z) &= M(k, z)\phi_{\text{nG}}(\mathbf{k}) = M(k, z)\phi_G(\mathbf{k}) + M(k, z)f_{\text{NL}} \int \frac{d^3\mathbf{q}}{(2\pi)^3} \phi_G(\mathbf{q})\phi_G(\mathbf{k}-\mathbf{q}) \\ &= \delta_p^{(1)}(\mathbf{k}, z) + f_{\text{NL}}\delta_p^{(2)}(\mathbf{k}, z).\end{aligned}\quad (5.21)$$

This primordial density perturbation is then evolved under the effect of gravity to produce late-time non-linear couplings due to gravitational clustering. The first and second-order density perturbations in the presence of gravity and primordial non-Gaussianity are given as

$$\begin{aligned}\text{First Order: } & \delta_p^{(1)}(\mathbf{k}, z), \\ \text{Second Order: } & \int \frac{d^3\mathbf{q}}{(2\pi)^3} \delta_p^{(1)}(\mathbf{q}, z)\delta_p^{(1)}(\mathbf{q}-\mathbf{k}, z)F_2(\mathbf{q}, \mathbf{k}-\mathbf{q}) + f_{\text{NL}}\delta_p^{(2)}(\mathbf{k}, z),\end{aligned}\quad (5.22)$$

where  $F_2$  is the second order gravitational coupling kernel. To summarise, the full expression for late-time matter density at second order is given by

$$\begin{aligned}\delta_m(\mathbf{k}, z) &= \delta_1(\mathbf{k}, z) + \int \frac{d^3\mathbf{q}}{(2\pi)^3} \delta_1(\mathbf{q}, z)\delta_1(\mathbf{q}-\mathbf{k}, z)F_2(\mathbf{q}, \mathbf{k}-\mathbf{q}) \\ &+ f_{\text{NL}}M(k, z) \int \frac{d^3\mathbf{q}}{(2\pi)^3} \phi_G(\mathbf{q})\phi_G(\mathbf{k}-\mathbf{q}),\end{aligned}\quad (5.23)$$

where we replaced  $\delta_p^{(1)}$  by  $\delta_1$  for simplicity of notation. We can now use Eq. (5.23) to expand the galaxy density field  $\delta_g$  to include non-linear mode couplings from gravity, biasing and primordial non-Gaussianity at second order in density perturbation [96]:

$$\begin{aligned}\delta_g(\mathbf{k}, z) &= b_1\delta_1(\mathbf{k}, z) + f_{\text{NL}}c_{01} \frac{\delta_1(\mathbf{k}, z)}{M(\mathbf{k}-\mathbf{q}, z)} \\ &+ \sum_{\alpha \in \{g, s, t\}} c_\alpha \int_{\mathbf{q}} \delta_1(\mathbf{q}, z)\delta_1(\mathbf{k}-\mathbf{q}, z)F_\alpha(\mathbf{q}, \mathbf{k}-\mathbf{q}) \\ &+ f_{\text{NL}} \sum_{\alpha \in \{\phi\phi, 01, 11\}} c_\alpha \int_{\mathbf{q}} \delta_1(\mathbf{q}, z)\delta_1(\mathbf{k}-\mathbf{q}, z)F_\alpha(\mathbf{q}, \mathbf{k}-\mathbf{q}) \\ &+ f_{\text{NL}}^2 c_{02} \int_{\mathbf{q}} \delta_1(\mathbf{q}, z)\delta_1(\mathbf{k}-\mathbf{q}, z)F_{02}(\mathbf{q}, \mathbf{k}-\mathbf{q}).\end{aligned}\quad (5.24)$$

We define mode-coupling functions  $F_\alpha$  and bias parameters  $c_\alpha$  in Table 5.1. The bias parameters  $c_{01}$ ,  $c_{11}$ , and  $c_{02}$  depend on further new parameters  $a_1$ ,  $a_2$  and  $\delta_c$ . These new parameters can be defined by the spherical collapse dynamics [166]. The coefficients  $a_i$  relate the linearly evolved Lagrangian density field with the overdensity in Eulerian space.  $\delta_c$  is the density threshold, which means that if at some region  $\delta > \delta_c$ , then that region

collapses to form a dark matter halo. In spherical collapse dynamics  $\delta_c = 1.69$ ,  $a_1 = 1$ , and  $a_2 = -17/21$ .

### 5.2.3 Noise and Contamination

In the previous sections, we derived a quadratic estimator formula using a galaxy field  $\delta_g$  which includes non-linearities from gravitational clustering, galaxy biasing and primordial non-Gaussianity. Taking into account all three of these non-linearities, we see there are seven quadratic mode-couplings. In this section, we discuss the reconstructed noise and the contamination due to various mode-couplings in the reconstructed field.

In Fig. 5.2 we plot noise curves  $N_{\alpha\alpha}$ , where  $\alpha \in \{g, s, t, \phi\phi, c11\}$ , as well as contamination arising due to different mode couplings for a DESI-like survey. The configuration of a DESI-like survey is given in Table 5.1. In the figure, we see the noise due to the growth estimator is the lowest among all mode-couplings. However, for a DESI-like survey, we can see that even the noise due to the growth term is more than the linear power spectrum  $P_{lin}$ . This is the reason for low signal-to-noise when we do the forecast to measure  $\sigma(f_{NL})$  in Sec. 5.4. The maximum wavenumber used to compute the noise curves is  $k_{max} = 0.15h$   $Mpc^{-1}$ . Increasing the  $k_{max}$  reduces the amplitude of the noise curves and therefore allows better reconstruction. In Sec. 5.3 we show that the theory predictions agree very well for the growth, shift and tidal estimators with  $k_{max} = 0.1h$   $Mpc^{-1}$  at redshift  $z = 0$ . For higher  $k_{max}$ , higher-order terms become important, which we do not take into account in this work. We also checked noise curves for other survey configurations and for some high redshift surveys the noise due to the growth estimator is in fact low which results in increasing  $\sigma(f_{NL})$  constraints. Because of lower noise due to the growth estimator compared with other mode couplings we use the growth estimator for our Fisher forecasts analysis in this work to constraint local  $f_{NL}$  in Sec. 5.4.

In the right panel of Fig. 5.2 we plot several contaminations arising due to several mode-couplings in the reconstructed field  $\delta_r$  from the growth estimator as given in Eq. (5.14). If we cross-correlate the estimator  $\hat{\Delta}_\alpha$  with the linear field we expect to get the linear power spectrum multiplied by a  $k$ -dependent bias factor which arises due to these contaminations. We can also clearly see that mode coupling due to  $f_{NL}$  ( $\phi\phi$ ,  $c02$ , and  $c11$ ) show  $1/k^2$  type behaviour. The local primordial non-Gaussianity has a unique  $1/k^2$  imprint on the galaxy field  $\delta_g$  [153]. As the large-scale reconstructed modes also have the same  $k^{-2}$  behaviour due to the local primordial non-Gaussianity, it is possible to use the reconstructed modes with the galaxy field to get better constraint on local  $f_{NL}$ . This is what we call "multi-tracer" analysis using a single tracer and will discuss in more detail in Sec. 5.4. We also show how we can use this method to cancel cosmic variance and get better  $f_{NL}$  constraints.

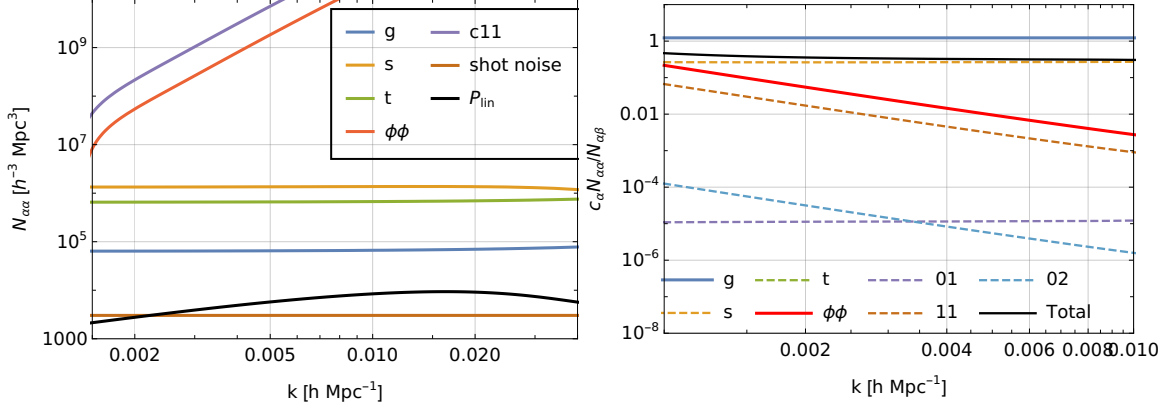


Fig. 5.2 Noise and contamination for a DESI-like survey, with a mean redshift  $\bar{z} = 1$ . LEFT PANEL: we plot noise curves  $N_{\alpha\alpha}$  where  $\alpha \in \{g, s, t, \phi\phi, c11\}$  and compare them with shot noise  $\bar{n}^{-1}$  and linear power spectrum  $P_{\text{lin}}$ . We do not plot noise corresponding to other remaining mode-couplings  $c_{01}$  and  $c_{02}$  because their amplitude is too large. RIGHT PANEL: Contamination by bias parameters to the growth estimator. The dashed curves represent negative contribution and the black solid line is the total contamination. The contribution by three  $f_{\text{NL}}$  terms ( $\phi\phi$ , 11, and 02) clearly show  $k^{-2}$  behaviour.

### 5.2.4 Bias-Hardening Case: Why doesn't it Work?

We see from Eq. (5.14) that other mode couplings induce mean-field contamination to the ensemble average of the density estimator  $\hat{\Delta}_{\alpha}$ . There is a way to construct a so-called "bias-hardened" estimator  $\hat{\Delta}_{\alpha}^{\text{H}}$  using a linear combination of other mode-couplings so that there is no mean-field contamination at the leading order [156, 88, 152]. We try to implement bias-hardening and find that the estimator corresponding to the shift term is unbiased, meaning that there is no mean-field contamination (if we neglect  $f_{\text{NL}}$  terms). However, bias-hardening blows up the noise, and therefore it is useless in this work.

Let us show this explicitly using three mode couplings only (g, s, and t). We describe "unbias-hardened" estimators in Matrix form in Eq. (5.15). We will refer to the  $3 \times 3$  matrix in that equation as  $M$ . We define bias-hardened estimators as:

$$\begin{pmatrix} \langle \hat{\Delta}_g^{\text{H}} \rangle \\ \langle \hat{\Delta}_s^{\text{H}} \rangle \\ \langle \hat{\Delta}_t^{\text{H}} \rangle \end{pmatrix} = \frac{1}{\det(M)} \begin{pmatrix} 1 - \frac{N_{\text{ss}}N_{\text{tt}}}{N_{\text{ts}}^2} & N_{\text{gg}} \left( \frac{N_{\text{tt}}}{N_{\text{gt}}N_{\text{ts}}} - \frac{1}{N_{\text{gs}}} \right) & N_{\text{gg}} \left( \frac{N_{\text{ss}}}{N_{\text{gs}}N_{\text{ts}}} - \frac{1}{N_{\text{gt}}} \right) \\ N_{\text{ss}} \left( \frac{N_{\text{tt}}}{N_{\text{gt}}N_{\text{ts}}} - \frac{1}{N_{\text{gs}}} \right) & 1 - \frac{N_{\text{gg}}N_{\text{tt}}}{N_{\text{gt}}^2} & N_{\text{ss}} \left( \frac{N_{\text{gg}}}{N_{\text{gs}}N_{\text{gt}}} - \frac{1}{N_{\text{ts}}} \right) \\ N_{\text{tt}} \left( \frac{N_{\text{ss}}}{N_{\text{gs}}N_{\text{ts}}} - \frac{1}{N_{\text{gt}}} \right) & N_{\text{tt}} \left( \frac{N_{\text{gg}}}{N_{\text{gs}}N_{\text{gt}}} - \frac{1}{N_{\text{ts}}} \right) & 1 - \frac{N_{\text{gg}}N_{\text{ss}}}{N_{\text{gs}}^2} \end{pmatrix} \begin{pmatrix} \langle \hat{\Delta}_g \rangle \\ \langle \hat{\Delta}_s \rangle \\ \langle \hat{\Delta}_t \rangle \end{pmatrix}. \quad (5.25)$$

The expectation of the bias-hardened estimators is thus given by

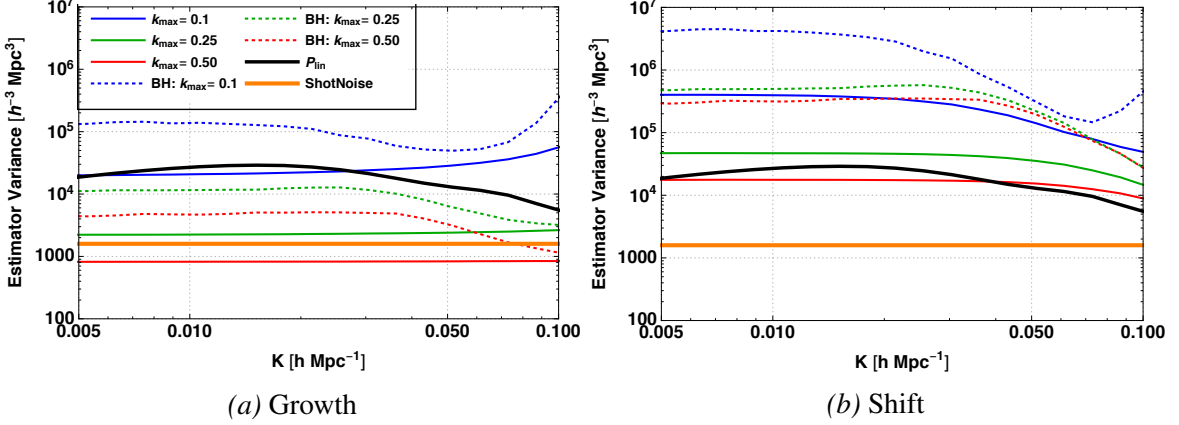


Fig. 5.3 Bias hardened and unbiased variance for growth (left) and shift (right) estimators for  $k_{\max} = 0.1h \text{ Mpc}^{-1}$ ,  $0.25h \text{ Mpc}^{-1}$ , and  $0.5h \text{ Mpc}^{-1}$ . The unbiased-hardened curves are plotted in solid curves, while bias-hardened curves are plotted in dotted curves. We also plot the shot noise (orange solid curve) and the linear power spectrum (black solid curve) to compare the overall noise with the signal. The bias hardening increases the reconstruction noise a lot. The effect is more severe in the shift estimator.

$$\langle \hat{\Delta}_{\alpha}^{\text{H}}(\mathbf{k}) \rangle = \sum_{\beta} (M^{-1})_{\alpha\beta} b_1 \left[ c_{\beta} + \sum_{\beta \neq \gamma} c_{\gamma} \frac{N_{\beta\beta}(\mathbf{k})}{N_{\beta\gamma}(\mathbf{k})} \right] \delta_1(\mathbf{k}) \quad (5.26)$$

For the shift term, it is  $\langle \hat{\Delta}_{\text{S}}^{\text{H}}(\mathbf{k}) \rangle = b_1 \delta_1(\mathbf{k})$ . In Fig. 5.3, we plot the variance of the growth and the shift estimators for bias-hardened and unbiased-hardened cases. We use three different  $k_{\max}$  ( $0.1h \text{ Mpc}^{-1}$ ,  $0.25h \text{ Mpc}^{-1}$ , and  $0.5h \text{ Mpc}^{-1}$ ) and also plot the linear power spectrum for comparison. Dotted lines represent bias-hardened curves. Although for the shift term we get unbiased estimator from bias-hardening, we can see that the noise is too large compared to the linear power spectrum. This is the reason why we only use the unbiased-hardened growth estimator, which has the lowest noise. The bias parameters that enter into the growth estimator formula can be measured either using  $N$ -body simulations or directly from data. In this work, we use fiducial values of bias parameters measured from numerical  $N$ -body simulations [2].

### 5.2.5 Shot Noise

Here we discuss the shot noise terms that may enter in the auto- and cross-correlations of quadratic estimators, as well as cross-correlations of quadratic estimators with the galaxy field. There are three contributions from shot noise that appear at the level of the power spectrum, bispectrum and the trispectrum in our analysis. The origin of the shot noise is the stochasticity bias (see [68] for more details). Usually, galaxy bias relation is deterministic, and we expand it in terms of operators which depends on the large scale density perturbations.

However, in reality, as we know that galaxies are discrete tracers and the location where galaxies are formed depends on small scale dynamics. The phases of the small scale perturbations are not determined, so we include this stochasticity separately in the bias expansion. The final galaxy bias expansion we write is given by

$$\delta_g(\mathbf{x}, \tau) = \sum_{\mathcal{O}} b_{\mathcal{O}} \mathcal{O}[\delta](\mathbf{x}, \tau) + \varepsilon(\mathbf{x}, \tau) + \sum_{\mathcal{O}} \varepsilon_{\mathcal{O}}(\mathbf{x}, \tau) \mathcal{O}[\delta](\mathbf{x}, \tau) \quad (5.27)$$

where  $\mathcal{O}[\delta]$  are bias operators,  $\varepsilon$  is the stochasticity,  $\varepsilon_{\mathcal{O}}$  is the stochasticity related to the randomness of the initial conditions on small scales (corresponding to bias operators). We now derive the expression contributing to shot noise at the power spectrum, bispectrum and trispectrum level. Let us consider a finite number of galaxies  $N$  confined in a finite volume  $V$  at positions  $\mathbf{x}_i$  in real space. We can define the discrete galaxy overdensity as

$$\delta_g(\mathbf{x}) = \frac{1}{\bar{n}} \sum_i \delta_D(\mathbf{x} - \mathbf{x}_i), \quad (5.28)$$

where  $\bar{n}$  is the mean number density of galaxies and  $\delta_D$  is the Dirac delta function. We define the number density of the tracer as  $n(\mathbf{x}) = \sum_i \delta_D(\mathbf{x} - \mathbf{x}_i)$ . In Fourier space, Eq. (5.28) can be expressed as

$$\delta_g(\mathbf{k}) = \frac{1}{\bar{n}} \sum_i \exp(i\mathbf{k} \cdot \mathbf{x}_i). \quad (5.29)$$

From this the power spectrum of the discrete galaxy overdensity can be computed as

$$\begin{aligned} P_{gg}(\mathbf{k}) &= \frac{1}{V} \langle \delta_g(\mathbf{k}) \delta_g(-\mathbf{k}) \rangle = \frac{V}{N^2} \left[ \sum_{i=j} \langle \exp(i\mathbf{k} \cdot (\mathbf{x}_i - \mathbf{x}_j)) \rangle + \sum_{i \neq j} \langle \exp(i\mathbf{k} \cdot (\mathbf{x}_i - \mathbf{x}_j)) \rangle \right] \\ &= \frac{1}{\bar{n}} + P_{gg, \text{cont}}(\mathbf{k}), \end{aligned} \quad (5.30)$$

where  $P_{gg, \text{cont}}$  is the continuous galaxy power spectrum and  $1/\bar{n}$  is the power spectrum shot noise. Now, we focus on how to derive the bispectrum shot noise  $N_{\alpha, \text{shot}}$  and the trispectrum shot noise  $N_{\alpha\beta, \text{shot}}$  described in Eq.(5.17) and Eq. (5.16) respectively. For calculating the bispectrum and the trispectrum shot noise terms we strictly follow the derivations given in [52]. We write the discrete 3-point function  $\zeta_d$  in real using Eq. (5.28) as

$$\zeta_d(\mathbf{x}_1, \mathbf{x}_2, \mathbf{x}_3) = \langle \delta_g(\mathbf{x}_1) \delta_g(\mathbf{x}_2) \delta_g(\mathbf{x}_3) \rangle = \frac{\langle n(\mathbf{x}_1) n(\mathbf{x}_2) n(\mathbf{x}_3) \rangle}{\bar{n}^3} - \left[ \frac{\langle n(\mathbf{x}_1) n(\mathbf{x}_2) \rangle}{\bar{n}^2} + 2\text{cyc.} \right] + 2, \quad (5.31)$$

where cyc describes the cyclic permutations. In Eq. (5.31) we describe the 3-point correlation function of  $n$  as

$$\begin{aligned}
\langle n(\mathbf{x}_1)n(\mathbf{x}_2)n(\mathbf{x}_3) \rangle &= \left\langle \sum_i \delta_D(\mathbf{x}_1 - \mathbf{x}_i) \delta_D(\mathbf{x}_2 - \mathbf{x}_i) \delta_D(\mathbf{x}_3 - \mathbf{x}_i) \right\rangle \\
&+ \left[ \left\langle \sum_{i,j} \delta_D(\mathbf{x}_1 - \mathbf{x}_i) \delta_D(\mathbf{x}_2 - \mathbf{x}_j) \delta_D(\mathbf{x}_3 - \mathbf{x}_j) \right\rangle + 2\text{cyc.} \right] \\
&+ \left\langle \sum_{i,j,k} \delta_D(\mathbf{x}_1 - \mathbf{x}_i) \delta_D(\mathbf{x}_2 - \mathbf{x}_j) \delta_D(\mathbf{x}_3 - \mathbf{x}_k) \right\rangle \\
&= \delta_D(\mathbf{x}_1 - \mathbf{x}_2) \delta_D(\mathbf{x}_1 - \mathbf{x}_3) \bar{n} + \left[ \bar{n}^2 \delta_D(\mathbf{x}_2 - \mathbf{x}_3) (1 + \xi_{12}) + 2\text{cyc.} \right] \\
&+ \bar{n}^3 (1 + \xi_{12} + \xi_{13} + \xi_{31} + \zeta),
\end{aligned} \tag{5.32}$$

where  $\xi_{ij}$  is the short notation for  $\xi(|\mathbf{x}_i - \mathbf{x}_j|)$  and  $\zeta$  is the continuous 3-point function. We substitute Eq. (5.32) in Eq.(5.31) to get

$$\zeta_d(\mathbf{x}_1, \mathbf{x}_2, \mathbf{x}_3) = \frac{1}{\bar{n}^2} \delta_D(\mathbf{x}_1 - \mathbf{x}_2) \delta_D(\mathbf{x}_1 - \mathbf{x}_3) + \left[ \frac{\delta_D(\mathbf{x}_2 - \mathbf{x}_3)}{\bar{n}} \xi_{12} + 2\text{cyc.} \right] + \zeta. \tag{5.33}$$

This equation in Fourier space describe the discrete bispectrum as

$$B_d(\mathbf{k}_1, \mathbf{k}_2, \mathbf{k}_3) = \frac{1}{\bar{n}^2} + \frac{1}{\bar{n}} \left( P_{g,\text{cont}}(\mathbf{k}_1) + P_{g,\text{cont}}(\mathbf{k}_2) + P_{g,\text{cont}}(\mathbf{k}_3) \right) + B_{g,\text{cont}}(\mathbf{k}_1, \mathbf{k}_2, \mathbf{k}_3), \tag{5.34}$$

where  $P_{g,\text{cont}}$  and  $B_{g,\text{cont}}$  are the continuous galaxy power spectrum and bispectrum respectively. In Eq. (5.34) the first two terms contribute to the bispectrum shot noise. In the cross-correlation of quadratic estimators with the galaxy field, the leading order noise term is the bispectrum shot noise as described in Eq. (5.17). This is because in the cross-correlation we have to compute the galaxy 3-point function  $\langle \delta_g \delta_g \delta_g \rangle$ . Now it is easy to see that the shot noise term  $N_{\alpha,\text{shot}}$  in Eq. (5.17) is described as

$$N_{\alpha,\text{shot}}(\mathbf{k}) = \int \frac{d^3 \mathbf{q}}{(2\pi)^3} g_\alpha(\mathbf{q}, \mathbf{k} - \mathbf{q}) \left[ \frac{1}{\bar{n}^2} + \frac{1}{\bar{n}} \left( P_{g,\text{cont}}(\mathbf{q}) + P_{g,\text{cont}}(\mathbf{k} - \mathbf{q}) + P_{g,\text{cont}}(-\mathbf{k}) \right) \right]. \tag{5.35}$$

In Sec. 5.4, we denote the bispectrum shot noise given by the above expression as  $P_{gr,\text{shot}}$ , where we denote  $\alpha = r$  for reconstruction due to the quadratic estimator. For auto- and cross-correlations of quadratic estimators, we need to compute the galaxy four point function  $\langle \delta_g \delta_g \delta_g \delta_g \rangle$ . The leading order covariance described in Eq. (5.16) depends on the normalisation factors and is of order  $\mathcal{O}(\delta^4)$ . The next-order contribution to the noise comes from the term which is of order  $\mathcal{O}(\delta^6)$  and contributes to the Poisson shot noise. This  $\mathcal{O}(\delta^6)$  is described as  $N_{\alpha\beta,\text{shot}}$  in Eq. (5.16) and is what we describe as the trispectrum shot noise

term. We now derive the full expression for this term. We write the discrete 4-point function  $\eta_d$  as

$$\begin{aligned} \eta_d(\mathbf{x}_1, \mathbf{x}_2, \mathbf{x}_3, \mathbf{x}_4) = & \frac{1}{\bar{n}^4} \langle n(\mathbf{x}_1)n(\mathbf{x}_2)n(\mathbf{x}_3)n(\mathbf{x}_4) \rangle - \left[ \frac{1}{\bar{n}^3} \langle n(\mathbf{x}_1)n(\mathbf{x}_2)n(\mathbf{x}_3) \rangle + 3\text{cyc.} \right] \\ & + \left[ \frac{1}{\bar{n}^2} \langle n(\mathbf{x}_1)n(\mathbf{x}_2) \rangle + 5\text{cyc.} \right] - 3. \end{aligned} \quad (5.36)$$

The four point correlation function of the number density can be described as

$$\begin{aligned} \langle n(\mathbf{x}_1)n(\mathbf{x}_2)n(\mathbf{x}_3)n(\mathbf{x}_4) \rangle = & \frac{1}{\bar{n}^3} \delta_D(\mathbf{x}_1 - \mathbf{x}_2) \delta_D(\mathbf{x}_1 - \mathbf{x}_3) \delta_D(\mathbf{x}_1 - \mathbf{x}_4) \\ & + \left[ \frac{1}{\bar{n}^2} \delta_D(\mathbf{x}_2 - \mathbf{x}_3) \delta_D(\mathbf{x}_2 - \mathbf{x}_4) \xi_{12} + 3\text{cyc.} \right] + \left[ \frac{1 + \xi_{13}}{\bar{n}^2} \delta_D(\mathbf{x}_1 - \mathbf{x}_2) \delta_D(\mathbf{x}_3 - \mathbf{x}_4) \xi_{12} + 2\text{cyc.} \right] \\ & + \left[ \frac{\delta_D(\mathbf{x}_1 - \mathbf{x}_2)}{\bar{n}} (\xi_{34} + \zeta_{234}) + 5\text{cyc.} \right] + \eta_{1234}. \end{aligned} \quad (5.37)$$

In Fourier space, we can write the discrete trispectrum expression as

$$\begin{aligned} T_d(\mathbf{k}_1, \mathbf{k}_2, \mathbf{k}_3, \mathbf{k}_4) = & \frac{1}{\bar{n}^3} + \frac{1}{\bar{n}^2} \left( P_{g,\text{cont}}(\mathbf{k}_1) + 3 \text{ cyc.} \right) + \frac{1}{\bar{n}^2} \left( \delta^{(D)}(\mathbf{k}_1 + \mathbf{k}_2) + P_{g,\text{cont}}(\mathbf{k}_1 + \mathbf{k}_2) \right. \\ & \left. + \delta^{(D)}(\mathbf{k}_1 + \mathbf{k}_3) + P_{g,\text{cont}}(\mathbf{k}_1 + \mathbf{k}_3) + \delta^{(D)}(\mathbf{k}_1 + \mathbf{k}_4) + P_{g,\text{cont}}(\mathbf{k}_1 + \mathbf{k}_4) \right) \\ & + \left\{ \frac{1}{\bar{n}} \left( \delta^{(D)}(\mathbf{k}_1 + \mathbf{k}_2) P_{g,\text{cont}}(\mathbf{k}_3) + B_{g,\text{cont}}(\mathbf{k}_1 + \mathbf{k}_2, \mathbf{k}_3, \mathbf{k}_4) \right) + 5 \text{ cyc.} \right\} + T_{g,\text{cont}}(k_1, k_2, k_3, k_4), \end{aligned} \quad (5.38)$$

where  $T_{g,\text{cont}}$  is the continuous trispectrum which contains both connected and disconnected diagrams. The rest of the terms are higher-order terms contributing to the shot noise. We denote them as  $T_{\text{shot}}$ , which is essentially the combined covariance of quadratic estimators described in Eq.(5.16). This expression can be written as

$$\begin{aligned}
T_{\text{shot}}(\mathbf{k}) &= \int \int \frac{d^3 \mathbf{q}}{(2\pi)^3} \frac{d^3 \mathbf{p}}{(2\pi)^3} g_\alpha(\mathbf{q}, \mathbf{k} - \mathbf{q}) g_\beta(\mathbf{p}, -\mathbf{k} - \mathbf{p}) T_{\text{shot}}(\mathbf{q}, \mathbf{k} - \mathbf{q}, \mathbf{p}, -\mathbf{k} - \mathbf{p}) \\
&= \int \int \frac{d^3 \mathbf{q}}{(2\pi)^3} \frac{d^3 \mathbf{p}}{(2\pi)^3} g_\alpha(\mathbf{q}, \mathbf{k} - \mathbf{q}) g_\beta(\mathbf{p}, -\mathbf{k} - \mathbf{p}) \left[ \frac{1}{\bar{n}^3} + \frac{1}{\bar{n}^2} (P_{\text{g,cont}}(\mathbf{q}) + 3 \text{ cyc.}) \right] \\
&\quad + \frac{1}{\bar{n}^2} \left( \delta^{(\text{D})}(\mathbf{k}) + P_{\text{g,cont}}(\mathbf{k}) + \delta^{(\text{D})}(\mathbf{q} + \mathbf{p}) + P_{\text{g,cont}}(\mathbf{q} + \mathbf{p}) + \delta^{(\text{D})}(-\mathbf{k} - \mathbf{p} + \mathbf{q}) \right. \\
&\quad \left. + P_{\text{g,cont}}(-\mathbf{k} - \mathbf{p} + \mathbf{q}) \right) + \left\{ \frac{1}{\bar{n}} \left( \delta^{(\text{D})}(\mathbf{k}) P_{\text{g,cont}}(\mathbf{p}) + B_{\text{g,cont}}(\mathbf{k}, \mathbf{p}, -\mathbf{k} - \mathbf{p}) \right) + 5 \text{ cyc.} \right\} \\
&\quad + 2 \int \frac{d^3 \mathbf{q}}{(2\pi)^3} g_\alpha(\mathbf{q}, \mathbf{k} - \mathbf{q}) g_\beta(\mathbf{q}, -\mathbf{k} + \mathbf{q}) \left[ \frac{1}{\bar{n}^2} + \frac{1}{\bar{n}} (P_{\text{g,cont}}(\mathbf{q}) + P_{\text{g,cont}}(\mathbf{k} - \mathbf{q})) \right] \\
&= \frac{N_{\alpha\alpha}(\mathbf{K}) N_{\beta\beta}(\mathbf{K})}{N_{\alpha\beta}(\mathbf{K})} + N_{\alpha\beta, \text{shot}}(\mathbf{K}).
\end{aligned} \tag{5.39}$$

After simplifying the above equation we find the following expression:

$$\begin{aligned}
N_{\alpha\beta, \text{shot}}(\mathbf{k}) &= \int \int \frac{d^3 \mathbf{q}}{(2\pi)^3} \frac{d^3 \mathbf{p}}{(2\pi)^3} g_\alpha(\mathbf{q}, \mathbf{k} - \mathbf{q}) g_\beta(\mathbf{p}, -\mathbf{k} - \mathbf{p}) \left[ \frac{1}{\bar{n}^3} + \frac{1}{\bar{n}^2} (P_{\text{g,cont}}(\mathbf{q}) + 3 \text{ cyc.}) \right] \\
&\quad + \frac{1}{\bar{n}^2} \left( P_{\text{lin}}(\mathbf{k}) + P_{\text{g,cont}}(\mathbf{q} + \mathbf{p}) + P_{\text{g,cont}}(-\mathbf{k} - \mathbf{p} + \mathbf{q}) \right) + \frac{1}{\bar{n}} \left( B_{\text{g,cont}}(\mathbf{k}, \mathbf{p}, -\mathbf{k} - \mathbf{p}) \right. \\
&\quad + B_{\text{g,cont}}(\mathbf{q} + \mathbf{p}, \mathbf{k} - \mathbf{q}, -\mathbf{k} - \mathbf{p}) + B_{\text{g,cont}}(\mathbf{q} - \mathbf{k} - \mathbf{p}, \mathbf{k} - \mathbf{q}, \mathbf{p}) + B_{\text{g,cont}}(\mathbf{k} - \mathbf{q} + \mathbf{p}, \mathbf{q}, -\mathbf{k} - \mathbf{p}) \\
&\quad \left. + B_{\text{g,cont}}(-\mathbf{q} - \mathbf{p}, \mathbf{q}, \mathbf{p}) + B_{\text{g,cont}}(\mathbf{p} - \mathbf{k} - \mathbf{p}, \mathbf{q}, \mathbf{k} - \mathbf{q}) \right),
\end{aligned} \tag{5.40}$$

where  $B_{\text{g,cont}}$  is the continuous galaxy bispectrum which is defined as

$$B_{\text{g,cont}}(\mathbf{q}_1, \mathbf{q}_2, \mathbf{q}_3) = b_1^2 \sum_{\alpha} c_{\alpha} \left( F_{\alpha}(\mathbf{q}_1, \mathbf{q}_2) P_{\text{lin}}(\mathbf{q}_1) P_{\text{lin}}(\mathbf{q}_2) + 2 \text{ cyc.} \right). \tag{5.41}$$

The first two lines in Eq. (5.40) are next-to-leading order trispectrum shot noise which we will denote in Sec. 5.4 by  $P_{\text{rr, shot}}$ . In Fig. 5.4, we plot contributions from shot noise to the power spectrum, bispectrum and trispectrum for the growth estimator. The amplitude of these contributions for bispectrum and trispectrum increase for higher maximum wavenumber,  $k_{\text{max}}$ , which means that as we increase  $k_{\text{max}}$  for our reconstruction analysis the bispectrum and trispectrum shot noise contributions become more significant.



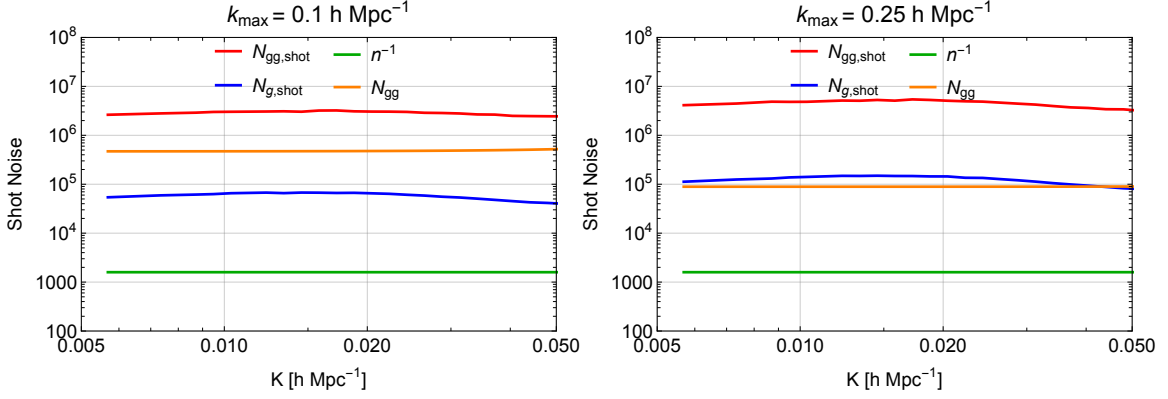


Fig. 5.4 Shot noise contributions to the power spectrum, bispectrum and trispectrum for  $k_{\max} = 0.1h \text{ Mpc}^{-1}$  (left) and  $k_{\max} = 0.25h \text{ Mpc}^{-1}$  (right). We used the growth estimator for density reconstruction. The bias parameters  $b_1$  and  $c_\alpha$  we used for the lowest mass bin I from simulations are defined in Table 5.2. The Poisson shot noise  $P_{\text{gg,shot}} = 1500h^{-3} \text{ Mpc}^3$  corresponding to halo number density  $\bar{n} = 675 \times 10^{-6}h^3 \text{ Mpc}^3$ .

## 5.3 $N$ -body Simulations

### 5.3.1 Setup

For testing the quadratic estimator framework presented in Sec. 5.4, we use a suite of 15 realisations of a cosmological  $N$ -body simulation. The initial conditions are generated with the second order Lagrangian Perturbation Theory (**2-LPT**) code [55, 52] at the initial redshift  $z_i = 99$  and are subsequently evolved using **Gadget-2** [197]. The simulations are performed with  $N_p = 1024^3$  dark matter particles in a cubic box of length  $L = 1500h^{-1} \text{ Mpc}$  with periodic boundary conditions. We assume a flat  $\Lambda$ CDM cosmology with the cosmological parameters  $\Omega_m = 0.272$ ,  $\Omega_\Lambda = 0.728$ ,  $h = 0.704$ ,  $n_s = 0.967$ .

Dark matter halos in the final  $z = 0$  density field are identified using the Friends-of-Friends (FoF) algorithm (see [118, 150]) with linking length  $l = 0.2$  times the mean inter-particle distance. The halos are binned in mass, with each bin spanning a factor of three in mass. The mass and number density of the lowest halo mass bin employed in this study are given in Table 5.2. Particles and halos are assigned to a regular grid using the Cloud-in-Cell (CIC) scheme. We Fourier transform the matter and halo density fields using the publicly available **FFTW** library<sup>1</sup>.

<sup>1</sup><http://www.fftw.org>

Mass Bin	Halo Mass [ $10^{13}h^{-1}M_{\odot}$ ]	$n_h$ [ $10^{-6}h^3 \text{ Mpc}^{-3}$ ]	$b_1$	$c_g$	$c_t$	$c_s$
I	0.77	627	1.07	0.62	1.14	1.07

Table 5.2 Halo mass bin employed in this study. We quote the mean mass of the sample, the number density of halos  $n_h$ , and the linear bias  $b_1$  for the lowest halo mass bin in the simulation.

### 5.3.2 Generation of Quadratic Estimators

We generate quadratic estimators from the halo density field  $\delta_g$  in  $N$ -body simulations using a sequence of multiplications with powers of wavenumbers in Fourier space, Fourier transforms, and subsequent multiplication of the weighted fields in configuration space. We generate three quadratic estimators corresponding to the growth term  $\delta^2$ , shift term  $\Psi \cdot \nabla \delta$ , and the tidal term  $s^2$ , with associated Fourier-space kernels given in Tab. (5.1). The first step in our procedure is to remove very small scale modes by applying a cut-off  $k_{\max}$  in Fourier space through the multiplication of the Fourier space density field with a filtering function. While the exact form of the cutoff is not important, we adopt a Gaussian filter  $W(R\mathbf{k}) = \exp(-k^2R^2/2)$  for numerical stability.

We define the smoothed density field by  $\delta_g^R(\mathbf{k})$ . We choose three external smoothing scales:  $R = 20h^{-1}$  Mpc,  $R = 10h^{-1}$  Mpc, and  $R = 4h^{-1}$  Mpc, corresponding to maximum wavenumbers  $k_{\max} \approx 0.05h \text{ Mpc}^{-1}$ ,  $k_{\max} \approx 0.1h \text{ Mpc}^{-1}$ , and  $k_{\max} \approx 0.25h \text{ Mpc}^{-1}$  respectively. The smoothing scale removes all wavenumbers  $k > k_{\max}$ , such that we reconstruct long wavelength modes using modes  $k < k_{\max}$  for three different cases.

$$\delta_A(\mathbf{k}) = \delta_g^R(\mathbf{k}) / (b_1^2 P_{\text{lin}}(\mathbf{k}) + n_g^{-1}) \quad (5.42)$$

$$\delta_B(\mathbf{k}) = (\delta_g^R(\mathbf{k}) P_{\text{lin}}(\mathbf{k})) / (b_1^2 P_{\text{lin}}(\mathbf{k}) + n_g^{-1}) \quad (5.43)$$

where  $b_1$  and  $n_g$  are the linear bias and halo number density corresponding to five halo mass bins defined in Table 5.2. Below we describe how we generate quadratic estimators:

1. **Growth Estimator:** We inverse Fourier transform both fields defined in (5.42) and (5.43) to obtain  $\delta_A(\mathbf{x})$  and  $\delta_B(\mathbf{x})$ . In configuration space, we multiply the product of both fields by 17/21 and then Fourier transform back to Fourier space to obtain the growth estimator.
2. **Shift Estimator:** In general, the shift term  $\Psi \cdot \nabla \delta$  can be generated by the displacement and the gradient of the density field. To generate the shift estimator we do the following. First we multiply  $\delta_A(\mathbf{k})$  by  $-\mathbf{k}$  in Fourier space to generate the gradient field  $\nabla \delta_A(\mathbf{k})$ . After that, we inverse Fourier transform  $\nabla \delta_A$  and  $\delta_B$  and multiply them in

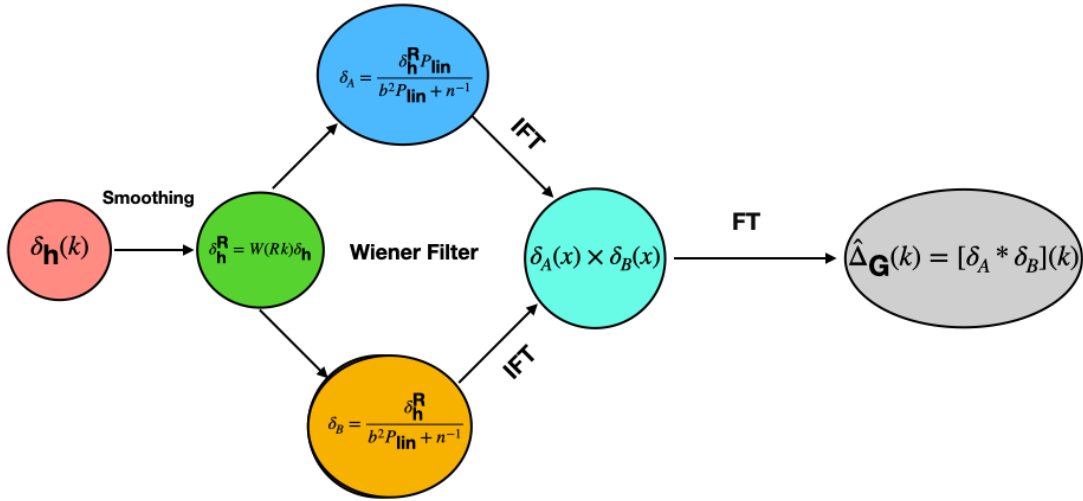


Fig. 5.5 Schematic diagram for showing how we generate a quadratic estimator in simulations. We only show the growth (G) estimator here. IFT and FT are inverse Fourier transform and Fourier transform respectively.

configuration space. The final operation is the generation of the displacement vector using the product field  $\delta_B \nabla \delta_A$ . We Fourier transform the product and multiply it by  $-\mathbf{k}/k^2$  in Fourier space to obtain the shift estimator.

3. **Tidal Estimator:** For the tidal estimator we multiply  $\delta_A(\mathbf{k})$  by  $(k_i k_j / k^2 - 1/3 \delta_{ij})$  in Fourier space to obtain  $s_{ij}^A(\mathbf{k})$ , where  $\delta_{ij}$  is the Kronecker delta. We do the inverse Fourier transform  $\delta_B(\mathbf{k})$  and  $s_{ij}^A(\mathbf{k})$  and multiply both in the configuration space. Finally, we multiply the product by  $(2/7)(k_i k_j / k^2 - 1/3 \delta_{ij})$  in Fourier space to obtain the tidal estimator.

Note that the main computational cost in generating quadratic estimators come from Fourier transforms. The auto- and cross-spectrum analysis of quadratic estimators require the computational cost of power spectrum analysis, which is quite efficient. In all our figures in this section, we estimate the error bars of our measurements using sample variance of 14 realisations and divide it by  $\sqrt{15}$  to get the mean error.

### 5.3.3 Simulations Checks with the Linear Field

To check our simulation code, we replace the galaxy field  $\delta_{\mathbf{g}}$  in the quadratic estimator formula with the linear density field  $\delta_{\mathbf{G}}$ . This now looks like a squared-field with a kernel representing the kernel of the quadratic field estimator. Cross-correlating the three squared-fields in simulations and checking that the simulation results agree with the corresponding theory curves can validate whether the kernel code in simulations has been rightly

implemented. The estimator formula with the linear field now looks like

$$\hat{\Delta}_{\alpha}^{\text{G}}(\mathbf{k}) = N_{\alpha\alpha}(\mathbf{k}) \int_{\mathbf{q}} \frac{f_{\alpha}(\mathbf{q}, \mathbf{k} - \mathbf{q})}{2P_{\text{tot}}(\mathbf{q})P_{\text{tot}}(\mathbf{k} - \mathbf{q})} \delta_{\text{lin}}(\mathbf{q}) \delta_{\text{lin}}(\mathbf{k} - \mathbf{q}). \quad (5.44)$$

The cross-correlations of two linear-field estimators are described as

$$\langle \hat{\Delta}_{\alpha}^{\text{G}}(\mathbf{k}) \hat{\Delta}_{\beta}^{\text{G}}(-\mathbf{k}) \rangle' = \int_{\mathbf{q}} \frac{f_{\alpha}(\mathbf{q}, \mathbf{k} - \mathbf{q}) f_{\beta}(\mathbf{q}, \mathbf{k} - \mathbf{q})}{\left(2P_{\text{tot}}(\mathbf{q})P_{\text{tot}}(\mathbf{k} - \mathbf{q})\right)^2} W(R\mathbf{q})^2 W(R(\mathbf{k} - \mathbf{q}))^2 P_{\text{lin}}(\mathbf{q}) P_{\text{lin}}(\mathbf{q} - \mathbf{k}). \quad (5.45)$$

In simulations we define estimators without the normalisation factor, so here we define  $N_{\alpha\alpha} = 1$ . We check these predictions with simulation results. In Fig 5.6, we compare simulation results with theory predictions for cross and auto-correlations of  $\hat{\Delta}_{\alpha}^{\text{G}}$ , where  $\alpha \in \{\text{g}, \text{s}, \text{t}\}$ . We use two different smoothing scales  $R = 20h^{-1}$  Mpc and  $R = 4h^{-1}$  Mpc which correspond to  $k_{\text{max}} = 0.05h$  Mpc $^{-1}$  and  $k_{\text{max}} = 0.25h$  Mpc $^{-1}$  respectively. We see that theory predictions in eq. (5.45) agree with simulation up to high very  $k_{\text{max}}$ . We also plot cross correlation co-efficients in Fig. 5.7 for the same two smoothing scales. We see that shape and amplitude are different for different smoothing scales. The reason is that for low smoothing scales there are a large number of modes, so small scales modes also contribute. For large smoothing scales we remove small scales after the cut-off induced by the smoothing scales and only large scale modes contribute to the cross-correlations.

The main reason for this section is to check whether we have correctly implemented quadratic estimator functions in simulations correctly. Also, we are sure that because of the linear field in the quadratic estimator formula there will not be higher-order perturbative terms. These are good checks for all our functions implemented in our simulation code.

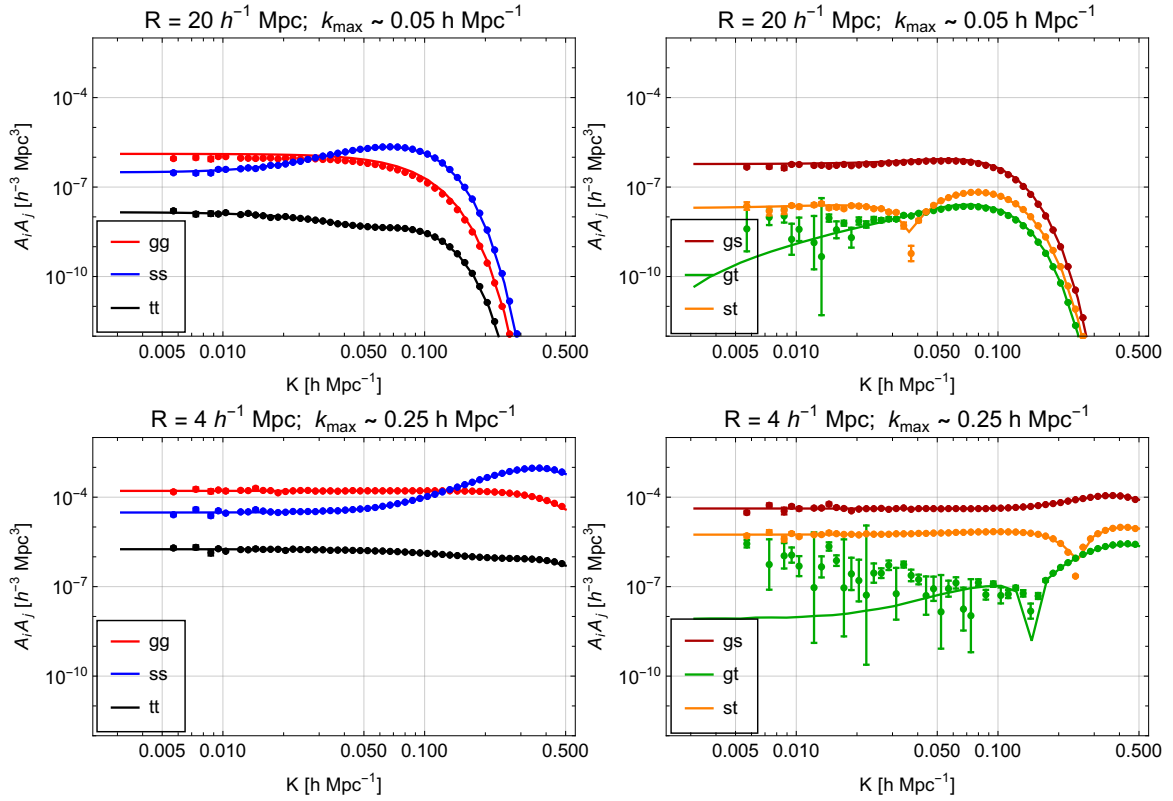


*Fig. 5.6* Auto- and cross-correlations of  $\hat{\Delta}_\alpha^G$  for two different smoothing scales,  $R = 20h^{-1}$  Mpc and  $R = 4h^{-1}$  Mpc. Theoretical predictions (solids curves) agree with simulations for three quadratic fields corresponding to the growth, shift and the tidal terms. The purpose of these tests is to check the correct implementation of the kernels of the quadratic estimators in simulations.

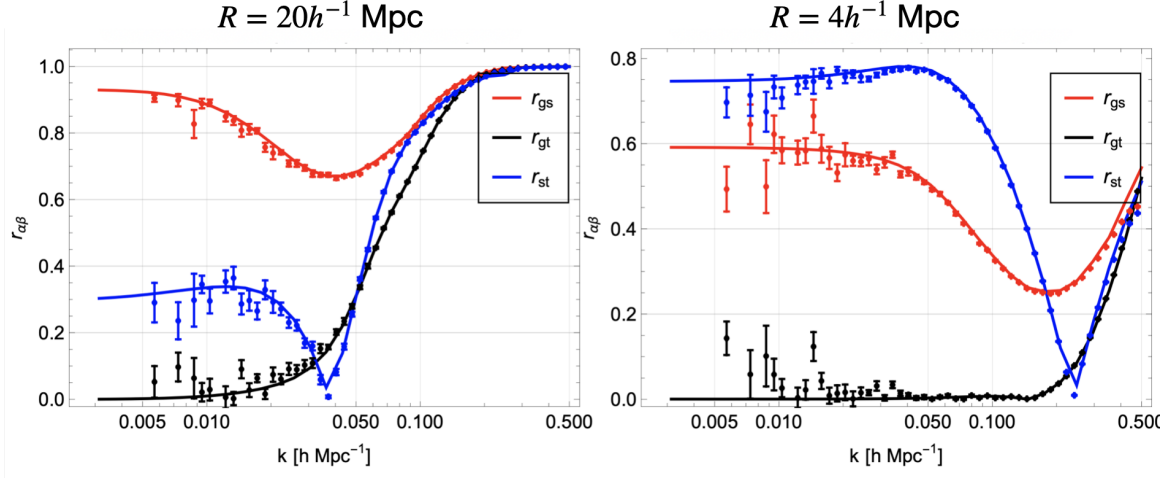


Fig. 5.7 Cross-correlation coefficients between two  $\hat{\Delta}_\alpha^G$ 's for two different smoothing scales  $R = 20h^{-1}$  Mpc and  $R = 4h^{-1}$ . Theoretical predictions agree with simulations, verifying that the kernels of quadratic estimators and Wiener filter are correctly implemented in simulations.

### 5.3.4 Cross-Correlation of Quadratic Estimators with the Linear Density Field

In this section, we describe our results for the cross-correlations of three quadratic estimators  $\hat{\Delta}_\alpha(\mathbf{k})$  with the initial linear field  $\delta_1(\mathbf{k})$ , and compare the theory predictions with simulations. The prediction is given by

$$\begin{aligned}
 \langle \hat{\Delta}_\alpha(\mathbf{k}) \delta_1(\mathbf{k}') \rangle' &= b_1 N_{\alpha\alpha}(\mathbf{k}) \sum_{\beta \in \{G,S,T\}} c_\beta P_{\text{lin}}(\mathbf{k}) \int_{\mathbf{q}} \frac{f_\alpha(\mathbf{q}, \mathbf{k} - \mathbf{q}) f_\beta(\mathbf{q}, \mathbf{k} - \mathbf{q})}{2P_{\text{tot}}(\mathbf{q}) P_{\text{tot}}(\mathbf{k} - \mathbf{q})} W(R\mathbf{q}) W(R(\mathbf{k} - \mathbf{q})) \\
 &\quad + P_{\alpha, \text{shot}}(\mathbf{k}) \\
 &= b_1 P_{\text{lin}}(\mathbf{k}) \sum_{\beta \in \{G,S,T\}} c_\beta \frac{N_{\alpha\alpha}(\mathbf{k})}{N_{\alpha\beta}(\mathbf{k})} + P_{\alpha, \text{shot}}(\mathbf{k}),
 \end{aligned} \tag{5.46}$$

where the prime on the left-hand side denotes that the factor of  $(2\pi)^3(\mathbf{k} + \mathbf{k}')$  has been omitted, and  $c_\beta$  are bias parameters corresponding to the growth, shift and tidal terms and can be measured from either simulations or data. In our analysis we use the bias parameters from Table 5.2, measured in simulations in [2]. In Eq. (5.46),  $P_{\alpha, \text{shot}}$  is the bispectrum shot noise term. Since one field is the linear field, all contribution to the shot noise comes from the stochastic bias terms in the two galaxy fields in the quadratic estimator, such as  $\varepsilon$  and  $\varepsilon_\delta \delta$  (see [67] for more discussion about stochastic bias terms). The expression for this shot

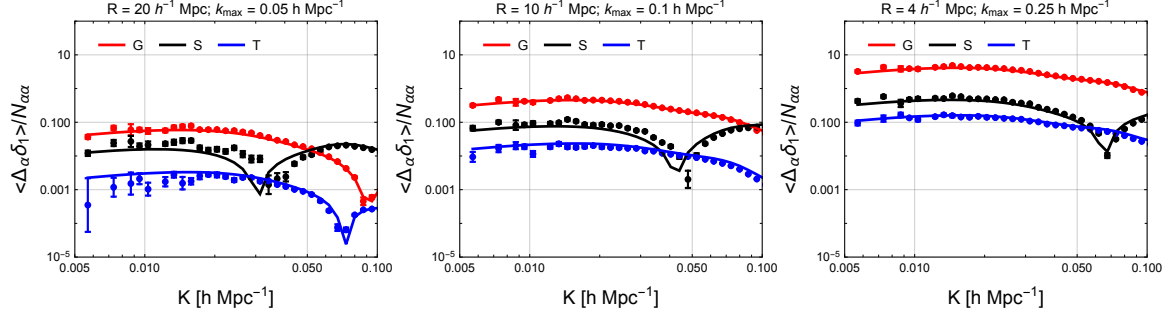


Fig. 5.8 Cross correlations of estimators  $\hat{\Delta}_\alpha$  corresponding to the growth, shift, and tidal mode-couplings with the linear density field  $\delta_1$ . We compare theory predictions (lines) with simulations (points) for three different smoothing scales,  $R = 20h^{-1}$  Mpc,  $R = 10h^{-1}$  Mpc and  $R = 4h^{-1}$  Mpc, corresponding to maximum wavenumbers  $k_{\max}$  of  $0.05h$  Mpc $^{-1}$ ,  $0.1h$  Mpc $^{-1}$ , and  $0.25h$  Mpc $^{-1}$  respectively. In this figure, we plot  $\langle \hat{\Delta}_\alpha \delta_1 \rangle / N_{\alpha\alpha}$ , which is the directly measurable quantity. In contrast to what is defined in Eq. (5.9), in simulations we define the estimators  $\hat{\Delta}_\alpha$  without a prefactor  $N_{\alpha\alpha}$ . We find very good agreement for the growth estimator for all smoothing scales, and also reasonably good agreement for other estimators.

noise contribution in this case can also be derived from Eq. (5.36) and it takes the form

$$P_{\alpha,\text{shot}}(\mathbf{k}) = \frac{b_1}{\bar{n}} P_{\text{lin}}(\mathbf{k}) N_{\alpha\alpha}(\mathbf{k}) \int_{\mathbf{q}} \frac{f_\alpha(\mathbf{q}, \mathbf{k} - \mathbf{q})}{2P_{\text{tot}}(\mathbf{q})P_{\text{tot}}(\mathbf{k} - \mathbf{q})} W(R\mathbf{q})W(R(\mathbf{k} - \mathbf{q})). \quad (5.47)$$

In Fig. 5.8, we compare theory with simulations for three different values of  $k_{\max}$ . Although for the Fisher analysis in this work, we only use the growth estimator, here we also compare results in simulations for the shift and the tidal estimators. For the growth estimator, we find that the theory predictions agree very well with simulation results for up to  $k_{\max} = 0.25h$  Mpc $^{-1}$  at redshift  $z = 0$ . For the other estimators, we also find reasonably good agreement; however, upon close inspection we can see small disagreements which might arise from higher-order terms ignored in our theory predictions.

Interestingly, for  $k_{\max} = 0.25h$  Mpc $^{-1}$ , we can see in Fig. 5.8 that the shape of the cross-correlation of growth estimators with the density field is very similar to the linear power spectrum on large scales. The scale-dependent bias factor in Eq. (5.46) is flat on large scales, indicating that the reconstruction works very well for large  $k_{\max}$ .

### 5.3.5 Auto- and Cross-Correlations of Quadratic Estimators

In this section we discuss our results for the auto- and cross-correlations of three quadratic estimators from simulations and compare the results with our linear order theoretical prediction,

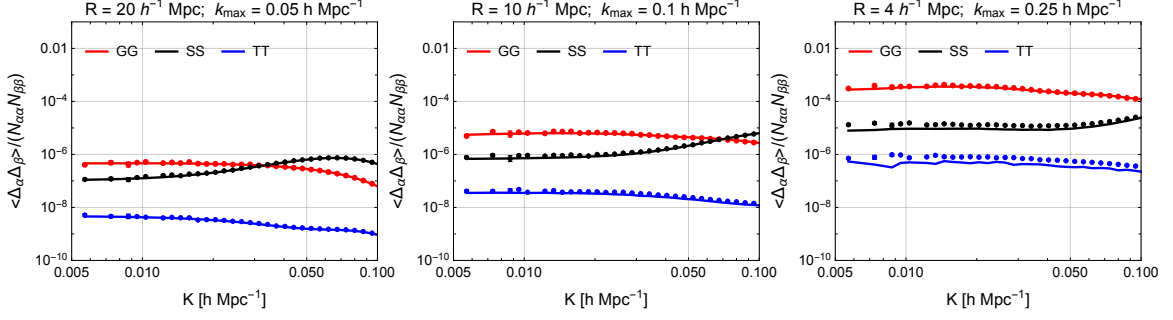


Fig. 5.9 Auto-correlations of the quadratic estimators  $\hat{\Delta}_{\alpha}$ , for the same smoothing scales shown in Fig. 5.8. The predictions for the growth estimator agree with simulations for all smoothing scales. However, for other estimators predictions agree with simulations for large smoothing scales but for the low smoothing scales, the predictions fail as higher-order terms become more important.

given by

$$\begin{aligned}
 \langle \hat{\Delta}_{\alpha}(\mathbf{k}) \hat{\Delta}_{\beta}(\mathbf{k}') \rangle' &= N_{\alpha\alpha}(\mathbf{k}) N_{\beta\beta}(\mathbf{k}) \int_{\mathbf{q}} \frac{f_{\alpha}(\mathbf{q}, \mathbf{k} - \mathbf{q}) f_{\beta}(\mathbf{q}, \mathbf{k} - \mathbf{q})}{[2P_{\text{tot}}(\mathbf{q}) P_{\text{tot}}(\mathbf{k} - \mathbf{q})]^2} W(R_f \mathbf{q})^2 W(R_f(\mathbf{k} - \mathbf{q}))^2 \\
 &\quad \times b_1^4 P_{\text{lin}}(\mathbf{q}) P_{\text{lin}}(\mathbf{k} - \mathbf{q}) \\
 &\quad + b_1^2 P_{\text{lin}}(\mathbf{k}) \sum_{i,j} c_i c_j \frac{N_{\alpha\alpha}(\mathbf{k}) N_{\beta\beta}(\mathbf{k})}{N_{\alpha i}(\mathbf{k}) N_{\beta j}(\mathbf{k})} + P_{\alpha\beta, \text{shot}}(\mathbf{k}) .
 \end{aligned} \tag{5.48}$$

The first term is of order  $\mathcal{O}(\delta^4)$ , while the second and third are of order  $\mathcal{O}(\delta^6)$ . The third term,  $P_{\alpha\beta, \text{shot}}$ , is the contribution arising from halo shot noise, and is given in Sec. 5.2.5.

In Fig. 5.9 we compare cross-correlation results from simulations with theory, for the growth, shift, and tidal estimators, using the same three smoothing scales as above. The simulations and theory agree very well up to  $k_{\text{max}} = 0.1 h \text{ Mpc}^{-1}$  at  $z = 0$ . For larger  $k_{\text{max}}$  we see great agreement for the growth estimator and reasonable agreement for the tidal and shift estimators. The small disagreement of linear predictions for the tidal and shift estimators with simulations for the higher  $k_{\text{max}}$  show that higher-order terms become important for these estimators. The detailed impact of these higher order corrections from biasing or scale dependent stochasticity will be subject of future inquiry. Although we appear to have excellent agreement for the growth term at higher  $k_{\text{max}}$ , to be conservative, we still set the scale  $k_{\text{max}} = 0.1 h \text{ Mpc}^{-1}$  at redshift  $z = 0$  in our forecasts in Sec. 5.4. We scale this to other redshifts by making use of the fact that perturbation theory and the bias expansion at a given order will be valid at higher  $k$  for higher redshifts.

In Fig. 5.10, we plot the auto spectra of the growth estimator, normalized with  $N_{\text{GG}}$  (unlike in the previous plots), in order to compare them to an approximation of the signal power spectrum, given by the second term in Eq. (5.48) (the first and third terms represent



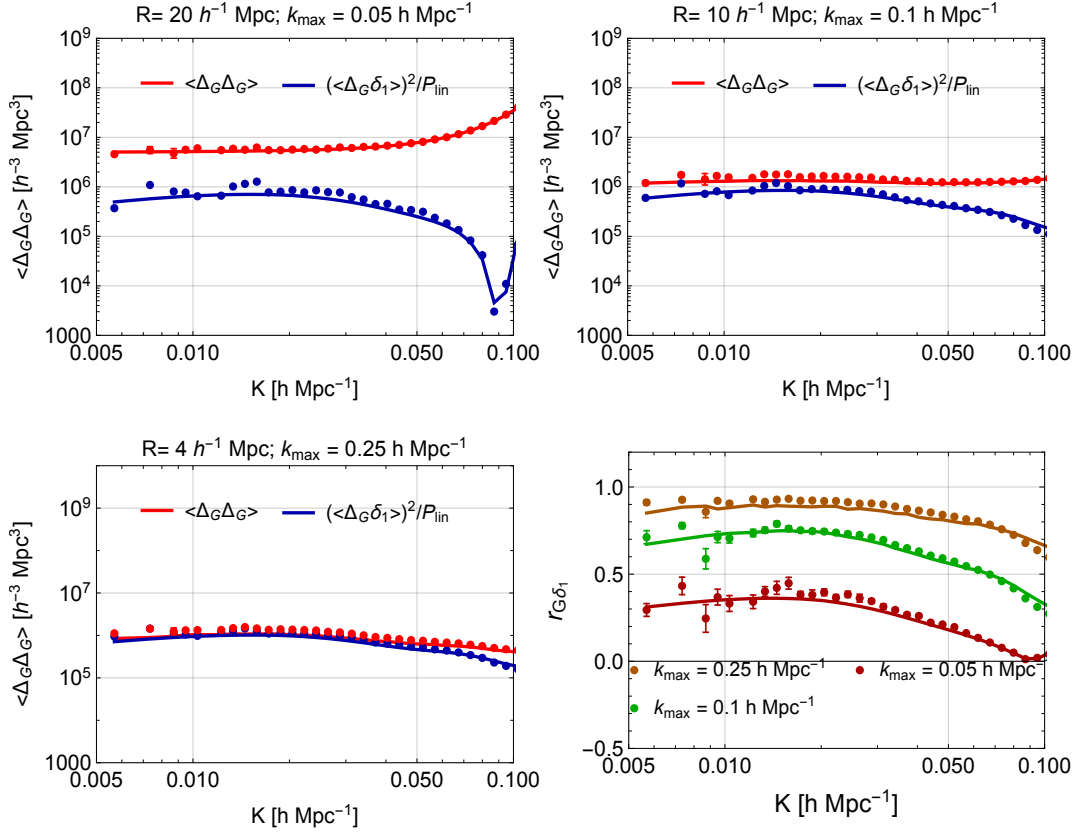


*Fig. 5.10* Comparison of the auto power spectrum of the growth estimator  $\hat{\Delta}_G$ , normalised by  $N_{GG}$  computed from theory, with the signal part which is defined as  $(\langle \hat{\Delta}_G \delta_1 \rangle)^2 / P_{\text{lin}}$ . We compare simulation results with theory predictions for the same smoothing scales as Figs. 5.8 and 5.9. We again find excellent agreement between simulations and theory. In the bottom right figure we plot the cross-correlation coefficient  $r_{G\delta_1}$  between the growth estimator and the linear density field for 3 smoothing scales. We see that  $r_{G\delta_1} > 0.9$  for  $R = 4h^{-1} \text{ Mpc}$  which is why in the bottom left figure  $\langle \hat{\Delta}_G \hat{\Delta}_G \rangle$  is signal dominated.

noise). Since the contribution of the cross-shot noise is small, the signal part can be approximated by cross-correlating the growth estimator with the linear density field and dividing it by the linear power spectrum to ensure the correct normalization, i.e.  $(\langle \hat{\Delta}_G \delta_1 \rangle)^2 / P_{\text{lin}}$ ; we show this in blue in Fig. 5.10. For the two larger smoothing scales, the spectra of the estimator are dominated by the noise contribution (which is white at low  $k$ ). The excellent agreement between theory (red solid lines) and simulations (red points) for all smoothing scales serves as an additional verification that the reconstruction procedure is working as expected for reasonable values of  $k_{\text{max}}$ . In addition to the auto spectra, to check how well the reconstruction is working, we plot the cross-correlation coefficients between the growth estimator and the linear density field in the bottom right panel of Fig. 5.10 for three different  $k_{\text{max}}$ . The cross-correlation coefficient for low  $k_{\text{max}}$  is very low,  $r_{G\delta_1} < 0.4$ , explaining why

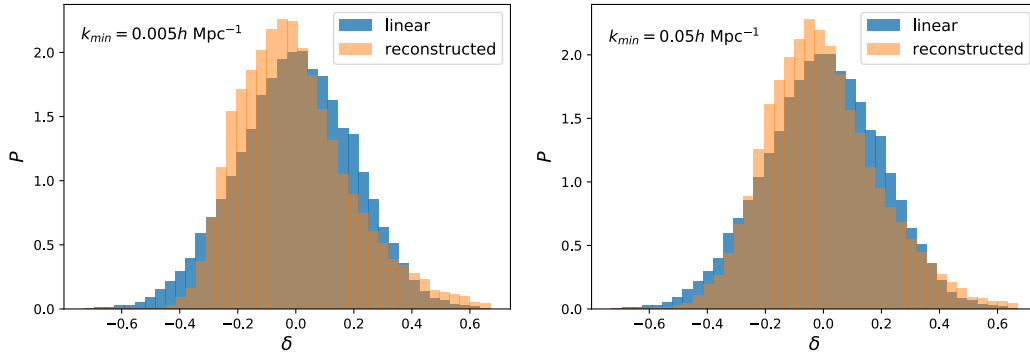


*Fig. 5.11* Probability distribution functions of the initial density field and the reconstructed field in  $N$ -body simulations. The right panel shows the probability distribution of the reconstructed field the  $k_{\min} = 0.05h \text{ Mpc}^{-1}$ , means that we do not include modes  $k < 0.05h \text{ Mpc}^{-1}$  in the reconstruction. In the left we use a lower  $k_{\min} = 0.005h \text{ Mpc}^{-1}$ . The PDFs of both are scaled and shifted around mean 0.

the auto spectra in the top left panel are noise dominated. However, for highest  $k_{\max}$  we consider,  $0.25h \text{ Mpc}^{-1}$ , the cross-correlation coefficient  $r_{G\delta_1} > 0.9$ , which explains why the reconstruction works very well and the auto spectra for high  $k_{\max}$  are signal dominated.

### 5.3.6 Visualisation of Reconstructed Field

To show how best we are reconstructing the initial density field on large scales in simulations, we plot projections of the initial Gaussian density field and the reconstructed field on a 2D plane in Fig. 5.12. We do the reconstruction using a very high  $k_{\max} = 0.25h \text{ Mpc}^{-1}$  which, as we have mentioned before, can be achieved by using a smoothing scale of  $R = 4h^{-1} \text{ Mpc}$ . In the reconstruction we also remove very large scale modes  $k < 0.05h \text{ Mpc}^{-1}$  and so we are only using modes in the range  $0.05h \text{ Mpc}^{-1} < k < 0.25h \text{ Mpc}^{-1}$ . In the end, we apply an external smoothing of  $R = 20h^{-1} \text{ Mpc}$  to both the initial Gaussian field and the reconstructed field. This external smoothing removes all modes  $k > 0.05h \text{ Mpc}^{-1}$ . In Fig. 5.12 we compare both plots and we can observe quite a lot of similarities.

In Fig. 5.11 we also plot the probability distribution functions of the initial Gaussian density field and the reconstructed field. We see the reconstructed field is nearly Gaussian. This is quite encouraging because in our Fisher analysis (later in this paper) we are using Gaussian covariances. However, if we do not remove very high scale modes, that is  $k < 0.05h \text{ Mpc}^{-1}$  in the reconstruction then the PDF of the reconstructed field is not fully Gaussian which will then require the inclusion of non-Gaussian covariances in our Fisher analysis. The probability distribution of the reconstructed field without removing very large scale modes in the reconstruction is shown in Fig. 5.11. we can see the PDF is not really Gaussian.

Estimating the constraining power of the reconstructed modes for cosmological applications would then require the inclusion of non-Gaussian covariances in our Fisher analysis.

## 5.4 Fisher Forecasts for Local $f_{\text{NL}}$

### 5.4.1 Multi-tracer Analysis

For forecast on  $\sigma(f_{\text{NL}})$  we use the multi-tracer analysis [178] using two fields: the galaxy density field  $\delta_{\text{g}}$  and the reconstructed field  $\delta_{\text{r}}$ . Although we can see in Fig. 5.11 that the PDF of the reconstructed field is not completely Gaussian, we still assume it Gaussian for the Fisher analysis in this section. The analysis with a non-Gaussian likelihood we leave for future work. Having said that we start by assuming both fields,  $\delta_{\text{g}}$  and  $\delta_{\text{r}}$ , follow a Gaussian likelihood on large scales [204]. In our analysis here we use four free parameters: three are galaxy bias parameters ( $b_1$ ,  $b_2$ , and  $b_{s^2}$ ) and one is local primordial non-Gaussianity parameter  $f_{\text{NL}}$ . Therefore we will write the full  $4 \times 4$  Fisher information matrix and at the end will marginalise over bias parameters to get constraints on  $\sigma(f_{\text{NL}})$ . The Fisher matrix tells us how well we can measure each parameter from the data. The full Fisher information matrix  $F_{\alpha\beta}$  per mode  $\mathbf{K}$  at the field level is defined as:

$$F_{\alpha\beta}(\mathbf{K}, z) = \frac{1}{2} \text{Tr} \left[ \frac{\partial C(\mathbf{K}, z)}{\partial \alpha} C^{-1}(\mathbf{K}, z) \frac{\partial C(\mathbf{K}, z)}{\partial \beta} C^{-1}(\mathbf{K}, z) \right]_{\mathbf{p}=\mathbf{p}_0} \quad (5.49)$$

where  $\mathbf{p} \in \{b_1, b_2, b_{s^2}, f_{\text{NL}}\}$  is the set of free parameters in our analysis and  $\mathbf{p}_0$  is a set of their fiducial values. Also in Eq. (5.49),  $C$  is the covariance matrix defined as

$$C(\mathbf{K}, z) = \begin{pmatrix} P_{\text{gg}}(\mathbf{K}, z) & P_{\text{gr}}(\mathbf{K}, z) \\ P_{\text{rg}}(\mathbf{K}, z) & P_{\text{rr}}(\mathbf{K}, z) \end{pmatrix} \quad (5.50)$$

and  $C^{-1}$  is the inverse covariance matrix

$$C^{-1}(\mathbf{K}, z) = \frac{1}{P_{\text{gg}}(\mathbf{K}, z)P_{\text{rr}}(\mathbf{K}, z)(1-r^2)} \begin{pmatrix} P_{\text{rr}}(\mathbf{K}, z) & -P_{\text{gr}}(\mathbf{K}, z) \\ -P_{\text{rg}}(\mathbf{K}, z) & P_{\text{gg}}(\mathbf{K}, z) \end{pmatrix}, \quad (5.51)$$

where  $r$  is the cross correlation coefficients between the galaxy field and the reconstructed field and is defined as

$$r(\mathbf{K}, z) = \frac{P_{\text{rg}}(\mathbf{K}, z)}{\sqrt{P_{\text{rr}}(\mathbf{K}, z)P_{\text{gg}}(\mathbf{K}, z)}}. \quad (5.52)$$

Moreover, in Eq. (5.50) and Eq. (5.51),  $P_{\text{gg}}$ ,  $P_{\text{rg}}$ , and  $P_{\text{rr}}$  correspond to galaxy auto power spectrum, cross power spectrum of the galaxy and reconstructed field and the auto power

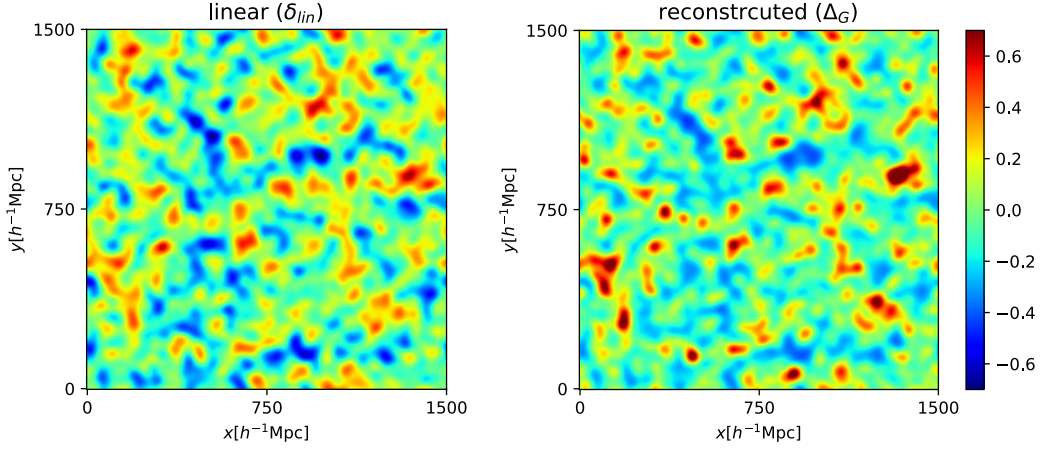


*Fig. 5.12* 2D slices of a 3D linear density field (left panel) and growth estimator  $\hat{\Delta}_G$  (right panel). For the growth estimator we used  $R = 4h^{-1}$  Mpc smoothing which corresponds to  $k_{\text{max}} = 0.25h$  Mpc<sup>-1</sup>. We apply an external smoothing of  $R = 20h^{-1}$  Mpc to both linear and reconstructed fields. As expected, we find that the reconstruction reproduces many of the large-scale features in the linear density field.

spectrum of the reconstructed field respectively. The galaxy auto power spectrum  $P_{\text{gg}}$  contains galaxy shot noise, the cross power spectrum  $P_{\text{gr}}$  contains the bispectrum shot noise, and the auto power spectrum of the reconstructed field  $P_{\text{rr}}$  contains the reconstruction noise  $N_{\text{rr}}$  as well as the trispectrum shot noise. We define these power spectra as follows:

$$P_{\text{gg}}(\mathbf{K}, z) = \left( b_1 + \frac{c_{01} f_{\text{NL}} D(z)}{M(\mathbf{K}, z)} \right)^2 P_{\text{lin}}(K, z) + P_{\text{gg,shot}}(K) \quad (5.53)$$

$$P_{\text{gr}}(\mathbf{K}, z) = \left( b_1 + \frac{c_{01} f_{\text{NL}} D(z)}{M(\mathbf{K}, z)} \right) \left( c_g + \sum_{\alpha \neq \beta} c_\beta \frac{N_{\text{gg}}}{N_{\text{g}\beta}} \right) P_{\text{lin}}(K, z) + P_{\text{gr,shot}}(K) \quad (5.54)$$

$$P_{\text{rr}}(\mathbf{K}, z) = b_1^2 \left( c_g + \sum_{\alpha \neq \beta} c_\beta \frac{N_{\text{gg}}}{N_{\text{g}\beta}} \right)^2 P_{\text{lin}}(K, z) + N_{\text{rr}}(\mathbf{K}, z) + P_{\text{rr,shot}}(K) \quad (5.55)$$

where  $\beta$  contains all six mode couplings defined in Table 5.1 except the growth term. Using the notation  $\partial P_{ij}/\partial\alpha = P_{ij,\alpha}$  we expand the trace in Eq. (5.49) to get

$$\begin{aligned}
F_{\alpha\beta}(\mathbf{K}, z) = & \frac{1}{2} \left( \frac{1}{P_{\text{rr}}P_{\text{gg}}(1-r^2)} \right)^2 \left[ P_{\text{gg}} \left\{ P_{\text{rg},\beta} (-P_{\text{rg}}P_{\text{rr},\alpha} + P_{\text{rr}}P_{\text{rg},\alpha}) + P_{\text{rr},\beta} (P_{\text{gg}}P_{\text{rr},\alpha} - P_{\text{rg}}P_{\text{rg},\alpha}) \right\} \right. \\
& - P_{\text{rg}} \left\{ P_{\text{gg},\beta} (-P_{\text{rg}}P_{\text{rr},\alpha} + P_{\text{rr}}P_{\text{rg},\alpha}) + P_{\text{rg},\beta} (P_{\text{gg}}P_{\text{rr},\alpha} - P_{\text{rg}}P_{\text{rg},\alpha}) \right\} \\
& - P_{\text{rg}} \left\{ P_{\text{rg},\beta} (-P_{\text{rg}}P_{\text{rg},\alpha} + P_{\text{rr}}P_{\text{gg},\alpha}) + P_{\text{rr},\beta} (P_{\text{gg}}P_{\text{rg},\alpha} - P_{\text{rg}}P_{\text{gg},\alpha}) \right\} \\
& \left. + P_{\text{rr}} \left\{ P_{\text{gg},\beta} (-P_{\text{rg}}P_{\text{rg},\alpha} + P_{\text{rr}}P_{\text{gg},\alpha}) + P_{\text{rg},\beta} (P_{\text{gg}}P_{\text{rg},\alpha} - P_{\text{rg}}P_{\text{gg},\alpha}) \right\} \right]_{\mathbf{p}=\mathbf{p}_0}. \tag{5.56}
\end{aligned}$$

The cumulative Fisher matrix can be computed by integrating Eq. (5.56) from  $K_{\text{min}}$ , which depends on the survey, to  $K_{\text{max}}$ . We write it as

$$F_{\alpha\beta} = \frac{V}{(2\pi)^2} \int_{K_{\text{min}}}^{K_{\text{max}}} dK K^2 \int_{-1}^1 d\mu F_{\alpha\beta}(K, \mu, z), \tag{5.57}$$

where  $V$  is the volume of the galaxy survey defined in Table 5.3 for three experiments. The unmarginalised error on one parameter is given by

$$\sigma(p_\alpha) = \left( \sqrt{F_{\alpha\alpha}} \right)^{-1} \tag{5.58}$$

where a simplified expression for  $F_{\alpha\alpha}$  is defined as

$$\begin{aligned}
F_{\alpha\alpha} = & \frac{1}{2(1-r^2)^2} \left[ \left( \frac{P_{\text{gg},\alpha}}{P_{\text{gg}}} - 2r^2 \frac{P_{\text{rg},\alpha}}{P_{\text{rg}}} \right)^2 + 2r^2(1-r^2) \left( \frac{P_{\text{rg},\alpha}}{P_{\text{rg}}} \right)^2 + \left( \frac{P_{\text{rr},\alpha}}{P_{\text{rr}}} \right)^2 \right. \\
& \left. + 2r^2 \frac{P_{\text{rr},\alpha}}{P_{\text{rr}}} \left( \frac{P_{\text{rr},\alpha}}{P_{\text{gg}}} - 2 \frac{P_{\text{rg},\alpha}}{P_{\text{rg}}} \right) \right]_{\mathbf{p}=\mathbf{p}_0}. \tag{5.59}
\end{aligned}$$

As we are only interested in  $f_{\text{NL}}$ , we have to marginalise over other free parameters. The marginalised error is defined as

$$\sigma(p_\alpha) = \sqrt{(F^{-1})_{\alpha\alpha}}. \tag{5.60}$$

## 5.4.2 Scales

In our forecast analysis, we use large scale modes of  $\delta_{\text{g}}$  and reconstructed field  $\delta_{\text{r}}$  for measuring local non-Gaussianity  $f_{\text{NL}}$ . The modes we use to measure local  $f_{\text{NL}}$  satisfy the relation  $K_{\text{min}} < K < K_{\text{max}}$  for combined analysis using both galaxy and reconstructed field

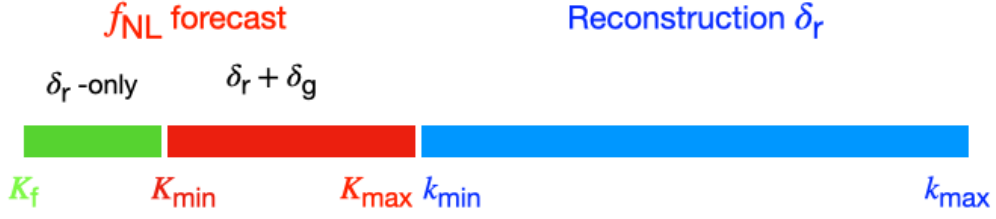


Fig. 5.13 This illustration shows scales we use for our Fisher analysis in this work. For the reconstruction of large-scale density modes we use wavenumbers  $k_{\text{min}} < K < k_{\text{max}}$  (shown in blue). For  $f_{\text{NL}}$  forecasts, however, we use very large scale modes  $K_{\text{min}} < K < K_{\text{max}}$  (shown in red) for  $\delta_{\text{g}} + \delta_{\text{r}}$  combined analysis (shown in red) and  $K_{\text{f}} < K < K_{\text{min}}$  for  $\delta_{\text{r}}$ -only (shown in green), where  $K_{\text{f}}$  is the lowest wavenumber we can measure in the galaxy survey.

	DESI-like $0.6 < z < 1.6$	MegaMapper-like $2 < z < 2.5$ $4.5 < z < 5$	
<b>Survey parameters</b>			
Survey volume ( $\text{Gpc}^3$ )	100	80	66
Mean galaxy density $\bar{n}$ ( $\text{Mpc}^{-3}$ )	$10^{-4}$	$6 \times 10^{-4}$	$2 \times 10^{-5}$
$K_{\text{max}}$ for $f_{\text{NL}}$ constraint ( $h\text{Mpc}^{-1}$ )	0.05	0.08	0.14
$k_{\text{max}}$ for reconstruction ( $h\text{Mpc}^{-1}$ )	0.15	0.24	0.4
<b>Fiducial bias parameters</b>			
$b_1$	1.6	2.9	7.0
$b_2$	-0.30	1.1	17
$b_{s^2}$	-0.17	-0.54	-1.7
$b_{11}$	-3.0	-2.5	37
$b_{02}$	-14	-21	85

Table 5.3 Survey characteristics used for our main forecasts. The DESI-like survey is based on the expected DESI emission-line galaxy sample and the MegaMapper-like survey is a next-generation survey targeting high-redshift “dropout” galaxies.

( $\delta_{\text{g}} + \delta_{\text{r}}$ ). We also use very large scale modes of the reconstructed field for Fisher analysis ( $\delta_{\text{r}}$ -only) satisfying the relation  $K_{\text{f}} < K < K_{\text{min}}$ , where  $K_{\text{f}}$  is the lowest wavenumber or the fundamental mode measured by the galaxy survey. This is because even though it is not possible to use such large modes from galaxy field, in theory it is possible to reconstruct those large-scale modes from the correlations of small-scale modes without worrying about the observational systematics. However, the systematic effects can definitely prevent us from measuring those large-scale  $\delta_{\text{g}}$  modes. We therefore only use  $K_{\text{min}}$  for  $\delta_{\text{g}}$  to account for possible systematic effects. We chose a range of  $K_{\text{min}}$  for our Fisher analysis. We describe the range of scales diagrammatically in Fig. 5.13.

### 5.4.3 Galaxy Surveys

The configurations of galaxy surveys we use in our work are summarised in Table 5.3. The first galaxy survey we use is a DESI-like galaxy survey [63]. For this we consider a  $14000 \text{ deg}^2$  survey over redshift range  $0.6 < z < 1.6$ , which roughly translates into a survey volume  $V = 100 \text{ Gpc}^3$  with mean redshift  $\bar{z} = 1$ . The mean number density we use is  $\bar{n} = 10^{-4} \text{ Mpc}^{-3}$ . The linear bias is assumed to be  $b_1 = 1.6$  with fiducial values of other bias parameters defined in Table 5.3. For reconstruction of large scale density modes we use  $K_{\text{max}} = 0.05h \text{ Mpc}^{-1}$  ( $= k_{\text{min}}$ ) and  $k_{\text{max}} = 0.15h \text{ Mpc}^{-3}$ , which is a good assumption as our quadratic bias expansion is valid for  $k < k_{\text{max}}$  at redshift  $z = 1$ . This is explained in simulation section where we show that linear order predictions for density reconstruction agree with simulations very well up to  $k_{\text{max}} = 0.1h \text{ Mpc}^{-1}$  at redshift  $z = 0$ . If we want to increase the  $k_{\text{max}}$  for reconstruction for DESI-like survey we need to include higher order terms in our predictions.

Another survey we assume is called MegaMapper which is a next generation spectroscopic survey for high-redshift "dropout" galaxies [86, 173]. Like the previous example, we use a  $14000 \text{ deg}^2$  survey and consider two redshift bins: (1)  $2 < z < 2.5$  and (2)  $4.5 < z < 5$ . For lower redshift bin the survey volume is  $V = 80 \text{ Gpc}^3$  with mean number density  $\bar{n} = 6 \times 10^{-4} \text{ Mpc}^{-3}$  and fiducial linear bias parameter  $b_1 = 2.9$ . The minimum wavenumber for reconstruction we use is  $K_{\text{min}} = 0.08h \text{ Mpc}^{-1}$  and maximum is  $K_{\text{max}} = 0.24h \text{ Mpc}^{-1}$ . For the second high redshift bin, we use the survey volume of  $V = 66 \text{ Gpc}^3$  with mean number density  $\bar{n} = 2 \times 10^{-5}$  and linear bias parameter  $b_1 = 7.0$ . The minimum and maximum wavenumber for reconstruction used for this redshift bins are  $K_{\text{min}} = 0.14h \text{ Mpc}^{-1}$  and  $K_{\text{max}} = 0.4h \text{ Mpc}^{-1}$  respectively. The reason for large  $K_{\text{max}}$  for this redshift survey is that the non-linear wavenumber  $k_{\text{NL}}$  up to which our predictions agree and quadratic bias expansion make sense increase with redshift.

### 5.4.4 Results

#### DESI

We now discuss our first forecast results for local  $f_{\text{NL}}$  for DESI-like survey. The results are shown in Fig. 5.14. In the right panel of Fig. 5.14 we show constraints on local  $f_{\text{NL}}$  from only galaxy field  $\delta_{\text{g}}$  (showed by red dotted) as well as combined analysis of galaxy field  $\delta_{\text{g}}$  and the reconstructed field  $\delta_{\text{r}}$  (shown by solid red curve). The left panel, however, shows the ratio of  $\sigma(f_{\text{NL}})$  obtained from  $\delta_{\text{g}}$  and  $\delta_{\text{g}} + \delta_{\text{r}}$ . We see that for lowest  $K_{\text{min}}$  the improvement in  $\sigma(f_{\text{NL}})$  is negligible, however as we increase the  $K_{\text{min}}$  we see significant improvement coming from extra modes in the reconstructed field. This is because the reconstructed noise obtained for a DESI-like survey is huge. For  $K_{\text{min}} = 0.02h \text{ Mpc}^{-1}$  we can get 15%

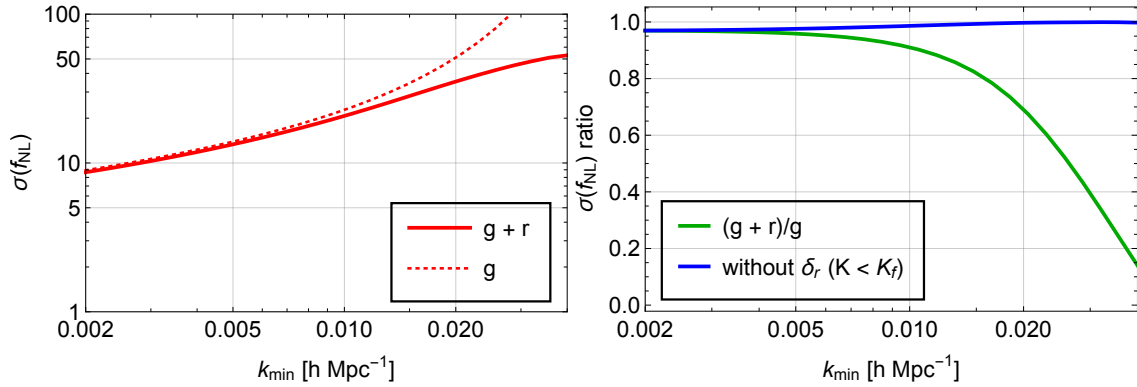


Fig. 5.14 DESI:  $\sigma(f_{\text{NL}})$  constraints for a DESI-like survey for a range of redshift  $0.6 < z < 1.6$ . LEFT PANEL:  $\sigma(f_{\text{NL}})$  obtained from  $\delta_{\text{g}}$  only (dotted red) and  $\delta_{\text{g}} + \delta_{\text{r}}$  (solid red). We also include constraints from  $\delta_{\text{r}}$ -only in combined analysis for modes  $0.002 < K < K_{\text{min}}$ . RIGHT PANEL: We plot ratio of constraints from combined analysis and galaxy-only. We also plot ratio without modes  $0.002 < K < K_{\text{min}}$ .

improvement in  $\sigma(f_{\text{NL}})$  when the reconstructed modes are used. This improvement from  $\delta_{\text{r}}$  mostly comes from the modes  $K < K_{\text{min}}$  which are inaccessible from  $\delta_{\text{g}}$ . This shows that, although we do not achieve cosmic variance cancellation in a DESI-survey due to large noise, we do, however, get improvement in  $\sigma(f_{\text{NL}})$  due to the fact that we can reconstruct very large-scale modes that are inaccessible in the galaxy field. With this method, even this small improvement is impressive as we do not require any additional dataset. To further explain this result, we plot the ratio of  $\sigma(f_{\text{NL}})$  when we don't include modes  $K < K_f$  in  $\delta_{\text{r}}$  (shown by solid blue curve). We can see that the blue curve shows there is no cosmic variance cancellation. This is the main advantage of using reconstructed modes that we can in principle reconstruct large scale modes which can never be accessible from  $\delta_{\text{g}}$  only.

To see the effects of other parameters we can vary number density  $\bar{n}$ ,  $k_{\text{max}}$  in the reconstruction, remove bispectrum and trispectrum shot noise, and vary quadratic bias parameters especially  $b_2$ . A more detailed analysis is given in the paper [59]. We summarise the results from the paper here. We show that by assuming a very high number density survey,  $\bar{n} = 10^{-2} \text{ Mpc}^{-3}$  we can obtain 10% improvement on  $f_{\text{NL}}$  constraints from only  $\delta_{\text{g}}$  and also some improvement from including  $\delta_{\text{r}}$ . Given these improvements are not significant, we understand that shot noise is not the most important factor which limits the constraints. Increasing  $k_{\text{max}}$  lowers the reconstructed noise but the improvement on  $\sigma(f_{\text{NL}})$  are still negligible. Same is the case if we do not include bispectrum  $P_{\text{gr,shot}}$  and trispectrum  $P_{\text{tr,shot}}$  shot noise terms. However, neglecting  $b_2$  does make a large impact on  $\sigma(f_{\text{NL}})$  (see [59] for more details.)



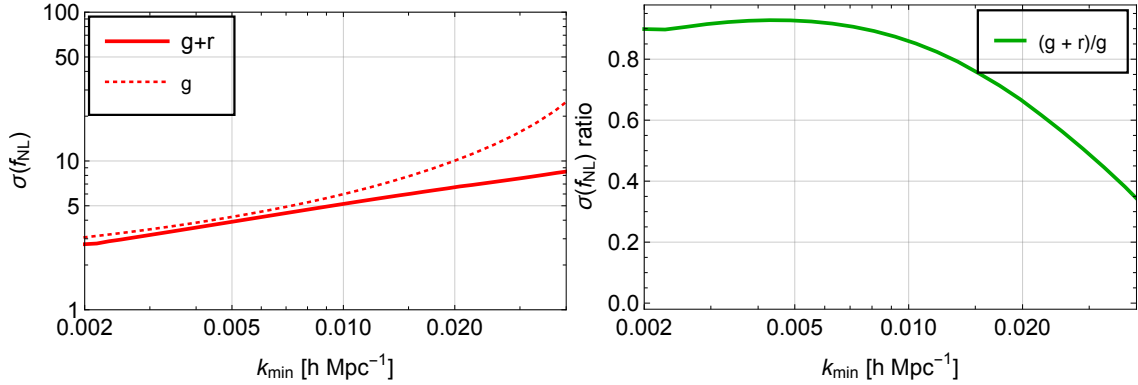


Fig. 5.15 MegaMapper low- $z$ :  $\sigma(f_{\text{NL}})$  constraints for a MegaMapper-like survey for low $z$ ,  $2 < z < 2.5$ . LEFT PANEL:  $\sigma(f_{\text{NL}})$  obtained from  $\delta_{\text{g}}$  only (dotted red) and  $\delta_{\text{g}} + \delta_{\text{r}}$  (solid red). RIGHT PANEL: We plot ratio of constraints from combined analysis and galaxy-only.

### MegaMapper

Our results for MegaMapper-like surveys for low and high redshift ranges are described in Fig. 5.15 and Fig. 5.16 respectively. For low- $z$ , unlike DESI, we can see we have high signal to reconstruction noise due to high number density, higher  $k_{\text{max}}$ , and higher bias. In the left panel of Fig. 5.15 we can see that, just like DESI, mostly the improvement in  $\sigma(f_{\text{NL}})$  mostly comes from extra large-scale modes  $K < K_{\text{min}}$  in the reconstructed field  $\delta_{\text{r}}$ . However, for high redshift range for MegaMapper-like survey we see a different behaviour as shown in Fig. 5.16. There we do get significant improvement in  $\sigma(f_{\text{NL}})$  and this improvement is the result of cosmic variance cancellation between  $\delta_{\text{g}}$  and  $\delta_{\text{r}}$ . As shown in [59], increasing the  $k_{\text{max}}$  as well as changing the fiducial  $b_2$  from 17 to 0 can significantly improve  $f_{\text{NL}}$  constraints. We further notice that low number density is not the limiting factor in the high- $z$  bin because if we increase the number density in the forecast the change in  $\sigma(f_{\text{NL}})$  is very modest [59].

## 5.5 Conclusion

In this chapter, we have developed a method to reconstruct large-scale density modes from a biased tracer field  $\delta_{\text{g}}$ . We have considered non-linearities from gravitational clustering, non-linear galaxy biasing and primordial non-Gaussianity. Our method of reconstruction is similar to the optimal quadratic estimator method in CMB lensing reconstruction [88, 155]. The idea is that we can define an optimal quadratic estimator  $\hat{\Delta}_{\alpha}$  using galaxy fields corresponding to a particular mode-coupling. The ensemble average of the estimator over short-scale modes by fixing the large-scale mode is proportional to the linear density field  $\delta_{\text{l}}(\mathbf{K})$  multiplied by a scale-dependent bias factor. The scale-dependent bias factor depends

on the bias parameters as well as contamination arising due to other mode couplings. We find that the noise due to the estimator defined from the growth term has the lowest amplitude among all other mode-couplings. We demonstrate density reconstruction using dark matter halos in numerical  $N$ -body simulations and show that analytical predictions agree pretty well with simulation results. We use the growth estimator for the Fisher forecast for  $f_{\text{NL}}$  for several galaxy surveys. The results from simulations show that our forecasts are realistic.

There are many applications of reconstructed modes in cosmology. For example, from this method, we reconstruct very large-scale modes which are generally inaccessible from the galaxy surveys due to observational systematics. We also show that we can use the reconstructed modes along with the galaxy field to constraint local-type of primordial non-Gaussianity. It is known that the local-type of primordial non-Gaussianity has the unique  $1/k^2$  imprint on large scale limits of galaxy clustering [153]. We see that the reconstructed modes from the quadratic estimator method also have the same  $1/k^2$  type contributions from  $f_{\text{NL}}$  terms (such as  $\phi\phi$ ,  $c_{01}$ , and  $c_{11}$ ). Due to this interesting behaviour we realise that the reconstructed modes can add extra information about local  $f_{\text{NL}}$  and if we do a combined analysis with  $\delta_{\text{g}}$  we can cancel cosmic variance and improve constraints on  $\sigma(f_{\text{NL}})$ . For Fisher analysis we use both  $\delta_{\text{g}}$  and  $\delta_{\text{r}}$ . The constraints on local  $f_{\text{NL}}$  therefore depends on the auto-correlation of the linear galaxy field,  $P_{\text{gg}}$ , the cross-correlation of the galaxy field with the reconstructed field,  $P_{\text{gr}}$ , and the auto-correlation of the reconstructed field,  $P_{\text{rr}}$ . For galaxy surveys, we use the configuration for a DESI-like survey with a redshift range  $0.6 < z < 1.6$  and a MeggaMapper-like survey for the low redshift range ( $2 < z < 2.5$ ) and the high redshift range ( $4.5 < z < 5$ ). The configurations for these surveys are given in Table 5.3. For a DESI-like survey, we find that we do not get significant improvement from adding the reconstructed field and the galaxy field together. However, if we also use the reconstructed modes  $K_{\text{f}} < K < K_{\text{min}}$  in the Fisher analysis, we get an improvement of 15% at  $K_{\text{min}} = 0.02h \text{ Mpc}^{-1}$ . This wavenumber is inaccessible from  $\delta_{\text{g}}$  alone but in principle can be accessed from our method of reconstruction. The constraints for  $\sigma(f_{\text{NL}})$  for a DESI-like survey are given in Fig. 5.14. Although we do not get a significant cosmic variance cancellation in a DESI-like survey, the improvements for  $\sigma(f_{\text{NL}})$  mostly comes from additional large-scale modes in the reconstructed field. For a MegaMapper-like survey we show that for the low- $z$  bin, just like DESI, we do not get a significant cosmic variance cancellation, however we do get a significant improvement due to additional large-scale in the reconstructed field, that is  $K < K_{\text{min}}$ , as shown in Fig. 5.15. Interestingly, for the high- $z$  bin of MegaMapper, unlike DESI and low- $z$  bin of MegaMapper, we do get significant cosmic variance cancellations as shown in Fig. 5.16. The method presented in this chapter has similarities with other work as well. In the literature, power spectrum and compressed bispectrum statistics have been used to constrain non-Gaussianities [176, 83, 73, 167, 99, 56, 43]. Our work has some similarities as well as differences from previous work done in this field. In terms of similarities, we

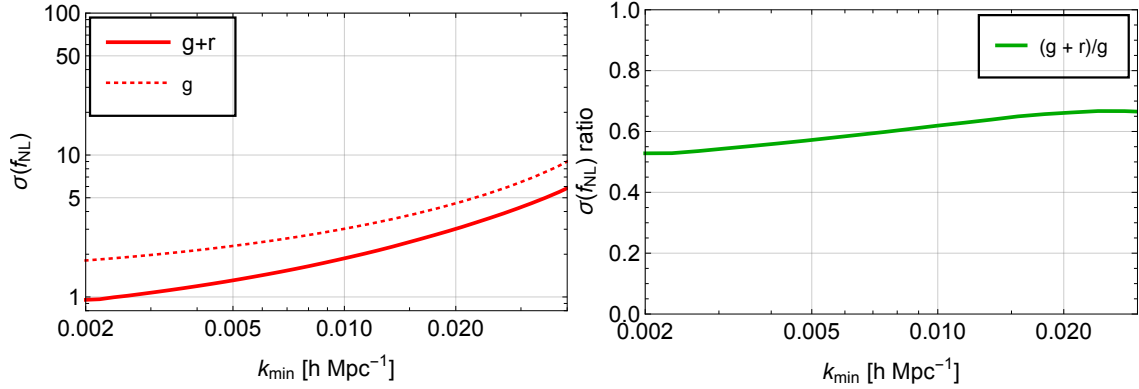


Fig. 5.16 MegaMapper high- $z$  bin:  $\sigma(f_{\text{NL}})$  constraints for a MegaMapper-like survey for high  $z$ ,  $4.5 < z < 5$ . LEFT PANEL:  $\sigma(f_{\text{NL}})$  obtained from  $\delta_{\text{g}}$  only (dotted red) and  $\delta_{\text{g}} + \delta_{\text{r}}$  (solid red). RIGHT PANEL: We plot ratio of constraints from combined analysis and galaxy-only.

are also using compressed statistics to capture information from higher-order correlation functions to constrain  $f_{\text{NL}}$ . The power spectrum and the bispectrum have often been used in the literature for analysis; however, in this work, we use power spectrum, bispectrum and trispectrum. Our quadratic estimator contains two  $\delta_{\text{g}}$ 's. Cross correlating it with the  $\delta_{\text{g}}$  contains the bispectrum information. Similarly auto-correlation of the quadratic estimator,  $P_{\text{rr}}$ , contains the trispectrum information.

We should mention we have quite a lot of similarities to the work we have done in [167]. However, the main difference which we emphasize is that, unlike the method proposed in that paper, our method of reconstruction is a tool and can directly be applied to data analysis of galaxy surveys. As an example, we implemented the quadratic estimators in numerical simulations and showed that indeed it is a practical tool to reconstruct the density field.

For future direction, there are several ways forward. One way is to increase  $k_{\text{max}}$  in the reconstruction and include higher-order perturbative terms in the cross-correlation of estimators. Increasing  $k_{\text{max}}$  will reduce the reconstruction noise and will improve constraints on  $f_{\text{NL}}$ . Another application is to apply this method to observation data coming from galaxy surveys in future. Furthermore, to get even better  $f_{\text{NL}}$  constraints, we can measure quadratic bias parameters from other methods (such as from the method developed in Chapter 6) and use the results as priors in the Fisher analysis. Marginalising over bias parameters with strong priors from data can definitely improve constraints on  $\sigma(f_{\text{NL}})$ .

## Constraining Nonlinear Galaxy Bias from CMB-LSS Cross Correlations

*Note: This chapter is my original work done under the supervision of Tobias Baldauf and Blake Sherwin. The results in this chapter will be submitted for publication soon.*

### 6.1 Introduction

There are several galaxy surveys planned for the future, such as the Large Synoptic Survey Telescope (LSST) [134], the Dark Energy Survey (DES), Euclid Satellite experiment [78], and NASA's WideField Infrared Survey Telescope (WFIRST)<sup>1</sup> [195]. These surveys will cover a larger fraction of sky and higher galaxy number densities at different redshift bins, and therefore will transform large-scale structure observations over the next decade.

Besides galaxy surveys, the gravitational lensing of the Cosmic Microwave Background (CMB) provides a promising probe to constrain cosmology [126]. The CMB radiation was released at the surface of the last scattering and provides the image of the Universe when it was 380,000 years old. The gravitational potential of the matter distribution in the Universe deflects the CMB photons, and therefore distorts the image of the surface of the last scattering. This entire process is called the gravitational lensing of the CMB, which is quite sensitive to the growth and structure of the matter distribution, and the geometry of the Universe. Therefore CMB lensing is a useful probe to constrain dark energy models, modifications of gravity on large scales, and the sum of neutrino mass. The first attempt to detect the CMB lensing potential was achieved using the temperature map provided by the Wilkinson Microwave Anisotropy Probe (WMAP)[112]. The detection was very weak at the order of  $< 2\sigma$  because of very high noise and low resolution of experiment [194, 82]. The cross-correlation of WMAP maps with radio galaxies from NRO VLA Sky surveys

---

<sup>1</sup><https://roman.gsfc.nasa.gov/>

detected the CMB lensing at the level of  $3.4\sigma$  [95, 54]. The measurements were further improved by subsequent work of [103, 60, 117, 199, 163, 61, 206, 200, 164]. The most recent measurements at the level of  $40\sigma$  are obtained from the recent Planck experiment using the non-Gaussianity measurements of the CMB temperature maps. Future CMB experiments such as Advanced ACT [62], the Simons Observatory [201] and the CMB-S4 [1] will provide much better resolution of the CMB maps, thereby opening new avenues for constraining cosmology with much better precision through CMB lensing measurements.

Since the CMB lensing kernel is quite broad in redshift and the fraction of sky covered by CMB experiments overlap with that of galaxy surveys, the cross-correlation of CMB lensing maps with galaxy clustering provides a useful tool to constrain cosmology at high redshifts. Cross-correlating the CMB lensing map with biased tracers of the large-scale structure can add further information to enhance our understanding of cosmology and astrophysics. Since future CMB experiments and galaxy surveys will have a substantial sky overlap, the cross-correlation between these two can cancel the cosmic variance and improve constraints on cosmological parameters [178]. For example, we can measure galaxy bias by cross-correlating CMB lensing with galaxies or quasars [189, 4]. Moreover, cross-correlating CMB lensing with other tracers such as the cosmic infrared background (CIB) or thermal Sunyaev-Zel'dovich (tSZ) effects can help us understand the relationship between dark matter and baryons in different regions in the Universe over the whole cosmic period [161, 106, 77].

Some applications of CMB lensing/galaxy clustering cross-correlations have been studied quite extensively in [178]. In that paper, the authors focused on constraining the amplitude of matter fluctuations  $\sigma_8$  as a function of redshift  $z$ , primordial non-Gaussianity  $f_{\text{NL}}$  and the sum of neutrino masses  $\sum_\nu m_\nu$ . They used a linear bias model for galaxy clustering that is  $\delta_g = b_1 \delta$ , for all their forecasts. The linear bias model, however, is only relevant for very large scales and requires the inclusion of higher-order non-linear terms if we want to go to a higher  $k_{\text{max}}$  to improve constraints.

In Large-scale structure (LSS) observations, the number of modes depends on the maximum wavenumber  $k_{\text{max}}$  as well as on volume of the survey. For a given survey, to improve constraints on cosmological parameters, it is necessary to increase the  $k_{\text{max}}$  using better modelling. The Effective Field Theory of Large-Scale Structure (EFTofLSS) provides a good framework to model LSS observable to a higher  $k_{\text{max}}$  by including loop corrections and appropriate counterterms [36, 45, 165, 188, 27, 7, 16, 39, 158]. The predictions of the EFTofLSS for the one-loop galaxy power spectrum and one-loop galaxy-lensing cross power spectra depends on galaxy bias parameters up to cubic order. If we model galaxy and lensing auto- and cross-bispectra, we will have to include bias parameters up to quadratic order at the tree level bispectra and up to quartic order for the one-loop bispectra. The authors in [148] studied the galaxy-lensing cross-correlations up to one-loop power spectra using

the Convolution Lagrangian Effective Field Theory (CLEFT). They show that for accurate modelling, one has to include several additional parameters such as linear bias, quadratic bias, derivative bias and stochastic terms. However, to get constraints on the amplitude of matter fluctuations  $\sigma_8$  one has to marginalise over all these additional parameters. They conclude that marginalising over additional parameters makes the constraints on  $\sigma_8$  worse. One way to make the constraints on cosmological parameters better is to measure higher-order bias parameters from data or simulations and use them as priors while marginalising over these additional parameters.

The natural statistics to estimate the linear bias parameter  $b_1$  is the tree-level galaxy-matter (galaxy-lensing) power spectrum. Quadratic bias parameters ( $b_2$  and  $b_{s,2}$ ) can naturally be estimated by the large-scale, tree-level bispectrum and cubic bias from large-scale, tree-level trispectrum. Higher order bias parameters up to cubic order are measured in  $N$ -body simulations in [2, 122] and it has been shown that using constraints from simulations, one can model the one-loop galaxy-matter power spectrum using the EFTofLSS framework which agrees with simulations very well up to  $k_{\max} = 0.1h \text{ Mpc}^{-1}$  [2]. At one-loop, if one includes the error in the model predicted from the EFTofLSS at two-loops, then the  $k_{\max}$  can be pushed further up to  $k_{\max} = 0.2h \text{ Mpc}^{-1}$  [13] and even higher if we include two-loop terms [47, 16].

Measuring higher-order bias parameters directly from data is a bit more involved as it requires modelling observational effects. One of the main effects which we should carefully consider are redshift space distortions (RSD). We can observe the angular distances of galaxies directly, but for the radial distances we need to infer it using the redshifts of the spectral lines. The inhomogeneities in the density field produce peculiar velocities beyond the Hubble flow. These peculiar velocities introduce distortions in redshifts, that is a shift between the actual distance and the observed distance. On large scales, we can model the RSD effect using the Kaiser formula [113]. On the other hand, the finger-of-god (FoG) effect introduces small scale non-linearities (see [67] for more details). Precise modelling of RSD for higher-point statistics requires us to consider both large and small-scale effects carefully. For example, for the bispectrum and the trispectrum, these effects introduce additional non-linearities and free parameters, and can therefore affect the precision of cosmological parameters.

To circumvent these problems and measure higher-order bias parameters effectively from high-redshift galaxy surveys, we develop projected field statistics in this chapter. The idea is that we start with projecting the three-dimensional (3D) galaxy field  $\delta_g$  along the line-of-sight to get a two-dimensional (2D) field  $\delta_{g,p}$ . Then we construct the quadratic field estimator using the projected density field (similar to the 3D quadratic field method presented in [176, 2]). Finally, we cross-correlate the 2D quadratic fields with the projected galaxy field. This cross-correlation contains the bispectrum information and is used to measure

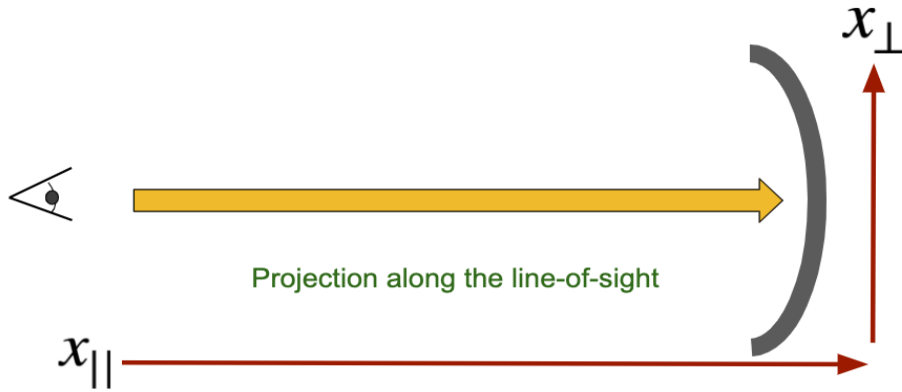


Fig. 6.1 An illustration of the projection along the line-of-sight.

quadratic non-linearities such as quadratic bias parameters. Using  $N$ -body simulations, we show that our analytical predictions for cross-correlations agree with simulation results, verifying that our Fisher analysis is realistic. Three main applications of projected statistics developed in this work are:

1. Cross correlating with the gravitational lensing of the CMB.
2. Constraining quadratic non-linearities such bias quadratic parameters and amplitude of matter fluctuations.
3. Suppressing non-linearities from redshift space distortions.

We focus on the first two applications, and for the third application we present the basic results and leave the full RSD modelling for Fisher analysis for future work.

The outline of this chapter is as follows. In Sec. 6.2, we develop the theory of projected statistics. We construct the 2D quadratic fields  $\mathcal{Q}_2[\delta_p]$ , where  $\delta_p \in \{\delta_{g,p}, \kappa\}$ , and cross-correlate it with the projected galaxy field or the CMB lensing convergence field. These cross-correlations contain information about the projected integrated bispectrum. We also discuss RSD effects and additional non-linearities introduced by RSD. In Sec. 6.3, we show that the theory developed in Sec. 6.2, for the cross-correlations of 2D quadratic fields indeed agree with  $N$ -body simulation results. In Sec. 6.4, we perform Fisher forecasts to obtain constraints on linear bias  $b_1$ , quadratic biases ( $b_2$  and  $b_{s,2}$ ) and amplitude of matter fluctuations. For forecasts, we use 2- and 3-point functions. For the 2-point functions we use combined analysis using the galaxy clustering and the CMB lensing convergence, similar to the multi-tracer analysis [178]. Finally, in Sec. 6.5, we discuss our results and present outline for future work.

## 6.2 Theory

### 6.2.1 2D Projections

In this section, we develop statistics for projected fields and introduce projected-squared fields. Consider a 3D random field  $\delta(\mathbf{x})$  and project it on to a 2D surface by using a window function. In real space we can perform this operation as

$$\delta_p(\mathbf{x}_\perp) = \int dx_{\parallel} W(x_{\parallel}/R_p) \delta(\mathbf{x}_\perp, x_{\parallel}) = \int dx_{\parallel} \int \frac{d^3 \mathbf{q}}{(2\pi)^3} e^{-i\mathbf{q} \cdot \mathbf{x}} W(x_{\parallel}/R_p) \tilde{\delta}(\mathbf{q}), \quad (6.1)$$

where  $x_{\parallel}$  represents the axis parallel to the line-of-sight,  $\mathbf{x}_\perp$  is the plane perpendicular to the line-of-sight, and  $R_p$  is the projection length along the line-of-sight. In the rest of the chapter the subscript 'p' describes that the 2D projected version of a 3D field. We define  $\tilde{\delta}(\mathbf{q})$  as the Fourier-transformed density field but to keep our notation clean and simple we represent it as  $\delta(\mathbf{q})$  in the rest of this work. Also in Eq.(6.1)  $W(x_{\parallel}/R_p)$  is the window function which only depends on the parallel axis. and the projection length. In Fourier space, Eq.(6.1) can be written as

$$\begin{aligned} \delta_p(\mathbf{k}_\perp) &= \int \frac{d^2 \mathbf{q}_\perp dq_{\parallel}}{(2\pi)^3} d^2 x_\perp dx_{\parallel} W(R_p x_{\parallel}) \tilde{\delta}(\mathbf{q}) e^{-i\mathbf{q} \cdot \mathbf{x}} e^{i\mathbf{k}_\perp \cdot \mathbf{x}_\perp} \\ &= \int dx_{\parallel} \frac{dq_{\parallel}}{2\pi} d^2 \mathbf{q}_\perp \delta_D(\mathbf{q}_\perp - \mathbf{k}_\perp) e^{-iq_{\parallel} x_{\parallel}} W(x_{\parallel}/R_p) \delta(\mathbf{q}) \\ &= \int \frac{dq_{\parallel}}{2\pi} W(-R_p q_{\parallel}) \delta(\mathbf{k}_\perp, q_{\parallel}). \end{aligned} \quad (6.2)$$

The projection commutes with Fourier transform. This means that if we take the Fourier transform of the 3D density field  $\delta$  and then project it on to a 2D surface we get the same result as if we first project the 3D field and then take the Fourier transform of the projected field. We want to relate the 3D power spectrum with the power spectrum of the projected field,  $P_{2D}$ . For this, we first remind ourselves that the power spectrum of a 3D field is given by

$$\langle \delta(\mathbf{k}_1) \delta(\mathbf{k}_2) \rangle = (2\pi)^3 \delta_D(\mathbf{k}_1 + \mathbf{k}_2) P(k_1). \quad (6.3)$$

where  $\delta_D$  is the Dirac delta function. Similarly the power spectrum of the projected field can be written as

$$\begin{aligned} \langle \delta_p(\mathbf{k}_{1\perp}) \delta_p(\mathbf{k}_{2\perp}) \rangle &= (2\pi)^2 \delta_D(\mathbf{k}_{1\perp} + \mathbf{k}_{2\perp}) P_{2D}(\mathbf{k}_{1\perp}) \\ &= \int \frac{dk_{1\parallel}}{2\pi} \frac{dk_{2\parallel}}{2\pi} W(R_p k_{1\parallel}) W(R_p k_{2\parallel}) (2\pi)^3 \delta_D(k_{1\parallel} + k_{2\parallel}) \delta_D(\mathbf{k}_{1\perp} + \mathbf{k}_{2\perp}) P(\sqrt{\mathbf{k}_{1\perp}^2 + k_{1\parallel}^2}) \end{aligned} \quad (6.4)$$



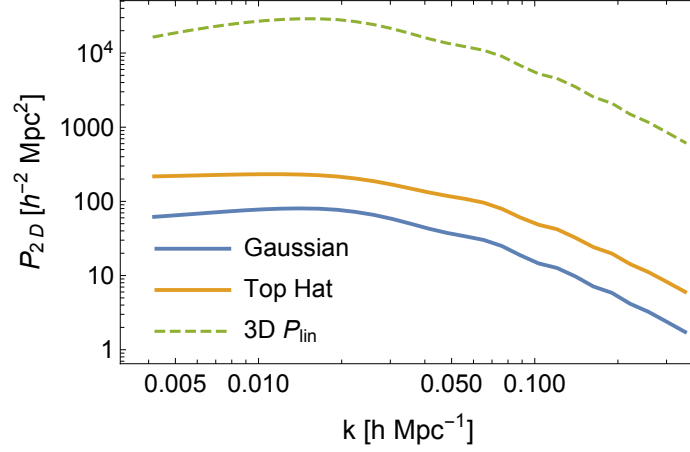


Fig. 6.2 Projected linear power spectrum  $P_{2D}$  using the Gaussian and the top-hat filters. The projection length used is  $R_p = 100h^{-1}$  Mpc. For comparison, the 3D linear power spectrum is shown with dashed-green curve (with units  $h^{-3}$  Mpc<sup>3</sup>).

The projected power spectrum as a function of the perpendicular modes is described as

$$P_{2D}(\mathbf{k}_\perp) = \int \frac{dk_\parallel}{2\pi} |W(R_p k_\parallel)|^2 P(\sqrt{\mathbf{k}_\perp^2 + k_\parallel^2}) \quad (6.5)$$

One can see that in the case of projection, the small scale modes feed the large scale modes. As we mentioned  $W(R_p k_\parallel)$  is a generic window function; for explicit examples we use a Gaussian and a Top-Hat window functions as below:

$$\text{Gaussian:} \quad W_G(R_p k_\parallel) = \exp\left[-(R_p k_\parallel)^2/2\right] \quad (6.6)$$

$$\text{Top-Hat:} \quad W_{TH}(R_p k_\parallel) = \frac{\sin(R_p k_\parallel/2)}{R_p k_\parallel/2}. \quad (6.7)$$

In Fig. 6.2 we plot the 3D linear power spectrum and the projected linear power spectrum using the Gaussian and the top-hat filters with the projection length  $R_p = 100h^{-1}$  Mpc.

### 6.2.2 CMB Lensing

The gravitational lensing of CMB provides the projected matter density back to the surface of the last scattering. CMB lensing is the cleanest probe available for the matter power spectrum compared to galaxy power spectrum or any other tracer of the matter distribution. The CMB photons are deflected by the gravitational potential  $\phi$  when they travel from the surface of the last scattering to us. This means that the temperature and polarization fields

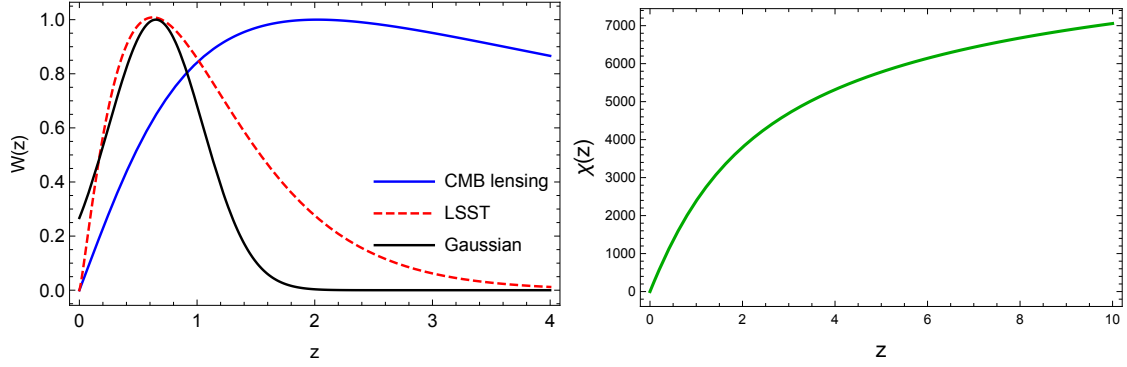


*Fig. 6.3* The CMB lensing kernel (solid blue) and galaxies kernels as function of redshift  $z$ . For galaxies we plot a Gaussian kernel and kernel for LSST galaxies peaked at around redshift  $z = 0.7$ . The kernels are normalised to a maximum value of 1.

observed are shifted by an angle of  $\alpha = \nabla_{\perp} \phi$ , where  $\nabla_{\perp}$  is the transverse gradient. We define the lensing convergence  $\kappa$  which is the transverse Laplacian of the gravitational potential and defined as  $\kappa = -1/2\nabla_{\perp}^2 \phi$ . The lensing convergence is a weighted projection of the matter density  $\delta$  along the line-of-sight:

$$\kappa(\theta) = \int_0^{\infty} dz W(z) \delta(\chi(z)\theta, z) \quad (6.9)$$

where  $\theta$  is the angular vector,  $\chi(z)$  is the comoving distance at redshift  $z$  and  $W(z)$  is the lensing projection kernel at redshift  $z$ . For a flat Universe, one can define the general kernel function for any source distribution as

$$W(z) = \frac{3}{2} \Omega_m H_0^2 \frac{(1+z)}{c^2 \chi(z)} \int_0^{\infty} dz_s \frac{dn(z_s)}{dz_s} \frac{\chi(z_s) - \chi(z)}{\chi(z_s)} \quad (6.10)$$

where  $\Omega_m$  is the matter density at redshift  $z = 0$ ,  $H_0$  represents the present-time value of the Hubble parameter,  $c$  is the speed of light,  $z_s$  is the source redshift, and  $n(z_s)$  is the number density of the source. The CMB photons are emitted from a single source plane at the time of the last scattering so for CMB lensing we define the distribution of the source number density as the Delta function,  $dn(z_s)/dz_s = \delta_D(z_s - z_*)$ , with  $z_* = 1100$  as the redshift of the last scattering surface. This allows us to write the lensing convergence kernel as

$$W_{\kappa}(z) = \frac{3}{2} \Omega_m H_0^2 \frac{(1+z)}{c^2} \frac{\chi(z_*) - \chi(z)}{\chi(z)\chi(z_*)} \quad (6.11)$$

This kernel is spread over a wide range of redshifts and it peaks at around  $z \approx 2$ . The CMB lensing kernel is plotted in the left panel of Fig. 6.3; the right panel shows the comoving distance as a function of redshift. In the Limber approximation, the angular power spectrum

of  $\kappa$  is defined as

$$C_l^{\kappa\kappa} = A^2 \int_0^\infty dz W_\kappa^2(z) P\left(k = \frac{l+1/2}{\chi(z)}, z\right) \quad (6.12)$$

where  $P(k, z)$  is the matter power spectrum and multipoles  $l$  represents the angular scales. We have also introduced another parameter  $A$  which is a relative amplitude of the matter fluctuations for some fiducial value of  $\sigma_8$ . As we can see that integral in Eq. (6.12) is extended to all redshifts and so for low redshifts  $\chi(z)$  is small which makes the wavenumber  $k$  very high. If  $k_{\text{NL}}$  is the scale up to where the perturbation theory is valid then we should be careful with low-redshifts auto-spectrum where we might end up to the regime where  $k > k_{\text{NL}}$ . If  $k < k_{\text{NL}}$  but still high then we should include higher-order perturbative terms in the matter power spectrum. For very high redshifts when  $k$  is small we can use the linear theory. In this work, we are interested in measuring bias parameters and the amplitude of fluctuations using the large-scale limit of 2- & 3-point functions so we will indeed use the linear theory in Eq.(6.12). However, if we are interested in constraining cosmological parameters such as the sum of neutrino masses then the constraints will get better as we have more modes, which means we should include either full non-linear matter spectrum or if we are using perturbation theory then higher-order loops terms. Here it is more convenient to work in the flat-sky limit in  $k$ -space so we can define the lensing convergence in  $k$ -space as

$$\kappa(\mathbf{k}_\perp) = A \int_0^\infty \frac{dk_\parallel}{2\pi} W_\kappa(k_\parallel) \delta(\mathbf{k}_\perp, k_\parallel) \quad (6.13)$$

where  $W_\kappa(k_\parallel)$  is the Fourier transform of Eq. (6.11) and is defined as

$$W_\kappa(k_\parallel) = \frac{3H_0^2 \Omega_m}{2c^2} \left[ -\frac{2 \cos(k_\parallel \chi(z_*)/2)}{k_\parallel^2} + \frac{4 \sin(k_\parallel \chi(z_*)/2)}{k_\parallel^3 \chi(z_*)} \right] \exp \left[ -ik_\parallel (\chi(z_*)/2) \right] \quad (6.14)$$

and the phase factor arises from the fact that the center has been shifted. The convergence auto-power spectrum in  $k$ -space is then defined as

$$P_{\kappa\kappa}(\mathbf{k}_\perp) = A^2 \int_{-\infty}^\infty \frac{dk_\parallel}{2\pi} |W_\kappa(k_\parallel)|^2 P(\sqrt{k_\parallel^2 + \mathbf{k}_\perp^2}, z=0) \quad (6.15)$$

where  $P$  is the matter power spectrum and can be modelled using the EFTofLSS [46, 17]. We can relate the angular power spectrum given in Eq. (6.12) and Eq. (6.15) using the Limber approximation discussed in detail in [133] and also in Appendix C. The transformation is given by  $l(l+1)C_l^{\kappa\kappa} = \mathbf{k}_\perp^2 P_{\kappa\kappa}(\mathbf{k}_\perp)$ .

### 6.2.3 Biased Tracers

Unlike the gravitational lensing of the CMB, galaxies are biased tracers of matter distribution. In general, the galaxy overdensity contrast can be expanded in terms of operators of dark matter density allowed by the symmetry of equations of motion [67, 10]. Beyond the linear bias model, we can write the 3D galaxy density in real space as

$$\begin{aligned}\delta_g(\mathbf{x}, z) &= \sum_{\mathcal{O}} b_{\mathcal{O}}(z) \mathcal{O}[\delta](\mathbf{x}, z) \\ &= b_1(z) (\delta^{(1)}(\mathbf{x}, z) + \delta^{(2)}(\mathbf{x}, z)) + \frac{b_2(z)}{2} \delta^2(\mathbf{x}, z) + b_{s^2}(z) s^2(\mathbf{x}, z) \\ &\quad + b_{\nabla^2}(z) \nabla^2 \delta(\mathbf{x}, z) + \varepsilon(\mathbf{x}, z) + \dots\end{aligned}\quad (6.16)$$

where we have expanded up to quadratic order in density field and the linear order in the derivative. In this expansion  $\delta^2$  is the growth term,  $s^2$  is the tidal term,  $\varepsilon$  is the stochasticity term. Also, we have expanded the matter density at second order in perturbation theory. The second-order density  $\delta^{(2)}$  further can be written in terms of the growth, tidal and the shift term as

$$\delta^{(2)}(\mathbf{x}, z) = \frac{17}{21} \delta^2(\mathbf{x}, z) - \psi(\mathbf{x}, z) \cdot \nabla \delta(\mathbf{x}, z) + \frac{2}{7} s^2(\mathbf{x}, z) \quad (6.17)$$

Given this relation, one can notice that the contribution of the shift term to the galaxy density field is sensitive to the linear bias  $b_1$ , the growth term depends on  $b_1$  and  $b_2$ , whereas the tidal term depends on the combination of  $b_1$  and  $b_{s^2}$ . In Fourier space we can write Eq. (6.16) as

$$\delta_g(\mathbf{k}, z) = b_1(z) \delta^{(1)}(\mathbf{k}, z) + \sum_{\mathcal{O}_2} \int \frac{d^3 \mathbf{q}}{(2\pi)^3} b_{\mathcal{O}_2}(z) \mathcal{K}_{\mathcal{O}_2}(\mathbf{q}, \mathbf{k} - \mathbf{q}) \delta^{(1)}(\mathbf{q}, z) \delta^{(1)}(\mathbf{k} - \mathbf{q}, z) + \varepsilon(\mathbf{k}, z) + \dots \quad (6.18)$$

where the dots represent higher-order terms (including the derivative biases) and  $\mathcal{O}_2 \in \{\delta^{(2)}, \delta^2, s^2\}$ . Here we will not consider the derivative bias term but it is important to mention that for correct modelling one has to take into account the derivative bias terms. It is shown in [2] using  $N$ -body simulations that the derivative bias term becomes important for  $k < 0.1h$   $\text{Mpc}^{-1}$  so it can not be neglected. In Eq. (6.18) the quadratic kernels  $\mathcal{K}_{\mathcal{O}_2} \in \{F_2, 1, S_2\}$  are defined as

$$F_2(\mathbf{q}_1, \mathbf{q}_2) = \frac{17}{21} + \frac{1}{2} \frac{\mathbf{q}_1 \cdot \mathbf{q}_2}{q_1 q_2} \left( \frac{q_1}{q_2} + \frac{q_2}{q_1} \right) + \frac{2}{7} \left[ \frac{(\mathbf{q}_1 \cdot \mathbf{q}_2)^2}{q_1^2 q_2^2} - \frac{1}{3} \right], \quad (6.19)$$

$$S_2(\mathbf{q}_1, \mathbf{q}_2) = \frac{(\mathbf{q}_1 \cdot \mathbf{q}_2)^2}{q_1^2 q_2^2} - \frac{1}{3}. \quad (6.20)$$

We now know how the galaxy density field looks like in 3D up to second order in linear density field. We can project this field along the line-of-sight to get the projected galaxy

field as

$$\delta_{g,p}(\mathbf{k}_\perp, z) = \int_0^\infty \frac{dk_\parallel}{2\pi} W_g(R_p k_\parallel) \delta_g(\mathbf{k}_\perp, k_\parallel, z) \quad (6.21)$$

where  $W_g(R_p k_\parallel)$  is the projected window kernel for galaxies. In case we choose a particular galaxy survey such as LSST this should depend on the distribution of the galaxy number density of the survey. For simplicity, we use the Gaussian window function shifted around some mean redshift  $z_m$ . The width of the Gaussian function depends on chosen redshift bins. In Fig. 6.3 along with the CMB lensing kernel we also plot the LSST kernel and a Gaussian approximation to the LSST kernel peaked at around  $z_m \approx 0.7$ . We define the auto galaxy power spectrum as

$$P_{gg}(\mathbf{k}_\perp, z) = \int_0^\infty \frac{dk_\parallel}{2\pi} |W_g(k_\parallel)|^2 P_{gg}^{3D}(\sqrt{\mathbf{k}_\perp^2 + k_\parallel^2}, z). \quad (6.22)$$

we can also define the cross power spectrum between galaxy and CMB lensing as

$$P_{g\kappa}(\mathbf{k}_\perp, z) = \int_0^\infty \frac{dk_\parallel}{2\pi} W_g(k_\parallel) W_\kappa(k_\parallel) \cos \left[ k_\parallel (\chi(z_*)/2 - \chi(z_m)) \right] P_{g\kappa}^{3D}(\sqrt{\mathbf{k}_\perp^2 + k_\parallel^2}, z) \quad (6.23)$$

In the cross-correlation of the galaxy density with CMB lensing field in Eq. (6.23), we have introduced the cosine factor. The shifted Gaussian galaxy kernel around the mean redshift source  $z_m$  combines with the phase factor of the shifted lensing kernel gives the cosine factor in Eq. (6.23). In Eq. (6.22) and (6.23)  $P_{gg}^{3D}$  and  $P_{g\kappa}^{3D}$  are defined as the 3D galaxy-galaxy and galaxy-matter power spectra. We define these spectra using the linear bias model because we are interested in large-scale limit of 2-point functions to constrain the linear bias and the amplitude of matter fluctuations. However, if we want to use the 2-point functions to constrain the sum of neutrino masses or other cosmological parameters we can include loop terms. Going to higher loops increase the number of available modes and therefore better constraints are expected. But one has to be careful with higher-order bias parameters. For example, the one-loop galaxy-galaxy and galaxy-matter power spectra require quadratic as well as cubic bias parameters [10, 2]. The one-loop 3D galaxy power spectrum is described as [23]

$$\begin{aligned} P_{gg}^{3D}(k, z) = & b_1^2 P(k, z) + A^4 \left[ b_{s^2} \left( b_{s^2} - \frac{5}{7} b_2 \right) \mathcal{I}_{s^2 s^2}(k, z) + 2b_1 \left( b_{s^2} + \frac{2}{5} b_{\Gamma_3} \right) \mathcal{F}_{s^2}(k, z) \right. \\ & \left. + 4b_2^2 \mathcal{I}_{\delta^2 \delta^2}(k, z) + 4b_1 \left( b_2 - \frac{2}{5} b_{s^2} \right) \mathcal{I}_{\delta^2}(k, z) \right] - A^2 b_1 b_{\nabla^2} k^2 P_{\text{lin}}(k, z) + s_p(z), \end{aligned} \quad (6.24)$$

and the one-loop galaxy-matter power spectrum as

$$P_{\text{gK}}^{3\text{D}}(k, z) = b_1 P(k, z) + A^4 \left[ \left( b_{s^2} + \frac{2}{5} b_{\Gamma_3} \right) \mathcal{F}_{s^2}(k, z) + \frac{1}{2} b_2 \mathcal{I}_{\delta^2 \delta^{(2)}}(k, z) + b_{s^2} \mathcal{I}_{\delta^{(2)} s^2}(k, z) \right] - A^2 b_{\nabla^2} k^2 P_{\text{lin}}(k, z) \quad (6.25)$$

where  $b_{\Gamma_3}$  is the cubic bias parameter, which can be constrained by trispectrum statistics,  $b_{\nabla^2}$  is the derivative bias and  $s_p$  is the shot noise term. The explicit form of functions  $\mathcal{I}_{\delta^2 \delta^2}$ ,  $\mathcal{I}_{\delta^2}$ ,  $\mathcal{I}_{\delta^2 \delta^{(2)}}$ ,  $\mathcal{I}_{\delta^2 s^2}$  and  $\mathcal{F}_{s^2}$  can be found in [10, 2]. It has been shown in [2] that if we constrain linear, quadratic and cubic biases from tree-level power spectrum, bispectrum and trispectrum statistics, and use the constraints to model one-loop galaxy-matter power spectrum, one gets very good agreements with  $N$ -body simulations results up to  $k_{\text{max}} = 0.1 h \text{ Mpc}^{-1}$  at redshift  $z = 0$ . The  $k_{\text{max}}$  in perturbation theory grows with redshift as [23]

$$k_{\text{max}}(z) = k_{\text{max}}(z = 0) \left( \frac{D_+(z)}{D_+(0)} \right)^{-4/3} \quad (6.26)$$

where  $D_+(z)$  is the growth factor as a function of redshift. This means for higher redshift surveys one can model power spectra up to very high wavenumbers which increases the number of modes substantially, resulting in better constraining power for cosmology. As mentioned before in this work, we only use the tree-level power spectra. We will show that combined analysis of galaxy and lensing using the tree-level auto- and cross power spectra is sufficient to break the degeneracy between  $b_1$  and  $A$ . In a later section, we show how we can constrain the higher-order quadratic bias parameters using the projected 3-point functions. How well other cosmological parameters using the bias constraints from 2- and 3-point functions and using the one-loop power spectra model can be constrained, we leave for future work.

### 6.2.4 Quadratic Fields in Projected Space

In this section, we introduce quadratic fields in projected space. The projection of the galaxy density field in Eq. (6.21) produces projected quadratic fields at second order in galaxy biasing. It was first proposed in [179] that cross-correlations of quadratic fields with the galaxy field capture all information of a squeezed bispectrum. This method was used in [2] to measure quadratic bias parameters in  $N$ -body simulations. Here we want to see if we can use this method in photometric surveys where we project fields. We construct quadratic fields with the projected fields or CMB lensing field and cross-correlate them with the projected galaxy fields. These cross-correlations contain cross-correlations of the projected quadratic

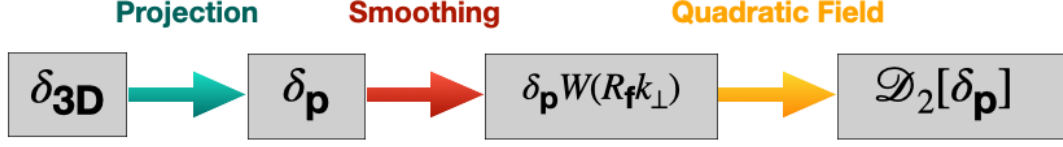


*Fig. 6.4* The illustration shows how one can construct a quadratic field  $\mathcal{D}_2[\delta_p]$  from a projected field  $\delta_p$ . The first step is to project a 3D density field  $\delta_{3D}$  using a Gaussian or a top-hat filter. The next step is to apply a smoothing function to the projected field in Fourier space with the smoothing scale  $R_f$ . Then we generate the quadratic field with a combination of Fourier and inverse Fourier transforms.

fields in Eq. (6.21) with the quadratic fields constructed with the projected field. We use these statistics to constrain quadratic bias parameters later in the chapter. We introduce a generic quadratic field estimator constructed from a projected field  $\delta_p$  as

$$\mathcal{D}_2[\delta_p](\mathbf{k}_{\perp}, z) = \int \frac{d^2 \mathbf{q}_{\perp}}{(2\pi)^2} \delta_p(\mathbf{q}_{\perp}, z) \delta_p(\mathbf{k}_{\perp} - \mathbf{q}_{\perp}, z) \mathcal{K}_{\mathcal{D}_2}(\mathbf{q}_{\perp}, \mathbf{k}_{\perp} - \mathbf{q}_{\perp}) W(R_f \mathbf{q}_{\perp}) W(R_f(\mathbf{k}_{\perp} - \mathbf{q}_{\perp})) \quad (6.27)$$

where  $\delta_p$  can be either the projected matter field<sup>2</sup>, projected galaxy field  $\delta_{g,p}$  or the CMB lensing convergence field  $\kappa$ . Eq. (6.27) is the convolution of projected density fields in 2D space. Because of the convolution integral, the quadratic field estimator will get contributions from all modes including the non-linear ones. Since we are interested in large-scale modes we should introduce a cut-off in the integral. This can be achieved by applying a smoothing function to  $\delta_p$  with a smoothing scale  $R_f$  which corresponds to the maximum wavenumber  $k_{\max} \approx 1/R_f$ . The  $k_{\max}$  is the cut-off in the bispectrum analysis. In Eq. (6.27) the kernels  $\mathcal{K}_2 \in \{1, H_2, S_2\}$  are the projected kernels corresponding to the growth term,  $\delta^2$ , the shift term,  $\psi \cdot \nabla \delta$ , and the tidal field,  $s^2$ . The kernels are defined as

$$H_2(\mathbf{q}_{1\perp}, \mathbf{q}_{2\perp}) = \frac{1}{2} \left[ \frac{\mathbf{q}_{1\perp} \cdot \mathbf{q}_{2\perp}}{\mathbf{q}_{1\perp} \cdot \mathbf{q}_{1\perp}} + \frac{\mathbf{q}_{1\perp} \cdot \mathbf{q}_{2\perp}}{\mathbf{q}_{1\perp} \cdot \mathbf{q}_{2\perp}} \right], \quad (6.28)$$

$$S_2(\mathbf{q}_{1\perp}, \mathbf{q}_{2\perp}) = \left[ \frac{(\mathbf{q}_{1\perp} \cdot \mathbf{q}_{2\perp})^2}{(\mathbf{q}_{1\perp} \cdot \mathbf{q}_{1\perp})(\mathbf{q}_{2\perp} \cdot \mathbf{q}_{2\perp})} - \frac{1}{2} \right]. \quad (6.29)$$

Let us assume that we construct the quadratic field with the projected galaxy field and cross-correlate it with the projected galaxy field itself. There are two types of contributions we would expect from Eq. 6.27 in the cross-correlation. First, when both fields inside the

<sup>2</sup>For convenience we now use  $\delta_p$  for the projected non-linear matter field and  $\delta_{g,p}$  for the projected galaxy field

integrals are linear fields. We define this as

$$\begin{aligned} \mathcal{D}_2^{(2)}[\delta_{g,p}](\mathbf{k}_\perp, z) &= b_1^2 \int \frac{d^2 \mathbf{q}_\perp}{(2\pi)^2} \delta_p^{(1)}(\mathbf{q}_\perp, z) \delta_p^{(1)}(\mathbf{k}_\perp - \mathbf{q}_\perp, z) \mathcal{H}_{\mathcal{D}_2}(\mathbf{q}_\perp, \mathbf{k}_\perp - \mathbf{q}_\perp) W(R_f \mathbf{q}_\perp) \\ &\quad \times W(R_f(\mathbf{k}_\perp - \mathbf{q}_\perp)). \end{aligned} \quad (6.30)$$

Second, when one field is linear and the second one is the second order galaxy field  $\delta_{g,p}^{(2)}$ , then Eq. (6.27) will become like a cubic field in terms of the linear density field  $\delta_p^{(1)}$  and we define these terms as  $\mathcal{D}_2^{(3)}$ :

$$\begin{aligned} \mathcal{D}_2^{(3)}[\delta_{g,p}](\mathbf{k}_\perp, z) &= \sum_{\mathcal{O}} b_1 b_{\mathcal{O}} \int \frac{d^2 \mathbf{q}_\perp}{(2\pi)^2} \delta_p^{(1)}(\mathbf{q}_\perp, z) \mathcal{O}[\delta]_p(\mathbf{k}_\perp - \mathbf{q}_\perp, z) \mathcal{H}_{\mathcal{D}_2}(\mathbf{q}_\perp, \mathbf{k}_\perp - \mathbf{q}_\perp) W(R_f \mathbf{q}_\perp) \\ &\quad \times W(R_f(\mathbf{k}_\perp - \mathbf{q}_\perp)). \end{aligned} \quad (6.31)$$

In Eq. (6.31) we have introduced  $\mathcal{O}[\delta]_p$  as the projected quadratic galaxy bias operators defined as

$$\mathcal{O}[\delta]_p(\mathbf{k}_\perp, z) = \int \frac{dk_{\parallel}}{2\pi} W_g(R_p k_{\parallel}) \int \frac{d^3 \mathbf{q}}{(2\pi)^3} \delta^{(1)}(\mathbf{q}, z) \delta^{(1)}(\mathbf{k} - \mathbf{q}, z) \mathcal{O}_2(\mathbf{q}, \mathbf{k} - \mathbf{q}) W(R_g \mathbf{q}) W(R_g(\mathbf{k} - \mathbf{q})) \quad (6.32)$$

where  $\mathcal{O}_2 \in \{\delta^{(2)}, \delta^2, s^2\}$  are quadratic bias operators in 3D,  $\delta^{(1)}$  is the linear density field in 3D, and  $R_g$  is the internal smoothing scale which is associated with the fact that the galaxies are formed inside finite size dark matter halos. The internal smoothing scale, the size of the Lagrangian patch which collapses to form a halo at late-times, introduces a Fourier space cut-off in Eq. (6.32) similar to  $k_{\max}^R \approx 1/R_g$ . As we don't know about this scale, we can either leave  $R_g$  as a free parameter or choose a particular value. Similar to what is done in [2] we choose  $R_g = 4h^{-1}$  Mpc in this work. We now write the full expression for the cross-correlation of  $\mathcal{D}_2[\delta_{g,p}]$  with the projected galaxy field as

$$\begin{aligned} \left\langle \mathcal{D}_2[\delta_{g,p}](\mathbf{k}_\perp, z) | \delta_{g,p}(\mathbf{k}_\perp, z) \right\rangle &= A_s^4 \left[ \sum_{\mathcal{O}} b_{\mathcal{O}} \left\langle \mathcal{D}_2^{(2)}[\delta_{g,p}](\mathbf{k}_\perp, z) | \mathcal{O}[\delta]_p(\mathbf{k}'_\perp, z) \right\rangle \right. \\ &\quad \left. + b_1 \left\langle \mathcal{D}_2^{(3)}[\delta_{g,p}](\mathbf{k}_\perp, z) | \delta_p^{(1)}(\mathbf{k}'_\perp, z) \right\rangle \right] + \text{shot noise} \end{aligned} \quad (6.33)$$

Here we have introduced the relative amplitude of matter fluctuations,  $A_s$ , to show the explicit dependence in the cross-correlations. The second terms in Eq. (6.33) are like propagators and are proportional to the projected linear power spectrum. The shot noise terms are discussed later in this chapter.



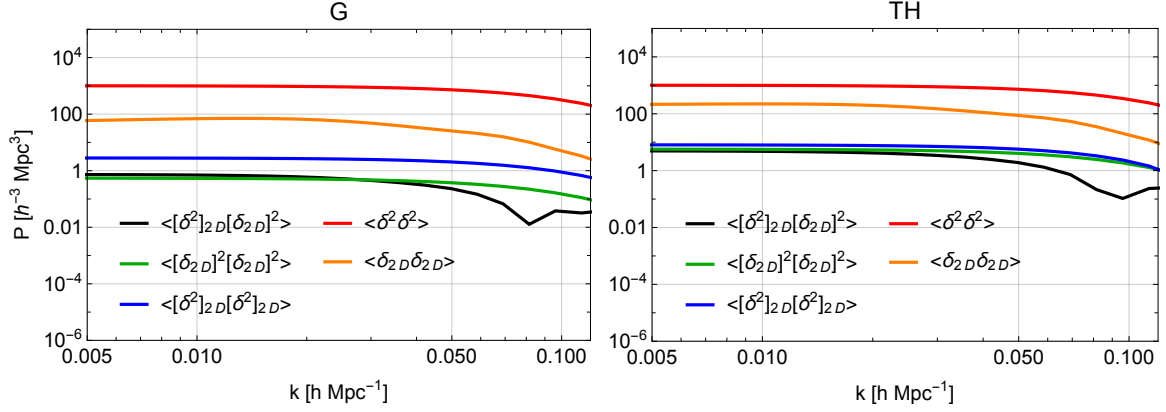


Fig. 6.5 Auto- cross correlations of quadratic fields in projected space using two different window functions: Gaussian and top-hat, with a projection scale  $R_p = 100h^{-1}\text{Mpc}$ . For a reference we also show the auto spectra of  $\delta^2$  in 3D (red curve).

### 6.2.5 Projected Bispectrum Estimator

The cross-correlation of projected quadratic fields with the the projected galaxy field is an integrated projected bispectrum:

$$\begin{aligned} \left\langle \mathcal{D}_2[\delta_{g,p}](\mathbf{k}_\perp, z) | \delta_{g,p}(\mathbf{k}'_\perp, z) \right\rangle' &= \int \frac{dk_\parallel}{2\pi} \int \frac{d^2\mathbf{q}_\perp}{(2\pi)^2} \int \frac{dq_\parallel}{2\pi} \int \frac{dp_\parallel}{2\pi} W_q(k_\parallel) W_g(-q_\parallel) W_g(-p_\parallel) \\ &\quad \times \mathcal{H}_{\mathcal{D}_2}(\mathbf{q}_\perp, \mathbf{k}_\perp - \mathbf{q}_\perp) \left\langle \delta_g(\mathbf{q}_\perp, q_\parallel, z) \delta_g(\mathbf{k}_\perp - \mathbf{q}_\perp, p_\parallel, z) \delta_g(\mathbf{k}'_\perp, k_\parallel, z) \right\rangle' \\ &\quad \times W(R_f \mathbf{q}_\perp) W(R_f(\mathbf{k}_\perp - \mathbf{q}_\perp)). \end{aligned} \quad (6.34)$$

It is obvious that  $\langle \delta_g \delta_g \delta_g \rangle'^3$  is the full 3D galaxy bispectrum. The projections remove modes along the line-of-sight and so the projected bispectrum defined above will have less modes as compared to the full 3D bispectrum. However, projections have other advantages such as suppressing non-linearities in redshift space distortions (discussed later) as well as cross correlating galaxies with the gravitational lensing of the CMB. Eq. (6.34) can be simplified as

$$\begin{aligned} \left\langle \mathcal{D}_2[\delta_{g,p}](\mathbf{k}_\perp, z) | \delta_{g,p}(\mathbf{k}'_\perp, z) \right\rangle' &= \int \frac{d^2\mathbf{q}_\perp}{(2\pi)^2} \mathcal{H}_{\mathcal{D}_2}(\mathbf{q}_\perp, \mathbf{k}_\perp - \mathbf{q}_\perp) B_{ggg}(\mathbf{k}'_\perp, \mathbf{q}_\perp, \mathbf{k}_\perp - \mathbf{q}_\perp, z) \\ &\quad \times W(R_f \mathbf{q}_\perp) W(R_f(\mathbf{k}_\perp - \mathbf{q}_\perp)) \end{aligned} \quad (6.35)$$

where  $B_{ggg}$  represents the bispectrum of the projected fields. The projected bispectrum can be estimated by counting the number of triangles formed from the wavenumber vectors in the projected plane. We consider three cross-correlations in this work:  $\langle \mathcal{D}_2[\delta_{g,p}] | \delta_{g,p} \rangle$ ,

<sup>3</sup>The prime on correlators here means that the Fourier space expectation value is equal to the power spectrum, that is  $\langle \delta(\mathbf{k}) \delta(\mathbf{k}') \rangle' = P(k)$  without considering the Delta function.

$\langle \mathcal{D}_2[\kappa] | \delta_{g,p} \rangle$ , and  $\langle \mathcal{D}_2[\kappa] | \kappa \rangle$ . These correlations have information about galaxy-galaxy-galaxy bispectrum, galaxy-matter-matter bispectrum and matter-matter-matter bispectrum respectively. Eq. (6.35) is given in Eq. (6.33), where we can see that it depends on the two distinct types of cross-correlations. The second term in Eq. (6.33) is proportional to the projected linear power spectrum.

### 6.2.6 Cross-Correlations of Quadratic Fields

In this section we present full expressions for the cross-correlations of quadratic fields. We will derive expressions for the auto and cross-correlations of  $\mathcal{D}_2$  fields which we will see appear in the covariance matrix. Then we discuss the auto- and cross-correlations of projected quadratic operators. Finally, we derive generic expressions for the cross-correlations of  $\mathcal{D}_2$  and projected quadratic fields  $\mathcal{O}[\delta]_p$  which we have seen appear in the bispectrum estimator expression defined above.

#### Auto- and Cross-Correlations of $\mathcal{D}_2$

The first case we discuss is the auto- and cross-correlations of two quadratic fields  $\mathcal{D}_2^\alpha$  constructed from the the projected density fields  $\delta_{X,p}$ , where  $X \in \{g, \kappa\}$  and  $\alpha$  represents the quadratic field corresponding to the growth, shift and tidal terms. The cross-correlations of two such quadratic fields can be written as

$$\begin{aligned} \left\langle \mathcal{D}_2^\alpha[\delta_{X,p}](\mathbf{k}_\perp, z_1) | \mathcal{D}_2^\beta[\delta_{Y,p}](\mathbf{k}'_\perp, z_2) \right\rangle' &= A_s^4 \int \frac{d^2 \mathbf{q}_\perp}{(2\pi)^2} \left\{ \mathcal{H}_{\mathcal{D}_2^\alpha}(\mathbf{q}_\perp, \mathbf{k}_\perp - \mathbf{q}_\perp) \mathcal{H}_{\mathcal{D}_2^\beta}(\mathbf{q}_\perp, \mathbf{k}_\perp - \mathbf{q}_\perp) \right. \\ &\times \left[ P_{XX}(\mathbf{q}_\perp) P_{YY}(|\mathbf{k}_{1\perp} - \mathbf{q}_\perp|) + P_{XY}(\mathbf{q}_\perp) P_{XY}(|\mathbf{k}_{1\perp} - \mathbf{q}_\perp|) \right] W^2(R_f(\mathbf{k}_\perp - \mathbf{q}_\perp)) \\ &\left. \times W^2(R_f \mathbf{q}_\perp) \right\} + P_{\text{shot}}^{\alpha\beta}(\mathbf{k}_\perp) \end{aligned} \quad (6.36)$$

where  $P_{\text{shot}}^{\alpha\beta}$  is the projected shot noise terms. If both  $X = Y = g$ , then  $P_{\text{shot}}^{\alpha\beta}$  is the projected shotnoise term. The trispectrum shotnoise terms in 3D are discussed in Sec. 5.2.5. In Eq. (6.36),  $P_{XY}$ ,  $P_{XX}$ , and  $P_{YY}$  are the projected power spectra, which also include the relevant cosine phase factor if we cross-correlate fields from two different redshift bins. If one of the fields is constructed from the CMB lensing convergence field then we choose the mean redshift as  $\chi(z_*)/2$ , where  $z_* = 1100$ . It is interesting to note that these cross-correlations can also be useful for density field reconstruction as we can think of  $\mathcal{D}_2$  as the quadratic estimator similar to the one used in the CMB lensing reconstruction (see Chapter 5 for density field reconstruction with quadratic estimators from biased tracers in 3D; or [59]).

In this work we neglect the trispectrum shot noise terms  $P_{\text{shot}}^{\alpha\beta}$  in these cross-correlations, however we do include the shot noise at the power spectrum level in  $P_{\text{gg}}$ . We will discuss specific examples of these correlations later in the covariances matrix section.

### Auto- and Cross-Correlations of $\mathcal{O}[\delta]_{\text{p}}$

In the second case we derive the expression for the auto- and cross-correlations of the projected quadratic field  $\mathcal{O}[\delta]_{\text{p}}$  defined in Eq. (6.32). These cross correlations can be written as

$$\begin{aligned} \left\langle \mathcal{O}^{\alpha}[\delta](\mathbf{k}_{\perp}) | \mathcal{O}^{\beta}[\delta](\mathbf{k}'_{\perp}) \right\rangle' &= 2A_s^4 \int_{-\infty}^{\infty} \frac{dk_{\parallel}}{2\pi} |W(-R_p k_{\parallel})|^2 \left[ \int \frac{d^3 \mathbf{q}}{(2\pi)^2} \mathcal{O}_2^{\alpha}(\mathbf{q}, \mathbf{k} - \mathbf{q}) \right. \\ &\quad \left. \times \mathcal{O}_2^{\beta}(\mathbf{q}, \mathbf{k} - \mathbf{q}) W(R_g \mathbf{q})^2 W(R_g(\mathbf{k} - \mathbf{q}))^2 P_{\text{lin}}(\mathbf{q}) P_{\text{lin}}(\mathbf{k} - \mathbf{q}) \right] \end{aligned} \quad (6.37)$$

where  $\mathcal{O}_2^{\alpha,\beta} \in \{\delta^{(2)}, \delta^2, S^2\}$  are quadratic operators in 3D,  $\mathcal{O}^{\alpha,\beta}[\delta]_{\text{p}}$  are projected versions of these operators, and finally  $P_{\text{lin}}$  is the 3D linear power spectrum.

### Cross-Correlations of $\mathcal{D}_2$ and $\mathcal{O}[\delta]_{\text{p}}$

The third case is about the cross-correlations of quadratic fields constructed from the projected fields,  $\mathcal{D}_2$ , and the projected quadratic fields,  $\mathcal{O}[\delta]_{\text{p}}$ . The generic expression for the cross-correlation of these two fields as defined as

$$\begin{aligned} \left\langle \mathcal{D}_2^{\alpha}[\delta_{\text{X,p}}](\mathbf{k}_{\perp}, z_1) | \mathcal{O}^{\beta}[\delta]_{\text{p}}(\mathbf{k}'_{\perp}, z_2) \right\rangle' &= A_s^4 \int \frac{d^2 \mathbf{q}_{\perp}}{(2\pi)^2} \int_{-\infty}^{+\infty} \frac{dk_{\parallel}}{2\pi} \int_{-\infty}^{+\infty} \frac{dq_{\parallel}}{2\pi} W(-R_p k_{\parallel}) W_{\text{X}}(-R_p q_{\parallel}) \\ &\quad \times W_{\text{X}}(-R_p(k_{\parallel} - q_{\parallel})) W(R_f \mathbf{q}_{\perp}) W(R_f(\mathbf{k}_{\perp} - \mathbf{q}_{\perp})) W(R_g(\mathbf{k}_{\perp} - \mathbf{q}_{\perp} + k_{\parallel} - q_{\parallel})) \\ &\quad \times W(R_g(\mathbf{q}_{\perp} + q_{\parallel})) P_{\text{lin}}\left(\sqrt{q_{\perp}^2 + q_{\parallel}^2}\right) P_{\text{lin}}\left(\sqrt{(k_{\perp} - q_{\perp})^2 + (k_{\parallel} - q_{\parallel})^2}\right) (b_1^{\text{X}})^2. \end{aligned} \quad (6.38)$$

If  $\text{X}=\text{g}$  in above equation then  $b_1^{\text{X}} = b_1$  for galaxy, but if  $\text{X} = \kappa$  then  $b_1^{\text{X}} = 1$ . It is important to note that is also a small contribution of stochastic shot noise from  $\mathcal{D}_2[\delta_{\text{g,p}}]$  which originates from  $\varepsilon$  and  $\varepsilon\delta$  type terms in the galaxy field.

## 6.2.7 Shot Noise

In this section, we discuss the shot noise contributions that appear in galaxy 2- and 3-point functions. We assume that the 3D number density of galaxies is  $n(z)$  at redshift  $z$ . In our forecast, we assume the number density does not evolve with redshift. But in reality, it

is a function of redshift  $z$  and depends on several factors including the survey properties, formation and evolution of galaxies, selection criteria etc. Although we consider a constant shot noises, but if one wants to consider other factors, these can be modelled using a power-law [23]

$$n(z) = n_0(1+z)^\alpha \quad (6.39)$$

where the new parameter  $\alpha$  captures dependence of several factors mentioned above and  $n_0$  is the 3D number density at redshift  $z = 0$  which is assumed to be  $n_0 = 10^{-2}h^3\text{Mpc}^{-3}$  or  $10^{-3}h^3\text{Mpc}^{-3}$ . The projected shot noise contribution to galaxy power spectrum defined in Eq. (6.22) is

$$P_{\text{gg, shot}}(\mathbf{k}_\perp, z) = \int \frac{dk_\parallel}{2\pi} |W_g(R_p k_\parallel)|^2 \frac{1}{n(z)}, \quad (6.40)$$

again to mention that  $R_p$  is the width of the redshift bin centered at  $z_m$ . The cross-correlation of the quadratic field  $\mathcal{D}_2[\delta_{\text{g,p}}]$  with the galaxy field  $\delta_{\text{g,p}}$  as defined in Eq. (6.34) also contains shot noise contributions at the bispectrum level. We know from Chapter 5 that shot noise contribution to full 3D galaxy bispectrum is given by

$$B_{\text{ggg}}(k_1, k_2, k_3) = \left\{ \frac{1}{n} \left( P_{\text{gg}}^c(k_1) + 2 \text{ perms} \right) + \frac{1}{n^2} \right\}. \quad (6.41)$$

where  $P_{\text{gg}}^c = b_1^2 P_{\text{lin}}$  is the continuous 3D galaxy power spectrum. Substituting this in Eq. (6.34) gives the projected shot noise contribution at the bispectrum level. For notational convenience we define  $P_{\mathcal{D}_2[\text{g,p}]} \equiv \langle \mathcal{D}_2[\delta_{\text{g,p}}] | \delta_{\text{g,p}} \rangle$ . The bispectrum projected shot noise as  $P_{\mathcal{D}_2[\text{g}]\text{g,shot}}$  can therefore be written as

$$\begin{aligned} P_{\mathcal{D}_2[\text{g}]\text{g,shot}}(\mathbf{k}_\perp, z) &= \int \frac{dk_\parallel}{2\pi} \int \frac{d^2\mathbf{q}_\perp}{(2\pi)^2} \int \frac{dq_\parallel}{2\pi} \int \frac{dp_\parallel}{2\pi} W_q(k_\parallel) W_g(-q_\parallel) W_g(-p_\parallel) \mathcal{K}_{\mathcal{D}_2}(\mathbf{q}_\perp, \mathbf{k}_\perp - \mathbf{q}_\perp) \\ &\times W(R_f \mathbf{q}_\perp) W(R_f(\mathbf{k}_\perp - \mathbf{q}_\perp)) \left[ \frac{1}{n(z)} \left( P_{\text{gg}}^c(\sqrt{\mathbf{k}_\perp^2 + k_\parallel^2}, z) + P_{\text{gg}}^c(\sqrt{\mathbf{q}_\perp^2 + q_\parallel^2}, z) \right. \right. \\ &\quad \left. \left. + P_{\text{gg}}^c(\sqrt{(\mathbf{k}_\perp - \mathbf{q}_\perp)^2 + p_\parallel^2}, z) \right) + \frac{1}{n(z)^2} \right]. \end{aligned} \quad (6.42)$$

This can be written in terms of 2D power spectrum as

$$\begin{aligned} P_{\mathcal{D}_2[\text{g}]\text{g,shot}}(\mathbf{k}_\perp, z) &= \int \frac{d^2\mathbf{q}_\perp}{(2\pi)^2} \mathcal{K}_{\mathcal{D}_2}(\mathbf{q}_\perp, \mathbf{k}_\perp - \mathbf{q}_\perp) W(R_f \mathbf{q}_\perp) W(R_f(\mathbf{k}_\perp - \mathbf{q}_\perp)) \\ &\times \left[ \frac{b_1^2(z)}{n(z)} \left( P_{\text{lin}}^{2\text{D}}(\mathbf{k}_\perp, z) + P_{\text{lin}}^{2\text{D}}(\mathbf{q}_\perp, z) + P_{\text{lin}}^{2\text{D}}(|\mathbf{k}_\perp - \mathbf{q}_\perp|, z) \right) + \frac{1}{n^2(z)} J(\mathbf{k}_\perp) \right] \end{aligned} \quad (6.43)$$

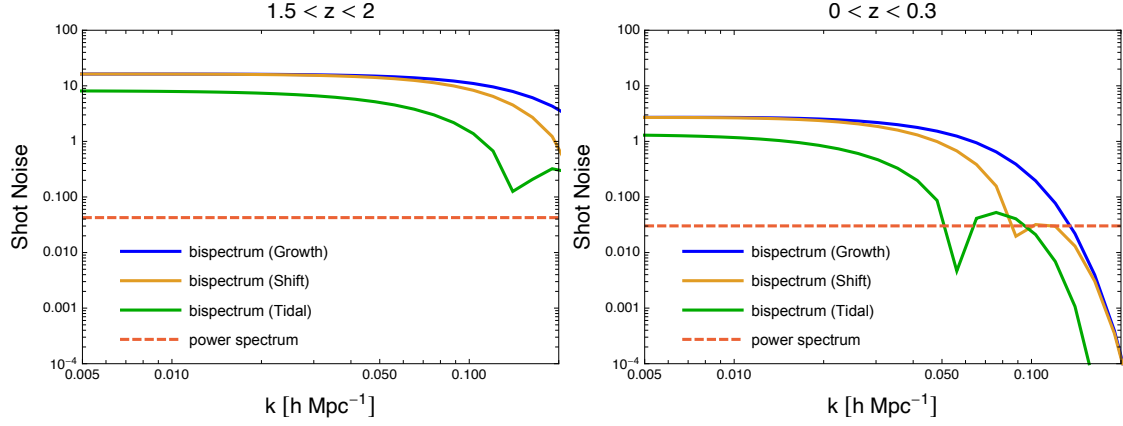


*Fig. 6.6* Projected shot noise contributions at the power spectrum and the bispectrum level using quadratic field  $\mathcal{D}_2$  corresponding to the growth, shift and the tidal terms. We use the constant 3D galaxy number density  $n_0 = 10^{-2} h^3 \text{Mpc}^{-3}$  and show the results for two galaxy redshift bins centered at  $z_m = 1.75$  and  $z_m = 0.15$ .

where

$$J(\mathbf{k}_\perp) = \int \frac{d^2 \mathbf{q}_\perp}{(2\pi)^2} \mathcal{H}_{\mathcal{D}_2}(\mathbf{q}_\perp, \mathbf{k}_\perp - \mathbf{q}_\perp) W(R_f \mathbf{q}_\perp) W(R_f(\mathbf{k}_\perp - \mathbf{q}_\perp)). \quad (6.44)$$

The contributions of the shot noise terms to the projected power spectra and cross-spectra of the quadratic field with the galaxy field are shown in Fig. 6.6. We show results for two different number densities of galaxies in 3D and choose the redshift bin centred at  $z_m = 0.15$ . In Fig. 6.7 we plot the bispectrum shot noise contributions for different redshift bins. Note that there are no shot noise contribution in  $P_{g\kappa}$  and  $\langle \mathcal{D}_2[\kappa] \delta_{g,p} \rangle$ , but there is still some contribution in  $\langle \mathcal{D}_2[\delta_{g,p}] \kappa \rangle$  defined by

$$P_{\mathcal{D}_2[g]\kappa, \text{shot}}(\mathbf{k}_\perp, z) = \frac{1}{n(z)} \int \frac{d^2 \mathbf{q}_\perp}{(2\pi)^2} \mathcal{H}_{\mathcal{D}_2}(\mathbf{q}_\perp, \mathbf{k}_\perp - \mathbf{q}_\perp) W(R_f \mathbf{q}_\perp) W(R_f(\mathbf{k}_\perp - \mathbf{q}_\perp)) P_{g\kappa}(\mathbf{k}_\perp, z). \quad (6.45)$$

### 6.2.8 Covariances

In this section, we discuss the covariances of the cross-spectra. Covariances are important to estimate bias parameters using the Fisher matrix so it is important to understand each term in the covariance matrix. We first obtain the most general expression and then define the expressions for specific examples we use in this work. The covariance of the two

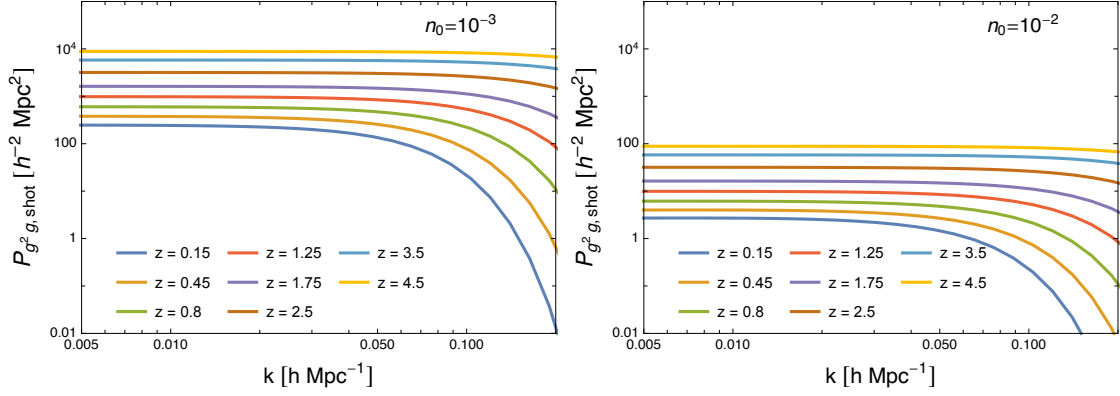


Fig. 6.7 Projected bispectrum shot noise corresponding to the growth field for 8 redshift bins. To show how the galaxy number density impacts bispectrum shotnoise terms, in the left panel we show the results for  $n_0 = 10^{-3} h^3 \text{ Mpc}^{-3}$  and in the right panel for  $n_0 = 10^{-2} h^3 \text{ Mpc}^{-3}$ .

cross-spectra are defined as

$$\begin{aligned} \text{Cov} \left( \left\langle \mathcal{D}_2^\alpha [\delta_{a,p}] \delta_{b,p} \right\rangle \left\langle \mathcal{D}_2^\beta [\delta_{c,p}] \delta_{d,p} \right\rangle \right) &= \frac{1}{N_k(z)} \left\{ \left\langle \mathcal{D}_2^\alpha [\delta_{a,p}] \delta_{b,p} \mathcal{D}_2^\beta [\delta_{c,p}] \delta_{d,p} \right\rangle \right. \\ &\quad \left. - \left\langle \mathcal{D}_2^\alpha [\delta_{a,p}] \delta_{b,p} \right\rangle \left\langle \mathcal{D}_2^\beta [\delta_{c,p}] \delta_{d,p} \right\rangle \right\} \\ &= \frac{1}{N_k(z)} \left\{ \left\langle \mathcal{D}_2^\alpha [\delta_{a,p}] \mathcal{D}_2^\beta [\delta_{c,p}] \right\rangle \left\langle \delta_{b,p} \delta_{d,p} \right\rangle + \left\langle \mathcal{D}_2^\alpha [\delta_{a,p}] \delta_{d,p} \right\rangle \left\langle \mathcal{D}_2^\beta [\delta_{c,p}] \delta_{b,p} \right\rangle + \dots \right\} \end{aligned} \quad (6.46)$$

where  $N_k$  are the number of modes in 2D redshift bins,  $\{a, b\} \in \{g, \kappa\}$  and "... " represents other connected terms which we do not include in this work. Here we are only interested in the leading-order covariances terms for fixed wavenumbers  $k_\perp = k'_\perp$ . Now we discuss different cases for variances and covariances of cross-spectra we use in the Fisher analysis.

**case 1:**  $a = b = c = d = g$

This case corresponds to the variance of  $\langle \mathcal{D}_2^\alpha [\delta_{g,p}] \delta_{g,p} \rangle$ . For this case, Eq. (6.36) can be simplified as

$$\begin{aligned} P_{\mathcal{D}_2^\alpha [g] \mathcal{D}_2^\alpha [g]}(\mathbf{k}_\perp, z) &\equiv \left\langle \mathcal{D}_2^\alpha [\delta_{g,p}](\mathbf{k}_\perp, z) \mathcal{D}_2^\alpha [\delta_{g,p}](\mathbf{k}'_\perp, z) \right\rangle' = 2 \int \frac{d^2 \mathbf{q}_\perp}{(2\pi)^2} \mathcal{H}_{\mathcal{D}_2^\alpha}(\mathbf{q}_\perp, \mathbf{k}_\perp - \mathbf{q}_\perp) \\ &\quad \times \mathcal{H}_{\mathcal{D}_2^\alpha}(\mathbf{q}_\perp, \mathbf{k}_\perp - \mathbf{q}_\perp) W^2(R_f \mathbf{q}_\perp) W^2(R_f(\mathbf{k}_\perp - \mathbf{q}_\perp)) P_{gg}(\mathbf{q}_\perp^2, z) P_{gg}(|\mathbf{k}_{1\perp} - \mathbf{q}_\perp|^2, z) \end{aligned} \quad (6.47)$$

where  $P_{\text{gg}}$  is the projected galaxy power spectrum defined in Eq. (6.22)<sup>4</sup>. The projected galaxy power spectrum also includes the projected shot noise at the power spectrum level. The second term in Eq. (6.46) is already defined in Eq. (6.33).

**case 2:**  $a = b = c = d = \kappa$

The second case we consider is when all fields are the CMB lensing convergence field  $\kappa$ . This case corresponds to the variance of  $\langle \mathcal{D}_2^\alpha[\kappa] \kappa \rangle$ . For this case, Eq. (6.36) can be takes the form as

$$P_{\mathcal{D}_2^\alpha[\kappa]\mathcal{D}_2^\alpha[\kappa]}(\mathbf{k}_\perp, z) \equiv \left\langle \mathcal{D}_2^\alpha[\kappa](\mathbf{k}_\perp, z) | \mathcal{D}_2^\alpha[\kappa](\mathbf{k}'_\perp, z) \right\rangle' = 2 \int \frac{d^2 \mathbf{q}_\perp}{(2\pi)^2} \mathcal{H}_{\mathcal{D}_2^\alpha}(\mathbf{q}_\perp, \mathbf{k}_\perp - \mathbf{q}_\perp) \\ \times \mathcal{H}_{\mathcal{D}_2^\alpha}(\mathbf{q}_\perp, \mathbf{k}_\perp - \mathbf{q}_\perp) W^2(R_f \mathbf{q}_\perp) W^2(R_f(\mathbf{k}_\perp - \mathbf{q}_\perp)) P_{\kappa\kappa}(\mathbf{q}_\perp^2, z) P_{\kappa\kappa}(|\mathbf{k}_{1\perp} - \mathbf{q}_\perp|^2, z) \quad (6.48)$$

where  $P_{\kappa\kappa}$  is the lensing convergence power spectrum, and

$$P_{\mathcal{D}_2^\alpha[\kappa]\kappa}(\mathbf{k}_\perp, z) \equiv \left\langle \mathcal{D}_2^\alpha[\kappa](\mathbf{k}_\perp, z) | \kappa(\mathbf{k}_\perp, z) \right\rangle \\ = A_s^4 \left[ \left\langle \mathcal{D}_2^\alpha[\kappa](\mathbf{k}_\perp, z) | [\kappa^{(2)}](\mathbf{k}'_\perp, z) \right\rangle + \left\langle \mathcal{D}_2^{\alpha(3)}[\kappa] | \kappa \right\rangle \right] \quad (6.49)$$

It is important to mention that we include the lensing reconstruction noise in the lensing power spectrum, but neglect the higher order contribution.

**case 3:**  $a = b = \mathbf{g}$  &  $c = d = \kappa$

The third specific example we consider is the covariance between  $\langle \mathcal{D}_2^\alpha[\delta_{\mathbf{g},\text{p}}] \delta_{\mathbf{g},\text{p}} \rangle$  and  $\langle \mathcal{D}_2^\beta[\kappa] \kappa \rangle$  which is given by

$$\text{Cov} \left( \left\langle \mathcal{D}_2^\alpha[\delta_{\mathbf{g},\text{p}}] \delta_{\mathbf{g},\text{p}} \right\rangle \left\langle \mathcal{D}_2^\beta[\kappa] \kappa \right\rangle \right) = \frac{1}{N_k(z)} \left\{ P_{\mathcal{D}_2^\alpha[\mathbf{g}]\mathcal{D}_2^\beta[\kappa]} P_{\mathbf{g}\kappa} + P_{\mathcal{D}_2^\alpha[\mathbf{g}]\kappa} P_{\mathcal{D}_2^\beta[\kappa]\mathbf{g}} \right\} \quad (6.50)$$

where

$$P_{\mathcal{D}_2^\beta[\kappa]\mathbf{g}}(\mathbf{k}_\perp, z) \equiv \left\langle \mathcal{D}_2^\beta[\kappa](\mathbf{k}_\perp, z) | \delta_{\mathbf{g}}(\mathbf{k}_\perp, z) \right\rangle = A_s^4 \left[ b_1(z) \left\langle \mathcal{D}_2^\beta[\kappa](\mathbf{k}_\perp, z) | [\delta^{(2)}]_{\text{p}}(\mathbf{k}'_\perp, z) \right\rangle \right. \\ \left. + \frac{b_2(z)}{2} \left\langle \mathcal{D}_2^\beta[\kappa](\mathbf{k}_\perp, z) | [\delta^2]_{\text{p}}(\mathbf{k}'_\perp, z) \right\rangle + b_{s^2}(z) \left\langle \mathcal{D}_2^\beta[\kappa](\mathbf{k}_\perp, z) | [s^2]_{\text{p}}(\mathbf{k}'_\perp, z) \right\rangle \right. \\ \left. + b_1(z) \left\langle \mathcal{D}_2^{\beta(3)}[\kappa] | \delta_{\text{p}}^{(1)} \right\rangle \right] + P_{\mathcal{D}_2^\alpha[\mathbf{g}]\kappa, \text{shot}}. \quad (6.51)$$

<sup>4</sup>We use  $P_{\text{gg}}^{\text{3D}} = b_1^2 A^2 P_{\text{lin}} + 1/\bar{n}$  in Eq. (6.36).

and

$$P_{\mathcal{D}_2^\alpha[\delta_g]\kappa}(\mathbf{k}_\perp, z) = A_s^4 \left[ \left\langle \mathcal{D}_2^\alpha[\delta_{g,p}](\mathbf{k}_\perp, z) | [\kappa^{(2)}](\mathbf{k}'_\perp, z) \right\rangle + \left\langle \mathcal{D}_2^{\alpha(3)}[\delta_{g,p}] | \kappa \right\rangle \right]. \quad (6.52)$$

We see there is a contribution in covariances from the cubic field  $\mathcal{D}_2^{\alpha(3)}$  which is defined in Eq. (6.31).

There are other terms as well which appear in the covariance matrix in Fisher analysis but we get the idea about how to calculate covariance terms.

## 6.2.9 Redshift Space Distortions

One of the main advantages of developing the projection statistics is to show that it can suppress nonlinearities from redshift space distortions at small scales. The angular distances of galaxies can be observed directly; however, the radial distances are inferred from the redshifts of the spectral lines from galaxies. The non-linearities in density field leads to peculiar velocities which induce a shift between the actual galaxy distances and that inferred from redshifts. These are called redshift space distortions. We will adopt the "plane-parallel" approximation, that is the line-of-sight is taken as a fixed direction such as the  $z$ -axis  $\hat{\mathbf{z}}$ . This is a fair assumption for faraway galaxies when their transverse speed is small compared to the distance. This approximation breaks the statistical isotropy, however, the statistical homogeneity is still satisfied and therefore we can expand the cosmological fields in Fourier modes. On the other hand, taking into account the radial distortions breaks the statistical isotropy too. Let us define the mapping between the real space position  $\mathbf{x}$  to redshift space  $\mathbf{s}$  [37]:

$$\mathbf{s} = \mathbf{x} - f v_z(\mathbf{x}) \hat{\mathbf{z}} \quad (6.53)$$

where  $f$  is the logarithmic growth rate of the linear perturbations,  $\mathbf{v} \equiv \mathbf{u}/(\mathcal{H}f)$  where we define the peculiar velocity in terms of the peculiar velocity field  $\mathbf{u}$ , and  $\mathcal{H}$  is the conformal Hubble parameter. The galaxy number conservation between real and redshift space is given by

$$(1 + \delta_s(\mathbf{s})) d^3 \mathbf{s} = (1 + \delta_g(\mathbf{x})) d^3 \mathbf{x} \quad (6.54)$$

where  $\delta_s(\mathbf{s})$  is the overdensity of galaxies in redshift space. This transformation looks very similar to the one for the density field between the Lagrangian to Eulerian space. The conservation of mass gives  $d^3 \mathbf{s} = J(\mathbf{x}) d^3 \mathbf{x}$ , where the Jacobian of the transformation in the plane-parallel approximation is defined as  $J(\mathbf{x}) = |1 - f \nabla_z v_z(\mathbf{x})|$ . This allows us to write galaxy overdensity in redshift space as

$$\delta_s(\mathbf{s}) = \frac{\delta_g(\mathbf{x}) + 1 - J(\mathbf{x})}{J(\mathbf{x})} = \frac{\delta_g(\mathbf{x}) + f \nabla_z v_z(\mathbf{x})}{|1 - f \nabla_z v_z(\mathbf{x})|} \quad (6.55)$$



which can be written in Fourier space as

$$\delta_s(\mathbf{k}) = \int \frac{d^3\mathbf{x}}{(2\pi)^3} e^{-i\mathbf{k}\cdot\mathbf{x}} e^{ifk_z v_z(\mathbf{x})} \left( \delta_g(\mathbf{x}) + f\nabla_z v_z(\mathbf{x}) \right). \quad (6.56)$$

Assuming that  $f\nabla_z v_z(\mathbf{x}) < 1$  we can expand the second exponential in series, and the density and velocity fields can be expanded using the perturbation theory. Expanding the second exponential gives

$$\begin{aligned} \delta_s(\mathbf{k}) &= \sum_{n=1}^{\infty} \int d^3\mathbf{k}_1 \dots d^3\mathbf{k}_n \delta^{(D)}(\mathbf{k} - \mathbf{k}_{1\dots n}) \left( \delta_g(\mathbf{k}_1) + f\mu_1^2 \theta(\mathbf{k}_1) \right) \frac{(f\mu k)^{n-1}}{(n-1)!} \\ &\quad \frac{\mu_2}{k_2} \theta(\mathbf{k}_2) + \dots + \frac{\mu_n}{k_n} \theta(\mathbf{k}_n) \\ &= \sum_{n=1}^{\infty} \int d^3\mathbf{k}_1 \dots d^3\mathbf{k}_n \delta^{(D)}(\mathbf{k} - \mathbf{k}_{1\dots n}) Z_n(\mathbf{k}_1, \dots, \mathbf{k}_n) \delta_1(\mathbf{k}_1) \dots \delta_1(\mathbf{k}_n) \end{aligned} \quad (6.57)$$

where  $\theta = \nabla \cdot v(\mathbf{x})$  is the velocity divergence field and  $\mu_i \equiv \mathbf{k}_i \cdot \hat{\mathbf{z}}/k_i = k_{i||}/k_i$  is the cosine between the line-of-sight and the wavevector  $k_i$ . We also define  $\mu \equiv \mathbf{k} \cdot (\hat{\mathbf{z}}/k)$  with  $\mathbf{k} = \mathbf{k}_1 + \dots + \mathbf{k}_n$ . For  $n = 1$  we obtain the well-known Kaiser formula [113]

$$\delta_s(\mathbf{k}) = \delta(\mathbf{k})(1 + f\mu^2). \quad (6.58)$$

The linear galaxy power spectrum in redshift space using the Kaiser formula can be written as

$$P_s(k, \mu) = b_1^2 (1 + \beta\mu^2)^2 P_{\text{lin}}(k) \quad (6.59)$$

where  $\beta = f/b_1$ . For  $n = 1$  and 2, the redshift space kernels are defined as

$$Z_1(\mathbf{k}) = (b_1 + f\mu^2), \quad (6.60)$$

$$\begin{aligned} Z_2(\mathbf{k}_1, \mathbf{k}_2) &= \frac{f\mu k}{2} \left[ \frac{\mu_1}{k_1} (b_1 + f\mu_2^2) + \frac{\mu_2}{k_2} (b_1 + f\mu_1^2) \right] + b_1 F_2(\mathbf{k}_1, \mathbf{k}_2) + f\mu^2 G_2(\mathbf{k}_1, \mathbf{k}_2) \\ &\quad + \frac{b_2}{2} + b_{s,2} S_2(\mathbf{k}_1, \mathbf{k}_2). \end{aligned} \quad (6.61)$$

The  $Z_2$  kernel for dark matter can be obtained by substituting  $b_2 = b_{s,2} = 0$  and  $b_1 = 1$  in Eq. (6.61).

### Finger of God Effect

On small scales, random motion within dark matter halos leads to suppression of clustering in redshift space. This effect squashes the 2-point function along the line-of-sight and is

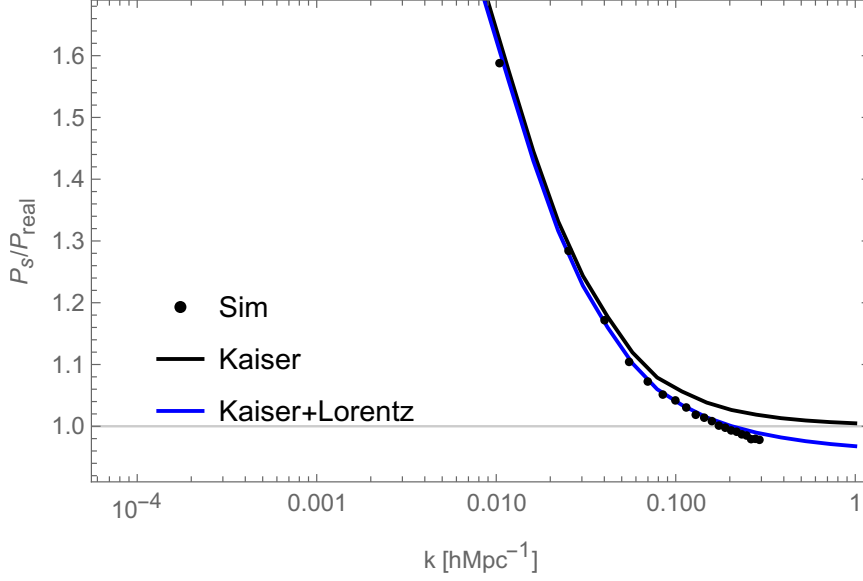


*Fig. 6.8* The ratio of the projected matter power spectrum in redshift space  $P_s$  and in real space  $P_{\text{real}}$ . We compare theory with simulations. We show three theory curves for modelling of RSD effects using the Kaiser formula (black) and Kaiser+FoG (blue). The projection length used is  $R_p = 100h^{-1}$  Mpc and the 1D velocity dispersion  $\sigma_v = 4h^{-1}$  Mpc.

referred to as the Finger of God effect (FoG) (see [102] for review). This effect can be modelled using some probability distribution function for the line-of-sight velocity  $F(v)$ . We choose an exponential velocity distribution [102, 30], which in Fourier space leads to a Lorentzian damping

$$\tilde{F}(k_{\parallel}) = \frac{1}{1 + k_{\parallel}^2 \sigma_v^2 / 2} \quad (6.62)$$

where  $\sigma_v$  is the 1D velocity dispersion. Using the Kaiser formula and the FoG effect, the galaxy power spectrum in redshift space can be written as:

$$P_s(k, \mu) = b_1^2 \frac{1}{1 + k_{\parallel}^2 \sigma_v^2 / 2} (1 + \beta \mu^2)^2 P_{\text{lin}}(k) \quad (6.63)$$

and this can smooth our the small-scale modes along the line-of-sight. In Fig. 6.8 we show a simple case how the projection can suppress non-linear RSD effects. We show the ratio of the the projected matter power spectrum in redshift space  $P_s$  and the projected power spectrum in real space  $P_{\text{real}}$ . We compare theory predictions with numerical  $N$ -body simulations (described in Sec.6.3. For theory we use the Kaiser formula defined in Eq. (6.58) and FoG defined in Eq.(6.62). The case with only the Kaiser formula in redshift power spectrum is shown by black curve and for Kasier+FoG in Blue. We see that on large-scales all agree with simulations, means on large scales we can only use the Kaiser formula. On

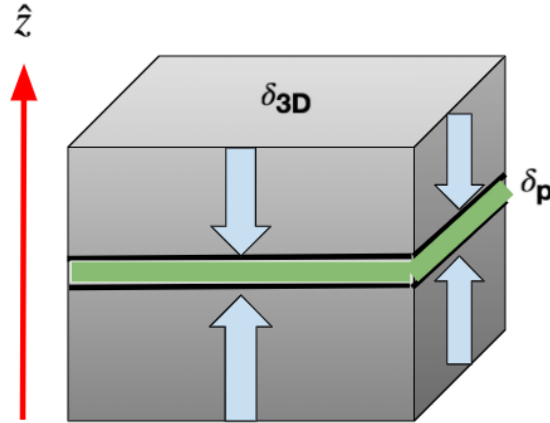


*Fig. 6.9* Projection of a 3D density field onto a 2D grid along the  $\hat{z}$  axis in simulations. The finite sized slices are summed up along the  $\hat{z}$  axis to get the projected field  $\delta_p$ . In the end, the projected field  $\delta_p$  should be properly normalised before using it for cross-correlations.

small scales, that is after  $k \geq 0.1h \text{ Mpc}^{-1}$ , when non-linearities become important, the Kaiser+FoG predictions agree with simulations pretty well.

We see the projection can suppress the FoG effects significantly; we still need to model it but the effects are less severe. However, in 3D these RSD effects would be more severe. This basic result is very promising and it shows that in projection statistics developed in this chapter we can model the RSD effects in the tree-level  $n$ -point functions using only the Kaiser and the FoG formulae. We leave the further development of this work for future, and so do not include the RSD effects in projection statistics for our Fisher analysis in this work.

## 6.3 $N$ -body Simulations

We carry out  $N$ -body simulation tests to check whether our analytical predictions of projection statistics agree with simulations. Like our previous works, we use a suite of 15 realisations of a cosmological  $N$ -body simulation. The initial conditions are generated with second order Lagrangian Perturbation Theory (**2-LPT**) code [182] at the initial redshift  $z_i = 99$  and are subsequently evolved using **Gadget-2** [196]. The simulations are performed with  $N_p = 1024^3$  dark matter particles in a cubic box of length  $L = 1500h^{-1} \text{ Mpc}$  with periodic boundary conditions. We assume a flat  $\Lambda$ CDM cosmology with the cosmological parameters  $\Omega_m = 0.272$ ,  $\Omega_\Lambda = 0.728$ ,  $h = 0.704$ ,  $n_s = 0.967$ . We perform the projections in  $N$ -body simulations as follows. First we project the 3D density field using the projection length of  $100h^{-1} \text{ Mpc}$ . In simulations we define the field on a 3D grid, so to get the 2D projected field we can sum slices in one direction, say  $\hat{z}$ . Once we get the projected density field with a finite width, we Fourier transform it, using the 2D version of FFTW, where we

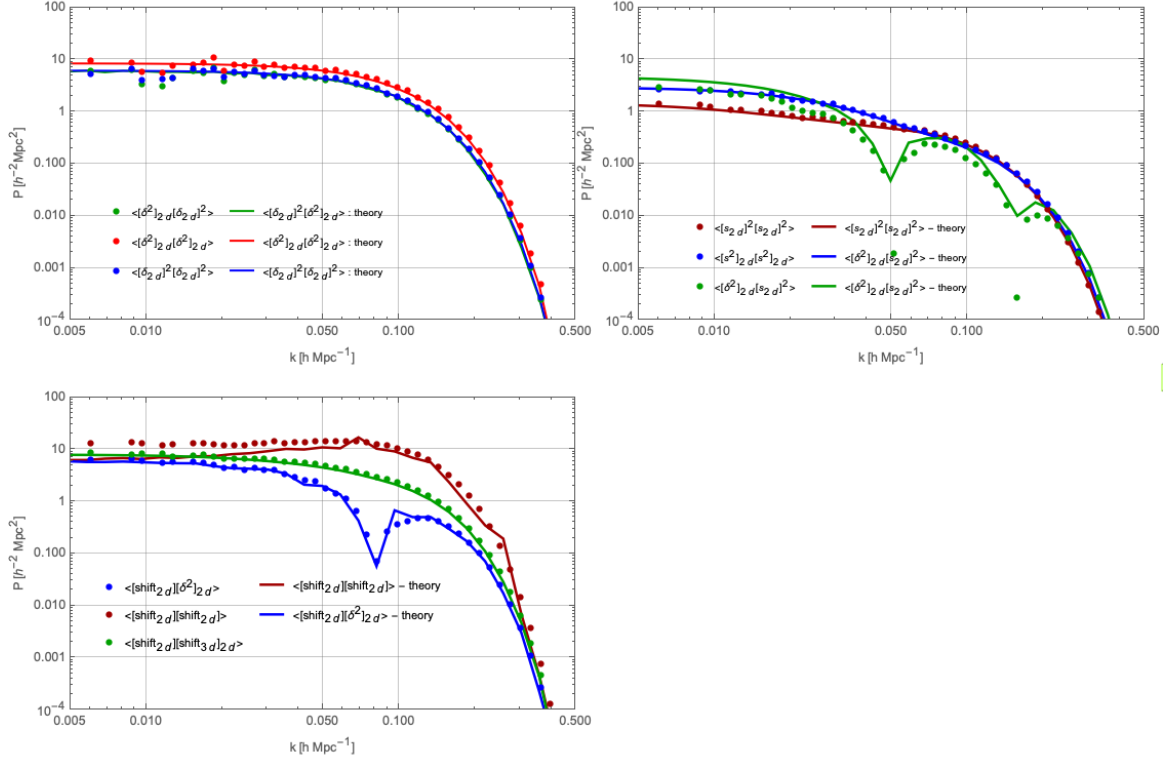


*Fig. 6.10* Auto- and Cross correlations of quadratic fields in projected space. Theoretical predictions (solid curves) agree with simulation results (dots). We show the results for quadratic fields corresponding to the growth, shift and the tidal terms.

multiply it by the Gaussian smoothing function. The smoothed projected field is transformed back to real space using the inverse Fourier transform where we can multiply it by itself to get the squared-field. We transform the squared-field to Fourier space using the Fourier transform. We generate other quadratic fields corresponding to the shift and the tidal kernels in 2D space. In this way we generate  $\mathcal{D}_2[\delta_p]$ . To generate  $\mathcal{O}[\delta]_p$ , we first construct the quadratic field in 3D space as discussed in [2] and then do the projection by adding up finite sized slices in the direction  $\hat{z}$ . In the end we properly normalise the projected fields in the 2D real space.

In Fig. 6.10, we show cross and auto-correlations of quadratic fields. We show quadratic fields corresponding to the growth shift and tidal terms. We use the projection length of  $100h^{-1}\text{Mpc}$  and the smoothing scale  $R_f = 10h^{-1}\text{Mpc}$ . We see excellent agreement between theory and simulations results, verifying that our theoretical expressions are indeed correct.

## 6.4 Fisher Forecasts

### 6.4.1 Setup

In this section, we set up the Fisher matrix for forecasting galaxy bias parameters and amplitude of fluctuations  $A_s$ . We use several statistics. We start from auto- and cross power spectra of the galaxy and CMB lensing and then add projected bispectrum information obtained using the projected squared-field method. For the projected squared field we use three statistics

#### Large-scale Power Spectrum

To perform the Fisher matrix analysis, we assume that the measured projected galaxy field  $\delta_g$  and the lensing field  $\kappa$  obey a Gaussian likelihood. This is a fair assumption as we are interested in large scale modes of these fields and the large scale modes are linear and follow a Gaussian distribution. Finally, at the field's level, we can write the Fisher Matrix (obtained from a Gaussian likelihood [205]; see also Appendix B for full derivation) for lensing-galaxy combined analysis as a function of wavenumber modes and redshift  $z$  as

$$F_{\alpha\beta}^{(2)} = \frac{1}{2} \sum_{z_i} \sum_{\mathbf{k}_\perp} \left[ \frac{\partial C(\mathbf{k}_\perp, z)}{\partial \theta_\alpha} C^{-1}(\mathbf{k}_\perp, z) \frac{\partial C(\mathbf{k}_\perp, z)}{\partial \theta_\beta} C^{-1}(\mathbf{k}_\perp, z) \right]_{\theta=\theta_0} \quad (6.64)$$

where the superscript '2' represents Fisher matrix corresponding to the power spectrum (2-pt functions). Also  $\theta \in \{b_1, b_2, b_{s2}, A_s\}$  is the set of free parameters in our analysis and  $\theta_0$  is a set of their fiducial values. Moreover, in Eq. (6.74)  $C$  is the covariance matrix defined as

$$C(\mathbf{k}_\perp, z) = \begin{pmatrix} C_{gg}(\mathbf{k}_\perp, z) & C_{g\kappa}(\mathbf{k}_\perp, z) \\ C_{\kappa g}(\mathbf{k}_\perp, z) & C_{\kappa\kappa}(\mathbf{k}_\perp, z) \end{pmatrix} \quad (6.65)$$

and  $C^{-1}$  is the inverse covariance matrix

$$C^{-1}(\mathbf{k}_\perp, z) = \frac{1}{C_{gg}(\mathbf{k}_\perp, z)C_{\kappa\kappa}(\mathbf{k}_\perp, z) - C_{g\kappa}(\mathbf{k}_\perp, z)^2} \begin{pmatrix} C_{\kappa\kappa}(\mathbf{k}_\perp, z) & -C_{g\kappa}(\mathbf{k}_\perp, z) \\ -C_{\kappa g}(\mathbf{k}_\perp, z) & C_{gg}(\mathbf{k}_\perp, z) \end{pmatrix} \quad (6.66)$$

We define the covariance matrix terms of galaxy and CMB lensing as follows:

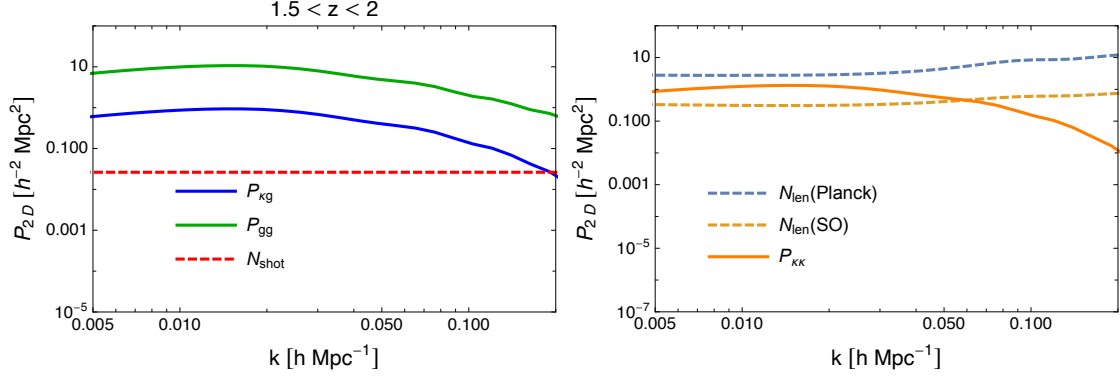


*Fig. 6.11* Here we plot auto- and cross-correlations of galaxy and CMB lensing for the redshift bin  $1.5 < z < 2$ . In the left panel we show lensing-galaxy and galaxy-galaxy power spectra as well as projected galaxy shot noise. In the right panel we show lensing auto power spectrum and lensing reconstruction noise. We show lensing reconstruction noise from Planck and Simons Observatory (SO) experiments obtained in  $k$ -space from  $l$ -space (multipoles) using the Limber approximation [133].

$$C_{\text{gg}}(\mathbf{k}_{\perp}, z) = \frac{1}{\sqrt{N_k(z)}} \left( P_{\text{gg}}(\mathbf{k}_{\perp}, z) + N_{\text{shot}}(\mathbf{k}_{\perp}, z) \right), \quad (6.67)$$

$$C_{\text{kg}}(\mathbf{k}_{\perp}, z) = \frac{1}{\sqrt{N_k(z)}} P_{\text{kg}}(\mathbf{k}_{\perp}, z) \quad (6.68)$$

$$C_{\text{kk}}(\mathbf{k}_{\perp}, z) = \frac{1}{\sqrt{N_k(z)}} \left( P_{\text{kk}}(\mathbf{k}_{\perp}, z) + N_{\text{len}}(\mathbf{k}_{\perp}, z) \right). \quad (6.69)$$

In the covariance matrix defined above we define the number of modes  $N_k(z)$  in each redshift bin as

$$N_k(z) = \frac{R_p(z) V^{2/3} k^2 dk}{2\pi f_{\text{sky}}} \quad (6.70)$$

where we used the 3D volume of the survey  $V = (2.5h^{-1} \text{ Gpc})^3$ , and  $R_p(z) = \chi(z_f) - \chi(z_i)$  is the width of each redshift bin  $z_i < z < z_f$ . For our analysis in this work we used  $f_{\text{sky}} = 0.5$ . We also introduce the galaxy shot noise  $N_{\text{shot}}$  and the lensing reconstruction noise  $N_{\text{len}}$  in the covariance matrix. In Eq. (6.67), Eq. (6.68) and Eq. (6.69) we choose the auto- and cross-correlations of galaxy and CMB lensing model to be defined as follows:

$$P_{\text{gg}}(\mathbf{k}_{\perp}, z) = b_1^2(z) A_s^2 \int_{-\infty}^{\infty} \frac{dk_{\parallel}}{2\pi} |W_g(R_p k_{\parallel})|^2 P_{\text{lin}}(\sqrt{k_{\parallel}^2 + \mathbf{k}_{\perp}^2}, z) \quad (6.71)$$

$$P_{\text{kg}}(\mathbf{k}_{\perp}, z) = b_1(z) A_s^2 \int_{-\infty}^{\infty} \frac{dk_{\parallel}}{2\pi} W_g(R_p k_{\parallel}) W_{\kappa}(k_{\parallel}) \cos \left[ k_{\parallel} (\chi(z_*)/2 - \chi(z_m)) \right] P_{\text{lin}}(\sqrt{k_{\parallel}^2 + \mathbf{k}_{\perp}^2}, z), \quad (6.72)$$

$$P_{\text{kk}}(\mathbf{k}_{\perp}, z) = A_s^2 \int_{-\infty}^{\infty} \frac{dk_{\parallel}}{2\pi} |W_{\kappa}(k_{\parallel})|^2 P_{\text{lin}}(\sqrt{k_{\parallel}^2 + \mathbf{k}_{\perp}^2}, z) \quad (6.73)$$

In Fig. 6.11 we plot  $P_{gg}$ ,  $P_{\kappa g}$  and  $P_{\kappa\kappa}$  along with projected galaxy shot noise and lensing reconstruction noise for a redshift bin  $1.5 < z < 2$ . We choose this redshift bin as it is close to where CMB lensing kernel peaks and so we expect better cross-correlation signal between galaxy and lensing. For the lensing reconstruction noise we transformed the noise data for Planck and Simons Observatory (SO) from  $l$ -space to  $k$ -space using the Limber approximation [133]:  $l(l+1)N_l = \mathbf{k}_\perp^2 N_{\text{len}}(\mathbf{k}_\perp)$ .

### Large-scale Integrated Bispectrum

For constraining quadratic bias parameters we need to set up the Fisher matrix using the quadratic field statistics. We consider a combined analysis using  $\langle \mathcal{D}_2[\delta_{g,p}] | \delta_{g,p} \rangle'$ ,  $\langle \mathcal{D}_2[\delta_{g,p}] | \kappa \rangle'$ , and  $\langle \mathcal{D}_2[\kappa] | \delta_{g,p} \rangle'$ , where  $\mathcal{D}_2 \in \{1, H_2, S_2\}$  corresponding to the growth (G), shift (S) and the tidal terms (T). The cross-correlation of the quadratic projected-field for the growth term with the galaxy field captures the  $b_2$  bias information, the shift field captures the  $b_1$  bias information and the tidal field provides information about the  $b_{s2}$  bias term. As we mentioned before, these cross-correlations contain 3-point function information but use the power spectrum analysis. Since we are interested in the tree-level, large-scale limit of these statistics, we assume that these statistics follow a Gaussian likelihood. At the power spectrum level, for one specific quadratic field, we write the Fisher matrix as

$$F_{\alpha\beta}^{(3)} = \sum_{z_i} \sum_{\mathbf{k}_\perp} \left[ \frac{\partial \mathbf{D}(\mathbf{k}_\perp, z_i)}{\partial \theta_\alpha} \left( C_D^{-1} \right)_{kk'} \frac{\partial \mathbf{D}(\mathbf{k}_\perp, z_i)}{\partial \theta_\beta} \right]_{\theta=\theta_0} \quad (6.74)$$

where the superscript '3' is for the 3-point Fisher matrix for the 3-point functions. We define the vector  $\mathbf{D} = \{P_{\mathcal{D}_2[\delta_g]\delta_g}, P_{\mathcal{D}_2[\delta_g]\kappa}, P_{\mathcal{D}_2[\kappa]\delta_g}\}$  and  $C_D$  is the combined covariance matrix for these three statistics, which is defined as

$$C_D(\mathbf{k}_\perp, z) = \begin{pmatrix} C_{ggg, ggg} & C_{ggg, gg\kappa} & C_{ggg, g\kappa\kappa} \\ C_{gg\kappa, ggg} & C_{gg\kappa, gg\kappa} & C_{gg\kappa, g\kappa\kappa} \\ C_{g\kappa\kappa, ggg} & C_{g\kappa\kappa, gg\kappa} & C_{g\kappa\kappa, g\kappa\kappa} \end{pmatrix}. \quad (6.75)$$

The individual terms in the covariance matrix can be described using expression given in Sec. 6.2.8 (see Eq. (6.46) for a generic expression). We write the expressions for these terms

as follows:

$$C_{\text{ggg,ggg}} = \frac{1}{N_k(z)} \left\{ (P_{\text{gg}} + N_{\text{shot}}) \langle \mathcal{D}_2[\delta_{\text{g,p}}] \mathcal{D}_2[\delta_{\text{g,p}}] \rangle + (P_{\mathcal{D}_2[\delta_{\text{g}}]\delta_{\text{g}}})^2 \right\} \quad (6.76)$$

$$C_{\text{ggg,gg}\kappa} = \frac{1}{N_k(z)} \left\{ P_{\kappa\text{g}} \langle \mathcal{D}_2[\delta_{\text{g,p}}] \mathcal{D}_2[\delta_{\text{g,p}}] \rangle + P_{\mathcal{D}_2[\delta_{\text{g}}]\delta_{\text{g}}} P_{\mathcal{D}_2[\delta_{\text{g}}]\kappa} \right\} \quad (6.77)$$

$$C_{\text{ggg,g}\kappa\kappa} = \frac{1}{N_k(z)} \left\{ (P_{\text{gg}} + N_{\text{shot}}) \langle \mathcal{D}_2[\delta_{\text{g}}] \mathcal{D}_2[\kappa] \rangle + P_{\mathcal{D}_2[\delta_{\text{g,p}}]\delta_{\text{g}}} P_{\mathcal{D}_2[\kappa]\delta_{\text{g}}} \right\} \quad (6.78)$$

$$C_{\text{g}\kappa\kappa,\text{g}\kappa\kappa} = \frac{1}{N_k(z)} \left\{ (P_{\text{gg}} + N_{\text{shot}}) \langle \mathcal{D}_2[\kappa] \mathcal{D}_2[\kappa] \rangle + (P_{\mathcal{D}_2[\kappa]\delta_{\text{g}}})^2 \right\} \quad (6.79)$$

$$C_{\text{g}\kappa\kappa,\text{gg}\kappa} = \frac{1}{N_k(z)} \left\{ P_{\kappa\text{g}} \langle \mathcal{D}_2[\delta_{\text{g,p}}] \mathcal{D}_2[\kappa] \rangle_{\kappa\text{g}} + P_{\mathcal{D}_2[\kappa]\delta_{\text{g}}} P_{\mathcal{D}_2[\delta_{\text{g}}]\kappa} \right\} \quad (6.80)$$

$$C_{\text{gg}\kappa,\text{gg}\kappa} = \frac{1}{N_k(z)} \left\{ (P_{\kappa\kappa} + N_{\kappa\kappa}) \langle \mathcal{D}_2[\delta_{\text{g,p}}] \mathcal{D}_2[\delta_{\text{g,p}}] \rangle_{\text{gg}} + (P_{\mathcal{D}_2[\delta_{\text{g}}]\kappa})^2 \right\} \quad (6.81)$$

The full Fisher matrix for the combined 3-point functions is the sum of the Fisher matrix from the individual quadratic-field statistics:

$$\mathbf{F}_{\alpha\beta}^{\text{D,Tot}} = \mathbf{F}_{\alpha\beta}^{\text{D=G}} + \mathbf{F}_{\alpha\beta}^{\text{D=S}} + \mathbf{F}_{\alpha\beta}^{\text{D=T}} \quad (6.82)$$

Here we assume that these statistics are independent and ignore any cross-correlations among them. We also do the combined 2-point and 3-point analysis, so the combined Fisher matrix is the sum of Eq. (6.74) and Eq. (6.82):

$$\mathbf{F}_{\alpha\beta}^{\text{Tot}} = \mathbf{F}_{\alpha\beta}^{(2)} + \mathbf{F}_{\alpha\beta}^{\text{D,Tot}}. \quad (6.83)$$

The Fisher matrix contains information about how well we can constrain parameters from the data. If we are only interested in one parameter  $\theta_i$  then we will have to marginalise over all the other parameters. Marginalised errors are defined as

$$\sigma(\theta_\alpha) = \sqrt{[(F^{\text{Tot}})^{-1}]_{\alpha\alpha}} \quad (6.84)$$

However, the unmarginalised error is defined as the inverse of the square-root of the Fisher matrix:

$$\sigma(\theta_\alpha) = \frac{1}{\sqrt{(F^{\text{Tot}})_{\alpha\alpha}}} \quad (6.85)$$



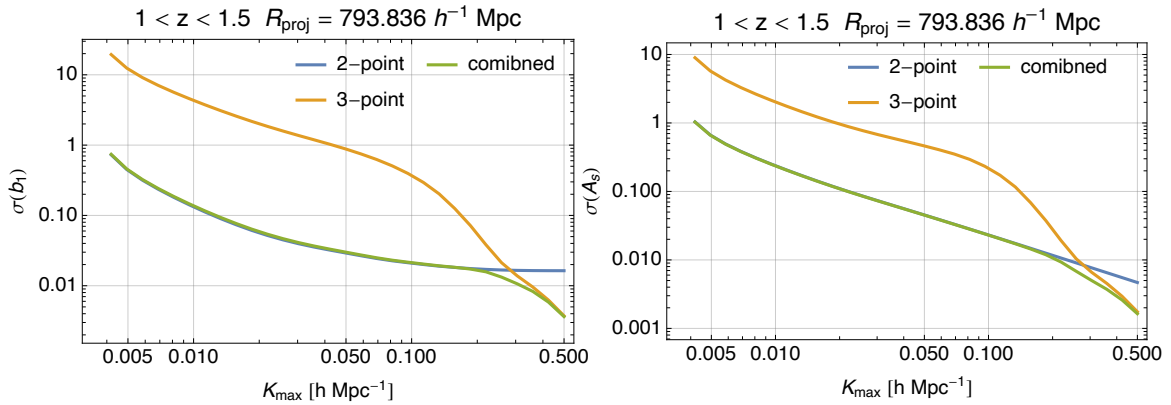


*Fig. 6.12* Constraints on  $b_1$  and  $A_s$  as function of  $k_{\max}$  using the combined 2-point functions of galaxy/lensing auto- and cross-correlations; 3-point functions; and combined, 2- and 3-point functions. The constraints are shown for one redshift bin  $1 < z < 1.5$ . We can see that 2-point functions tightly constraints  $b_1$  and  $A_s$ . The 3-point functions only started to dominate at very high  $k_{\max}$ .

### Parameters and Priors

Our model depends on four parameters:  $\theta \in \{A_s, b_1, b_2, b_{s,2}\}$ . We are only interested in how well we can use the method developed in this work to measure linear and quadratic bias parameters as well as the relative amplitude of matter fluctuations. In our derivations of shot noise contribution to the cross-correlations of various quadratic fields, we assume that the galaxy noise is Poissonian. However, it has been shown that the shot noise is sub-Poissonian or super-Poissonian depending on mass samples [101, 22]. If we take into consideration this deviation of shot noise from the Poissonian distribution, then we should add two more parameters for stochasticity (at the power spectrum and the bispectrum levels). We don't add any new stochastic parameters in our models for now, but for the future work free stochastic parameters will be considered. We choose no priors and the fiducial values we use for parameters are

$$\theta_0 = \{1, 1.067, -0.364, 0.021\}. \quad (6.86)$$

These fiducial values are measured from simulation at redshift  $z=0$  for the lowest mass bins [2]. For higher redshift we consider the redshift dependence of these parameters by multiplying by the growth factor appropriately.

### 6.4.2 Results

In Fig. 6.12, we show our results for constraints on  $b_1$  and the relative amplitude of fluctuations  $A_s$  using the 2-point, 3-point and combine 2- & 3-point functions for a single redshift bin  $1 < z < 1.5$ . It is obvious that the combined 2-point function analysis of galaxy clustering

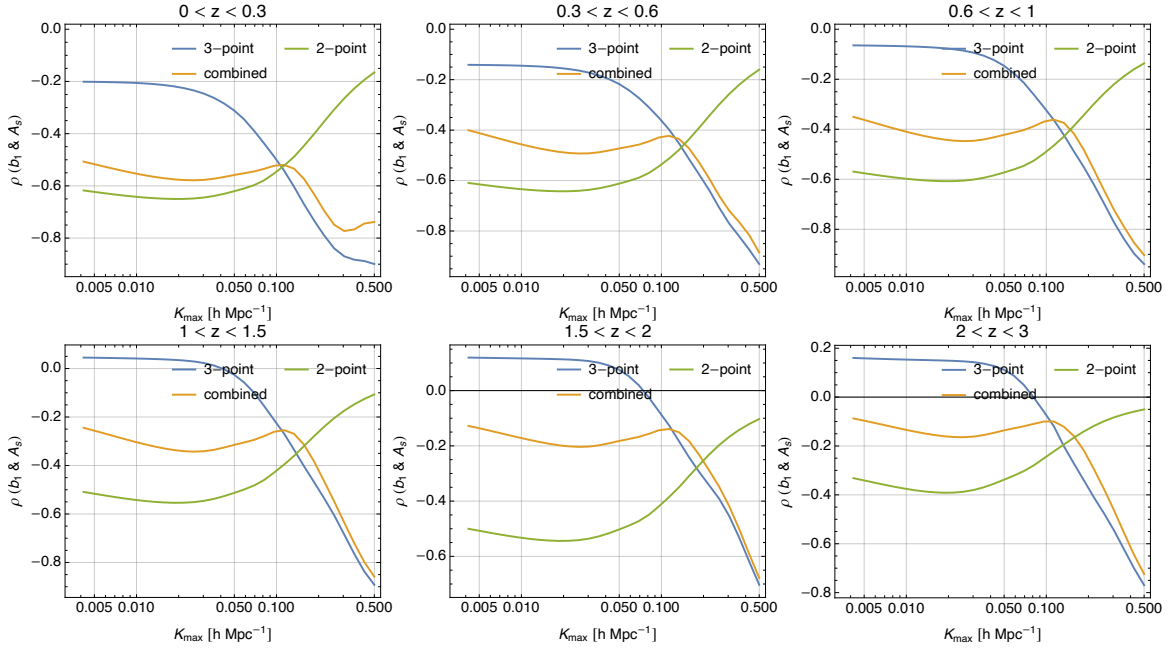


*Fig. 6.13* Correlation coefficients between  $b_1$  and amplitude of fluctuations  $A_s$  for six redshift ranges. We plot correlation coefficients using 2-point functions, 3-point functions and combined 2- and 3-point functions. These plots show that adding 3-point functions, as well as going to higher redshift, indeed break the degeneracy between  $b_1$  and  $A_s$  compare to just using 2-point functions.

and CMB lensing provide all constraints on  $b_1$  and  $A_s$  on large scales. The 3-point functions do not add extra information on large-scales, however, we can add the 3-point functions provide more information on very small scales, that is when we go to very high  $k_{\max}$ . In Fig. 6.13, we show cross-correlation coefficients  $\rho$  between  $b_1$  and  $A_s$  for various redshift bins. The combined power spectrum analysis of galaxy clustering and CMB lensing breaks the  $b_1 - A_s$  degeneracy.

In Fig. 6.14, we show constraints on non-linear quadratic bias parameters from the combined Fisher analysis. The constraints on non-linear biases,  $b_2$  and  $b_{s,2}$ , comes from large-scale limits of 3-point functions. The constraints on  $b_1$  and  $A_s$  comes mostly from the combined 2-point functions, as discussed in the previous section above. Moreover, we see that constraints get better when we go to higher  $k_{\max}$ , which means we include more modes. In Fig. 6.15 we show correlation coefficients between parameters.

In Fig. 6.15, we show our marginalised constraints on non-linear bias parameters as well as the relative amplitude of matter fluctuations using the combined 2- & 3-point functions analysis for four different redshift bins as function of  $k_{\max}$ . We see that it is indeed possible to constrain non-linear bias parameters from projected statistics up to less than 10% for lower redshifts and even better for high redshift bins if we go to higher  $k_{\max}$ . The constraints on  $A_s$  can be 1% or better for higher redshifts. Besides these constraints, in

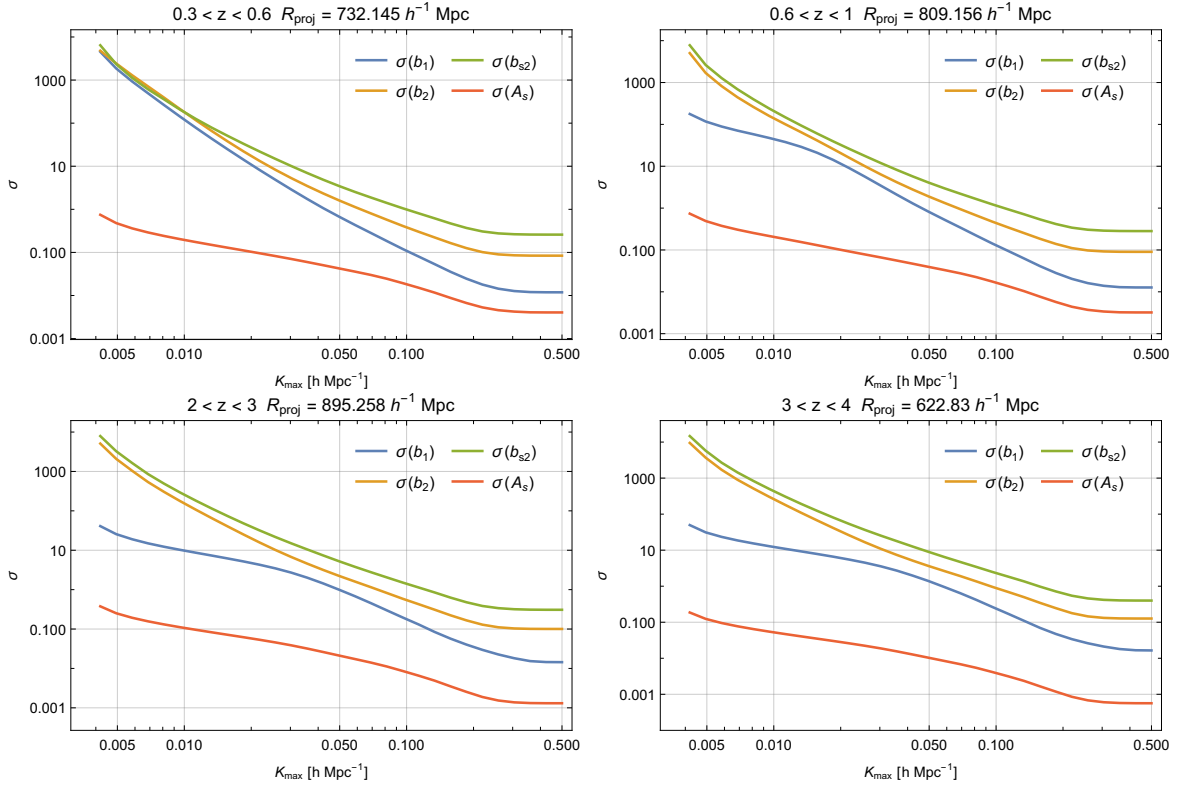


*Fig. 6.14* Constraints on bias parameters as well as the relative amplitude of fluctuations from combined 2- and 3-point functions analysis for different redshift bins. We show the constraints as function of maximum wavenumber  $k_{\max}$  in our model. The constraints get better as we go to higher wavenumber, which make sense because we are including more modes and hence more information.

*Fig. 6.15* we show, for one redshift bin  $0.3 < z < 0.6$ , correlation coefficients  $\rho$  between the parameters. As mentioned before, the 3-point functions do break the degeneracy between  $b_1$  and  $A_s$ . In the top left panel, we see that the correlation coefficient between  $b_1$  and  $A_s$  is roughly  $\rho(b_1 \& A_s) \approx -0.5$ , but if we add 3-point functions the correlation coefficients becomes  $\rho(b_1 \& A_s) \approx -0.3$ . The combined correlation coefficients between  $A_s$  and non-linear bias gets slightly better with the combined analysis, as 2-point functions add additional information on  $A_s$ . Furthermore, we see that  $\rho(b_1 \& b_2)$  and  $\rho(b_1 \& b_{s2})$  are almost one for lower  $k_{\max}$  indicating that on large scales non-linear bias are degenerate with  $b_1$  and with each other if we only use the 3-point functions. However, if we add information from 2-point functions, and go to higher  $k_{\max}$  in 3-point functions, the degeneracies between  $b_1$  non-linear bias break completely. These are encouraging results because, as we mentioned in the beginning, tree-level 2-point functions are natural statistics to constrain linear bias, and tree-level 3-point functions are natural statistics to constrain non-linear bias parameters.

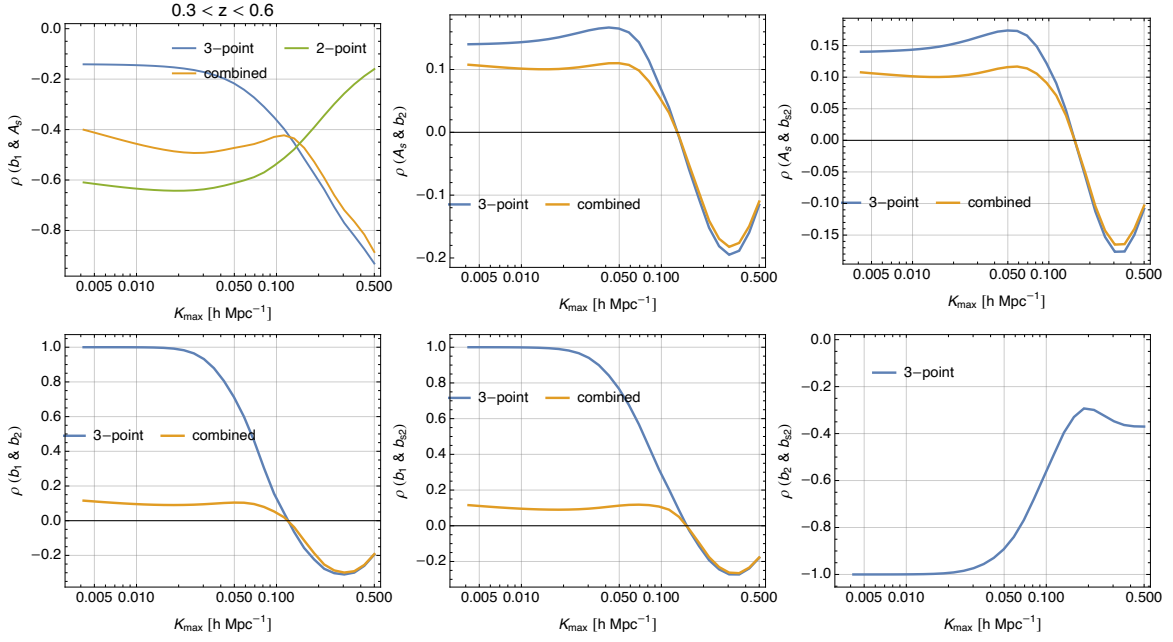


Fig. 6.15 Correlation coefficients between bias parameters and  $A_s$  for one redshift slice,  $0.3 < z < 0.6$ .

## 6.5 Conclusions

Current and future galaxy surveys are planned to cover a more substantial fraction of sky and higher galaxy number densities up to high redshifts. This means these surveys will transform large-scale structure observations in this decade, and will therefore substantially improve our understanding of cosmology. Besides, galaxy surveys, current and future CMB surveys will have higher resolution and low-noise CMB lensing maps. Therefore the gravitational lensing of the CMB will also be a useful tool to constrain cosmology. Since galaxy surveys and future CMB surveys will have a considerable overlap of the sky they cover, the combined analysis using both can help cancel cosmic variance and measure cosmological parameters with better precision.

To fully utilise the potential of these surveys, we need to improve theoretical modelling. One of the main challenges in modelling LSS observables is non-linear galaxy biasing, which introduces more nuisance parameters. If we marginalise over these parameters, the constraints on other cosmological parameters get worse [148]. Moreover, to improve modelling of galaxy-galaxy and galaxy-lensing power spectra up to high  $k_{\max}$ , we need to include higher-order non-linear bias parameter. These non-linear bias parameters are measured either the observational data or numerical simulations [2]. The natural statistics to constrain the linear bias parameter are the large-scale limit of galaxy-galaxy and galaxy-lensing power spectra. On the other hand, the natural statistics to measure non-linear bias

parameters are tree-level, the large-scale limit of 2-point functions (or bispectrum in Fourier space) [10, 2]. The combined 2-point function analysis of galaxy clustering and CMB lensing can also break the degeneracy between the linear bias  $b_1$  and the relative amplitude of matter fluctuations.

In this chapter, we develop a novel method to measure non-linear bias parameters and the amplitude of matter fluctuations using the 2- and 3-point functions of the projected galaxy clustering in correlation with the CMB lensing. We further develop the work done in [2] and bring the method introduced in that work closer to data. We present the concept of quadratic fields, introduced in [176, 2], in projected space. The idea is that we project a 3D density field to get the 2D projected density field. We construct the quadratic fields from the projected field corresponding to the growth, shift and tidal terms, and cross-correlate these quadratic fields with the projected galaxy field or the CMB lensing field. These cross-correlations contain useful information about the projected integrated bispectrum, and therefore, we use these statistics to constrain non-linear bias parameters. To confirm that the analytical formulae we derived for the cross-correlations are correct, we do numerical  $N$ -body simulations. We show that indeed the analytical expressions agree with simulations. These checks also indicate that our Fisher analysis is realistic for the configurations we are using in this chapter. Besides measuring non-linear bias parameters from data, another advantage of projection statistics is that the projection suppresses non-linear RSD effects. Using the projected matter power spectrum in real and redshift space in simulations, we show that the projections can indeed suppress non-linear RSD effects. The power spectrum in redshift space in simulations agree with the theoretical prediction using the Kaiser and the FoG formulae up to  $k \approx 0.1h \text{ Mpc}^{-1}$ . The projections suppress the non-linear RSD terms significantly; we still need to model it but the effects are less severe compare to 3D where the effects are much severe. We leave this for future work where we will compare RSD modelling in projection statistics with analytical predictions and will do the Fisher analysis with RSD.

There are several future directions for this work. First, we can include one-loop terms in the 2-point functions of galaxy clustering and CMB lensing. The one-loop power spectra of galaxy-galaxy and galaxy-lensing depend on bias parameters up to cubic order [2, 10]. Second, we can see if we use the non-linear bias constraints from this work and use them as priors, how much we can improve constraints for other cosmological parameters (basically extending the forecasts in [178] where they only use the linear bias model). Finally, it would be interesting to apply this method directly to data analysis for real galaxy surveys.

## 7.1 Summary

Our understanding of the Universe has been tremendously improved, mainly, by the measurements of temperature fluctuations in Cosmic Microwave Background (CMB). The temperature fluctuations in the CMB have a linear relation to the initial conditions generated in the very early Universe, which has allowed us to connect CMB observables to the statistics of the initial density perturbations generated by inflation. However, due to the two-dimensional nature of the CMB observables, there is a limitation on how well we can constrain cosmological parameters. Alternatively, large-scale structures (LSS), that is the distribution of matter and luminous objects, contains much more cosmological information because of its three-dimensional nature. Extracting cosmological information from LSS surveys, however, poses different challenges. One of the challenges is understanding non-linearities in clustering of matter and biased tracers of matter distribution, which requires better modelling of LSS observables. There are three types of non-linearities that can affect the modelling of the late-time observables:

1. Non-linearity due to gravity in matter clustering.
2. Non-linear galaxy biasing, that is the relationship between the clustering of galaxies (and dark matter halos) with the matter distribution.
3. Primordial non-Gaussianity which induces non-linearities in the initial conditions generated by inflation and affect the statistics of LSS.

To extract information about cosmology from LSS, we need a reliable model or theory to describe the statistics of LSS given the initial conditions generated by inflation in the very early Universe. The perturbations in the density field generated by inflation undergo gravitational collapse at late-times as the Universe evolves. Therefore, the perturbations in

the matter density at late-times are non-linear. In LSS, we can divide the scales into two regimes: (1) *quasi-linear scales* where the perturbation theory converges; (2) and *non-linear scales* where perturbation theory does not converge. To extract maximum cosmological information, we define the statistics of LSS in the quasi-linear scales using the framework of the Effective Field Theory of Large-Scale Structure (EFTofLSS) and push the maximum wavenumber, that is  $k_{\max}$ , in our model as far as we can. EFTofLSS suggests that the  $k_{\max}$  in the model can be increased by adding higher-order loop terms with appropriate counterterms in the statistics of LSS. The EFT counterterms contain information about the physics of small scales and can be measured in cosmological  $N$ -body simulations or data. It has been shown that the EFTofLSS prediction for the two-loop dark matter power spectrum agrees with 1% precision to the  $N$ -body simulations up to  $k_{\max} \approx 0.3h \text{ Mpc}^{-1}$  [44, 15] and the one-loop bispectrum up to  $k_{\max} \approx 0.22h \text{ Mpc}^{-1}$  at redshift  $z = 0$  [28].

These are indeed remarkable results; however, another challenge is that galaxy surveys do not observe the matter distribution directly. In fact, in reality, what they measure is the distribution of tracers of the matter distribution. The relation between the matter distribution and the biased tracers (such as galaxies or dark matter halos) is called galaxy (or halo) biasing. This relation is very complicated because galaxies and dark matter halos are complicated non-linear objects and their formation depends on small-scale physics (see [146] for a review). Given the symmetries of equations of motion, the effective field theory allows us to write the most general galaxy bias relation in terms of finite operators of matter density field at each order in perturbation theory. These operators are called *bias operators* and they are quantified by *bias parameters*. These bias parameters encode all unknown, complicated physics of galaxy formation and non-linear dynamics, and, similar to EFT counterterms, can be measured in  $N$ -body simulations or observational data.

This thesis improves our understanding of higher order couplings in the galaxy (halo) bias and the statistics of biased tracers using the EFTofLSS and numerical  $N$ -body simulations. The models presented in this thesis will eventually be applied to on-going and future galaxy surveys, and will improve the precision of the measurements of the cosmological parameters. The main results of this thesis are summarized as follows.

### 7.1.1 Cubic Halo Bias in Eulerian and Lagrangian Space

To improve modelling of the statistics of biased tracers of LSS, we need to understand non-linearities due to biasing. The predictions of EFTofLSS for the one-loop halo-matter depends on bias parameters up to cubic order. In the first part of this thesis, we studied the measurements of bias parameters up to cubic order from cross-correlations of quadratic and cubic bias operators with the dark matter halo field in suite of  $N$ -body simulations. The natural statistics to measure the linear bias parameter is the large-scale, tree-level halo-matter

power spectrum. The natural statistics for the quadratic and cubic bias parameters are tree-level bispectrum and trispectrum, respectively. Since these statistics are computationally quite expensive, we used efficient quadratic and cubic field estimators to constrain quadratic and cubic biases. These quadratic and cubic estimators contain full information of the integrated bispectrum and trispectrum respectively, but only require the computational cost of power spectrum analysis. We constrain bias parameters using these statistics in Eulerian and Lagrangian space. We find clear evidence for non-zero quadratic and cubic non-local bias operators in Eulerian space. The amplitudes of the detected non-local bias do not agree with the predictions of the evolved local Lagrangian bias model at quadratic and cubic order. We also find clear evidence for the presence of the non-local quadratic bias operator in Lagrangian space for all mass bins, and the presence of cubic non-local terms for the highest mass bin. We studied the co-evolution of the dark matter and halos and show that the Lagrangian bias model with the non-local tidal term accurately predicts the amplitudes of non-local quadratic and cubic bias operators in Eulerian space. Finally, we use the bias constraints to model the one-loop halo-matter power spectrum and show that the results agree with simulations up to  $k_{\max} = 0.1h \text{ Mpc}^{-1}$  once an additional  $k^2$  derivative bias is implemented. These results have been published in [2].

### 7.1.2 Density Field Reconstruction from Biased Tracers

In the second part of the thesis, we studied density field reconstruction from biased tracers and its application to primordial non-Gaussianity [59]. Large scale modes of the density field contain relevant information, especially about the physics of inflation. For example, it has been shown that on large scales, the LSS power spectrum has a unique  $1/k^2$  imprint due to local type primordial non-Gaussianity [153]. The precision of the cosmological measurements from galaxy surveys is limited by several factors, including the cosmic variance on large scales. Moreover, very large scale modes can sometimes be inaccessible from galaxy surveys due to observational systematics. To circumvent these problems, and to learn more about inflation, we develop a formalism to reconstruct large scale modes of the density field based on quadratic couplings in galaxy clustering. Because the large-scale modes correlate with the two non-linear modes, we write down a quadratic estimator that probes these correlations of different short modes and can give us an estimate of the large scale modes from the statistical properties of small scale modes. This method is similar to CMB lensing reconstruction [88]. In our quadratic estimator we include non-linearities from gravity, non-linear galaxy biasing, and primordial non-Gaussianity. We show that constructing an unbiased estimator of the density field is not practical because its variance blows up. We show that the biased estimator corresponding to the growth term  $\delta^2$  has the smallest variance and can be used for practical analysis. Although we use the growth



estimator for Fisher analysis, we also construct biased estimators corresponding to the shift term  $\Psi \cdot \nabla \delta$  and the tidal term  $s^2$ .

We demonstrate density reconstructions using three biased estimators using dark matter halos in numerical  $N$ -body simulations. We study the cross-correlations of estimators with the linear density field, as well as auto- and cross-correlations of estimators for three different smoothing scales  $R = 20h^{-1}$  Mpc,  $R = 10h^{-1}$  Mpc and  $R = 4h^{-1}$  Mpc. These smoothing scales correspond to the maximum wavenumber  $k_{\max} = 0.05h$  Mpc $^{-1}$ ,  $k_{\max} = 0.1h$  Mpc $^{-1}$ , and  $k_{\max} = 0.25h$  Mpc $^{-1}$  respectively in our model. We show that the reconstruction works very well even if we use a higher  $k_{\max} = 0.25h$  Mpc $^{-1}$ , where the correlation coefficient of the growth estimator with the linear density field is  $r_{G\delta_1} > 0.9$ . For lower  $k_{\max}$  the cross-correlations are noise dominated. Although we get good agreement for the analytical predictions for the growth estimator with simulations for  $k_{\max} = 0.25h$  Mpc $^{-1}$ , we still choose a conservative  $k_{\max} = 0.1h$  Mpc $^{-1}$  at redshift  $z = 0$  for Fisher forecasts. Finally, we carry out a Fisher forecast using the combined analysis of the reconstructed field and the galaxy field for different galaxy surveys (DESI and MegaMapper). We show that we can improve constraints on local-type primordial non-Gaussianity by 10s of percents compared to the standard analysis using only the galaxy field. In some cases the improvement on constraints comes from cosmic variance cancellation; in other cases, it comes from the additional modes in the reconstructed field which are not accessible in the galaxy field due to observational systematics. Once observational effects, such as redshift space distortions, are incorporated in our quadratic estimator method, then this method can be applied to galaxy data from current and future galaxy surveys.

### 7.1.3 Constraints on Non-Linear Bias Parameters

In third part of the thesis, we develop a method to measure non-linear galaxy bias parameters using the two- and three-point functions of the projected galaxy clustering, CMB lensing convergence, and their cross-correlations. This work further develops the method introduced in the first part of the thesis and brings it closer to data. Measuring non-linear bias parameters from data requires inclusion of observational effects such as redshift space distortions (RSD) in the three-point functions. Modelling of RSD in three- or higher-point functions is quite complicated. The quadratic field methods for projected fields developed in this thesis can suppress the non-linear RSD effects. We perform the Fisher forecast analysis to show that this method can practically be used to constrain bias parameters as well as the amplitude of matter fluctuations. We use a combined analysis of two- and three-point functions for different redshift bins. Although combined two-point functions of galaxy clustering and CMB lensing break the degeneracy between the linear bias and amplitude of matter fluctuations, we show that the three-point functions add more information and hence further

break the degeneracy. We also perform numerical  $N$ -body simulation tests to verify that our derived analytical predictions for the auto- and cross-correlations of quadratic fields in projected space indeed agree with simulations. We also perform a quick test of the effect of projections on suppressing RSD effects. In simulations we show, using the projected matter power spectrum in real and redshift space, that projections indeed suppress non-linear RSD effects. We still to model them using the Kaiser and FoG formulae, however, the effect is less severe as compare to RSD effects in 3D statistics. This demonstrates that our Fisher forecast results are realistic and can be applied to data analysis.

## 7.2 Future Outlooks

One future direction of this work could be to model the halo bispectrum at the next-to-leading order, that is one-loop, using the framework of EFTofLSS. At one-loop, all bias operators up to quartic order are important. A careful modeling of stochasticity is also important because it affects  $B_{\text{hhm}}$  and  $B_{\text{hhh}}$  as well as bispectrum covariances. After careful modeling of halo statistics, we can make forecasts of cosmological parameters to see how much we can improve the constraints on  $f_{\text{NL}}$ , neutrino masses  $M_{\nu}$ , and other cosmological parameters.

Another direction is to go beyond the one-loop halo-matter power spectrum. At the two-loop order in halo-matter and halo-halo power spectra, we expect bias parameters up to higher order as well more additional EFT counterterms and stochastic bias parameters. It would be interesting to measure higher-order bias parameters (such as quartic) by extending the quadratic and cubic field methods and introduce quartic fields. We can use the cross-correlation of quartic fields with the halo field and use the power spectrum analysis in the numerical  $N$ -body simulation similar to the work presented in this thesis. Besides the cross-correlations, we can also use the bispectrum statistics and use quadratic, cubic and quartic fields to measure the higher-order bias parameters. One of the advantages of going to the two-loop in halo matter is that we can push the modelling to higher  $k_{\text{max}}$ , which can also be useful in the density field reconstruction from biased tracers presented in Chapter 5. There we used  $k_{\text{max}} = 0.1h \text{ Mpc}^{-1}$  for the reconstruction of large scale modes, but it has been shown in simulations that reconstruction works better if we go to the higher  $k_{\text{max}}$ . Going to higher  $k_{\text{max}}$  requires careful modelling of higher-order terms, which will more likely improve constraints on local  $f_{\text{NL}}$  significantly [59].

In the end, it would be useful to apply the methods presented in this thesis to data from current and future galaxy and CMB lensing surveys. If we can measure bias parameters from data and use the information as priors before marginalising over these parameters, we can significantly improve constraints on useful cosmological parameters.

## References

- [1] Kevork N. Abazajian et al. *CMB-S4 Science Book, First Edition*. Tech. rep. 2016. arXiv: 1610.02743. URL: <http://arxiv.org/abs/1610.02743>.
- [2] Muntazir Mehdi Abidi and Tobias Baldauf. “Cubic Halo Bias in Eulerian and Lagrangian Space”. In: (2018). DOI: 10.1088/1475-7516/2018/07/029. arXiv: 1802.07622. URL: <http://arxiv.org/abs/1802.07622><http://dx.doi.org/10.1088/1475-7516/2018/07/029>.
- [3] P. A. R. Ade et al. “Planck 2015 results. XVII. Constraints on primordial non-Gaussianity”. In: *Astron. Astrophys.* 594 (2016), A17. DOI: 10.1051/0004-6361/201525836. arXiv: 1502.01592 [astro-ph.CO].
- [4] R Allison et al. *Towards a cosmological neutrino mass detection*. Tech. rep. arXiv: 1509.07471v1.
- [5] Marcelo Alvarez et al. “Testing Inflation with Large Scale Structure: Connecting Hopes with Reality”. In: (2014). arXiv: 1412.4671. URL: <http://arxiv.org/abs/1412.4671>.
- [6] Raul Angulo et al. “On the Statistics of Biased Tracers in the Effective Field Theory of Large Scale Structures”. In: *JCAP* 1509.09 (2015), p. 029. DOI: 10.1088/1475-7516/2015/09/029, 10.1088/1475-7516/2015/9/029. arXiv: 1503.08826 [astro-ph.CO].
- [7] Raul E. Angulo et al. “The One-Loop Matter Bispectrum in the Effective Field Theory of Large Scale Structures”. In: *JCAP* 1510.10 (2015), p. 039. DOI: 10.1088/1475-7516/2015/10/039. arXiv: 1406.4143 [astro-ph.CO].
- [8] Nima Arkani-Hamed and Juan Maldacena. *Cosmological Collider Physics*. Tech. rep. 2015. arXiv: 1503.08043v1.
- [9] Valentin Assassi, Daniel Baumann, and Fabian Schmidt. “Galaxy Bias and Primordial Non-Gaussianity”. In: (2015). DOI: 10.1088/1475-7516/2015/12/043. arXiv: 1510.03723. URL: <http://arxiv.org/abs/1510.03723><http://dx.doi.org/10.1088/1475-7516/2015/12/043>.
- [10] Valentin Assassi et al. “Renormalized Halo Bias”. In: (2014), p. 44. ISSN: 14757516. DOI: 10.1088/1475-7516/2014/08/056. arXiv: 1402.5916. URL: <http://arxiv.org/abs/1402.5916>.

- [11] Valentin Assassi et al. “Renormalized Halo Bias”. In: *JCAP* 1408 (2014), p. 056. DOI: [10.1088/1475-7516/2014/08/056](https://doi.org/10.1088/1475-7516/2014/08/056). arXiv: [1402.5916](https://arxiv.org/abs/1402.5916) [astro-ph.CO].
- [12] Tobias Baldauf. *Field Theory in Cosmology Statistics, non-Linearity and the CMB*. Tech. rep. 2020.
- [13] Tobias Baldauf and Vincent Desjacques. “Phenomenology of baryon acoustic oscillation evolution from Lagrangian to Eulerian space”. In: *Phys. Rev. D* 95.4 (2017), p. 043535. DOI: [10.1103/PhysRevD.95.043535](https://doi.org/10.1103/PhysRevD.95.043535). arXiv: [1612.04521](https://arxiv.org/abs/1612.04521) [astro-ph.CO].
- [14] Tobias Baldauf, Vincent Desjacques, and Uros Seljak. “Velocity bias in the distribution of dark matter halos”. In: *Phys. Rev. D* 92 (2015), p. 123507. DOI: [10.1103/PhysRevD.92.123507](https://doi.org/10.1103/PhysRevD.92.123507). arXiv: [1405.5885](https://arxiv.org/abs/1405.5885) [astro-ph.CO].
- [15] Tobias Baldauf, Lorenzo Mercolli, and Matias Zaldarriaga. “Effective field theory of large scale structure at two loops: The apparent scale dependence of the speed of sound”. In: *Physical Review D* 92.12 (2015), p. 123007. ISSN: 1550-7998. DOI: [10.1103/PhysRevD.92.123007](https://doi.org/10.1103/PhysRevD.92.123007). arXiv: [1507.02256](https://arxiv.org/abs/1507.02256). URL: <http://arxiv.org/abs/1507.02256>.
- [16] Tobias Baldauf, Lorenzo Mercolli, and Matias Zaldarriaga. “Effective field theory of large scale structure at two loops: The apparent scale dependence of the speed of sound”. In: *Phys. Rev. D* 92.12 (2015), p. 123007. DOI: [10.1103/PhysRevD.92.123007](https://doi.org/10.1103/PhysRevD.92.123007). arXiv: [1507.02256](https://arxiv.org/abs/1507.02256) [astro-ph.CO].
- [17] Tobias Baldauf, Lorenzo Mercolli, and Matias Zaldarriaga. *The Effective Field Theory of Large Scale Structure at Two Loops: the apparent scale dependence of the speed of sound*. Tech. rep. arXiv: [1507.02256v2](https://arxiv.org/abs/1507.02256v2).
- [18] Tobias Baldauf, Uros Seljak, and Leonardo Senatore. “Primordial non-Gaussianity in the Bispectrum of the Halo Density Field”. In: *JCAP* 1104 (2011), p. 006. DOI: [10.1088/1475-7516/2011/04/006](https://doi.org/10.1088/1475-7516/2011/04/006). arXiv: [1011.1513](https://arxiv.org/abs/1011.1513) [astro-ph.CO].
- [19] Tobias Baldauf, Uroš Seljak, and Leonardo Senatore. “Primordial non-Gaussianity in the bispectrum of the halo density field”. In: *Journal of Cosmology and Astroparticle Physics* 2011.04 (2011), pp. 006–006. ISSN: 1475-7516. DOI: [10.1088/1475-7516/2011/04/006](https://doi.org/10.1088/1475-7516/2011/04/006). arXiv: [1011.1513](https://arxiv.org/abs/1011.1513). URL: <http://arxiv.org/abs/1011.1513>.
- [20] Tobias Baldauf et al. “Evidence for Quadratic Tidal Tensor Bias from the Halo Bispectrum”. In: *Physical Review D - Particles, Fields, Gravitation and Cosmology* 86.8 (2012). DOI: [10.1103/PhysRevD.86.083540](https://doi.org/10.1103/PhysRevD.86.083540). arXiv: [1201.4827](https://arxiv.org/abs/1201.4827). URL: <http://arxiv.org/abs/1201.4827><http://dx.doi.org/10.1103/PhysRevD.86.083540>.
- [21] Tobias Baldauf et al. “Evidence for Quadratic Tidal Tensor Bias from the Halo Bispectrum”. In: *Phys. Rev. D* 86 (2012), p. 083540. DOI: [10.1103/PhysRevD.86.083540](https://doi.org/10.1103/PhysRevD.86.083540). arXiv: [1201.4827](https://arxiv.org/abs/1201.4827) [astro-ph.CO].
- [22] Tobias Baldauf et al. “Halo stochasticity from exclusion and nonlinear clustering”. In: *Physical Review D* 88.8 (2013), p. 083507. ISSN: 1550-7998. DOI: [10.1103/PhysRevD.88.083507](https://doi.org/10.1103/PhysRevD.88.083507). arXiv: [1305.2917](https://arxiv.org/abs/1305.2917). URL: <http://arxiv.org/abs/1305.2917>.
- [23] Tobias Baldauf et al. “Large Scale Structure Statistics for Precision Cosmology”. In: (2016).
- [24] Tobias Baldauf et al. *LSS constraints with controlled theoretical uncertainties*. Tech. rep. arXiv: [1602.00674v1](https://arxiv.org/abs/1602.00674v1). URL: <https://arxiv.org/pdf/1602.00674.pdf>.

- [25] Tobias Baldauf et al. “LSS constraints with controlled theoretical uncertainties”. In: (2016), p. 18. arXiv: [1602.00674](https://arxiv.org/abs/1602.00674). URL: <http://arxiv.org/abs/1602.00674>.
- [26] Tobias Baldauf et al. “The Bispectrum in the Effective Field Theory of Large Scale Structure”. In: (2014). DOI: [10.1088/1475-7516/2015/05/007](https://doi.org/10.1088/1475-7516/2015/05/007). arXiv: [1406.4135](https://arxiv.org/abs/1406.4135). URL: <http://arxiv.org/abs/1406.4135><http://dx.doi.org/10.1088/1475-7516/2015/05/007>.
- [27] Tobias Baldauf et al. “The Bispectrum in the Effective Field Theory of Large Scale Structure”. In: *JCAP* 1505.05 (2015), p. 007. DOI: [10.1088/1475-7516/2015/05/007](https://doi.org/10.1088/1475-7516/2015/05/007). arXiv: [1406.4135](https://arxiv.org/abs/1406.4135) [[astro-ph.CO](https://arxiv.org/abs/1406.4135)].
- [28] Tobias Baldauf et al. “The bispectrum in the Effective Field Theory of Large Scale Structure”. In: *Journal of Cosmology and Astroparticle Physics* 2015.05 (2015), pp. 007–007. ISSN: 1475-7516. DOI: [10.1088/1475-7516/2015/05/007](https://doi.org/10.1088/1475-7516/2015/05/007). arXiv: [1406.4143](https://arxiv.org/abs/1406.4143). URL: <http://arxiv.org/abs/1406.4143><http://www.arxiv.org/pdf/1406.4143.pdf><http://stacks.iop.org/1475-7516/2015/i=05/a=007?key=crossref.edd197f388bf8ca4366d7a49904d001c>.
- [29] Mario Ballardini, William L. Matthewson, and Roy Maartens. *Constraining primordial non-Gaussianity using two galaxy surveys and CMB lensing*. Tech. rep. 2019, pp. 0–000. arXiv: [1906.04730v2](https://arxiv.org/abs/1906.04730v2). URL: <https://github.com/dhanson/quicklens>.
- [30] W. E. Ballinger, J. A. Peacock, and A. F. Heavens. “Measuring the cosmological constant with redshift surveys”. In: (1996). DOI: [10.1093/mnras/282.3.877](https://doi.org/10.1093/mnras/282.3.877). arXiv: [9605017](https://arxiv.org/abs/9605017) [[astro-ph](https://arxiv.org/abs/9605017)]. URL: <http://arxiv.org/abs/astro-ph/9605017><http://dx.doi.org/10.1093/mnras/282.3.877>.
- [31] J. M. Bardeen et al. “The statistics of peaks of Gaussian random fields”. In: *The Astrophysical Journal* 304 (1986), p. 15. ISSN: 0004-637X. DOI: [10.1086/164143](https://doi.org/10.1086/164143). URL: <http://adsabs.harvard.edu/doi/10.1086/164143>.
- [32] Daniel Baumann. “Cosmology - Mathematical Tripos”. In: (2011), p. 130. URL: <http://www.damtp.cam.ac.uk/user/db275/Cosmology/Lectures.pdf>.
- [33] Daniel Baumann. *Primordial Cosmology*. Tech. rep.
- [34] Daniel Baumann. “TASI Lectures on Inflation”. In: *Physics of the large and the small, TASI 09, proceedings of the Theoretical Advanced Study Institute in Elementary Particle Physics, Boulder, Colorado, USA, 1-26 June 2009* (2009), pp. 523–686. arXiv: [0907.5424](https://arxiv.org/abs/0907.5424). URL: <http://arxiv.org/abs/0907.5424>.
- [35] Daniel Baumann et al. “Cosmological Non-Linearities as an Effective Fluid”. In: (2010). DOI: [10.1088/1475-7516/2012/07/051](https://doi.org/10.1088/1475-7516/2012/07/051). arXiv: [1004.2488](https://arxiv.org/abs/1004.2488). URL: <http://arxiv.org/abs/1004.2488><http://dx.doi.org/10.1088/1475-7516/2012/07/051>.
- [36] Daniel Baumann et al. “Cosmological Non-Linearities as an Effective Fluid”. In: *JCAP* 1207 (2012), p. 051. DOI: [10.1088/1475-7516/2012/07/051](https://doi.org/10.1088/1475-7516/2012/07/051). arXiv: [1004.2488](https://arxiv.org/abs/1004.2488) [[astro-ph.CO](https://arxiv.org/abs/1004.2488)].
- [37] F. Bernardeau et al. “Large scale structure of the universe and cosmological perturbation theory”. In: *Phys. Rept.* 367 (2002), pp. 1–248. DOI: [10.1016/S0370-1573\(02\)00135-7](https://doi.org/10.1016/S0370-1573(02)00135-7). arXiv: [astro-ph/0112551](https://arxiv.org/abs/astro-ph/0112551) [[astro-ph](https://arxiv.org/abs/astro-ph/0112551)].
- [38] F. Bernardeau et al. “Large-scale structure of the Universe and cosmological perturbation theory”. In: *Physrep* 367. December 2001 (2002), pp. 1–3. ISSN: 03701573. DOI: [10.1016/S0370-1573\(02\)00135-7](https://doi.org/10.1016/S0370-1573(02)00135-7). arXiv: [0112551](https://arxiv.org/abs/0112551) [[astro-ph](https://arxiv.org/abs/0112551)]. URL: <http://adsabs.harvard.edu/cgi-bin/nph-bib?query=bibcode=2002PhR...367....1B{&db{&key=AST>.

- [39] Daniele Bertolini et al. “The Trispectrum in the Effective Field Theory of Large Scale Structure”. In: *JCAP* 1606.06 (2016), p. 052. DOI: [10.1088/1475-7516/2016/06/052](https://doi.org/10.1088/1475-7516/2016/06/052). arXiv: [1604.01770](https://arxiv.org/abs/1604.01770) [astro-ph.CO].
- [40] Edmund Bertschinger. “Multiscale Gaussian Random Fields for Cosmological Simulations”. In: *The Astrophysical Journal Supplement Series* 137.1 (2001), pp. 1–20. DOI: [10.1086/322526](https://doi.org/10.1086/322526). arXiv: [0103301](https://arxiv.org/abs/0103301) [astro-ph]. URL: <http://arxiv.org/abs/astro-ph/0103301><http://dx.doi.org/10.1086/322526>.
- [41] Edmund Bertschinger and James M Gelb. “Cosmological N-Body Simulations”. In: *Citation: Computers in Physics* 5 (1991), p. 164. DOI: [10.1063/1.4822978](https://doi.org/10.1063/1.4822978). URL: <https://doi.org/10.1063/1.4822978>.
- [42] F. R. Bouchet et al. *Perturbative Lagrangian Approach to Gravitational Instability*. 1994. arXiv: [9406013](https://arxiv.org/abs/9406013) [astro-ph]. URL: <http://arxiv.org/abs/astro-ph/9406013> (visited on 06/07/2020).
- [43] Joyce Byun et al. “Towards optimal cosmological parameter recovery from compressed bispectrum statistics”. In: (2017). DOI: [10.1093/mnras/stx1681](https://doi.org/10.1093/mnras/stx1681). arXiv: [1705.04392](https://arxiv.org/abs/1705.04392). URL: <http://arxiv.org/abs/1705.04392><http://dx.doi.org/10.1093/mnras/stx1681>.
- [44] Jjm Carrasco and Simon Foreman. “The 2-loop matter power spectrum and the IR-safe integrand”. In: *arXiv preprint arXiv: ...* (2013), p. 27. ISSN: 14757516. DOI: [10.1088/1475-7516/2014/07/056](https://doi.org/10.1088/1475-7516/2014/07/056). arXiv: [1304.4946](https://arxiv.org/abs/1304.4946). URL: <http://arxiv.org/abs/1304.4946>.
- [45] John Joseph M. Carrasco, Mark P. Hertzberg, and Leonardo Senatore. “The Effective Field Theory of Cosmological Large Scale Structures”. In: *JHEP* 09 (2012), p. 082. DOI: [10.1007/JHEP09\(2012\)082](https://doi.org/10.1007/JHEP09(2012)082). arXiv: [1206.2926](https://arxiv.org/abs/1206.2926) [astro-ph.CO].
- [46] John Joseph M Carrasco, Mark P. Hertzberg, and Leonardo Senatore. “The effective field theory of cosmological large scale structures”. In: *Journal of High Energy Physics* 2012.9 (2012), pp. 1–41. ISSN: 11266708. DOI: [10.1007/JHEP09\(2012\)082](https://doi.org/10.1007/JHEP09(2012)082). arXiv: [1206.2926](https://arxiv.org/abs/1206.2926).
- [47] John Joseph M. Carrasco et al. “The 2-loop matter power spectrum and the IR-safe integrand”. In: *JCAP* 1407 (2014), p. 056. DOI: [10.1088/1475-7516/2014/07/056](https://doi.org/10.1088/1475-7516/2014/07/056). arXiv: [1304.4946](https://arxiv.org/abs/1304.4946) [astro-ph.CO].
- [48] Emanuele Castorina and Martin White. *Measuring the growth of structure with intensity mapping surveys*. Tech. rep. 2019. arXiv: [1902.07147v1](https://arxiv.org/abs/1902.07147v1). URL: <https://arxiv.org/pdf/1902.07147.pdf>.
- [49] Emanuele Castorina et al. “Excursion set peaks: the role of shear”. In: (2016). arXiv: [1611.03619](https://arxiv.org/abs/1611.03619) [astro-ph.CO].
- [50] Kwan Chuen Chan, Roman Scoccimarro, and Ravi K. Sheth. “Gravity and Large-Scale Non-local Bias”. In: *Physical Review D - Particles, Fields, Gravitation and Cosmology* 85.8 (2012). DOI: [10.1103/PhysRevD.85.083509](https://doi.org/10.1103/PhysRevD.85.083509). arXiv: [1201.3614](https://arxiv.org/abs/1201.3614). URL: <http://arxiv.org/abs/1201.3614><http://dx.doi.org/10.1103/PhysRevD.85.083509>.
- [51] Kwan Chuen Chan, Roman Scoccimarro, and Ravi K. Sheth. “Gravity and Large-Scale Non-local Bias”. In: *Phys. Rev. D* 85 (2012), p. 083509. DOI: [10.1103/PhysRevD.85.083509](https://doi.org/10.1103/PhysRevD.85.083509). arXiv: [1201.3614](https://arxiv.org/abs/1201.3614) [astro-ph.CO].
- [52] Kwan Chuen Chan and Linda Blot. *Assessment of the Information Content of the Power Spectrum and Bispectrum*. Tech. rep. arXiv: [1610.06585v3](https://arxiv.org/abs/1610.06585v3).

- [53] Nick Cole, Shaun; Kaiser. *Biased clustering in the cold dark matter cosmogony*. - NASA/ADS. URL: <https://ui.adsabs.harvard.edu/abs/1989MNRAS.237.1127C/abstract> (visited on 06/11/2020).
- [54] J. J. Condon et al. “The NRAO VLA Sky Survey”. In: *The Astronomical Journal* 115.5 (1998), pp. 1693–1716. ISSN: 00046256. DOI: 10.1086/300337. URL: <https://ui.adsabs.harvard.edu/abs/1998AJ....115.1693C/abstract>.
- [55] Martín Crocce, Sebastián Pueblas, and Román Scoccimarro. “Transients from initial conditions in cosmological simulations”. In: *Monthly Notices of the Royal Astronomical Society* 373.1 (2006), pp. 369–381. ISSN: 00358711. DOI: 10.1111/j.1365-2966.2006.11040.x. arXiv: 0606505 [astro-ph]. URL: <http://arxiv.org/abs/astro-ph/0606505http://dx.doi.org/10.1111/j.1365-2966.2006.11040.x>.
- [56] Ji-Ping Dai, Licia Verde, and Jun-Qing Xia. “What Can We Learn by Combining the Skew Spectrum and the Power Spectrum?” In: (2020). arXiv: 2002.09904. URL: <http://arxiv.org/abs/2002.09904>.
- [57] Neal Dalal et al. “Imprints of primordial non-Gaussianities on large-scale structure: Scale-dependent bias and abundance of virialized objects”. In: *Physical Review D - Particles, Fields, Gravitation and Cosmology* 77.12 (2008). ISSN: 15507998. DOI: 10.1103/PhysRevD.77.123514. arXiv: 0710.4560. URL: <http://arxiv.org/abs/0710.4560http://dx.doi.org/10.1103/PhysRevD.77.123514>.
- [58] Guido D’Amico et al. “The Cosmological Analysis of the SDSS/BOSS data from the Effective Field Theory of Large-Scale Structure”. In: (2019). DOI: 10.1088/1475-7516/2020/05/005. arXiv: 1909.05271. URL: <http://arxiv.org/abs/1909.05271http://dx.doi.org/10.1088/1475-7516/2020/05/005>.
- [59] Omar Darwish et al. “Density reconstruction from biased tracers and its application to primordial non-Gaussianity”. In: (2020). arXiv: 2007.08472. URL: <http://arxiv.org/abs/2007.08472>.
- [60] Sudeep Das et al. “Detection of the power spectrum of cosmic microwave background lensing by the atacama cosmology telescope”. In: *Physical Review Letters* 107.2 (2011), p. 021301. ISSN: 00319007. DOI: 10.1103/PhysRevLett.107.021301. arXiv: 1103.2124. URL: <https://ui.adsabs.harvard.edu/abs/2011PhRvL.107b1301D/abstract>.
- [61] Sudeep Das et al. “The atacama cosmology telescope: A measurement of the cosmic microwave background power spectrum at 148 and 218 ghz from the 2008 southern survey”. In: *Astrophysical Journal* 729.1 (2011), p. 62. ISSN: 15384357. DOI: 10.1088/0004-637X/729/1/62. arXiv: 1009.0847. URL: <https://ui.adsabs.harvard.edu/abs/2011ApJ...729...62D/abstract>.
- [62] F De Bernardis et al. *Survey strategy optimization for the Atacama Cosmology Telescope*. Tech. rep. 2016. arXiv: 1607.02120v1.
- [63] DESI Collaboration et al. *The DESI Experiment Part I: Science, Targeting, and Survey Design*. Tech. rep. 2016. arXiv: 1611.00036. URL: <http://arxiv.org/abs/1611.00036>.
- [64] V Desjacques and U Seljak. *Primordial non-Gaussianity from the large scale structure*. Tech. rep. 2010. arXiv: 1003.5020v1.
- [65] Vincent Desjacques. “Baryon acoustic signature in the clustering of density maxima”. In: *Phys. Rev. D* 78 (2008), p. 103503. DOI: 10.1103/PhysRevD.78.103503. arXiv: 0806.0007 [astro-ph].

- [66] Vincent Desjacques, Donghui Jeong, and Fabian Schmidt. “Large-Scale Galaxy Bias”. In: (2016). arXiv: 1611.09787 [astro-ph.CO].
- [67] Vincent Desjacques, Donghui Jeong, and Fabian Schmidt. “Large-Scale Galaxy Bias”. In: (2016), p. 232. arXiv: 1611.09787. URL: <http://arxiv.org/abs/1611.09787>.
- [68] Vincent Desjacques, Donghui Jeong, and Fabian Schmidt. *Large-Scale Galaxy Bias*. Tech. rep. 2019. arXiv: 1611.09787v5.
- [69] Vincent Desjacques et al. “Modeling scale-dependent bias on the baryonic acoustic scale with the statistics of peaks of Gaussian random fields”. In: *Phys. Rev. D* 82 (2010), p. 103529. DOI: 10.1103/PhysRevD.82.103529. arXiv: 1009.3449 [astro-ph.CO].
- [70] Eleonora Di Valentino, Eric Linder, and Alessandro Melchiorri. “A Vacuum Phase Transition Solves  $H_0$  Tension”. In: *Physical Review D* 97.4 (2017). DOI: 10.1103/PhysRevD.97.043528. arXiv: 1710.02153. URL: <http://arxiv.org/abs/1710.02153><http://dx.doi.org/10.1103/PhysRevD.97.043528>.
- [71] Eleonora Di Valentino et al. “Reducing the  $H_0$  and  $\Omega_m$  tensions with Dark Matter-neutrino interactions”. In: *Physical Review D* 97.4 (2017), p. 043513. DOI: 10.1103/PhysRevD.97.043513. arXiv: 1710.02559. URL: <http://arxiv.org/abs/1710.02559><http://dx.doi.org/10.1103/PhysRevD.97.043513>.
- [72] Robert H. Dicke and Robert H. “Gravitation and the universe”. In: *grun* (1970). URL: <https://ui.adsabs.harvard.edu/abs/1970grun.conf.....D/abstract>.
- [73] Azadeh Moradinezhad Dizgah et al. *Capturing Non-Gaussianity of the Large-Scale Structure with Weighted Skew-Spectra*. Tech. rep. 2019. arXiv: 1911.05763v1.
- [74] G. Efstathiou et al. “Numerical techniques for large cosmological N-body simulations”. In: *The Astrophysical Journal Supplement Series* 57 (1985), p. 241. ISSN: 0067-0049. DOI: 10.1086/191003. URL: <https://ui.adsabs.harvard.edu/abs/1985ApJS...57..241E/abstract>.
- [75] Albert Einstein. *Die Feldgleichungen der Gravitation - NASA/ADS*. URL: <https://ui.adsabs.harvard.edu/abs/1915SPAW.....844E/abstract> (visited on 05/27/2020).
- [76] Albert Einstein. *Kosmologische Betrachtungen zur allgemeinen Relativitätstheorie - NASA/ADS*. URL: <https://ui.adsabs.harvard.edu/abs/1917SPAW.....142E/abstract> (visited on 05/27/2020).
- [77] A. van Engelen et al. “CMB Lensing Power Spectrum Biases from Galaxies and Clusters using High-angular Resolution Temperature Maps”. In: (2013). DOI: 10.1088/0004-637X/786/1/13. arXiv: 1310.7023. URL: <http://arxiv.org/abs/1310.7023><http://dx.doi.org/10.1088/0004-637X/786/1/13>.
- [78] ESA. *Definition Study Report Euclid Mapping the geometry of the dark Universe European Space Agency*. Tech. rep. 2011. URL: <https://arxiv.org/ftp/arxiv/papers/1110/1110.3193.pdf>.
- [79] Marcelo Alvarez Et. al. “Testing Inflation with Large Scale Structure: Connecting Hopes with Reality”. In: *arXiv* (2014).
- [80] P A R Ade Et al. “Planck 2013 Results. XXIV. Constraints on primordial non-Gaussianity”. In: *Astron. Astrophysics* A24.571 (2014).



- [81] Hume A. Feldman et al. “Constraints on Galaxy Bias, Matter Density, and Primordial Non-Gaussianity from the PSCz Galaxy Redshift Survey”. In: (2000). DOI: [10.1103/PhysRevLett.86.1434](https://doi.org/10.1103/PhysRevLett.86.1434). arXiv: 0010205 [astro-ph]. URL: <http://arxiv.org/abs/astro-ph/0010205><http://dx.doi.org/10.1103/PhysRevLett.86.1434>.
- [82] Chang Feng et al. “Reconstruction of Gravitational Lensing Using WMAP 7-Year Data”. In: *Physical Review D - Particles, Fields, Gravitation and Cosmology* 85.4 (2011), p. 043513. DOI: [10.1103/PhysRevD.85.043513](https://doi.org/10.1103/PhysRevD.85.043513). arXiv: 1111.2371. URL: <http://arxiv.org/abs/1111.2371><http://dx.doi.org/10.1103/PhysRevD.85.043513>.
- [83] J R Fergusson, D M Regan, and E P S Shellard. *Rapid Separable Analysis of Higher Order Correlators in Large Scale Structure*. Tech. rep. 2011. arXiv: 1008.1730v2.
- [84] James Fergusson. *Part III Cosmology*. Tech. rep.
- [85] S. Ferraro et al. “On the correspondence between barrier crossing, peak-background split and local biasing”. In: *MNRAS* 435 (Oct. 2013), pp. 934–942. DOI: [10.1093/mnras/stt1272](https://doi.org/10.1093/mnras/stt1272). arXiv: 1209.2175 [astro-ph.CO].
- [86] Simone Ferraro et al. “Inflation and Dark Energy from spectroscopy at  $z > 2$ ”. In: (2019). arXiv: 1903.09208. URL: <http://arxiv.org/abs/1903.09208>.
- [87] D. J. Fixsen. “The Temperature of the Cosmic Microwave Background”. In: (2009). DOI: [10.1088/0004-637X/707/2/916](https://doi.org/10.1088/0004-637X/707/2/916). arXiv: 0911.1955. URL: <http://arxiv.org/abs/0911.1955><http://dx.doi.org/10.1088/0004-637X/707/2/916>.
- [88] Simon Foreman et al. “Lensing reconstruction from line intensity maps: the impact of gravitational nonlinearity”. In: (2018). DOI: [10.1088/1475-7516/2018/07/046](https://doi.org/10.1088/1475-7516/2018/07/046). arXiv: 1803.04975. URL: <http://arxiv.org/abs/1803.04975><http://dx.doi.org/10.1088/1475-7516/2018/07/046>.
- [89] A. Friedman. “Über die Krümmung des Raumes”. In: *Zeitschrift für Physik* 10.1 (1922), pp. 377–386. ISSN: 14346001. DOI: [10.1007/BF01332580](https://doi.org/10.1007/BF01332580).
- [90] J. N. Fry and Enrique Gaztanaga. “Biasing and Hierarchical Statistics in Large-scale Structure”. In: *The Astrophysical Journal* (1993), p. 11. ISSN: 0004-637X. DOI: [10.1086/173015](https://doi.org/10.1086/173015). arXiv: 9302009 [astro-ph]. URL: <http://arxiv.org/abs/astro-ph/9302009>.
- [91] James N. Fry and Enrique Gaztanaga. “Biasing and hierarchical statistics in large scale structure”. In: *Astrophys. J.* 413 (1993), pp. 447–452. DOI: [10.1086/173015](https://doi.org/10.1086/173015). arXiv: astro-ph/9302009 [astro-ph].
- [92] Tomohiro Fujita et al. “Very Massive Tracers and Higher Derivative Biases”. In: (2016). arXiv: 1609.00717 [astro-ph.CO].
- [93] E. Gaztanaga and J. Frieman. “Bias and high-order galaxy correlation functions in the APM Galaxy Survey”. In: *The Astrophysical Journal* 437 (1994), p. L13. DOI: [10.1086/187671](https://doi.org/10.1086/187671). arXiv: 9407079 [astro-ph]. URL: <http://arxiv.org/abs/astro-ph/9407079><http://dx.doi.org/10.1086/187671>.
- [94] E. Gaztañaga and R. Scoccimarro. “The three-point function in large-scale structure: Redshift distortions and galaxy bias”. In: *Monthly Notices of the Royal Astronomical Society* 361.3 (2005), pp. 824–836. ISSN: 00358711. DOI: [10.1111/j.1365-2966.2005.09234.x](https://doi.org/10.1111/j.1365-2966.2005.09234.x).
- [95] T. Giannantonio et al. “CMB lensing tomography with the DES Science Verification galaxies”. In: *Monthly Notices of the Royal Astronomical Society* 456.3 (2016), pp. 3213–3244. ISSN: 13652966. DOI: [10.1093/mnras/stv2678](https://doi.org/10.1093/mnras/stv2678).

- [96] Tommaso Giannantonio and Cristiano Porciani. “Structure formation from non-Gaussian initial conditions: multivariate biasing, statistics, and comparison with N-body simulations”. In: (2009). DOI: [10.1103/PhysRevD.81.063530](https://doi.org/10.1103/PhysRevD.81.063530). arXiv: [0911.0017](https://arxiv.org/abs/0911.0017). URL: <http://arxiv.org/abs/0911.0017><http://dx.doi.org/10.1103/PhysRevD.81.063530>.
- [97] Tommaso Giannantonio et al. “Improved primordial non-Gaussianity constraints from measurements of galaxy clustering and the integrated Sachs-Wolfe effect”. In: *Physical Review D - Particles, Fields, Gravitation and Cosmology* 89.2 (2014), p. 023511. ISSN: 15507998. DOI: [10.1103/PhysRevD.89.023511](https://doi.org/10.1103/PhysRevD.89.023511). arXiv: [1303.1349](https://arxiv.org/abs/1303.1349). URL: <https://journals.aps.org/prd/abstract/10.1103/PhysRevD.89.023511>.
- [98] Héctor Gil-Marín et al. “Dark matter and halo bispectrum in redshift space: theory and applications”. In: (2014). DOI: [10.1088/1475-7516/2014/12/029](https://doi.org/10.1088/1475-7516/2014/12/029). arXiv: [1407.1836](https://arxiv.org/abs/1407.1836). URL: <http://arxiv.org/abs/1407.1836><http://dx.doi.org/10.1088/1475-7516/2014/12/029>.
- [99] Davide Gualdi et al. *Geometrical compression: a new method to enhance the BOSS galaxy bispectrum monopole constraints*. Tech. rep. 2018, pp. 1–6. arXiv: [1901.00987v1](https://arxiv.org/abs/1901.00987v1).
- [100] Alan H Guth. *Inflationary universe: A possible solution to the horizon and flatness problems*. Tech. rep.
- [101] Nico Hamaus et al. “Minimizing the stochasticity of halos in large-scale structure surveys”. In: (2010). DOI: [10.1103/PhysRevD.82.043515](https://doi.org/10.1103/PhysRevD.82.043515). arXiv: [1004.5377](https://arxiv.org/abs/1004.5377). URL: <http://arxiv.org/abs/1004.5377><http://dx.doi.org/10.1103/PhysRevD.82.043515>.
- [102] A. J. S. Hamilton. *The Evolving Universe*. Ed. by Donald Hamilton. Vol. 231. Astrophysics and Space Science Library. Dordrecht: Springer Netherlands, 1998, p. 91. ISBN: 978-94-010-6082-0. DOI: [10.1007/978-94-011-4960-0](https://doi.org/10.1007/978-94-011-4960-0). arXiv: [9708102](https://arxiv.org/abs/9708102) [[astro-ph](https://arxiv.org/abs/9708102)]. URL: <http://arxiv.org/abs/astro-ph/9708102>.
- [103] Christopher M. Hirata et al. “Correlation of CMB with large-scale structure: II. Weak lensing”. In: *Physical Review D - Particles, Fields, Gravitation and Cosmology* 78.4 (2008), p. 043520. DOI: [10.1103/PhysRevD.78.043520](https://doi.org/10.1103/PhysRevD.78.043520). arXiv: [0801.0644](https://arxiv.org/abs/0801.0644). URL: <http://arxiv.org/abs/0801.0644><http://dx.doi.org/10.1103/PhysRevD.78.043520>.
- [104] Shirley Ho et al. “Sloan Digital Sky Survey III Photometric Quasar Clustering: Probing the Initial Conditions of the Universe using the Largest Volume”. In: (2013). DOI: [10.1088/1475-7516/2015/05/040](https://doi.org/10.1088/1475-7516/2015/05/040). arXiv: [1311.2597](https://arxiv.org/abs/1311.2597). URL: <http://arxiv.org/abs/1311.2597><http://dx.doi.org/10.1088/1475-7516/2015/05/040>.
- [105] R W Hockney and J W Eastwood. *Computer Simulation Using Particles - R.W Hockney, J.W Eastwood - Google Books*. URL: [https://books.google.co.il/books?hl=en&lr=&id=nTOFkmnCQuIC&oi=fnd&pg=PR15&dq=Hockney,+R.+W.+Eastwood,+J.+W.+Computer+simulation+using+particles{\\%}3B{\\&}ots=\\\\_ESe8ZUOza{\\&}sig=JtmDT0qTUY2jpAN8Wf7mtQYRLgs{\\&}redir{\\\\_}esc=y{\\#}v=onepage{\\&}q=Hockney{\\%}2CR.W.{\\%}3BEastwood](https://books.google.co.il/books?hl=en&lr=&id=nTOFkmnCQuIC&oi=fnd&pg=PR15&dq=Hockney,+R.+W.+Eastwood,+J.+W.+Computer+simulation+using+particles&ots=\\_ESe8ZUOza&sig=JtmDT0qTUY2jpAN8Wf7mtQYRLgs&redir\\_esc=y{\\#}v=onepage{\\&}q=Hockney{\\%}2CR.W.{\\%}3BEastwood) (visited on 07/29/2020).
- [106] G. P. Holder et al. “A COSMIC MICROWAVE BACKGROUND LENSING MASS MAP AND ITS CORRELATION WITH THE COSMIC INFRARED BACKGROUND”. In: *The Astrophysical Journal Letters* 771.1 (2013), p. L16. ISSN: 2041-8205. DOI: [10.1088/2041-8205/771/1/L16](https://doi.org/10.1088/2041-8205/771/1/L16).

- [107] Wayne Hu. “Angular trispectrum of the cosmic microwave background”. In: *Physical Review D* 64.8 (2001). ISSN: 05562821. DOI: [10.1103/PhysRevD.64.083005](https://doi.org/10.1103/PhysRevD.64.083005). arXiv: [0105117v3](https://arxiv.org/abs/0105117v3) [arXiv:astro-ph]. URL: <http://arxiv.org/abs/astro-ph/0105117http://dx.doi.org/10.1103/PhysRevD.64.083005>.
- [108] E. Hubble. “A relation between distance and radial velocity among extra-galactic nebulae”. In: *Proceedings of the National Academy of Sciences* 15.3 (1929), pp. 168–173. ISSN: 0027-8424. DOI: [10.1073/pnas.15.3.168](https://doi.org/10.1073/pnas.15.3.168).
- [109] Johnathan Hung, James R. Fergusson, and E. P. S. Shellard. “Advancing the matter bispectrum estimation of large-scale structure: a comparison of dark matter codes”. In: August (2019). arXiv: [1902.01830](https://arxiv.org/abs/1902.01830). URL: <http://arxiv.org/abs/1902.01830>.
- [110] Mikhail M. Ivanov, Marko Simonović, and Matias Zaldarriaga. “Cosmological Parameters from the BOSS Galaxy Power Spectrum”. In: (2019). DOI: [10.1088/1475-7516/2020/05/042](https://doi.org/10.1088/1475-7516/2020/05/042). arXiv: [1909.05277](https://arxiv.org/abs/1909.05277). URL: <http://arxiv.org/abs/1909.05277http://dx.doi.org/10.1088/1475-7516/2020/05/042>.
- [111] Donghui Jeong and Eiichiro Komatsu. *PRIMORDIAL NON-GAUSSIANITY, SCALE-DEPENDENT BIAS, AND THE BISPECTRUM OF GALAXIES*. Tech. rep. 2009. arXiv: [0904.0497v2](https://arxiv.org/abs/0904.0497v2). URL: <http://hetdex.org/pdfs/research/Jeong3.pdf>.
- [112] Gerard Jungman et al. “Cosmological-Parameter Determination with Microwave Background Maps”. In: *Physical Review D - Particles, Fields, Gravitation and Cosmology* 54.2 (1995), pp. 1332–1344. DOI: [10.1103/PhysRevD.54.1332](https://doi.org/10.1103/PhysRevD.54.1332). arXiv: [9512139](https://arxiv.org/abs/9512139) [astro-ph]. URL: <http://arxiv.org/abs/astro-ph/9512139http://dx.doi.org/10.1103/PhysRevD.54.1332>.
- [113] N. Kaiser. “On the spatial correlations of Abell clusters”. In: *The Astrophysical Journal* 284 (1984), p. L9. ISSN: 0004-637X. DOI: [10.1086/184341](https://doi.org/10.1086/184341). URL: <http://adsabs.harvard.edu/doi/10.1086/184341>.
- [114] B. Kalus et al. “A map-based method for eliminating systematic modes from galaxy clustering power spectra with application to BOSS”. In: (2018). DOI: [10.1093/mnras/sty2655](https://doi.org/10.1093/mnras/sty2655). arXiv: [1806.02789](https://arxiv.org/abs/1806.02789). URL: <http://arxiv.org/abs/1806.02789http://dx.doi.org/10.1093/mnras/sty2655>.
- [115] Naim Goksel Karacayli and Nikhil Padmanabhan. “Anatomy of Cosmic Tidal Reconstruction”. In: (2019). DOI: [10.1093/mnras/stz964](https://doi.org/10.1093/mnras/stz964). arXiv: [1904.01387](https://arxiv.org/abs/1904.01387). URL: <http://arxiv.org/abs/1904.01387http://dx.doi.org/10.1093/mnras/stz964>.
- [116] Issha Kayo and Masahiro Takada. “Cosmological parameters from weak lensing power spectrum and bispectrum tomography: including the non-Gaussian errors”. In: *Mon. Not. R. Astron. Soc* 000.0000 (2013), pp. 0–000. arXiv: [1306.4684](https://arxiv.org/abs/1306.4684). URL: <http://arxiv.org/abs/1306.4684>.
- [117] R. Keisler et al. “A measurement of the damping tail of the cosmic microwave background power spectrum with the South Pole Telescope”. In: *Astrophysical Journal* 743.1 (2011), p. 28. ISSN: 15384357. DOI: [10.1088/0004-637X/743/1/28](https://doi.org/10.1088/0004-637X/743/1/28). arXiv: [1105.3182](https://arxiv.org/abs/1105.3182). URL: <https://ui.adsabs.harvard.edu/abs/2011ApJ...743...28K/abstract>.
- [118] Alexander Knebe et al. *Haloes gone MAD : The Halo-Finder Comparison Project*. Tech. rep. 2010, pp. 1–27. arXiv: [1104.0949v1](https://arxiv.org/abs/1104.0949v1).

- [119] E. Komatsu et al. “Five-Year Wilkinson Microwave Anisotropy Probe (WMAP) Observations: Cosmological Interpretation”. In: (2008). DOI: [10.1088/0067-0049/180/2/330](https://doi.org/10.1088/0067-0049/180/2/330). arXiv: [0803.0547](https://arxiv.org/abs/0803.0547). URL: <http://arxiv.org/abs/0803.0547><http://dx.doi.org/10.1088/0067-0049/180/2/330>.
- [120] E. Komatsu et al. “Non-Gaussianity as a Probe of the Physics of the Primordial Universe and the Astrophysics of the Low Redshift Universe”. In: (2009). arXiv: [0902.4759](https://arxiv.org/abs/0902.4759). URL: <http://arxiv.org/abs/0902.4759>.
- [121] Titouan Lazeyras and Fabian Schmidt. “Beyond LIMD bias: a measurement of the complete set of third-order halo bias parameters”. In: (2017). arXiv: [1712.07531](https://arxiv.org/abs/1712.07531) [[astro-ph.CO](https://arxiv.org/abs/1712.07531)].
- [122] Titouan Lazeyras and Fabian Schmidt. *Beyond LIMD bias: a measurement of the complete set of third-order halo bias parameters*. Tech. rep. 2018. arXiv: [1712.07531v3](https://arxiv.org/abs/1712.07531v3).
- [123] Boris Leistedt, Hiranya V. Peiris, and Nina Roth. “Constraints on primordial non-gaussianity from 800000 photometric quasars”. In: *Physical Review Letters* 113.22 (2014), p. 221301. ISSN: 10797114. DOI: [10.1103/PhysRevLett.113.221301](https://doi.org/10.1103/PhysRevLett.113.221301). arXiv: [1405.4315](https://arxiv.org/abs/1405.4315). URL: <https://journals.aps.org/prl/abstract/10.1103/PhysRevLett.113.221301>.
- [124] G. Lemaître, Lemaître, and G. *Un Univers homogène de masse constante et de rayon croissant rendant compte de la vitesse radiale des nébuleuses extra-galactiques*. Tech. rep. 1927, pp. 49–59.
- [125] Julien Lesgourgues. “The Cosmic Linear Anisotropy Solving System (CLASS) I: Overview”. In: (2011). arXiv: [1104.2932](https://arxiv.org/abs/1104.2932). URL: <http://arxiv.org/abs/1104.2932>.
- [126] Antony Lewis and Anthony Challinor. “Weak Gravitational Lensing of the CMB”. In: (2006). DOI: [10.1016/j.physrep.2006.03.002](https://doi.org/10.1016/j.physrep.2006.03.002). arXiv: [0601594](https://arxiv.org/abs/0601594) [[astro-ph](https://arxiv.org/abs/0601594)]. URL: <http://arxiv.org/abs/astro-ph/0601594><http://dx.doi.org/10.1016/j.physrep.2006.03.002>.
- [127] Antony Lewis, Anthony Challinor, and Anthony Lasenby. “Efficient Computation of Cosmic Microwave Background Anisotropies in Closed Friedmann-Robertson-Walker Models”. In: *The Astrophysical Journal* 538.2 (2000), pp. 473–476. ISSN: 0004-637X. DOI: [10.1086/309179](https://doi.org/10.1086/309179). URL: [www.mrao.cam.ac.uk/Dam11005/cmb..](http://www.mrao.cam.ac.uk/Dam11005/cmb..)
- [128] Dongzi Li, Hong-Ming Zhu, and Ue-Li Pen. “Cross-correlation of the kinematic Sunyaev-Zel’dovich effect and 21 cm intensity mapping with tidal reconstruction”. In: *Physical Review D* 100.2 (2019), p. 023517. ISSN: 2470-0010. DOI: [10.1103/PhysRevD.100.023517](https://doi.org/10.1103/PhysRevD.100.023517). URL: <https://journals.aps.org/prd/abstract/10.1103/PhysRevD.100.023517>.
- [129] Peikai Li, Rupert A. C. Croft, and Scott Dodelson. “Large Scale Structure Reconstruction with Short-Wavelength Modes: Halo Bias and Light Cone Formalism”. In: (2020). arXiv: [2007.00226](https://arxiv.org/abs/2007.00226). URL: <http://arxiv.org/abs/2007.00226>.
- [130] Peikai Li, Scott Dodelson, and Rupert A.C. Croft. “Large scale structure reconstruction with short-wavelength modes”. In: *Physical Review D* 101.8 (2020), p. 083510. ISSN: 24700029. DOI: [10.1103/PhysRevD.101.083510](https://doi.org/10.1103/PhysRevD.101.083510). arXiv: [2001.02780](https://arxiv.org/abs/2001.02780). URL: <https://journals.aps.org/prd/abstract/10.1103/PhysRevD.101.083510>.

- [131] A. D. Linde. “A new inflationary universe scenario: A possible solution of the horizon, flatness, homogeneity, isotropy and primordial monopole problems”. In: *Physics Letters B* 108.6 (1982), pp. 389–393. ISSN: 03702693. DOI: [10.1016/0370-2693\(82\)91219-9](https://doi.org/10.1016/0370-2693(82)91219-9).
- [132] R Henry Liu and Patrick C Breysse. *Coupling parsec and gigaparsec scales: primordial non-Gaussianity with multi-tracer intensity mapping*. Tech. rep. 2019, pp. 1–12. arXiv: [2002.10483v1](https://arxiv.org/abs/2002.10483v1).
- [133] Marilena Loverde and Niayesh Afshordi. *Extended Limber Approximation*. Tech. rep. 2008. arXiv: [0809.5112v1](https://arxiv.org/abs/0809.5112v1). URL: <https://arxiv.org/pdf/0809.5112.pdf>.
- [134] The Lsst. *The LSST Science Book*. Tech. rep. November. 2009, p. 596. arXiv: [0912.0201](https://arxiv.org/abs/0912.0201). URL: <http://arxiv.org/abs/0912.0201>.
- [135] Sabino Matarrese and Massimo Pietroni. “Resumming cosmic perturbations”. In: *Journal of Cosmology and Astroparticle Physics* 2007.06 (2007), pp. 026–026. ISSN: 1475-7516. DOI: [10.1088/1475-7516/2007/06/026](https://doi.org/10.1088/1475-7516/2007/06/026). arXiv: [0703563](https://arxiv.org/abs/0703563) [astro-ph]. URL: <http://arxiv.org/abs/astro-ph/0703563>.
- [136] Takahiko Matsubara. “Resumming Cosmological Perturbations via the Lagrangian Picture: One-loop Results in Real Space and in Redshift Space”. In: *Phys. Rev. D* 77 (2008), p. 063530. DOI: [10.1103/PhysRevD.77.063530](https://doi.org/10.1103/PhysRevD.77.063530). arXiv: [0711.2521](https://arxiv.org/abs/0711.2521) [astro-ph].
- [137] Cameron K. McBride et al. “Three-Point Correlation Functions of SDSS Galaxies: Constraining Galaxy-Mass Bias”. In: (2010). DOI: [10.1088/0004-637X/739/2/85](https://doi.org/10.1088/0004-637X/739/2/85). arXiv: [1012.3462](https://arxiv.org/abs/1012.3462). URL: <http://arxiv.org/abs/1012.3462><http://dx.doi.org/10.1088/0004-637X/739/2/85>.
- [138] Patrick McDonald. “Clustering of dark matter tracers: renormalizing the bias parameters”. In: (2006). DOI: [10.1103/PhysRevD.74.103512](https://doi.org/10.1103/PhysRevD.74.103512). arXiv: [0609413](https://arxiv.org/abs/0609413) [astro-ph]. URL: <http://arxiv.org/abs/astro-ph/0609413><http://dx.doi.org/10.1103/PhysRevD.74.103512>.
- [139] Patrick McDonald. “Clustering of dark matter tracers: Renormalizing the bias parameters”. In: *Phys. Rev. D* 74 (2006). [Erratum: *Phys. Rev. D* 74, 129901 (2006)], p. 103512. DOI: [10.1103/PhysRevD.74.103512](https://doi.org/10.1103/PhysRevD.74.103512), [10.1103/PhysRevD.74.129901](https://doi.org/10.1103/PhysRevD.74.129901). arXiv: [astro-ph/0609413](https://arxiv.org/abs/astro-ph/0609413) [astro-ph].
- [140] Patrick McDonald. *How to measure redshift-space distortions without sample variance*. Tech. rep. 2008. arXiv: [0810.0323v1](https://arxiv.org/abs/0810.0323v1).
- [141] Patrick McDonald and Arabindo Roy. “Clustering of dark matter tracers: generalizing bias for the coming era of precision LSS”. In: (2009). arXiv: [arXiv:0902.0991v1](https://arxiv.org/abs/0902.0991v1). URL: <https://arxiv.org/pdf/0902.0991.pdf>.
- [142] Patrick McDonald and Arabindo Roy. “Clustering of dark matter tracers: generalizing bias for the coming era of precision LSS”. In: *JCAP* 0908 (2009), p. 020. DOI: [10.1088/1475-7516/2009/08/020](https://doi.org/10.1088/1475-7516/2009/08/020). arXiv: [0902.0991](https://arxiv.org/abs/0902.0991) [astro-ph.CO].
- [143] P. Daniel Meerburg et al. “Primordial Non-Gaussianity”. In: *Jonás Chaves-Montero* 33 (2019), p. 34. arXiv: [1903.04409](https://arxiv.org/abs/1903.04409). URL: <http://arxiv.org/abs/1903.04409>.
- [144] Mehrdad Mirbabayi, Fabian Schmidt, and Matias Zaldarriaga. “Biased Tracers and Time Evolution”. In: *JCAP* 1507.07 (2015), p. 030. DOI: [10.1088/1475-7516/2015/07/030](https://doi.org/10.1088/1475-7516/2015/07/030). arXiv: [1412.5169](https://arxiv.org/abs/1412.5169) [astro-ph.CO].

- [145] H. J. Mo and S. D. M. White. “An analytic model for the spatial clustering of dark matter haloes”. In: (1995). DOI: [10.1093/mnras/282.2.347](https://doi.org/10.1093/mnras/282.2.347). arXiv: [9512127](https://arxiv.org/abs/9512127) [astro-ph]. URL: <http://arxiv.org/abs/astro-ph/9512127><http://dx.doi.org/10.1093/mnras/282.2.347>.
- [146] Houjun Mo, Frank C. van den Bosch, and Simon White. “Galaxy Formation and Evolution”. In: *gfe* (2010). URL: <https://ui.adsabs.harvard.edu/abs/2010gfe..book.....M/abstract>.
- [147] Chirag Modi, Emanuele Castorina, and Uros Seljak. “Halo bias in Lagrangian Space: Estimators and theoretical predictions”. In: *Mon. Not. Roy. Astron. Soc.* 472.4 (2017), pp. 3959–3970. DOI: [10.1093/mnras/stx2148](https://doi.org/10.1093/mnras/stx2148). arXiv: [1612.01621](https://arxiv.org/abs/1612.01621) [astro-ph.CO].
- [148] Chirag Modi, Martin White, and Zvonimir Vlah. *Modeling CMB Lensing Cross Correlations with CLEFT*. Tech. rep. 2017. arXiv: [1706.03173v1](https://arxiv.org/abs/1706.03173v1). URL: <https://www.lsst.org>.
- [149] Chirag Modi et al. “Reconstructing large-scale structure with neutral hydrogen surveys”. In: (2019). DOI: [10.1088/1475-7516/2019/11/023](https://doi.org/10.1088/1475-7516/2019/11/023). arXiv: [1907.02330](https://arxiv.org/abs/1907.02330). URL: <http://arxiv.org/abs/1907.02330><http://dx.doi.org/10.1088/1475-7516/2019/11/023>.
- [150] Surhud More et al. “THE OVERDENSITY AND MASSES OF THE FRIENDS-OF-FRIENDS HALOS AND UNIVERSALITY OF HALO MASS FUNCTION”. In: *The Astrophysical Journal Supplement Series* 195.1 (2011), p. 4. ISSN: 0067-0049. DOI: [10.1088/0067-0049/195/1/4](https://doi.org/10.1088/0067-0049/195/1/4).
- [151] Moritz Münchmeyer et al. *Constraining local non-Gaussianities with kSZ tomography*. Tech. rep. arXiv: [1810.13424v1](https://arxiv.org/abs/1810.13424v1). URL: <https://arxiv.org/pdf/1810.13424.pdf>.
- [152] Toshiya Namikawa, Duncan Hanson, and Ryuichi Takahashi. *Bias-Hardened CMB Lensing*. Tech. rep. 0000. 2013, pp. 0–000. arXiv: [1209.0091v2](https://arxiv.org/abs/1209.0091v2).
- [153] Dragan Huterer Neal Dalal Olivier Dore and Alexander Shirokov. “The imprints of primordial non-Gaussianities on large-scale structure: scale dependent bias and abundance of virialized objects,” in: *Phys.Rev D* 77 (2008).
- [154] Wei Tou Ni. *Solar-system tests of the relativistic gravity*. 2016. DOI: [10.1142/S0218271816300032](https://doi.org/10.1142/S0218271816300032). arXiv: [1611.06025](https://arxiv.org/abs/1611.06025).
- [155] S. J. Osborne, D. Hanson, and O. Doré. “Extragalactic Foreground Contamination in Temperature-based CMB Lens Reconstruction”. In: (2013). DOI: [10.1088/1475-7516/2014/03/024](https://doi.org/10.1088/1475-7516/2014/03/024). arXiv: [1310.7547](https://arxiv.org/abs/1310.7547). URL: <http://arxiv.org/abs/1310.7547><http://dx.doi.org/10.1088/1475-7516/2014/03/024>.
- [156] Stephen J Osborne, Duncan Hanson, and Olivier Doré. *Extragalactic Foreground Contamination in Temperature-based CMB Lens Reconstruction*. Tech. rep. arXiv: [1310.7547v1](https://arxiv.org/abs/1310.7547v1).
- [157] Enrico Pajer and Matias Zaldarriaga. “On the Renormalization of the Effective Field Theory of Large Scale Structures”. In: (2013). DOI: [10.1088/1475-7516/2013/08/037](https://doi.org/10.1088/1475-7516/2013/08/037). arXiv: [1301.7182](https://arxiv.org/abs/1301.7182). URL: <http://arxiv.org/abs/1301.7182><http://dx.doi.org/10.1088/1475-7516/2013/08/037>.
- [158] Enrico Pajer and Matias Zaldarriaga. “On the Renormalization of the Effective Field Theory of Large Scale Structures”. In: *JCAP* 1308 (2013), p. 037. DOI: [10.1088/1475-7516/2013/08/037](https://doi.org/10.1088/1475-7516/2013/08/037). arXiv: [1301.7182](https://arxiv.org/abs/1301.7182) [astro-ph.CO].

- [159] Ue-Li Pen et al. “Cosmic Tides”. In: (2012). arXiv: 1202.5804. URL: <http://arxiv.org/abs/1202.5804>.
- [160] Planck Collaboration et al. “Planck 2018 results. VI. Cosmological parameters”. In: (2018). arXiv: 1807.06209. URL: <http://arxiv.org/abs/1807.06209>.
- [161] Planck Planck Collaboration et al. “Planck 2013 results. XVI. Cosmological parameters”. In: (2013). DOI: 10.1051/0004-6361/201321591. arXiv: 1303.5076. URL: <http://arxiv.org/abs/1303.5076><http://dx.doi.org/10.1051/0004-6361/201321591>.
- [162] Planck Planck Collaboration et al. “Planck 2013 Results. XXIV. Constraints on primordial non-Gaussianity”. In: (2013). DOI: 10.1051/0004-6361/201321554. arXiv: 1303.5084. URL: <http://arxiv.org/abs/1303.5084><http://dx.doi.org/10.1051/0004-6361/201321554>.
- [163] Planck Planck Collaboration et al. “Planck 2013 Results. XXIV. Constraints on primordial non-Gaussianity”. In: (2013). DOI: 10.1051/0004-6361/201321554. arXiv: 1303.5084. URL: <http://arxiv.org/abs/1303.5084><http://dx.doi.org/10.1051/0004-6361/201321554>.
- [164] Planck Planck Collaboration et al. “Planck 2015 results. XVII. Constraints on primordial non-Gaussianity”. In: (2015). DOI: 10.1051/0004-6361/201525836. arXiv: 1502.01592. URL: <http://arxiv.org/abs/1502.01592><http://dx.doi.org/10.1051/0004-6361/201525836>.
- [165] Rafael A. Porto, Leonardo Senatore, and Matias Zaldarriaga. “The Lagrangian-space Effective Field Theory of Large Scale Structures”. In: *JCAP* 1405 (2014), p. 022. DOI: 10.1088/1475-7516/2014/05/022. arXiv: 1311.2168 [astro-ph.CO].
- [166] William H Press and Paul Schechter. “FORMATION OF GALAXIES AND CLUSTERS OF GALAXIES BY SELF-SIMILAR GRAVITATIONAL CONDENSATION\*”. In: *The Astrophysical Journal* 187 (1974), pp. 425–438. URL: [http://articles.adsabs.harvard.edu/cgi-bin/nph-iarticle?\\_query=1974ApJ...187..425P%26data%26type=PDF%26HIGH%26whole%26paper=YES%26type=PRINTER%26filetype=.pdf](http://articles.adsabs.harvard.edu/cgi-bin/nph-iarticle?_query=1974ApJ...187..425P%26data%26type=PDF%26HIGH%26whole%26paper=YES%26type=PRINTER%26filetype=.pdf).
- [167] Roland de Putter. “Primordial physics from large-scale structure beyond the power spectrum”. In: (2018). arXiv: 1802.06762. URL: <http://arxiv.org/abs/1802.06762>.
- [168] Adam Riess, Riess, and Adam. “SHOES-Supernovae, HO, for the Equation of State of Dark energy”. In: *hst* (2006), p. 10802.
- [169] Adam G. Riess et al. “Large Magellanic Cloud Cepheid Standards Provide a 1% Foundation for the Determination of the Hubble Constant and Stronger Evidence for Physics Beyond LambdaCDM”. In: (2019). DOI: 10.3847/1538-4357/ab1422. arXiv: 1903.07603. URL: <http://arxiv.org/abs/1903.07603><http://dx.doi.org/10.3847/1538-4357/ab1422>.
- [170] H. P. Robertson. “Kinematics and World-Structure”. In: *The Astrophysical Journal* 82 (1935), p. 284. ISSN: 0004-637X. DOI: 10.1086/143681.
- [171] Ashley J. Ross et al. “The Clustering of Galaxies in SDSS-III DR9 Baryon Oscillation Spectroscopic Survey: Constraints on Primordial Non-Gaussianity”. In: (2012). DOI: 10.1093/mnras/sts094. arXiv: 1208.1491. URL: <http://arxiv.org/abs/1208.1491><http://dx.doi.org/10.1093/mnras/sts094>.
- [172] Shun Saito et al. “Understanding higher-order nonlocal halo bias at large scales by combining the power spectrum with the bispectrum”. In: *Phys. Rev. D* 90.12 (2014), p. 123522. DOI: 10.1103/PhysRevD.90.123522. arXiv: 1405.1447 [astro-ph.CO].

- [173] David J. Schlegel et al. “Astro2020 APC White Paper: The MegaMapper: a  $z > 2$  spectroscopic instrument for the study of Inflation and Dark Energy”. In: (2019). arXiv: 1907.11171. URL: <http://arxiv.org/abs/1907.11171>.
- [174] Fabian Schmidt, Donghui Jeong, and Vincent Desjacques. “Peak-Background Split, Renormalization, and Galaxy Clustering”. In: *Phys. Rev. D* 88.2 (2013), p. 023515. DOI: 10.1103/PhysRevD.88.023515. arXiv: 1212.0868 [astro-ph.CO].
- [175] Fabian Schmidt and Marc Kamionkowski. “Halo clustering with nonlocal non-Gaussianity”. In: (). DOI: 10.1103/PhysRevD.82.103002.
- [176] Marcel Schmittfull, Tobias Baldauf, and Uroš Seljak. “Near optimal bispectrum estimators for large-scale structure”. In: *Physical Review D - Particles, Fields, Gravitation and Cosmology* 91.4 (2015), pp. 1–28. ISSN: 15502368. DOI: 10.1103/PhysRevD.91.043530. arXiv: 1411.6595.
- [177] Marcel Schmittfull, Tobias Baldauf, and Uroš Seljak. “Near optimal bispectrum estimators for large-scale structure”. In: *Phys. Rev. D* 91.4 (2015), p. 043530. DOI: 10.1103/PhysRevD.91.043530. arXiv: 1411.6595 [astro-ph.CO].
- [178] Marcel Schmittfull, Tobias Baldauf, and Matias Zaldarriaga. “Iterative initial condition reconstruction”. In: (2017). DOI: 10.1103/PhysRevD.96.023505. arXiv: 1704.06634. URL: <http://arxiv.org/abs/1704.06634><http://dx.doi.org/10.1103/PhysRevD.96.023505>.
- [179] Marcel Schmittfull et al. *Modeling Biased Tracers at the Field Level*. Tech. rep. arXiv: 1811.10640v1. URL: <https://arxiv.org/pdf/1811.10640.pdf>.
- [180] Román Scoccimarro. “Redshift-space distortions, pairwise velocities, and nonlinearities”. In: *Physical Review D* 70.8 (2004), p. 083007. ISSN: 1550-7998. DOI: 10.1103/PhysRevD.70.083007. arXiv: 0407214 [astro-ph]. URL: <http://arxiv.org/abs/astro-ph/0407214>.
- [181] Roman Scoccimarro et al. “How Many Galaxies Fit in a Halo? Constraints on Galaxy Formation Efficiency from Spatial Clustering”. In: *The Astrophysical Journal* 546.1 (2001), pp. 20–34. ISSN: 0004-637X. DOI: 10.1086/318261. arXiv: 0006319 [astro-ph]. URL: <http://arxiv.org/abs/astro-ph/0006319>.
- [182] Roman Scoccimarro et al. “Large-scale Bias and Efficient Generation of Initial Conditions for Non-Local Primordial Non-Gaussianity”. In: *Phys. Rev. D* 85 (2012), p. 083002. DOI: 10.1103/PhysRevD.85.083002. arXiv: 1108.5512 [astro-ph.CO].
- [183] Roman Scoccimarro et al. “Nonlinear Evolution of the Bispectrum of Cosmological Perturbations”. In: *The Astrophysical Journal* 496.2 (1998), pp. 586–604. ISSN: 0004-637X. DOI: 10.1086/305399. arXiv: 9704075 [astro-ph].
- [184] Emiliano Sefusatti et al. “Cosmology and the Bispectrum”. In: (2006). DOI: 10.1103/PhysRevD.74.023522. arXiv: 0604505 [astro-ph]. URL: <http://arxiv.org/abs/astro-ph/0604505><http://dx.doi.org/10.1103/PhysRevD.74.023522>.
- [185] Uros Seljak. “Measuring primordial non-gaussianity without cosmic variance”. In: (2008). DOI: 10.1103/PhysRevLett.102.021302. arXiv: 0807.1770. URL: <http://arxiv.org/abs/0807.1770><http://dx.doi.org/10.1103/PhysRevLett.102.021302>.
- [186] Uros Seljak and Matias Zaldarriaga. “A Line of Sight Approach to Cosmic Microwave Background Anisotropies”. In: *The Astrophysical Journal* 469 (1996), p. 437. DOI: 10.1086/177793. arXiv: 9603033 [astro-ph]. URL: <http://arxiv.org/abs/astro-ph/9603033><http://dx.doi.org/10.1086/177793>.



- [187] Leonardo Senatore. “Bias in the Effective Field Theory of Large Scale Structures”. In: *JCAP* 1511.11 (2015), p. 007. DOI: [10.1088/1475-7516/2015/11/007](https://doi.org/10.1088/1475-7516/2015/11/007). arXiv: [1406.7843](https://arxiv.org/abs/1406.7843) [astro-ph.CO].
- [188] Leonardo Senatore and Matias Zaldarriaga. “The IR-resummed Effective Field Theory of Large Scale Structures”. In: *JCAP* 1502.02 (2015), p. 013. DOI: [10.1088/1475-7516/2015/02/013](https://doi.org/10.1088/1475-7516/2015/02/013). arXiv: [1404.5954](https://arxiv.org/abs/1404.5954) [astro-ph.CO].
- [189] Blake D Sherwin. *CMB Lensing Cross--correlations*. Tech. rep. URL: <https://cmb-s4.org/wiki/images/archive/20150922061651/{%}21Crosses.pdf>.
- [190] Ravi K. Sheth and Giuseppe Tormen. “Large-scale bias and the peak background split”. In: *Monthly Notices of the Royal Astronomical Society* 308.1 (1999), pp. 119–126. ISSN: 0035-8711. DOI: [10.1046/j.1365-8711.1999.02692.x](https://doi.org/10.1046/j.1365-8711.1999.02692.x). arXiv: [9901122](https://arxiv.org/abs/9901122) [astro-ph]. URL: <https://academic.oup.com/mnras/article-lookup/doi/10.1046/j.1365-8711.1999.02692.x>.
- [191] Ravi K. Sheth and Giuseppe Tormen. “Large scale bias and the peak background split”. In: *Mon. Not. Roy. Astron. Soc.* 308 (1999), p. 119. DOI: [10.1046/j.1365-8711.1999.02692.x](https://doi.org/10.1046/j.1365-8711.1999.02692.x). arXiv: [astro-ph/9901122](https://arxiv.org/abs/astro-ph/9901122) [astro-ph].
- [192] The Simons Observatory Collaboration et al. *Frederick Matsuda 30*. Tech. rep. arXiv: [1808.07445v1](https://arxiv.org/abs/1808.07445v1). URL: <https://simonsobservatory.org/publications..>
- [193] Anže Slosar et al. *Constraints on local primordial non-Gaussianity from large scale structure*. Tech. rep. 2008. arXiv: [0805.3580v2](https://arxiv.org/abs/0805.3580v2). URL: <https://arxiv.org/pdf/0805.3580.pdf>.
- [194] Joseph Smidt et al. “A Constraint on the Integrated Mass Power Spectrum Out to  $z = 1100$  from Lensing of the Cosmic Microwave Background”. In: *ApJL* 728.1 (2011), p. L1. ISSN: 0004-637X. DOI: [10.1088/2041-8205/728/1/L1](https://doi.org/10.1088/2041-8205/728/1/L1). arXiv: [arXiv: 1012.1600](https://arxiv.org/abs/1012.1600). URL: <https://ui.adsabs.harvard.edu/abs/2011ApJ...728L...1S/abstract>.
- [195] D Spergel et al. *WFIRST-2.4: What Every Astronomer Should Know Science Definition Team Study Team*. Tech. rep.
- [196] Volker Springel. “The Cosmological simulation code GADGET-2”. In: *Mon. Not. Roy. Astron. Soc.* 364 (2005), pp. 1105–1134. DOI: [10.1111/j.1365-2966.2005.09655.x](https://doi.org/10.1111/j.1365-2966.2005.09655.x). arXiv: [astro-ph/0505010](https://arxiv.org/abs/astro-ph/0505010) [astro-ph].
- [197] Volker Springel. “The cosmological simulation code GADGET-2”. In: *Mon. Not. R. Astron. Soc* 364 (2005), pp. 1105–1134. DOI: [10.1111/j.1365-2966.2005.09655.x](https://doi.org/10.1111/j.1365-2966.2005.09655.x).
- [198] Volker Springel, Naoki Yoshida, and Simon D M White. *GADGET: a code for collisionless and gasdynamical cosmological simulations*. Tech. rep. 2001, pp. 79–117. URL: [www.elsevier.nl/locate/newast](http://www.elsevier.nl/locate/newast).
- [199] K. T. Story et al. “A MEASUREMENT OF THE COSMIC MICROWAVE BACKGROUND DAMPING TAIL FROM THE 2500-SQUARE-DEGREE SPT-SZ SURVEY”. In: *The Astrophysical Journal* 779.1 (2013), p. 86. ISSN: 0004-637X. DOI: [10.1088/0004-637X/779/1/86](https://doi.org/10.1088/0004-637X/779/1/86).
- [200] K. T. Story et al. “A MEASUREMENT OF THE COSMIC MICROWAVE BACKGROUND GRAVITATIONAL LENSING POTENTIAL FROM 100 SQUARE DEGREES OF SPTPOL DATA”. In: *The Astrophysical Journal* 810.1 (2015), p. 50. ISSN: 0004-637X. DOI: [10.1088/0004-637X/810/1/50](https://doi.org/10.1088/0004-637X/810/1/50). URL: <https://iopscience.iop.org/article/10.1088/0004-637X/810/1/50https://iopscience.iop.org/article/10.1088/0004-637X/810/1/50/meta>.

- [201] A Suzuki et al. *The POLARBEAR-2 and the Simons Array Experiments*. Tech. rep. 2015. arXiv: [1512.07299v1](https://arxiv.org/abs/1512.07299v1).
- [202] A. S. Szalay. “Constraints on the biasing of density fluctuations”. In: *APJ* 333 (Oct. 1988), pp. 21–23. DOI: [10.1086/166721](https://doi.org/10.1086/166721).
- [203] Ryuichi Takahashi. “Third-Order Density Perturbation and One-Loop Power Spectrum in Dark-Energy-Dominated Universe”. In: *Progress of Theoretical Physics* 120.3 (2008), pp. 549–559. DOI: [10.1143/PTP.120.549](https://doi.org/10.1143/PTP.120.549). arXiv: [0806.1437](https://arxiv.org/abs/0806.1437). URL: <http://arxiv.org/abs/0806.1437http://dx.doi.org/10.1143/PTP.120.549>.
- [204] Max Tegmark. *Consciousness as a State of Matter*. Tech. rep. arXiv: [1401.1219v3](https://arxiv.org/abs/1401.1219v3). URL: <https://arxiv.org/pdf/1401.1219.pdf>.
- [205] Max Tegmark, Andy Taylor, and Alan Heavens. “Karhunen-Loeve eigenvalue problems in cosmology: how should we tackle large data sets?” In: *The Astrophysical Journal* 480.1 (1996), pp. 22–35. DOI: [10.1086/303939](https://doi.org/10.1086/303939). arXiv: [9603021](https://arxiv.org/abs/9603021) [astro-ph]. URL: <http://arxiv.org/abs/astro-ph/9603021http://dx.doi.org/10.1086/303939>.
- [206] A. Van Engelen et al. “A measurement of gravitational lensing of the microwave background using south pole telescope data”. In: *Astrophysical Journal* 756.2 (2012), p. 142. ISSN: 15384357. DOI: [10.1088/0004-637X/756/2/142](https://doi.org/10.1088/0004-637X/756/2/142). arXiv: [1202.0546](https://arxiv.org/abs/1202.0546). URL: <https://ui.adsabs.harvard.edu/abs/2012ApJ...756..142V/abstract>.
- [207] Licia Verde et al. “The 2dF Galaxy Redshift Survey: the bias of galaxies and the density of the Universe”. In: *Monthly Notices of the Royal Astronomical Society* 335.2 (2002), pp. 432–440. ISSN: 0035-8711. DOI: [10.1046/j.1365-8711.2002.05620.x](https://doi.org/10.1046/j.1365-8711.2002.05620.x). URL: <https://academic.oup.com/mnras/article-lookup/doi/10.1046/j.1365-8711.2002.05620.x>.
- [208] Y. B. Zel’Dovich. *Gravitational instability: an approximate theory for large density perturbations*. 1970. URL: [https://ui.adsabs.harvard.edu/abs/1970A{ }26A.....5...84Z/abstract](https://ui.adsabs.harvard.edu/abs/1970A%7B%7D26A.....5...84Z/abstract) (visited on 06/07/2020).
- [209] Hong Ming Zhu et al. “Cosmic tidal reconstruction”. In: *Physical Review D* 93.10 (2016), p. 103504. ISSN: 24700029. DOI: [10.1103/PhysRevD.93.103504](https://doi.org/10.1103/PhysRevD.93.103504). arXiv: [1511.04680](https://arxiv.org/abs/1511.04680). URL: <https://journals.aps.org/prd/abstract/10.1103/PhysRevD.93.103504>.
- [210] Hong Ming Zhu et al. “Recovering lost 21 cm radial modes via cosmic tidal reconstruction RECOVERING LOST 21 CM RADIAL MODES VIA COSMIC HONG-MING ZHU et al.” In: *Physical Review D* 98.4 (2018), p. 043511. ISSN: 24700029. DOI: [10.1103/PhysRevD.98.043511](https://doi.org/10.1103/PhysRevD.98.043511). URL: <https://journals.aps.org/prd/abstract/10.1103/PhysRevD.98.043511>.

## EFT Counterterms

### A.1 Basis

The authors in [6, 92] define a basis of operators

$$\mathcal{B}_{\text{FMSVA}} = \{\mathbb{C}_{\delta,1}^{(3)}, \mathbb{C}_{\delta,2}^{(3)}, \mathbb{C}_{\delta,3}^{(3)}, \mathbb{C}_{\delta^2,1}^{(3)}, \mathbb{C}_{\delta^2,2}^{(3)}, \mathbb{C}_{\delta^3,1}^{(3)}, \mathbb{C}_{s^2,2}^{(3)}\} \quad (\text{A.1})$$

Note that their basis is equivalent to our basis

$$\mathcal{B}_{\text{here}} = \{F_3, 1, \mathcal{G}_3 + \frac{1}{9}, \mathcal{G}_2 \delta + \frac{2}{3}, \Gamma_3 + \frac{16}{63}, \delta^{(1)} \delta^{(2)}, s_{ij}^{(1)} s_{ji}^{(2)}\} \quad (\text{A.2})$$

$$\mathcal{B}_{\text{here}} = \mathcal{M} \mathcal{B}_{\text{FMSVA}} \quad (\text{A.3})$$

where

$$\mathcal{M} = \begin{pmatrix} 1 & 1 & 1 & 0 & 0 & 0 & 0 \\ 0 & 0 & 0 & 0 & 0 & 1 & 0 \\ 0 & 0 & -\frac{45}{4} & 0 & \frac{151}{16} & -\frac{613}{72} & \frac{3}{4} \\ 0 & 0 & 0 & 0 & \frac{7}{4} & -\frac{17}{6} & 0 \\ 0 & 0 & -9 & 0 & \frac{79}{12} & -\frac{661}{126} & 1 \\ 0 & 0 & 0 & 1 & 1 & 0 & 0 \\ 0 & \frac{7}{2} & 0 & -\frac{17}{6} & 0 & 0 & 1 \end{pmatrix}. \quad (\text{A.4})$$

### A.2 UV-sensitivity and EFT Counterterms

#### A.2.1 $R_h$ -dependence of Quadratic and Cubic Correlations

In this section we discuss the UV sensitivity of the correlations of quadratic fields with the quadratic bias operators and cubic fields with the cubic bias operators. As discussed in the

main text, the quadratic field correlations are represented by a one-loop power spectrum diagram. To show the UV sensitivity of these diagrams, we calculate them theoretically using  $R_h = 4h^{-1}\text{Mpc}$  and  $R_h = 6h^{-1}\text{Mpc}$  and take the ratio at a fixed wavenumber  $k = 0.017h\text{Mpc}^{-1}$ . We show the results in Table A.1. We can see a change at the 5% level at the chosen wavenumber.

	$F_2$	$\delta^2$	$S_2$
$\delta^2$	0.002	0.039	0.049
$-\Psi \cdot \nabla \delta$	0.010	0.041	0.049
$S_2$	0.012	0.049	0.052

Table A.1 Quadratic fields: Relative change in the amplitude of cross-correlations of quadratic fields with the quadratic bias operators at  $k = 0.042h\text{Mpc}^{-1}$  as we change the halo smoothing scale from  $R_h = 4h^{-1}\text{Mpc}$  to  $R_h = 6h^{-1}\text{Mpc}$ .

We then repeat the same exercise for cubic correlations. We will show that the two-loop irreducible diagrams are more UV-sensitive than two-loop reducible diagrams. We show the results in Tables A.2, A.3, and A.4 for irreducible diagrams, reducible diagrams and the total contribution, respectively. One can see in Table A.3 that most of the reducible two-loop diagrams of cubic correlations change by more than 80% as we change the halo smoothing scale from  $4h^{-1}\text{Mpc}$  to  $6h^{-1}\text{Mpc}$ . On the other hand, the irreducible two-loop diagrams show a weaker change at the 5% level. Note that in Tables A.2, A.3, A.4, and A.1 we use  $k = 0.042h\text{Mpc}^{-1}$ .

	$F_3$	$\delta^3$	$\mathcal{G}_3$	$\mathcal{G}_2\delta$	$\Gamma_3$	$\delta\delta^{(2)}$	$s^{(3)}$
$F_3$	0.023	-0.143	0.026	-0.067	0.013	-0.009	0.012
$\delta^3$	-0.143	0.085	0.098	0.073	0.048	0.086	0.112
$\mathcal{G}_3$	0.026	0.099	0.053	0.045	0.075	0.058	0.042
$\mathcal{G}_2\delta$	-0.067	0.073	0.045	0.078	0.046	0.083	0.104
$\Gamma_3$	0.013	0.048	0.075	0.046	0.049	0.049	0.053
$\delta\delta^{(2)}$	-0.009	0.086	0.058	0.083	0.050	0.086	0.086
$s^{(3)}$	0.012	0.112	0.042	0.104	0.053	0.086	0.108

Table A.2 Irreducible: Relative change in the amplitude of irreducible diagrams of the cross-correlations of cubic fields at  $k = 0.042h\text{Mpc}^{-1}$  as we change the halo smoothing scale from  $R_h = 4h^{-1}\text{Mpc}$  and  $R_h = 6h^{-1}\text{Mpc}$ .

	$F_3$	$\delta^3$	$\mathcal{G}_3$	$\mathcal{G}_2\delta$	$\Gamma_3$	$\delta\delta^{(2)}$	$s^{(3)}$
$\delta^3$	0.119	0.820	-	0.813	0.196	0.825	0.913

Table A.3 Reducible: Relative change in the amplitude of reducible diagrams of the cross-correlations of cubic fields at  $k = 0.042h \text{ Mpc}^{-1}$  as we change the halo smoothing scale from  $R_h = 4h^{-1} \text{ Mpc}$  to  $R_h = 6h^{-1} \text{ Mpc}$ .

	$F_3$	$\delta^3$	$\mathcal{G}_3$	$\mathcal{G}_2\delta$	$\Gamma_3$	$\delta\delta^{(2)}$	$s^{(3)}$
$F_3$	0.048	0.815	0.026	0.812	0.242	0.867	0.950
$\delta^3$	0.129	0.771	0.099	0.749	0.165	0.787	0.886
$\mathcal{G}_3$	0.026	0.099	0.053	0.045	0.075	0.058	0.042
$\mathcal{G}_2\delta$	0.128	0.750	0.045	0.721	0.164	0.773	0.872
$\Gamma_3$	0.153	0.752	0.075	0.722	0.135	0.762	0.874
$\delta\delta^{(2)}$	0.153	0.787	0.058	0.772	0.185	0.792	0.888
$s^{(3)}$	0.105	0.798	0.042	0.809	0.184	0.801	0.930

Table A.4 Full theory: Relative change in the amplitude full cross-correlations of cubic fields (reducible + irreducible) at  $k = 0.042h \text{ Mpc}^{-1}$  as we change the halo smoothing scale from  $R_h = 4h^{-1} \text{ Mpc}$  to  $R_h = 6h^{-1} \text{ Mpc}$ .

## A.2.2 Quadratic EFT Counterterms

After showing that the quadratic and orthogonalised cubic correlations in our model do indeed show some dependency on the halo smoothing scale, we want to discuss possible EFT counterterms to remove these UV-sensitivities. First, let us consider again the correlations of the quadratic fields  $\mathcal{D}_2$  with quadratic bias operators  $\mathcal{O}_2$ :

$$\langle \mathcal{D}_2 | \mathcal{O}_2 \rangle = \int_{\mathbf{q}} W_{R_h}(|\mathbf{k} - \mathbf{q}|) W_{R_h}(q) P_{\text{lin}}(q) P_{\text{lin}}(|\mathbf{k} - \mathbf{q}|) \mathcal{K}_{\mathcal{D}_2}(\mathbf{k} - \mathbf{q}, \mathbf{q}) \mathcal{K}_{\mathcal{O}_2}(\mathbf{k} - \mathbf{q}, \mathbf{q}) W_{R_f}(|\mathbf{k} - \mathbf{q}|) W_{R_f}(q), \quad (\text{A.5})$$

where  $\mathcal{D}_2 \in \{\delta^2, \Psi \cdot \nabla \delta, s^2\}$ ,  $\mathcal{O}_2 \in \{\delta^{(2)}, \delta^2, s^2\}$ , and  $q = kr_1$ . We write the low- $k$  limits of the described above in a matrix notation as

$$\lim_{q \rightarrow \infty} \langle \mathcal{D}_2^i | \mathcal{O}_2^j \rangle = \int_{\mathbf{q}} W_{R_f}(q)^2 P_{\text{lin}}(q)^2 \mathcal{M}_{\mathcal{D}_2 \mathcal{O}_2}^{ij}(k, r_1; R_h) \quad (\text{A.6})$$

Eq. (A.6) is a  $3 \times 3$  matrix of the cross-correlations of quadratic fields with quadratic bias operators. The matrix  $\mathcal{M}_{\mathcal{D}_2 \mathcal{O}_2}$  represents the UV limits of the product of two kernels in terms

of halo smoothing scale

$$\mathcal{M}_{D_2 B_2} = \begin{pmatrix} \frac{1}{21}k^2 R_h^2 - \frac{q^4}{21k^4} & 2 - \frac{2k^6 R_h^2}{q^4} & -\frac{4k^6 R_h^2}{3q^4} + \frac{4}{3}k^2 R_h^2 - \frac{4q^4}{3k^4} + \frac{4}{3} \\ \frac{q^4}{42k^4} - \frac{1}{42}k^2 R_h^2 & 0 & \frac{4}{15}k^2 R_h^2 - \frac{4q^4}{15k^4} \\ \frac{2}{63}k^2 R_h^2 - \frac{2q^4}{63k^4} & -\frac{4k^6 R_h^2}{3q^4} + \frac{4}{3}k^2 R_h^2 - \frac{4q^4}{3k^4} + \frac{4}{3} & -\frac{8k^6 R_h^2}{9q^4} + \frac{16}{9}k^2 R_h^2 - \frac{16q^4}{9k^4} + \frac{8}{9} \end{pmatrix} \quad (\text{A.7})$$

This shows that the halo smoothing affects the low- $k$  limit of quadratic correlations and hence the measurements of bias parameters. This dependency should be removed by adding appropriate counterterm. At the leading order we can add a constant and a  $k^2$  counter term. There are two ways to include these counter term: (1) power spectrum level and (2) at field level. We discuss both cases now.

1. **At the power spectrum level:** The counterterms at the power spectrum are constant terms  $\alpha_0$  and the  $k^2$ , the coefficient of which is denoted by  $\alpha_2$ . These two counterterms take into account the effects of the smoothing. The final expression thus reads:

$$\langle \delta^2 | \delta_h \rangle' = b_1 \langle \delta^2 | \delta^{(2)} \rangle' + b_2 \langle \delta^2 | \delta^2 \rangle' + b_{s^2} \langle \delta^2 | s^2 \rangle' + \alpha_1 + \beta_1 k^2 \quad (\text{A.8})$$

$$\langle -\Psi \cdot \nabla \delta | \delta_h \rangle' = b_1 \langle -\Psi \cdot \nabla \delta | \delta^{(2)} \rangle' + b_2 \langle -\Psi \cdot \nabla \delta | \delta^2 \rangle' + b_{s^2} \langle -\Psi \cdot \nabla \delta | s^2 \rangle' + \alpha_2 + \beta_2 k^2 \quad (\text{A.9})$$

$$\langle s^2 | \delta_h \rangle' = b_1 \langle s^2 | \delta^{(2)} \rangle' + b_2 \langle s^2 | \delta^2 \rangle' + b_{s^2} \langle s^2 | s^2(\mathbf{k}') \rangle' + \alpha_3 + \beta_3 k^2 \quad (\text{A.10})$$

The functional form of  $\alpha_i$  and  $\beta_i$  (where  $i = 1, 2$  and  $3$ ) in these statistics come from the large scale limit of the quadratic field kernels. We can easily define them from Eq. (A.7) as follows:

$$\begin{aligned} \alpha_1 &= \frac{1}{50} (2b_{s^2} + 3b_2) (363360R_h^2 + 145318897) \\ \beta_1 &= -\frac{1}{700} (28b_{s^2} + b_1) (25103R_h^2 + 9902453) \end{aligned} \quad (\text{A.11})$$

$$\begin{aligned} \alpha_2 &= 0 \\ \beta_2 &= \frac{(5b_1 - 56b_{s^2}) (25103R_h^2 + 9902453)}{7000} \end{aligned} \quad (\text{A.12})$$

$$\begin{aligned} \alpha_3 &= \frac{1}{75} (2b_{s^2} + 3b_2) (363360R_h^2 + 145318897) \\ \beta_3 &= -\frac{(56b_{s^2} + b_1 + 42b_2) (25103R_h^2 + 9902453)}{1050} \end{aligned} \quad (\text{A.13})$$

One can easily see that  $\alpha_3 = \frac{2}{3}\alpha_1$  and  $\alpha_2 = 0$  which eventually brings down the number of counterterms to four ( $\alpha_1, \beta_1, \beta_2, \beta_3$ ). One disadvantage of defining the

counterterms at the power spectrum rather than field level, is that it doesn't allow for cosmic variance cancellation.

2. **At the field level:** at the field level the EFT counterterms correspond to two derivative operators:

$$\delta_h(\mathbf{x}) = b_1 \delta(\mathbf{x}) + b_2 \delta^2(\mathbf{x}) + b_{s^2} s^2(\mathbf{x}) + \beta \nabla^2 \delta^2(\mathbf{x}) + \alpha \delta \nabla^2 \delta(\mathbf{x}) + \dots \quad (\text{A.14})$$

On large scales, the cross correlation of  $\delta^2$  with the counterterms give

$$\lim_{k \rightarrow 0} \langle \delta^2 | \nabla^2 \delta^2 \rangle = -k^2 \int_{\mathbf{q}} P_{\text{lin}}(q)^2 W_{R_f}(q)^2 W_{R_h}(q)^2 \Rightarrow k^2 \times \text{constant} \quad (\text{A.15})$$

$$\lim_{k \rightarrow 0} \langle \delta^2 | \delta \nabla^2 \delta \rangle = - \int_{\mathbf{q}} q^2 P_{\text{lin}}(q)^2 W_{R_f}(q)^2 W_{R_h}(q)^2 \Rightarrow \text{constant} \quad (\text{A.16})$$

For the three quadratic statistics, there are total of six counterterms. However, as already shown above, two counterterms can be eliminated giving us final four counterterms. The advantage of including the EFT counterterms at the field level is that we can not only compare the magnitudes of Fourier components but also their phases. In other words, we can obtain the constraints by minimizing  $\langle D_2[\delta] | \delta_h^{\text{sim}} - \delta_h^{\text{model}} \rangle$ . If we compute the terms in  $\delta_h^{\text{model}}$  with the same phase as  $\delta_h^{\text{sim}}$ , the random fluctuations (from sampling initial conditions) will be canceled and the bias constraints will improved significantly.

### A.2.3 Cubic EFT Counterterms

Exactly the same procedure can be applied to study the cubic EFT counter term. First, let us consider the UV limits of smoothed cubic kernels  $\mathcal{O}_3^{R_h}(\mathbf{k}, -\mathbf{q}, \mathbf{q}) = W_{R_h}(q)^2 W_{R_h}(k) \mathcal{O}_3(\mathbf{k}, -\mathbf{q}, \mathbf{q})$ , which appear in the reducible diagrams :

$$\begin{aligned}
\lim_{k \rightarrow 0} F_3^{R_h}(\mathbf{k}, -\mathbf{q}, \mathbf{q}) &\approx \left( \frac{61R_h^2}{1890} - \frac{61}{1890q^2} \right) + \frac{37k^4R_h^2}{3780q^2} + k^2 \\
\lim_{k \rightarrow 0} \delta^{3,R_f}(\mathbf{k}, -\mathbf{q}, \mathbf{q}) &\approx -\frac{1}{2}k^2R_h^2 - q^2R_h^2 + 1 \\
\lim_{k \rightarrow 0} \mathcal{G}_3^{R_h}(\mathbf{k}, -\mathbf{q}, \mathbf{q}) &\approx 0 \\
\lim_{k \rightarrow 0} \delta \mathcal{G}_2^{R_h}(\mathbf{k}, -\mathbf{q}, \mathbf{q}) &\approx \frac{2}{9}k^2R_h^2 + \frac{4}{9}q^2R_h^2 - \frac{4}{9} \\
\lim_{k \rightarrow 0} \Gamma_3^{R_h}(\mathbf{k}, -\mathbf{q}, \mathbf{q}) &\approx \frac{32k^4R_h^2}{2205q^2} + k^2 \left( \frac{64R_h^2}{315} - \frac{64}{315q^2} \right) \\
\lim_{k \rightarrow 0} \delta F_2^{R_h}(\mathbf{k}, -\mathbf{q}, \mathbf{q}) &\approx -\frac{17}{63}k^2R_h^2 - \frac{34}{63}q^2R_h^2 + \frac{34}{63} \\
\lim_{k \rightarrow 0} S_2 F_2^{R_h}(\mathbf{k}, -\mathbf{q}, \mathbf{q}) &\approx k^2 \left( \frac{2R_h^2}{27} - \frac{16}{63q^2} \right) + \frac{8k^4R_h^2}{441q^2} - \frac{68}{189}q^2R_h^2 + \frac{68}{189}
\end{aligned} \tag{A.17}$$

The UV limits of smoothed cubic irreducible kernels  $\lim_{k \rightarrow 0} \mathcal{O}_3^{R_h}(\mathbf{k} - \mathbf{q} - \mathbf{p}, \mathbf{q}, \mathbf{p}) = \lim_{k \rightarrow 0} W_{R_h}(|\mathbf{k} - \mathbf{p} - \mathbf{q}|)W_{R_h}(p)W_{R_h}(q)\mathcal{O}_3(\mathbf{k} - \mathbf{q} - \mathbf{p}, \mathbf{q}, \mathbf{p})$  contain many terms and it is therefore not convenient to write down the full expressions here. However, we refer to [16] where one can find a good discussion about the UV limits of the two-loop power spectrum integrals and gravitational kernels in detail. In addition, to get an intuition of the low- $k$  behaviour of the orthogonality cubic correlations we refer to Fig 4.7.

Similar to quadratic statistics, the UV limits of cubic kernels require the inclusion of two counter terms (a constant term  $\alpha$  and a  $k^2$  term  $\beta$ ) for each cubic statistic. At the field level, these two counter terms correspond to two higher derivative bias operators, that is  $\delta^2 \nabla^2 \delta$  and  $\nabla^2 \delta^3$  for constant and  $k^2$  counterterms respectively. To summarise, we need at least two EFT counterterms for each quadratic and cubic statistics which means that to obtain consistent halo bias constraints up to cubic order from three quadratic and seven cubic statistics one is required to include  $\mathcal{O}(15)$ - $\mathcal{O}(20)$  EFT counterterms. The large number of the EFT counterterms for bias measurements is the main motivation for us to use the Taylor expansion method described in the main text.



## Fisher Information Matrix

In literature we have seen that people often use two different versions of the Fisher matrix. One at the fields level and one at the power spectrum level. For our understanding we derive the Fisher information matrix and compare both formulae. We use an example to measure  $\sigma(b_1)$  and  $\sigma(A_s)$  from both formulae and show that they are basically the same. So at the end we have to be careful what observational data vector we have and then we should decide which formula to use.

The derivation and discussion in this section is based on [205]. Suppose we have an  $n$ -dimensional data vector  $\mathbf{d} = \{d_1, d_2, \dots, d_n\}$ . The data points  $x_i$  represent measurements in cosmology, for instance it could be temperature in the  $n$  pixels of a CMB sky or the counts-in-cells of a galaxy redshift survey or observed galaxy density field. The data vector  $\mathbf{d}$  can be thought of as a random variable with some probability distribution  $p(\mathbf{d}, \Theta)$ , where  $\Theta$  vector depends on model parameters  $\Theta = \{\theta_1, \theta_2, \dots, \theta_n\}$ . This of vector of parameters is also a random variable. If  $\Theta_0$  represents the vector of true values of model parameters then we would like to it to be unbiased, that is  $\langle \Theta \rangle = \Theta_0$ , which means the error bars on the parameters are as small as possible. We can define Fisher information Matrix as follows

$$\mathbf{F}_{\alpha\beta} = \left\langle \frac{\partial^2 \mathcal{L}}{\partial \theta_\alpha \partial \theta_\beta} \right\rangle, \quad (\text{B.1})$$

where  $\mathcal{L} \equiv -\ln p(\mathbf{d}, \Theta)$  and is called the likelihood function.

We now explicitly compute the Fisher matrix in eq. (B.10) for the case when the probability distribution  $p(\mathbf{x}, \Theta)$  is Gaussian, that is

$$p(\mathbf{d}, \Theta) = \frac{1}{(2\pi \det(\mathbf{C}))^{N/2}} \exp\left(-\frac{(\mathbf{d} - \boldsymbol{\mu})\mathbf{C}^{-1}(\mathbf{d} - \boldsymbol{\mu})^t}{2}\right) \quad (\text{B.2})$$

where  $\mu$  is the mean of the data vector  $\langle \mathbf{d} \rangle = \mu$  and  $\mathbf{C}$  is the covariance matrix. We define the covariance matrix  $\mathbf{C}$  and the data matrix  $\mathbf{D}$  as

$$\mathbf{C} = \langle (\mathbf{d} - \mu)(\mathbf{d} - \mu)^t \rangle \quad (\text{B.3})$$

and

$$\mathbf{D} = (\mathbf{d} - \mu)(\mathbf{d} - \mu)^t \quad (\text{B.4})$$

respectively. We can now define the maximum likelihood function  $\mathcal{L}$  as (by ignoring the constant part)

$$2\mathcal{L} = \ln \det(\mathbf{C}) + (\mathbf{d} - \mu)\mathbf{C}^{-1}(\mathbf{d} - \mu)^t \quad (\text{B.5})$$

In matrix form we can write eq. (B.5) as

$$2\mathcal{L} = \text{Tr} \left[ \ln \mathbf{C} + \mathbf{C}^{-1} \mathbf{D} \right]. \quad (\text{B.6})$$

As the covariance matrix is a symmetric matrix, its derivative will also be a symmetric matrix. Taking the first derivative of eq. (B.6) with respect to parameters  $\theta_\alpha$  and after using some matrix identities we get

$$2 \frac{\partial \mathcal{L}}{\partial \theta_\alpha} = \text{Tr} \left[ \mathbf{C}^{-1} \frac{\partial \mathbf{C}}{\partial \theta_\alpha} - \mathbf{C}^{-1} \frac{\partial \mathbf{C}}{\partial \theta_\alpha} \mathbf{C}^{-1} \mathbf{D} + \mathbf{C}^{-1} \frac{\partial \mathbf{D}}{\partial \theta_\alpha} \right]. \quad (\text{B.7})$$

Remember that we evaluate the covariance and the mean at the data vector at the true parameter values, which gives the following relations:

$$\begin{aligned} \langle \mathbf{D} \rangle &= \mathbf{C}, \\ \left\langle \frac{\partial \mathbf{D}}{\partial \theta_\alpha} \right\rangle &= 0, \\ \left\langle \frac{\partial^2 \mathbf{D}}{\partial \theta_\alpha \partial \theta_\beta} \right\rangle &= \frac{\partial \mu}{\partial \theta_\alpha} \frac{\partial \mu^t}{\partial \theta_\beta} + \frac{\partial \mu}{\partial \theta_\beta} \frac{\partial \mu^t}{\partial \theta_\alpha}. \end{aligned} \quad (\text{B.8})$$

Using these relations we obtain  $\langle \mathcal{L}_{,\alpha} \rangle = 0$ , where the comma notation represents the derivative. Taking another derivative of eq. (B.7) we get

$$\begin{aligned} 2 \frac{\partial^2 \mathcal{L}}{\partial \theta_\alpha \partial \theta_\beta} &= \text{Tr} \left[ -\mathbf{C}^{-1} \frac{\partial \mathbf{C}}{\partial \theta_\alpha} \mathbf{C}^{-1} \frac{\partial \mathbf{C}}{\partial \theta_\beta} + \mathbf{C}^{-1} \left( \frac{\partial \mathbf{C}}{\partial \theta_\alpha} \mathbf{C}^{-1} \frac{\partial \mathbf{C}}{\partial \theta_\beta} + \frac{\partial \mathbf{C}}{\partial \theta_\beta} \mathbf{C}^{-1} \frac{\partial \mathbf{C}}{\partial \theta_\alpha} \right) \mathbf{C}^{-1} \mathbf{D} \right. \\ &\quad + \mathbf{C}^{-1} \frac{\partial^2 \mathbf{C}}{\partial \theta_\alpha \partial \theta_\beta} - \mathbf{C}^{-1} \left( \frac{\partial \mathbf{C}}{\partial \theta_\alpha} \mathbf{C}^{-1} \frac{\partial \mathbf{C}}{\partial \theta_\beta} + \frac{\partial \mathbf{C}}{\partial \theta_\beta} \mathbf{C}^{-1} \frac{\partial \mathbf{D}}{\partial \theta_\alpha} \right) - \mathbf{C}^{-1} \frac{\partial^2 \mathbf{C}}{\partial \theta_\alpha \partial \theta_\beta} \mathbf{C}^{-1} \mathbf{D} \\ &\quad \left. + \mathbf{C}^{-1} \frac{\partial^2 \mathbf{D}}{\partial \theta_\alpha \partial \theta_\beta} \right]. \end{aligned} \quad (\text{B.9})$$

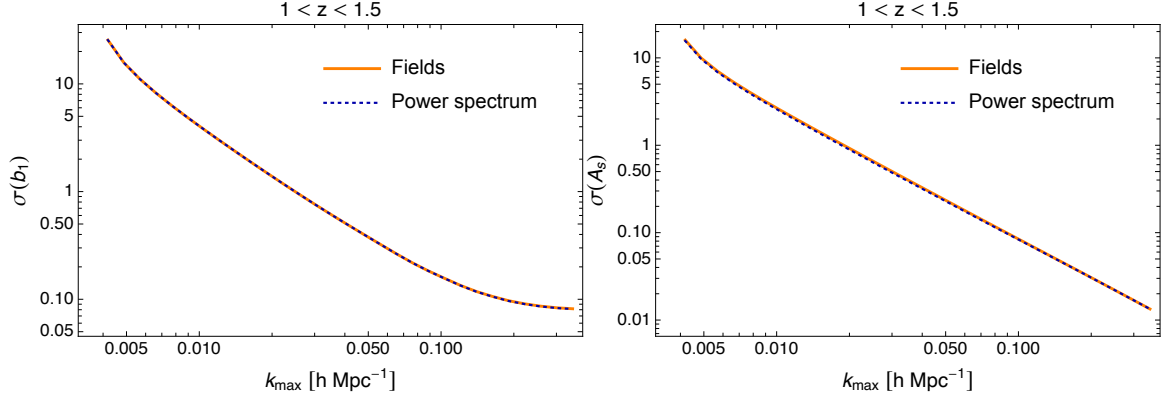


*Fig. B.1* Constraints on  $b_1$  and  $A_s$  using combined galaxy-lensing 2-point functions. We show results Fisher analysis at the power spectrum level, given by Eq. (B.12), and at the fields level, given by Eq. (B.11).

Finally we substitute eq. (B.9) in eq. (B.10) and to get the final expression for Fisher matrix:

$$\mathbf{F}_{\alpha\beta} = \left\langle \frac{\partial^2 \mathcal{L}}{\partial \theta_\alpha \partial \theta_\beta} \right\rangle = \frac{1}{2} \text{Tr} \left[ \mathbf{C}^{-1} \frac{\partial \mathbf{C}}{\partial \theta_\alpha} \mathbf{C}^{-1} \frac{\partial \mathbf{C}}{\partial \theta_\beta} + \mathbf{C}^{-1} \left( \frac{\partial \mu}{\partial \theta_\alpha} \frac{\partial \mu^t}{\partial \theta_\beta} + \frac{\partial \mu}{\partial \theta_\beta} \frac{\partial \mu^t}{\partial \theta_\alpha} \right) \right]. \quad (\text{B.10})$$

If we write the Fisher matrix at the field's level we can choose the mean of the data vector  $\langle \mathbf{d} \rangle = \mu = 0$  and so eq. (B.10) becomes

$$\mathbf{F}_{\alpha\beta} = \frac{1}{2} \text{Tr} \left[ \mathbf{C}^{-1} \frac{\partial \mathbf{C}}{\partial \theta_\alpha} \mathbf{C}^{-1} \frac{\partial \mathbf{C}}{\partial \theta_\beta} \right]. \quad (\text{B.11})$$

whereas if the data vector comprise of power spectrum then eq. (B.10) can be simplified to

$$\mathbf{F}_{\alpha\beta} = \text{Tr} \left[ \frac{\partial \langle \mathbf{d} \rangle}{\partial \theta_\alpha} \mathbf{C}^{-1} \frac{\partial \langle \mathbf{d}^t \rangle}{\partial \theta_\beta} \right], \quad (\text{B.12})$$

No matter which one we use we should get the same results. In this work we will use both eq. (B.11) and eq. (B.12). In a later section we discuss results from auto- and cross correlations of galaxy with the CMB lensing using 2-pt, 3-pt and 2- & 3-pt functions analysis. For the 2-pt functions we use eq. (B.11) and for 3-pt we use eq. (B.12).

In Fig. B.1 we show that constraints obtained from Eq. (B.11) and Eq. (B.12) are the same.



## Limber Approximation

the derivation in this appendix is adapted from [133]. Let us think about the 2D power spectrum in the flat sky limit (for a comparison with the angular power spectrum). For this we use  $x_{\parallel}$  as the line-of-sight direction and  $x_{\perp}$  the perpendicular direction. We integrate the density field along the line of sight direction.

$$\delta_{2D}(x_{\perp}) = \int dx_{\parallel} W(x_{\parallel}) \delta(x_{\perp}, x_{\parallel}) \quad (\text{C.1})$$

and in Fourier space

$$\delta_{2D}(k_{\perp}) = \int dx_{\perp} \exp(-ik_{\perp} \cdot x_{\perp}) \int dx_{\parallel} W(x_{\parallel}) \delta(x_{\perp}, x_{\parallel}) \quad (\text{C.2})$$

so the 2D power spectrum is given by

$$\begin{aligned} \langle \delta_{2D}^A(k_{\perp}) \delta_{2D}^B(k'_{\perp}) \rangle &= \int dx_{\parallel}^A W_A(x_{\parallel}) \int dx_{\parallel}^B W_B(x_{\parallel}) \int \frac{dk_{\parallel}}{(2\pi)} \exp(-ik_{\parallel}(x_{\parallel}^A - x_{\parallel}^B)) \\ &P_{AB}(k_{\perp}, k_{\parallel}) (2\pi)^2 \delta^{(2D)}(k_{\perp} + k'_{\perp}) \end{aligned} \quad (\text{C.3})$$

Expanding the power spectrum about  $k_{\parallel} = 0$  and assuming  $P_{AB}(k_{\perp}, k_{\parallel}) = P_{AB}(\sqrt{k_{\parallel}^2 + k_{\perp}^2})$  gives

$$P_{2D}(k_{\perp}) = \int dx_{\parallel} W(x_{\parallel})_A W(x_{\parallel})_B \left\{ 1 + \frac{1}{2} \frac{1}{x_{\parallel}^2 k_{\perp}^2} \left( \frac{d \ln P_{AB}}{d \ln k} \frac{d \ln W(x_{\parallel})_A}{d \ln x_{\parallel}} \frac{d \ln W(x_{\parallel})_B}{d \ln x_{\parallel}} + \mathcal{O}((k_{\perp} x_{\parallel})^{-4}) \right) \right\} \quad (\text{C.4})$$

where the derivatives of  $P_{AB}$  are evaluated at  $k_{\parallel} = 0$ . Notice that all of the  $P_{AB}$  factors are independent of  $x_{\parallel}$ . Angular power spectrum is related to the 2D projected power spectrum as

$$l(l+1)C_l \approx k_{\perp}^2 P(k_{\perp}) \quad (\text{C.5})$$

for large  $l$ .

Now consider two random fields  $A(x)$  and  $B(x)$ . We define the angular power spectrum in spherical harmonics as follows

$$C_{AB}(l) = \int k dk P_{AB}(k) \int dr_1 f_A(r_1) J_{l+1/2}(kr_1) \int dr_2 f_B(r_2) J_{l+1/2}(kr_2) \quad (\text{C.6})$$

where  $j_l$ 's are spherical Bessel functions of rank  $l$  and  $f$ 's are defined as

$$f_i(r) \equiv \frac{W_i(r)}{\sqrt{r}} \quad i \in \{A, B\}. \quad (\text{C.7})$$

and  $kr = v = l + 1/2$

after some simplification (and algebraic manipulation) we get

$$C_{AB}(l) = \int \frac{dk}{k} P_{AB}(k) f_A(r) f_B(r) \left\{ 1 + \frac{v^{-2}}{2} \left[ \frac{d \ln f_A}{d \ln r} \frac{d \ln f_B}{d \ln r} s(k) - p(k) \right] + \mathcal{O}(v^{-4}) \right\} \quad (\text{C.8})$$

where

$$s(k) = \frac{d \ln P_{AB}(k)}{d \ln k} \quad \text{and} \quad p(k) = \frac{k^2 \left( 3P_{AB}''(k) + kP_{AB}'''(k) \right)}{3P_{AB}(k)} \quad (\text{C.9})$$

Eqs. (C.8) and (C.9) show the first systematic correction to the Limber approximation which can be used to reduce the error in the approximation from  $l^{-2}$  to  $l^{-4}$ . There are some observations:

- We see that the convergence of the Limber expansion depends on both  $v = l + 1/2$  and the kernels  $f_A, f_B$
- If the both the kernels are peaked at the same distance  $\bar{r}$ , the  $1/v^2$  term is subdominant when  $v \geq \bar{r} \max[\sigma_A, \sigma_B]$  where  $\sigma$ 's are the width of the kernels.
- If the kernels are peaked at different distances, say  $r_A \geq r_B + \sigma_B$  where  $r_A$  and  $r_B$  are the location of the maxima, truncating the expansion requires  $v \geq \bar{r}(r_A - r_B)/\sigma_A \sigma_B$

Now going back to Eq. (C.5), let us expand  $\frac{1}{r^2} P(v/r)$  around  $r = \bar{r}$  where  $\bar{r}$  is the peak distance of kernels  $W_A(r)W_B(r)$  and compare it with Eq. (C.4) we can see that indeed  $l(l+1)C_l \approx k_{\perp}^2 P_{2D}(k_{\perp})$  for  $l + 1/2 = \bar{r}k_{\perp}$ .